Approximate vs. Purely Numerical Approaches for Full Waveform Modelling of Global Earth Structure

A thesis submitted to the School of Environmental Sciences
of the University of East Anglia in partial fulfilment
of the requirements for the degree of Doctor of Philosophy

Laura Parisi

September 2015

© This copy of the thesis has been supplied on condition that anyone who consults it is understood to recognise that its copyright rests with the author and that use of any information derived there from must be in accordance with current UK Copyright Law. In addition, any quotation or extract must include full attribution.

© Copyright 2015
Laura Parisi

ABSTRACT

This thesis focuses on the global seismic forward modelling of body and surface waveforms in realistic 3-D Earth models using approximate and purely numerical methods. Firstly, we investigate two techniques: (i) the Born approximation, which should be valid for media with weak heterogeneity; and, (ii) the full ray theory approach, which should be valid for smooth media. We find that the Born approximation has a very limited domain of validity. It only models accurately surface waveforms with wave periods longer than T~80 s–90 s in existing earth models, and for T>120 s–130 s when models with stronger heterogeneity are considered. On the other hand, the full ray theory is valid for almost all the earth models considered, failing only for unrealistically rough models. Hence, there is scope to build future improved global tomographic models using this technique, which is computationally very efficient. We then use a purely numerical technique, the spectral element method, to assess the quality of a recently built global radially anisotropic mantle model (SGLOBE-rani). We find that it explains independent seismic data slightly better than a previous widely used model (S40RTS). Moreover, our tests find small data misfit differences between isotropic and anisotropic versions of the models considered, which highlight the difficulties in constraining 3-D radially anisotropic structure. Finally, we carry out forward modelling experiments of short-period (T>5 s) body waves travelling through the Earth's lowermost mantle and investigate the effects of isotropic (1-D and 3-D), anisotropic and attenuation structure on wave propagation. We find that phase interference can change the shape and apparent arrival-time of wave pulses. This can give rise to apparent SH-SV wave splitting, even when isotropic earth models are used. This suggests that caution should be taken when interpreting SH-SV splitting of deep mantle body waves exclusively in terms of anisotropy in the lowermost mantle.

ACKNOWLEDGEMENTS

I thank Ana Ferreira for her supervision, collaboration and support during my PhD experience. She often believed in me more than I did. She kept me inspired and motivated even when the logistics was not on our side. I still remember when I came to Norwich for the first time: after the two interviews (of which one with Ana), she asked me whether I wanted to continue our conversation on the PhD project, and I said NO. Thanks for understanding it was not a lack of interest. My brain was just exhausted after a few hours of various conversations in English!

I thank the QUEST project for its funding and training. QUEST allowed me to work without worrying about financial issues. It also allowed me to attend several national and international conferences, which kept me ambitious and introduced me into the global seismology people network.

I thank Yann Capdeville for his collaboration, support and for letting me feel home during my visit in Nantes. I also thank Marco Calò for conveying his passion for seismic imaging and because he kept me "shallow" during my "global" studies. I thank Jenni Barclay for her support at UEA and Wadud Miah for his technical help.

I thank my seismology group for reciprocal help and company. I thank Kostas Lentas and Sung-Joon Chang whose help was important during the first months of my PhD. I thank Lewis Schardong and Andrea Berbellini for our scientific conversations using unconventional media. They really helped me to feel part of the group even when I was physically distant from it.

I thank Ana Domingues for her friendship. Plenty of patient, she helped me to improve my speaking at the beginning of this experience (even inventing new English-Italian-Portuguese words!). I also thank her because, despite she is a seismologist as well, we never talk about seismology. Just a bit of "scientific gossip".

I thank my Italian friends Desiré Di Silvio and Veronica Steri. Without their friendships, our mother-tongue conversations and our trips, this experience would have been much more difficult.

I thank all the new friends I made during conferences and workshops. Lucia Gualtieri, Julie Baron, the German mathematician Philip, Fabien Engels and many other people really added some fun to my job.

I thank my parents and their grandpa taxi and caring services for my son Bruno. Without their support my PhD would have been even heavier for Bruno and I would have missed many important opportunities during my PhD. I also thank them because they trusted me and my ambitions and materially helped me achieve my personal and professional goals.

My special thank goes to Bruno. He attended Math lectures when he was still inside me.

He used to ask me: "when you finish studying will you play with me, mum?" when he was a toddler. He graduated with me. He learnt to speak and write in other two languages to follow my ambitions. Now he corrects my pronunciation before my oral presentations and looks at every kind of global maps with me with genuine interest. Thanks for understanding that everything I have done is also to give a better future to you.

At last (but not least!), I thank Luigi for his love. Thank you for being my biggest fan, for following me everywhere, for surviving to live with a student in seismology, for our sleepless nights to save plots for my reports. Grazie!

The research in this thesis was carried out on the
High Performance Computing Cluster supported
by the Research and Specialist Computing
Support service at the University of East Anglia

CONTENTS

List of Figures

List of Tables

1

INTRODUCTION

1.1 GLOBAL SEISMOLOGY

The USGS (United States Geological Survey) estimates that every year more than 1.4 million earthquakes with magnitude larger than 2.0 occur worldwide. Large magnitude earthquakes (Mw $\geq$ 5.5) generate seismic waves that propagate around the globe and are recorded by seismometers worldwide. Seismologists use these recordings—seismograms—to investigate the kinematics and dynamics of earthquakes. Moreover, they use seismograms as probes of the structure of the Earth's interior. This is the fascinating geoscience discipline of global seismology and this thesis is a contribution in this field.

The outer shell of the Earth (~100 km–200 km) forms the lithosphere, which is subdivided in ~15 (almost) rigid tectonic plates, which move relatively to each other at the speed of a few cm per year. The movements occur over the weaker asthenosphere and are the main cause of earthquake occurrence, which is why most of the world's seismicity takes place on tectonic plate boundaries. Fig. 1.1 depicts the global spatial distribution of seismicity and its clear relation with plate boundaries.

From a seismic perspective, the subdivision of the Earth into crust, mantle, outer and inner core is normally used. Fig. 1.2 presents PREM (Dziewoński & Anderson, 1981, Preliminary Reference Earth Model), the most used 1-D global reference model. PREM has a 24.4 km-thick two-layer crust separated from the mantle by a strong discontinuity of the seismic properties (named Mohorovičić or Moho). The core-mantle boundary (CMB) at 2 891 km depth separates the mantle from the liquid outer core, where S waves cannot propagate. Finally, the inner-core boundary (ICB) separates the outer core from the solid inner core, where S waves can propagate again generated by the conversion of P waves crossing the liquid core.

This thesis investigates global seismic wave propagation in realistic 3-D media in order to better understand the Earth's mantle structure.

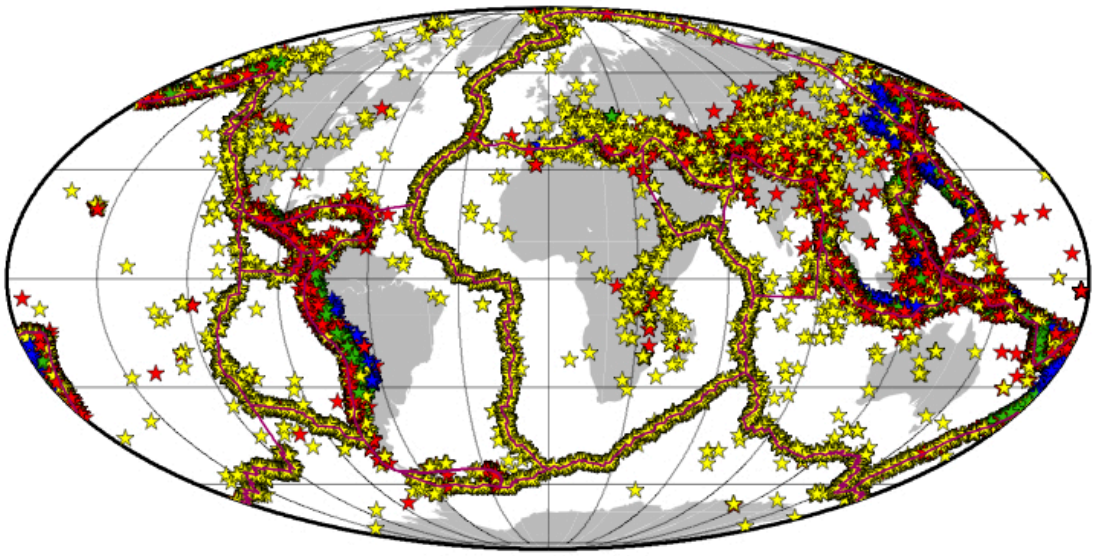

Figure 1.1: Global seismicity that occurred between 1976–2013 from the Global CMT catalogue (Mw>5.5, www.globalcmt.org). Events are shown with centroid depth: (i) shallower than 25 km (yellow); (ii) between 25 km and 100 km (red); (iii) between 100 km and 300 km (green); and, (iv) deeper than 300 km (blue). Lines in purple denote plate boundaries.

1.2 EARTH'S MANTLE INVESTIGATIONS

In this section we present the most common techniques used to probe the Earth's mantle. We start by briefly presenting seismic tomography—the large-scale imaging of the Earth's interior—followed by an introduction to target studies that model specific parts of the Earth, often with higher resolution than in tomography studies. Both classes of methods use the information carried by seismic waves propagating within the Earth to model the interior of our planet.

1.2.1 SEISMIC TOMOGRAPHY

Seismic tomography is a powerful geophysical tool to build images of the Earth's interior by characterising the spatial distribution of its seismic properties (e.g., Vp, Vs, anisotropy and attenuation). The first images of the Earth's mantle were produced in 1977 (e.g., Dziewoński *et al.*, 1977), based on P wave travel-times, and in 1984 from seismic waveforms (e.g., Woodhouse & Dziewoński, 1984). These early studies revealed many large-scale features of the Earth's interior (e.g., low velocity regions associated with ridges and high velocities with cratons), which are now well-known and reproducible. These analyses, as well as more recent tomography studies rely on ray theory, which is an infinite frequency approximation that represents a body or surface wave as a ray whose travel-time is only affected by the structure along the ray path. The numerical simplicity of this approach has enabled the use of large datasets to build new tomographic models in an efficient way, which may at least partly compensate the theoretical approximations used.

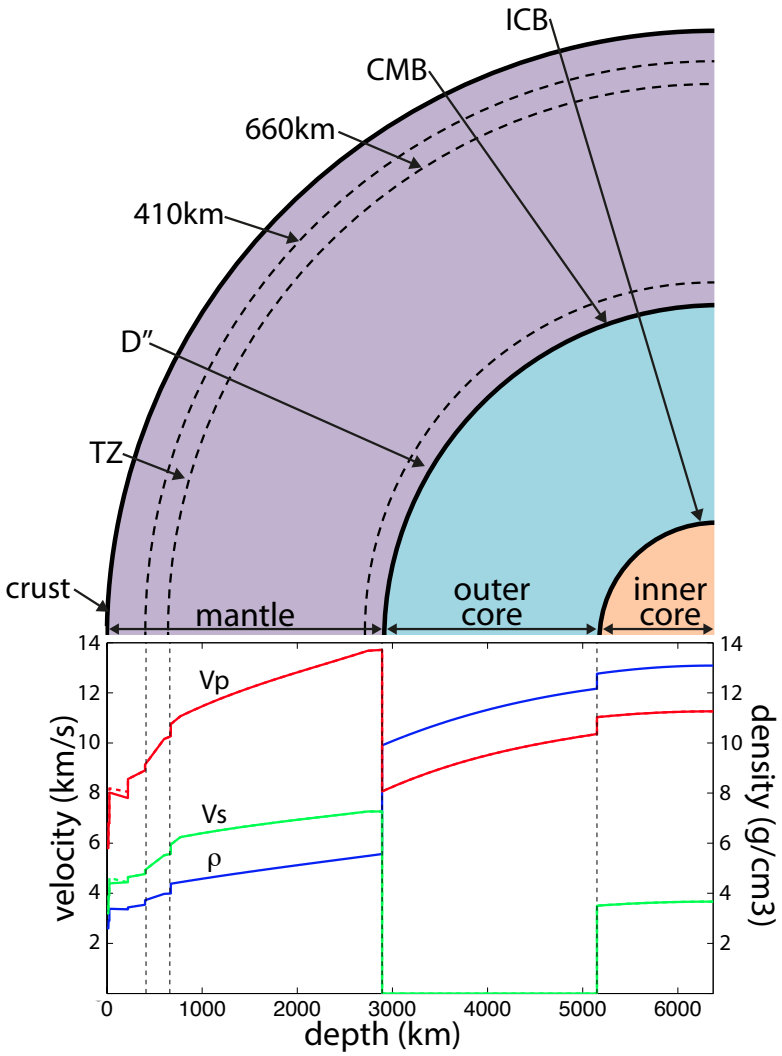

Figure 1.2: Schematic representation of the interior of the Earth following the Preliminary Reference Earth Model (PREM, Dziewoński & Anderson (1981)). Vp and Vs are compressional and shear seismic wave velocities, respectively. PREM includes radial anisotropy in the upper most mantle. Thus, green and red dashed lines are used to represent Vsh and Vph when these are different from Vsv and Vpv, respectively. ρ is the density. TZ: mantle transition zone; 410 km: seismic discontinuity within the upper mantle at 410 km; 660 km: seismic discontinuity at 660 km separating the upper from the lower mantle; D": D" layer (bottom of the lower most mantle); CMB: core-mantle-boundary at 2 891 km; ICB: inner-core-boundary at 5 150 km.

Body-wave travel times and surface wave dispersion data are complementary datasets. Surface waves are well suited for global tomographic studies because they offer excellent global coverage. However, their sensitivity is limited to down to ~1000 km depth (upper mantle, transition zone and uppermost lower mantle). Fig. 1.3 compares three recent shear wave speed tomographic models, SL2013sv (Schaeffer & Lebedev, 2013), SEMum2 (French *et al.*, 2013) and DR2012 (Debayle & Ricard, 2012) of the upper mantle strongly based on surface wave data. The models are defined as perturbations of Vs with respect to PREM. The correlation among these models is significant in the shallower 200 km (uppermost mantle),

where the heterogeneity is stronger and follows the long wave-length tectonic patterns (e.g, low velocity anomalies under oceanic ridges and high velocity anomalies under the continental shields). The main features of the mantle transition zone (TZ, around 410 km–660 km) are the fast anomalies corresponding to subducted slabs but significant discrepancies arise from the comparison of these models (e.g., in the Pacific Ocean at 600 km and 700 km) where the resolution of surface wave data starts to vanish.

On the other hand, body-waves have deeper ray paths than surface waves allowing the sampling of the lower mantle (particularly of the lowermost mantle). Tomographic models obtained by inverting body-wave data have a good resolution in proximity of the subduction zones. However, the lack of dense seismic stations in the oceans limits the resolution in such regions. Body waves have been used in whole mantle tomography either alone (e.g., Montelli *et al.*, 2004; Fukao & Obayashi, 2013) or in combination with surface waves and/or normal mode data (e.g., Ritsema *et al.*, 2011; Chang *et al.*, 2015). Fig. 1.4 compares five recent whole mantle tomographic models: S362WANI+M by Moulik & Ekström (2014), SAW642ANb by Lekić *et al.* (2010), S40RTS by Ritsema *et al.* (2011), SAVANI by Auer *et al.* (2014) and SGLOBE-rani by Chang *et al.* (2015) in which data from both surface and body waves are employed. As already seen for the upper mantle models, there is a certain level of agreement among the whole mantle tomographic models for the first hundreds of km and for the large scale heterogeneity. Between ~1 000 km–2000 km depth, the tomographic maps are characterised by weak heterogeneity except for 2 stronh slow anomalies beneath the African continent. At the bottom of the mantle, two robust low velocity anomalies under Africa and Pacific ocean (Large Low Shear Velocity Provinces, LLSVPs) dominate in all the tomographic models.

1.2.2 TARGETED SEISMIC STUDIES

Whilst seismic tomography produces extensive and smooth images of the Earth, several targeted studies have been performed to resolve the fine earth structure of specific regions of the globe. We here report some examples of key findings from such studies.

As seen in section 1.1, the movements of the lithosphere over the asthenosphere are the basis of plate tectonics. Thus, processes at the lithosphere-asthenosphere boundary (LAB) are fundamental to understand the dynamics of the Earth. These have been investigated inverting and modelling reflected body-waves (see Fischer *et al.* (2010) for a review). Whilst reverberations of the ScS phase (S wave reflected off the CMB) from the LAB have been observed in oceanic environments (e.g., Bagley & Revenaugh, 2008), studies based on P-to-s (Ps) and S-to-p (Sp) converted phases at the LAB are common in both oceanic and continental environments (Fischer *et al.* (2010) and references therein). The correlation between LAB's depth and plate tectonics is strong. For example, Rychert & Shearer (2009), using Ps phases, imaged a surface whose depth varies from about 95 km under the continental shields to 70 km under the ocean islands. Moreover, Kawakatsu *et al.* (2009), employing Sp and Ps phases, showed that the position of the LAB in the oceanic plates is sharp and age-dependent.

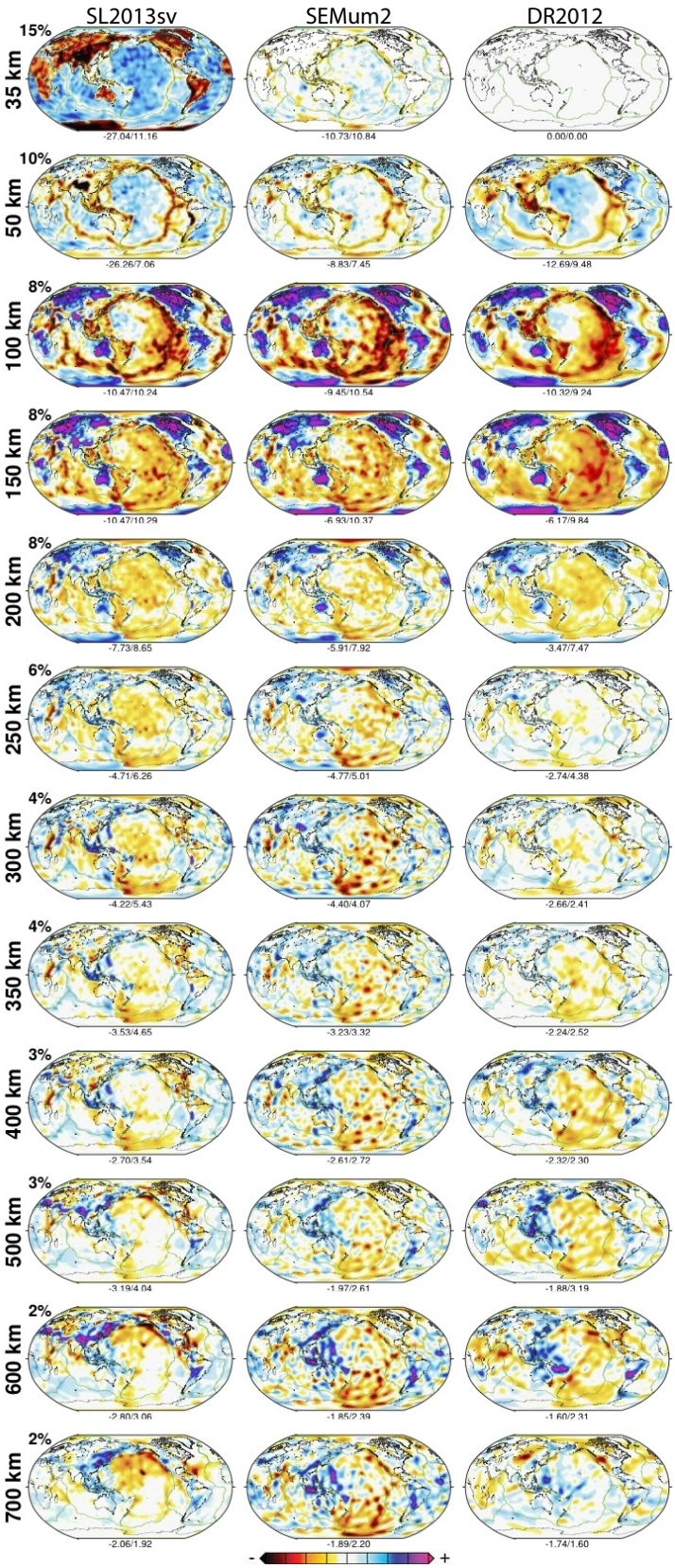

Figure 1.3: Comparison between recent upper mantle global tomographic models by Schaeffer & Lebedev (2013); French *et al.* (2013); Debayle & Ricard (2012) (from left to right). Shear wave speed perturbations are plotted in percentage with respect to the mean value for that model. The minimum and maximum values are indicated underneath each map, and the same linear colour scale spans from negative to positive saturation values indicated for each depth (at left). Plot courtesy of Andrew Schaeffer.

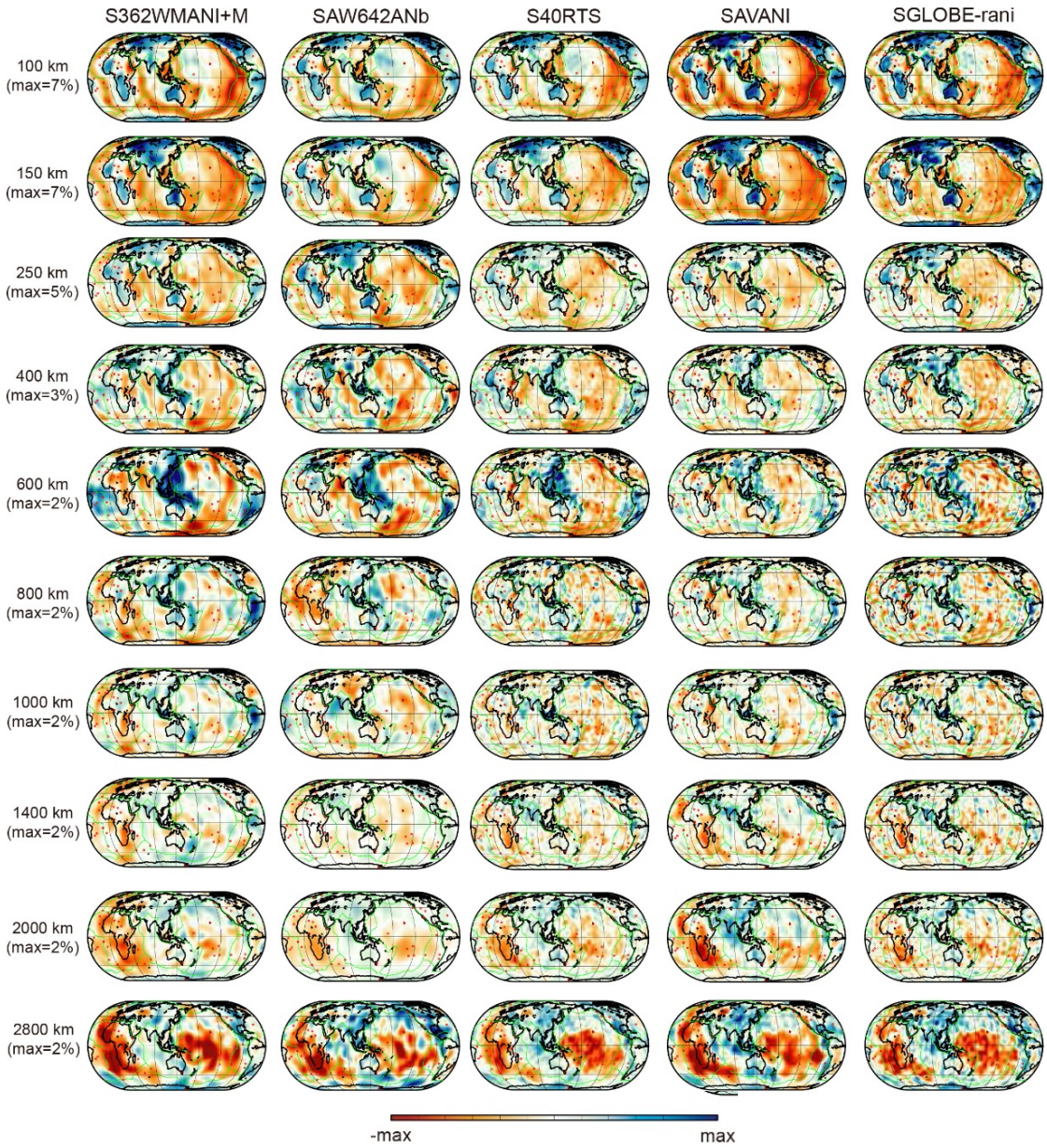

Figure 1.4: Comparison of whole mantle global tomographic models by Moulik & Ekström (2014); Lekić *et al.* (2010); Ritsema *et al.* (2011); Auer *et al.* (2014); Chang *et al.* (2015) (from left to right). Shear speed perturbations with respect to the PREM model are plotted with the same linear colour scale, which spans negative to positive values shown for each depth (on the left). Figure modified from Chang *et al.* (2015).

The mantle TZ (Fig. 1.2) divides the upper from the lower mantle and is defined by two seismic discontinuities located at approximately 410 km and 660 km. The TZ is believed to be a reservoir of water contained in high-pressure minerals (e.g., Bercovici & Karato, 2003). Its properties could potentially distinguish between whole-mantle and layered-mantle convection (Hofmann, 1997). The topography of these discontinuities has been inferred from the differential arrival-times of stacked SS phases (S waves downside reflection at the Earth's surface), and relative precursors (S410S and S660S), and converted phases (e.g., Shearer

& Masters, 1992; Deuss & Woodhouse, 2001; Gu & Dziewoński, 2002; Tauzin *et al.*, 2008). The isochemical phase transition nature of these discontinuities, due to the rapid pressure increase with depth, is still debated (e.g, Lebedev *et al.* (2002); Schmerr & Garnero (2007). The detection and nature of the 410-km and 660-km discontinuities could also be complicated by the presence of a low velocity layer above the 410-km discontinuity (Tauzin *et al.*, 2010) and multiple phase transitions around the 660-km discontinuity (Deuss *et al.*, 2006).

Another region of the Earth, which has represented the subject of several imaging studies, is the D" layer. The latter includes a region of 150 km–300 km at the bottom of the lowermost mantle (Fig. 1.2) and it represents a thermal boundary between the mantle and the liquid core. The thermal instability at the CMB could represent the cause of the existence of deep mantle plumes. Wysession *et al.* (1998) demonstrated the presence of a sharp velocity increase at the top of the D". This has been explained with the presence of subducted slabs at the bottom of the mantle (e.g., Wysession, 1996; Loubet *et al.*, 2009). Many seismic studies of the D" layer targeted the LLSVPs, which are believed to have distinctive composition because of of their very low S wave velocity, moderately low P wave velocity and possibly high density (e.g, McNamara & Zhong (2005); Garnero & McNamara (2008); Lekić *et al.* (2012)). Seismic anisotropy, which is the directional dependence of seismic velocity and can generate the splitting of horizontal and vertically polarised body-waves, was observed in the D" layer by several authors, mainly using S and ScS phases (e.g., Vinnik *et al.*, 1995, 1998; Pulliam & Sen, 1998; Ritsema *et al.*, 1998; Kendall & Silver, 1998; Fouch *et al.*, 2001). However, modelling studies showed that anisotropy may not be the only cause for the SH-SV splitting observed (see, e.g., Maupin, 1994; Komatitsch *et al.*, 2010b).

1.3 CHALLENGES AND DIRECTIONS

In section 1.2.1 we presented some tomographic models defined in terms of Vs perturbations. However, in order to understand the geodynamical behavior of our planet we need to image other properties such as attenuation and anisotropy. In this section, we present the main current challenges in global tomography to retrieve different seismic attributes and discuss some key issues that global tomographers are facing.

Seismic attenuation in the mantle is a function of its composition, temperature, water content and partial melt. Hence, the joint interpretation of elastic and anelastic structure is important to better understand these properties of the Earth's interior. Attenuation tomography is lagging behind elastic seismic tomography. Most of the previous attenuation tomography imaged the attenuation structure in the upper mantle using either surface waves or body-waves (e.g., Romanowicz, 1995; Bhattacharyya *et al.*, 1996; Selby & Woodhouse, 2002; Gung & Romanowicz, 2004; Dalton *et al.*, 2008). The main result of such studies is the correlation at shallow depths (down to 200 km–250 km) with tectonics (Dalton *et al.*, 2009) but strong differences among these models remain. There have also been attempts to resolve attenuation structure in the lower mantle using body-waves (Lawrence & Wysession, 2006; Hwang *et al.*, 2011) but a strong disagreement came from these results. The main difficulties

in attenuation tomography are to accurately measure wave amplitudes and to separate the effects of elastic and anelastic structure on the seismograms. When surface waves are used, the latter issue can be addressed e.g. by considering amplitude ratios of consecutive Rayleigh wave trains around the globe. (e.g., Durek & Ekström, 1996; Dalton *et al.*, 2008). However, very long-time, high-quality time series are needed for such analyses.

The reference model PREM includes radial anisotropy in the uppermost mantle to explain the systematic delay of Rayleigh waves with respect to Love waves (see Fig. 1.2) observed since the 1960s (e.g., Hess, 1964). Moreover, observations of seismic anisotropy in the whole mantle have led to several attempts to constrain 3-D anisotropic variations in the mantle (e.g., Ekström & Dziewonski, 1998; Shapiro & Ritzwoller, 2002; Ferreira *et al.*, 2010; Lekić & Romanowicz, 2011; French & Romanowicz, 2014; Chang *et al.*, 2015). Seismic anisotropy in the mantle is a fundamental piece of information to infer the geometry of mantle flow when interpreted together with mineral physics. However, despite recent progress, there are still discrepancies in the radially anisotropic structure in the most recent tomographic models (e.g., Auer *et al.*, 2014; Moulik & Ekström, 2014; French & Romanowicz, 2014; Chang *et al.*, 2015). For example, Chang *et al.* (2014) showed that a trade-off between isotropic heterogeneities and anisotropic structure in the D" is a possible cause of these discrepancies. Ferreira *et al.* (2010) and Bozdağ & Trampert (2008) discussed also the issues related to the influence of the crust when inferring radial anisotropy.

Crustal effects are an important issue in global tomography even when only the isotropic structure is considered. In fact, the crust has a strong influence on surface wave dispersion even at the long periods usually considered in such studies (T>60 s). The effects of the crust need to be separated from those due to the mantle prior to the inversion. To properly account for crustal effects, the crustal structure has to be known and the corrections must be accurately calculated. Traditionally, linear crustal corrections have been used (e.g., Woodhouse & Dziewoński, 1984) because of the minimal associated computational cost and physical simplicity of the approach. However, Vs and Moho variations in the crust are too large to be handled by linear corrections. More complete approaches have been formulated (e.g., Montagner & Jobert, 1988; Boschi & Ekström, 2002; Lekić *et al.*, 2010; Chang *et al.*, 2015) but these increase the cost of the computations and their effects on the tomographic models are still debated.

Other heavily debated topics in global seismology are the data and methods used. Most of the global tomographic models are based on so-called secondary observables of the seismograms. That is, for example, phase delays of body waves and dispersion curves of surface waves are obtained from the seismograms, and thus all the other information potentially carried by the seismic traces is neglected. The secondary observables are usually linearly related to the model's heterogeneity and hence are often modelled using asymptotic and ray-based approaches (e.g., Woodhouse & Dziewoński, 1984; Ritsema *et al.*, 2011; Chang *et al.*, 2015). As discussed in section 1, this class of methods is computationally affordable and enables the inversion of large datasets. On the opposite end-member, there is the exploitation of all the information contained in the seismograms, without the need to identify

any particular seismic phase (e.g., Fichtner *et al.*, 2009). The full (or more realistically, a reasonable portion of the) waveform is non-linearly related to the model's heterogeneity and then iterative improvements of the model are necessary following a non-linear inversion approach.

The complete global seismic wavefield can be modelled with purely numerical methods (Komatitsch & Vilotte, 1998, e.g., the spectral element method;). However, tomographic methods using these approaches are numerically expensive. This has limited the application of the method to few local and regional models (e.g., Chen *et al.*, 2007; Tape *et al.*, 2009; Fichtner *et al.*, 2009; Chen *et al.*, 2015). French & Romanowicz (2014) developed the first global model based on this approach but a hybrid inversion scheme was applied. Other models are based on waveform inversion but only individual wave trains are used. These models are either based on ray theory (e.g., Schaeffer & Lebedev, 2013; Debayle & Ricard, 2012) or finite-frequency theory (e.g., Nolet & Dahlen, 2000; Montelli *et al.*, 2004; Zaroli *et al.*, 2010). This dichotomous aspect of the global tomography will be further discussed in this thesis (see section 1.4 and in chapters 3 and 4).

The possibility of building full waveform global tomographic models lies on the evolution of computer power. More powerful machines allow for the inversion of larger datasets and the employment of more sophisticated theories. High-performance computing (HPC) has allowed, for example, the implementation of numerical methods as SPECFEM (e.g., Komatitsch & Tromp, 2002a,b) and Axisem (Nissen-Meyer *et al.*, 2014) that are freely available to the seismological community.

Other important advances in global seismology concern the increase of the available data. IRIS (Incorporated Research Institutions for Seismology, www.iris.edu) and Orpheus (Observatories and Research Facilities for European Seismology, http://www.orfeus eu.org) manages and provieds free access to huge amounts of observed and derived data for the global earth science community. Fig. 1.5 shows the map of the global seismic network managed by or in collaboration with IRIS. However, both Figs. 1.1 and 1.5 highlight that there are large areas in the planet not covered by seismic sources and receivers. To improve the seismic coverage, the community is moving toward using other data types such as e.g. ambient seismic noise, which allows probing the Earth's interior without earthquakes. To improve the receiver distribution, the extensive deployment of Ocean Bottom Seismometers (OBS) and temporary dense array on the continents are key ways forward. For example, the Ocean Hemisphere Network Project distributes seismic data collected by different OBS networks in the West Pacific. Another example is the USarray experiment, a 15-year deployment whereby a large traveling network of 400 high-quality portable seismographs are being placed in temporary sites across the United States in a rolling fashion (Fig. 1.6).

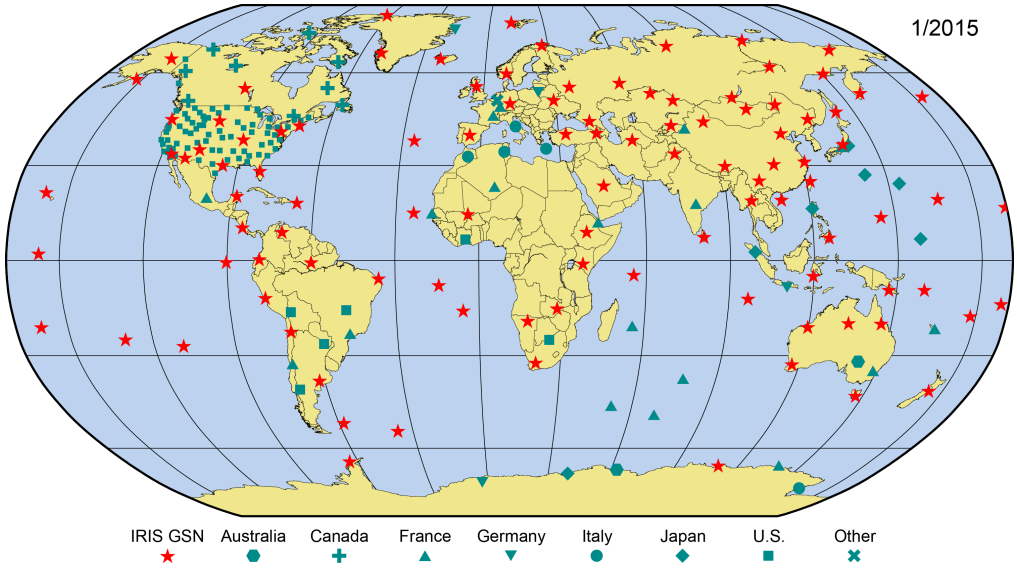

Figure 1.5: Map of the global seismic network managed by or in collaboration with IRIS (figure downloaded from www.iris.edu), updated to January 2015.

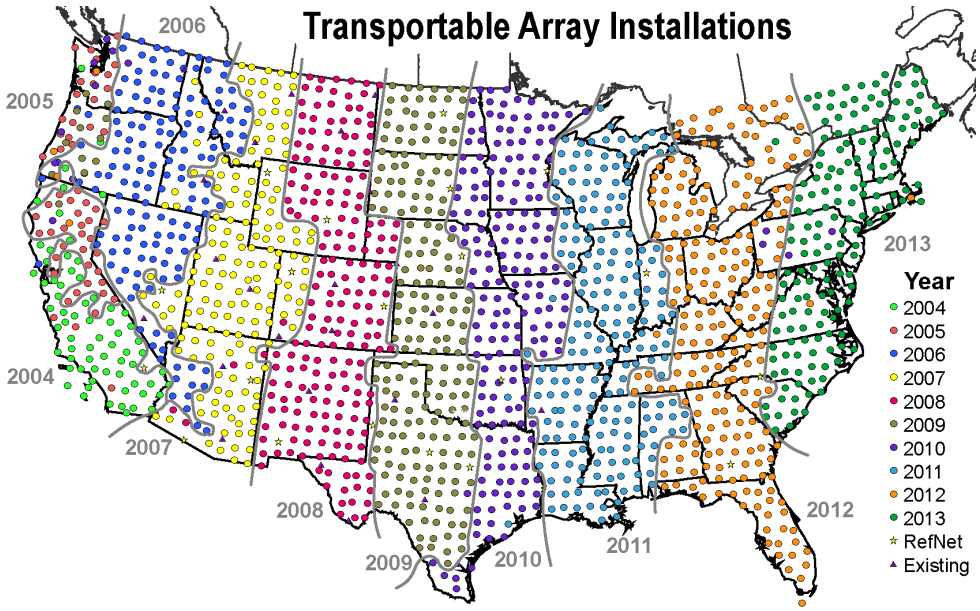

Figure 1.6: Map of the spatial and temporal distribution of the USarray experiment (figure downloaded from www.iris.edu).

1.4 FORWARD MODELLING OF GLOBAL EARTH STRUCTURE: THESIS OUTLINE

A large part of the global seismology applications summarised in section 1.2 involves the calculation of theoretical seismograms. The process yielding to the calculation of synthetic

seismic data is referred as seismic forward modelling and it is the main subject of this thesis. In particular, here we are interested in computing relatively long-period surface waveforms (T~60 s–150 s) and relatively short-period body waves (T~6 s–7 s). Fig. 1.7 shows an example of real and synthetic three component synthetic waveforms typically used in this thesis.

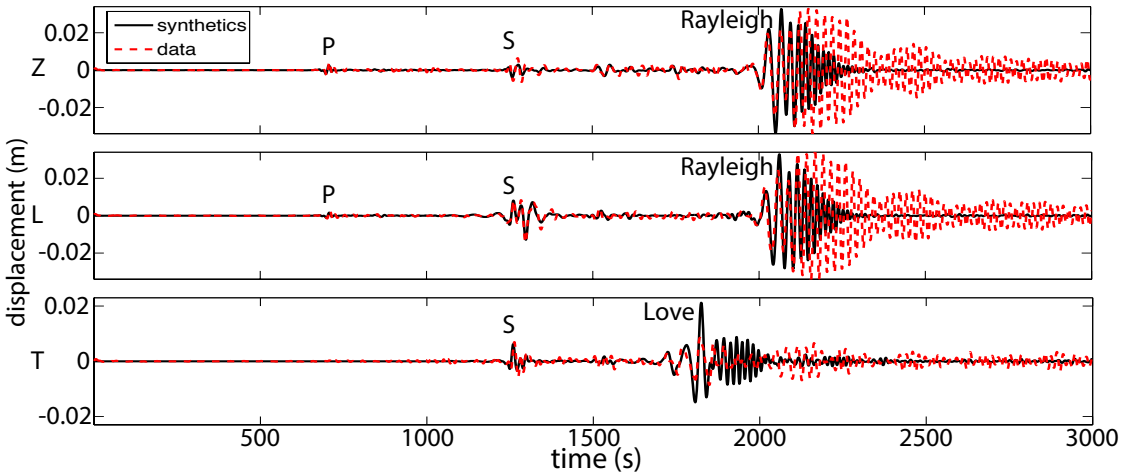

Figure 1.7: Example of synthetic and real three component (Z: vertical; L: radial; T: transverse) displacement seismograms for the Mw 6.4 earthquake that occurred at depth of ~50 km on Dec 19 2009 in Taiwan and recorded at the station KIP (epicentral distance: 73°; azimuth: 74°). Body (P and S) and surface (Rayleigh and Love) wave arrivals are indicated on the seismograms. Synthetics are calculated with the spectral element method using the S40RTS mantle model (Ritsema *et al.*, 2011).

In addition to earthquake source studies, the seismic forward modelling is used in global seismology for: i) seismic tomography: differences between observed and theoretical seismograms are minimised by successively modifying earth models; ii) assessment of tomographic models: checking how the synthetics calculated in the tomographic model fit the data. iii) targeted imaging studies, not involving a proper inverse problem: a hypothetical model is "manually" changed by a trial and error procedure until the synthetics fit the data sufficiently well.

Semi-analytical solutions for the calculation of synthetic seismograms in spherically symmetric earth models are available at a reasonable computational cost (e.g., Takeuchi & Saito, 1972; Friederich & Dalkolmo, 1995). For seismic wavefield simulations in laterally varying earth models, several methods are available for computing both the full waveforms or secondary observables. The accuracy of these methods depends on the theory used in the calculations and usually is anticorrelated with the computational cost. For example, as seen in section 1.3, the ray theory approach solves asymptotically the wave equation (Woodhouse & Dziewoński, 1984). Due to its approximations, ray-theory is computationally inexpensive but finite-frequency, scattering and diffraction effects are neglected. Another example is the spectral element method (e.g., Komatitsch & Vilotte, 1998), which solves numerically the wave equation. Due to the lack of physical approximations, it calculates the complete wavefield with high accuracy but this accuracy is paid with a high computational cost. Hence, the choice

of the method should depend on the particular problem to be addressed and the available computing facilities.

Identifying accurate and computationally affordable forward modelling schemes is crucial for the construction of the next generation of global images of the Earth's interior. Thus, our main goal is to investigate whether existing approximate, numerically efficient seismic forward modelling methods are useful to calculate long-period surface waveforms (T~60 s–150 s) when building future global tomography images. On the other hand, highly accurate calculations of the complete seismic wavefield, based on a purely numerical approach, are key to independently assess the quality of 3-D Earth models and to interpret fine structures in the Earth's interior.

Advantages and disadvantages of the *approximate* and *purely numerical* methods for the calculation of the seismic wave field are discussed in chapter 2. In the same chapter, we also give the theoretical background and the implementation's details of the methods used in this thesis for the calculation of synthetic seismograms.

This thesis then addresses three main different applications of seismic forward modelling, which are presented in chapters 3 to 6:

1. **In the framework of global waveform tomography based on long-period surface waves, we compare the accuracy of two approximate techniques against a purely numerical approach**. In particular, we compare synthetic surface waveforms calculated in 3-D realistic earth models with the Born approximation (e.g., Capdeville, 2005) and the full ray theory (e.g., Ferreira & Woodhouse, 2007a) to the solutions of the spectral element method (e.g., Komatitsch & Vilotte, 1998). Correlating errors due to the physical approximations to parameters of the earth models, we define the domain of validity of the Born approximation and full ray theory. Chapters 3 and 4 present and discuss the synthetics experiments performed on the Born approximation and full ray theory, respectively.

2. Often the assessment of tomographic models is performed calculating synthetic data based on the same approximate theory as used for building the model, notably by using checkerboard tests. However, errors due to the theory cannot be estimated with this approach (Leveque *et al.*, 1993). Conversely, if a different and more accurate technique is employed to assess the quality of the model, it is possible to highlight the errors of the model due to the theory used in the tomographic inversion. Hence, **we use the accurate spectral element method** (e.g., Komatitsch & Vilotte, 1998) **to assess the quality of a new whole mantle radially anisotropic model** (Chang *et al.*, 2015) developed on the basis of ray theory. Moreover, the performances of this model and some of its variants are compared with predictions for the S40RTS mantle model (Ritsema *et al.*, 2011). The results of this assessment are presented and discussed in chapter 5.

3. **In the framework of targeted studies of the structure of the Earth's interior, we use the spectral element method** (e.g., Komatitsch & Vilotte, 1998) **to model the structure**

of the lowermost mantle under the Indian Ocean. We study the effects of elastic, anelastic and anisotropic structure on short-period body waveforms and investigate whether seismic anisotropy is the only plausible cause of observed shear wave splitting beneath the study region. The results of these synthetic experiments are presented and discussed in chapter 6.

Finally, the main points and key findings of this thesis are discussed and summarised in chapter 7.

2

FORWARD MODELLING OF THE GLOBAL SEISMIC WAVEFIELD

2.1 SUMMARY

In seismology the forward modelling of the seismic wavefield involves the calculation of synthetic seismograms for different purposes. It can be used as part of inverse problems for earthquake source parameters and earth structure, it can be employed to model earth structure without a proper inverse problem and it also finds applications as a validating procedure of existing tomographic and source models.

Basically, a forward modelling method must solve the seismic wave equation. While in 1-D earth models the normal mode summation method is routinely used and can be considered exact, modelling of the seismic propagation in heterogeneous earth models is one of the biggest challenges in seismology because of the complexity and computation demand of such mathematical problem.

Here, we present a brief overview of some of the main forward modelling methods in seismology. We start by presenting a brief summary of the normal mode formulation of the wave equation, which is useful for understanding some of the methods extensively used in this thesis. Then, we present the basis theory of two approximate methods, the Born approximation and the full ray theory, for the calculation of long-period waveforms in heterogeneous media. Approximate methods are usually fast and computationally affordable but they have a limited domain of validity. For example, the Born approximation should be valid when the heterogeneity of the earth models is weak while the full ray theory should be applicable for media with smooth heterogeneity. In principle, these different and possibly complementary domains of validity make these two methods attractive for the development of hybrid forward modelling schemes.

Moreover, we present the spectral element method, which is a purely numerical forward modelling method enabling the calculation of the complete seismic wavefield in

highly heterogeneous media. It is more accurate than approximate techniques but also computationally more expensive. In addition, the Gemini method for the fast computation of seismograms in spherically symmetric earth models will also be presented.

When the solutions from different methods for waveform modelling in heterogeneous models are compared, it is important to ensure that exactly the same earth models are used by the different methods. Thus, we present the procedure we apply for this purpose.

2.2 INTRODUCTION

In geophysics, the term forward modelling refers to the mathematical calculation of a response, given a physical model. In global seismology, the goal of the forward modelling is to solve the seismic wave equation and calculate what would be recorded by a seismic station at a given location, following the seismic wave propagation through a given earth model and generated by a given source.

Seismic forward modelling is used in several seismological applications. It is a fundamental part of the inverse problem for both source and earth structure and the solutions of such problems strongly rely on the choice of the forward modelling scheme employed. Moreover, the modelling of seismic propagation can be used to assess the quality of tomographic and/or source models (e.g., by checking how the synthetics calculated in a given model fit the data). Finally, seismic forward modelling can be performed to constrain Earth structure without formally setting up an inverse problem. For example, the Earth structure can be iteratively and "manually" changed to produce seismograms that fit the data well.

Two main sources of errors affect the seismic forward modelling problem. The first one comes from the inaccuracy of the theory used to solve the wave equation. For example, scattering, diffraction and coupling between waves are often ignored by some approximate, asymptotic and semi-analytical methods. On the other hand, numerical methods are often affected by numerical dispersion (artificial dispersion due to the discretisation of the domain) and instability.

The second source of error arises from the inaccuracy of the earth and source models used. We do not know exactly the parameters of the source and how the subsurface is made. Moreover, the parametrisation of the earth (and source) model is only one of the possible representations of the earth (and source) model itself, it is not the true earth (and source) model.

Several forward modelling techniques are available for global seismology applications. Such methods can be roughly subdivided into two large families: i) *numerical* approaches, which enable the calculation of accurate seismograms in complex media usually by means of heavy computations; and ii) *approximate* approaches, which apply mathematical and/or physical simplifications of the wave propagation problem in order to solve it in an efficient way. The latter are usually computationally more affordable but their efficiency is obtained at the cost of reduced accuracy. Although the distinction between these two families is useful, it must be borne in mind that their boundary is not always completely well defined. Numerical

methods actually also use some approximations (e.g., by discretising the medium) and are subject to numerical dispersion and instability. On the other hand, approximate methods often employ numerical algorithms (e.g., integration solvers) to solve the wave equation.

In the following, we summarise the normal mode theory (section 2.3) whose basis and terminology is needed to explain some of the forward modelling methods used in this thesis. We then present two approximate techniques, the Born approximation and full ray theory (section 2.4), and two numerical methods, the spectral element method and Gemini (section 2.5). For these methods we report the basis theory and we explain how we use them in this thesis. Finally, we present a scheme that we developed for the consistent implementation of 3-D earth models for seismic waveform calculations using different forward modelling approaches (section 2.6).

2.3 NORMAL MODE FORMALISM

Most applications in short-period seismology (T less than ~20 s) are essentially based on the ray theory, an infinite frequency approximation, which provides an intuitive picture of seismic wave propagation, being very useful for the interpretation of seismic observations. On the other hand, in long-period seismology a common theoretical framework used to model the seismic wavefield is the normal mode approach.

In this section we describe the fundamentals and the main aspects of the normal mode approach that are useful for the approximate methods used in this thesis. For a complete review of the normal mode theory, we refer to the studies of, e.g., Takeuchi & Saito (1972); Woodhouse & Girnius (1982); Woodhouse (1983).

The seismic wave equation, with displacement $\mathbf{u}$ can be written as:

$$(\mathscr{H} + \rho\partial_t^2)\mathbf{u} = \mathbf{f} \tag{2.1}$$

where $\mathscr{H}$ is the integro-differential operator representing the elastic and gravitational equations, ρ is the density distribution, ∂_t denotes the partial differentiation with respect to time, and $\mathbf{f} = f(\mathbf{x}, t)$ is the body force equivalent of the seismic source. Taking the Fourier transform in time and considering the homogeneous equation ($\mathbf{f}$=0), Eq. 2.1 can be written in terms of an eigenfunction ($\mathbf{s}_k$) - eigenvalue (ω_k) problem:

$$\mathscr{H}\mathbf{s}_k = \rho\omega_k^2\mathbf{s}_k \tag{2.2}$$

with $k = 1, 2, ..., \infty$. $\mathbf{s}_k(\mathbf{x})$ represents the k^{th} free oscillation (normal mode) of the earth with the angular frequency ω_k. It can be shown that the solution of Eq. 2.1 can be expressed as an expansion in terms of the eigenfunctions $\mathbf{s}_k$:

$$\mathbf{u}(\mathbf{x}, t) = \sum_k \left[1 - e^{-\alpha_k(t-t_s)}\right] M_{ij} e_{ij}^k(\mathbf{x}_s)\mathbf{s}_k(\mathbf{x}) \tag{2.3}$$

where α_k denotes the decay of the k^{th} mode due to the attenuation $\left(\alpha_k = \frac{\omega_k}{2Q_k}\right)$. $\mathbf{x}_s$ and t_s represent the spatial and temporal centroid of the source. M_{ij} is the moment tensor of the source and e^k_{ij} is the strain in the k^{th} mode evaluated at the source's location.

A synthetic seismogram $\mathbf{u}(\mathbf{x},t)$ can thus be obtained by summation of the k modes of the Earth (NMS, Takeuchi & Saito (1972)). When all the modes are included, the Eq. 2.3 is the exact solution to the wave equation, being one of the most commonly used methods for the computation of theoretical seismograms in 1-D earth models (at least for long-period seismology applications). The NMS technique is often used to validate other forward modelling methods (both numerical and approximate techniques). In this thesis we use the NMS method to calculate the reference waveforms used in Born approximation's experiments (see section 2.4.1).

To apply Eq. 2.3, the complete set of eigenfunctions $\mathbf{s}_k(\mathbf{x})$ and the corresponding eigenfrequencies ω_k must be calculated. Following the classical approach (e.g., Morse & Feshbach, 1953; Pekeris & Jarosch, 1958), $\mathbf{s}_k(\mathbf{x})$ are expanded in spherical harmonic functions (special functions defined on the surface of a sphere, Phinney & Burridge (1973)):

$$s_r = U(r)\,Y_l^m(\theta,\Phi) \tag{2.4}$$

$$s_\theta = V(r)\partial_\theta Y_l^m(\theta,\Phi) + W(r)\partial_\Phi Y_l^m(\theta,\Phi) \tag{2.5}$$

$$s_\Phi = V(r)\csc\theta\partial_\Phi Y_l^m(\theta,\Phi) - W(r)\partial_\theta Y_l^m(\theta,\Phi) \tag{2.6}$$

$$\Gamma' = P(r)\,Y_l^m(\theta,\Phi) \tag{2.7}$$

where Γ' corresponds to the perturbations in the gravitational potential. $U(r)$, $V(r)$, $W(r)$, and $P(r)$ are often denoted as scalar eigenfunctions, being the expansion coefficients of the spheric harmonics $Y_l^m(\theta,\Phi)$ defined as:

$$Y_l^m(\theta,\Phi) = (-1)^m \left[\frac{(2l+1)(l-m)!}{4\pi(l+m)!}\right]^{\frac{1}{2}} P_l^m(\cos\theta)e^{im\Phi} \tag{2.8}$$

with $l = 0,1,2,\ldots; -l < m < l$. P_l^m are the associated Legendre functions:

$$P_l^m(x) = \frac{(1-x^2)^{\frac{m}{2}}}{2^l l!}\frac{d^{l+m}}{dx^{l+m}}(x^2-1)^l \tag{2.9}$$

where l and m denote the angular and azimuthal orders. When Eqs. 2.4-2.7 are substituted into Eq. 2.2 for a SNREI model (spherical, non-rotating, elastic, isotropic) a system of ordinary differential equations for $U(r)$, $V(r)$, $W(r)$, and $P(r)$ is obtained. These equations have solution only for discrete values of ω_k, which are the angular frequencies of the free oscillations of the Earth. The system of equations leads to two types of solutions, one for $U = V = P = 0$, giving rise to the toroidal modes and one for $W = 0$, corresponding to the spheroidal modes. The type of normal mode, toroidal or spheroidal, is defined by the index q. The overtone number n is used for enumerating the eigenfrequencies in increasing order for

a given q and l. When $n = 0$, the mode is named fundamental mode. For $n > 0$ the modes are named overtones. n represents the number of nodes in the radial direction, while l represents the number of nodes at the Earth's surface. The $2l + 1$ modes for each q, l and n form a *multiplet* and the individual modes of the multiplet are named *singlets*. A multiplet is usually denoted as ${}_nS_l^m$ (spheroidal modes) and ${}_nT_l^m$ (toroidal modes). However, in a SNREI model, ω_k does not depend on m and the multiplet is termed degenerate. Spheroidal modes for the PREM model are shown in Fig. 2.1.

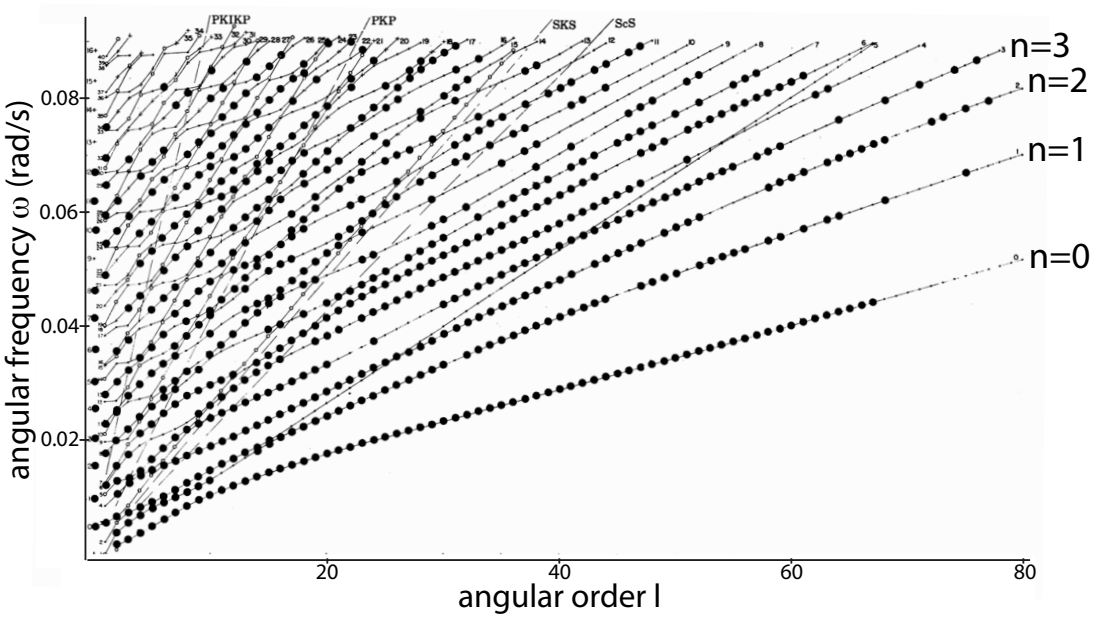

Figure 2.1: Spheroidal modes for the PREM model (Dziewoński & Anderson, 1981). The various mode branches are labeled: n=0 (fundamental model), n=1 (first overtone), n=2 (second overtone), etc. Modified from Woodhouse & Dziewoński (1984).

A consequence of the non-sphericity, rotation and 3-D structure of the Earth is the splitting of the modes (loss of the degeneracy). The splitting involves that the singlets of a multiplet have angular frequency slightly different from each other. Another consequence is the mode coupling that occur when the singlets are very close in frequency and cannot be distinguished. While for 1-D Earth models the normal mode summation technique provides a straightforward way to compute synthetic seismograms, for 3-D media it is more cumbersome and computationally expensive (e.g., Lognonné, 1991; Deuss & Woodhouse, 2001). For these reasons, several approximations to solve the Eq. 2.3 have been developed in the context of surface waves and long period body-waves. For example, the great-circle path theory approximates the wave to a ray of infinite frequency only sensitive to the earth structure along the great-circle path (Woodhouse & Dziewoński, 1984). On the other hand, non-linear asymptotic techniques extend the wave's sensitivity to the 2-D structure along the path accounting for across-branch coupling between modes (Li & Tanimoto, 1993; Li & Romanowicz, 1995). In the following section, we present two other fundamental approximate

forward modelling schemes, which are the ones used in this thesis.

2.4 APPROXIMATE APPROACHES

In this thesis, we focus on two approximations for the calculation of synthetic seismograms in heterogeneous earth models. The first method is the Born approximation, which is based on the perturbation theory (see Backus & Gilbert (1967); Woodhouse (1976) for a detailed description). In this framework, one starts from a reference model (usually 1-D) and calculates the reference seismograms in such a model and then computes the perturbations of the seismograms caused by variations in the model defined with respect to the reference one. In order to maintain the linearity between the variations in the models and the perturbations of the seismograms, the heterogeneity must be sufficiently *weak*.

The second method studied in this thesis is the full ray theory, an asymptotic approach based on the assumption that the scale length of heterogeneity is larger than the wave length of the seismic wave. In other words, the full ray theory is expected to work for earth models sufficiently *smooth*. Although the definitions of *weak* and *smooth* are not defined quantitatively in the literature, the two domains of validity are different and in principle complementary. The complementarity of the validity domain of these two approaches makes them potentially attractive to build a hybrid tomographic inversions method based on long-period data.

2.4.1 BORN APPROXIMATION

In the framework of normal modes and perturbation theory of long-period seismograms $u(t)$ in the time domain, we can write:

$$u(t) = u_0(t) + \delta u(t) \tag{2.10}$$

where u_0 is the seismogram calculated for a reference earth model (e.g, a 1-D earth model like PREM (Dziewoński & Anderson, 1981)) and $\delta u(t)$ is the perturbation of the seismogram due to the heterogeneity in the earth defined with respect to the reference model. The perturbed wavefield can be calculated as (e.g., Woodhouse, 1983; Romanowicz, 1987):

$$\delta u(t) = \sum_{kk\prime} \frac{e^{i\omega_k t} - e^{i\omega_{k'} t}}{\omega_k^2 - \omega_{k'}^2} A_{kk\prime} \tag{2.11}$$

where the real part is considered. k and k' denote two multiplets. $A_{kk\prime}$ is defined as:

$$A_{kk\prime} = \sum_{mm'} R_k^m H_{kk'}^{mm'} S_{k'}^{m'} \tag{2.12}$$

where m, m' are the azimuthal orders of singlets within each of these multiplets. $H_{kk'}^{mm'}$ is the splitting matrix including the linear functionals of the aspherical and spherical model

perturbations and terms related to the gravitation and ellipticity of the Earth (Woodhouse, 1983; Tanimoto, 1984). S_k^m and R_k^m are the source and receiver terms as functions of colatitude θ and longitude Φ defined by Woodhouse & Girnius (1982):

$$S_k^m(\theta_s\Phi_s) = \sum_{N=-1}^{N=1} S_{kN} Y_l^{Nm}(\theta_s, \Phi_s) \tag{2.13}$$

$$R_k^m(\theta_r\Phi_r) = \sum_{N=-1}^{N=1} R_{kN} Y_l^{Nm}(\theta_r, \Phi_r) \tag{2.14}$$

S_{kN} and R_{kN} include the seismic moment tensor and eigenfunctions under the source and receiver.

The Eq. 2.11 can be linearised (Woodhouse, 1983; Tanimoto, 1984) giving rise to the first-order Born approximation (BORN):

$$\delta u(t) = \sum_k \left[\sum_k \frac{it}{2\omega_k} \sum_{mm'} R_k^m H_{kk}^{mm'} S_k^{m'} + \sum_{k\neq k'} \frac{e^{i\omega_k t}}{\omega_k^2 - \omega_{k'}^2} \sum_{mm'} R_k^m H_{kk'}^{mm'} S_{k'}^{m'} \right] \tag{2.15}$$

While the first term of Eq. 2.15 accounts for self-coupling (coupling within a multiplet), the second term accounts for coupling between all multiplets. It is worthy to note that Eq. 2.15 is proportional to the time, with the term containing t being called secular because it grows without bounds. For this reason BORN is a short-time approximation, which is expected to break down for long time series. The Born approximation equation is solved by integrating (summing) for all the scattering points due to heterogeneity. Each scattering point is considered only once (no multiple scattering). Thus, being a single scattering approximation it is valid in models with weak heterogeneity. Eq. 2.15 is also the basis of the so-called finite-frequency theory (e.g., Montelli *et al.*, 2004; Zhou *et al.*, 2004), although further approximations are applied in that case.

The summation over all the scattering points can be computationally heavy. In the classical literature the BORN equation is solved analytically using a spherical harmonics approach (e.g., Woodhouse & Girnius, 1982) or asymptotically with the stationary phase approach (Romanowicz, 1987). Another class of methods involves the summation of the effects of all scattering points numerically (e.g., Snieder & Romanowicz, 1988; Capdeville *et al.*, 2000). When BORN is dealt numerically, the summation over k and k' is performed down to a given l_{max}, for each pair of source-receivers. Then, if n_r is the number of receivers and n_s the number of sources, the numerical cost grows as a function of $n_r n_s l_{max}^4$ because the corner frequency of the source (chosen as cut-off frequency) is proportional to l_{max}^2. In this thesis, we use BORN following the approach of Capdeville (2005) in which a forward wavefield from the source to the scattering point is convolved with a backward wavefield from the scattering integration point to the receiver, for each scattering point. With this strategy the numerical cost is lower because it grows as a function of $(n_r + n_s) l_{max}^2$. A mesh similar to the one used in the spectral element method (SEM, see section 2.5.1) is used to parametrise and integrate over the volume of the Earth.

BORN is used in chapter 3 to model long-period surface waveforms. Once that Eq. 2.15 is solved for obtaining the perturbations of the seismograms δu, these are summed to u_0 calculated with the normal mode summation method (e.g., Takeuchi & Saito, 1972, see Fig. 2.2). These waveforms are then compared with the spectral element method's solution (see section 2.5.1), used as ground truth, to assess the accuracy of this approximation and to evaluate the domain of validity of BORN.

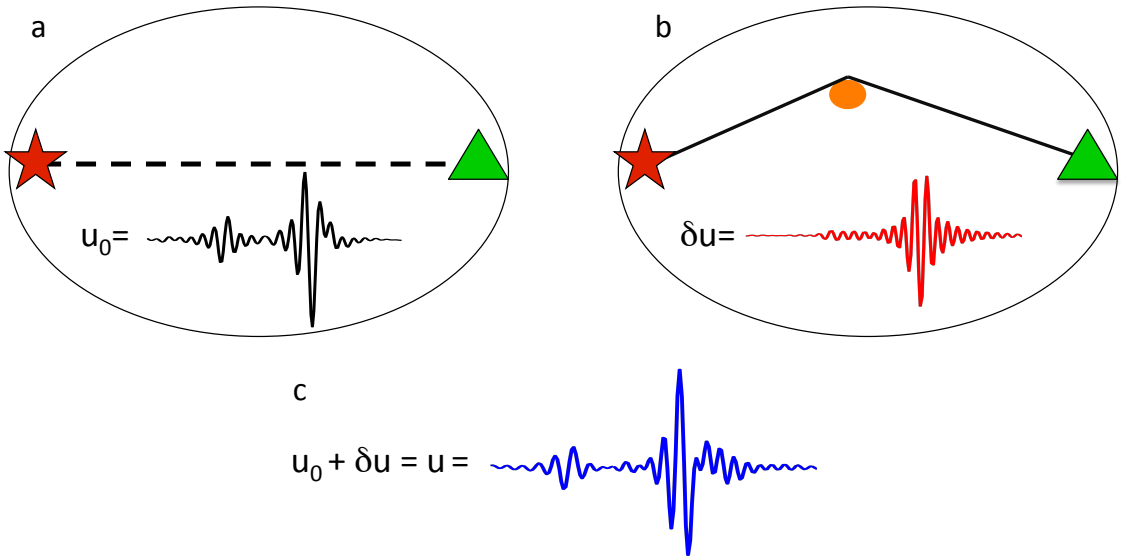

Figure 2.2: Sketch of the BORN algorithm. The red star and green triangle represent the source and receiver, respectively. a) Schematic 1-D earth model. The reference seismogram u_0 is calculated by normal mode summation (Eq. 2.3). The wave path is the great-circle (dashed line). b) Schematic heterogeneous earth model. The orange patch represents the heterogeneity of the earth model (scattering point). The perturbation of the seismogram δu due to the scattering point is calculated with BORN (Eq. 2.15). c) The seismogram u is calculated by summing the reference seismogram and the perturbation seismogram (Eq. 2.10).

2.4.2 FULL RAY THEORY

The surface wave full ray theory (FRT) is an efficient tool to calculate synthetic waveforms of surface waves. It combines the concept of local modes (Woodhouse, 1974) and exact ray tracing (Woodhouse & Wong, 1986). Here, we will briefly give a theoretical introduction and a schematic summary of the implementation of the method. For a more detailed description we refer to Ferreira (2005); Ferreira & Woodhouse (2007a); Woodhouse (1974); Woodhouse & Wong (1986); Tromp & Dahlen (1992a,b).

For a non-rotating, self-gravitating, anelastic earth model with smooth heterogeneity and anisotropy, the displacement of surface waves in the frequency domain ($u(\omega)$), travelling from the source (s) to the receiver (r) along the path (p), can be expressed as (Woodhouse, 1974;

Tromp & Dahlen, 1992a,b):

$$u(\omega) = \sum_{n=0}^{\infty} \sum_{\alpha=1}^{\infty} A(\omega) e^{-i\phi(\omega)} \tag{2.16}$$

with

$$A(\omega) = A_s A_p A_r \tag{2.17}$$

and

$$\phi(\omega) = \phi_s + \phi_p + \phi_r \tag{2.18}$$

The displacement $u(\omega)$ is calculated as a double sum over the dispersion branches ($n = 0, 1, 2, ..., \infty$) and the wave orbits (Rayleigh waves: R1, R2, R3, ... and Love waves: G1, G2, G3, ...). The amplitude A is the product, and the phase ϕ is the sum, of the terms due to the source, path and receiver. The source term is expressed as:

$$A_s e^{-i\phi_s} = \frac{1}{\sqrt{C_s}} \mathbf{M} : \mathbf{E}_s e^{i\frac{\pi}{4}} \tag{2.19}$$

where C_s is the angular group velocity under the source and is defined as $C_s = \frac{\partial \omega}{\partial \lambda}$ where λ is related to the local wavenumber k ($\lambda = ka$ where a is the radius of the Earth). The expression $\mathbf{M} : \mathbf{E}_s$ differs for Rayleigh and Love waves but in both cases includes the moment tensor of the source, the local mode beneath the source, and the take-off angle of the ray. The receivers term is defined as:

$$A_r e^{-i\phi_r} = \frac{1}{\sqrt{C_r}} \hat{v} \cdot \mathbf{s}_r \tag{2.20}$$

where $\hat{v}$ denotes the component of the surface wave displacement. C_r, analogously to the source term, is the angular group velocity under the receiver. $\mathbf{s}_r$ is different for Rayleigh and Love waves but in both cases it is a function of the eigenfunction calculated for the structure beneath the receiver and the arrival azimuth angle. The path term is given by:

$$A_p e^{-i\phi_p} = \sqrt{\frac{\lambda_s}{8\pi S}} e^{\int_{path}(-i\lambda_l - \frac{\alpha_l}{C_l})dl + iN\frac{\pi}{2}} \tag{2.21}$$

where $\sqrt{S}$ is the geometrical spreading of a monochromatic wave accounting for the focussing and defocussing effects in the wave amplitudes due to heterogeneity. The term $e^{\int_{path}(-i\lambda_l - \frac{\alpha_l}{C_l})dl + iN\frac{\pi}{2}}$ is the phase delay accumulated along the ray path. The factor $e^{iN\frac{\pi}{2}}$ is the so-called caustic phase shift with N taking into account the number of passages of the wave through the caustic. The exponential term also includes α_l ($\alpha_l = \frac{\omega}{2Q}$) to account for the attenuation effects. It is a common assumption that Q is frequency dependent but within the Earth it has been observed to be constant within bands of frequencies (e.g., Liu *et al.*, 1976). In this implementation of the algorithm, the dispersion for a medium with constant Q_μ is

calculated as:

$$\frac{\mu(\omega)}{\mu(\omega_0)} \approx 1 + \frac{2}{\pi Q_\mu} ln \frac{\omega}{\omega_0} \tag{2.22}$$

A similar equation relates κ and Q_κ. The reference angular frequency ω_0 is 2π rad/s.

The following ordinary differential equation (Woodhouse & Wong, 1986; Ferreira & Woodhouse, 2007a):

$$\frac{d^2\gamma}{d\Phi^2} + \gamma = \left(1 + \frac{\nu^2}{1+\gamma^2}\right)(\partial_\theta - \nu\partial_\Phi) \ln c(\omega, \theta, \Phi) \tag{2.23}$$

is used to calculate the exact ray path in the phase velocity map $c(\omega, \theta, \Phi)$. This is solved for $\gamma(\Phi) = \cot\theta$ where θ is the colatitude and Φ the longitude on a sphere. ν is calculated as $\nu = -\frac{d\gamma}{d\Phi} = -(1+\gamma^2)\tan(\xi - \frac{\pi}{2})$ where ξ is the azimuth. For $c = const$, the solution is the great-circle path. The Eq. 2.23 is solved numerically. Instead of using the shooting method of Woodhouse & Wong (1986) valid only for small deviations from the great-circle path, a more complete scheme (e.g., Tape, 2003) is applied. This method involves the shooting of a fan of rays reaching the longitude of the receiver. This shooting fan builds a function $f(\psi)$ where f is the finishing latitude as a function of the take-off angle ψ. The Newton's method is then used to find the take-off angle of the rays reaching the receiver. This method allows one to consider multipathing effects (more than one path between the source and receiver). A sketch of the method is shown in Fig. 2.3

The algorithm accounts for the ellipticity of the Earth (e.g, Dahlen & Tromp (1998)) and the effects of the Earth's gravitational field (Gilbert, 1980). Topography and bathymetry are also incorporated by using the global ETOPO5 bathymetry and topography model (NOAA, 1988).

In this thesis, the earth models for the FRT calculations are given as depth profiles (ρ, Vpv, Vph, Vsv, Vsh, Q_κ, Q_μ, η as functions of depth) (see section 2.6). These profiles are used to calculate the local excitations at the source and receivers and to build the phase velocity maps needed for the ray tracing.

The FRT algorithm is computationally very cheap. It needs only few minutes to calculate 90 mins of seismograms accurate down to 40 s for a source and 20 stations using a single processor. However, the pre-calculation of Rayleigh and Love wave phase velocity maps (in a period range of 40 s–270 s) needed as input for the FRT algorithm is heavier. Nevertheless, since these are only calculated once and for all, the associated computational burden is not problematic.

The FRT is referred as JWKB approximation or exact ray theory in other studies (e.g., Wang & Dahlen, 1994, 1995; Tromp & Dahlen, 1992a,b). For its theoretical simplicity and negligible numerical cost, the FRT is comparable to the great-circle path approximation (Woodhouse & Dziewoński, 1984). Nevertheless, the FRT has already demonstrated to be more accurate than the great-circle path approximation (Wang & Dahlen, 1994; Larson *et al.*, 1998; Peter *et al.*, 2009) because it considers frequency-dependent off great-circle effects. Hence, the FRT might be a valid and more accurate alternative to the great-circle path approximation for forward modelling surface waveforms in the framework of waveform tomography.

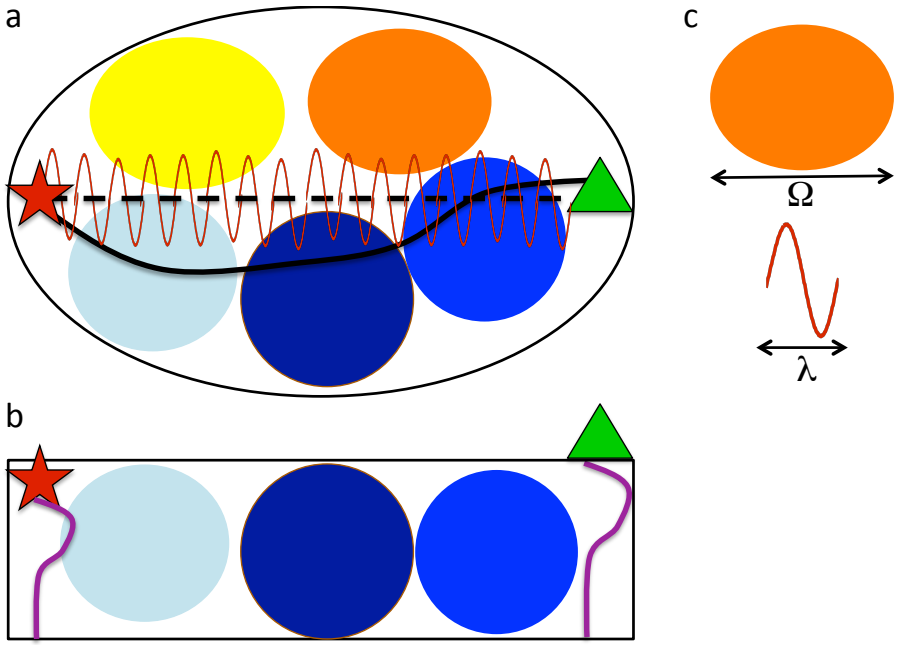

Figure 2.3: Sketch of the FRT algorithm. The red star and green triangle represent the source and receiver, respectively. Colourful patches represent the heterogeneity of the earth model. The red wave is the surface wave. a) Schematic phase velocity map with low (yellow/orange) and high (light/dark blue) phase velocity heterogeneity. If there was no heterogeneity (constant phase velocity, no colourful patches), the path of the surface wave would be the great-circle (dashed black line). Because of the heterogeneity, the actual path of the surface wave (calculated with Eq. 2.23) deviates from the source-receiver great-circle (solid black line). b) Schematic depth section of the shear speed perturbations model. The source (Eq. 2.19) and the path (Eq. 2.20) terms account for the local modes (curves in purple) under the source and receiver, respectively. c) Representation of the scale length of the heterogeneity (Ω) and the wave length of the surface wave (λ). Theoretically, the FRT is valid when $\lambda \ll \Omega$.

Being a high-frequency approximation, the FRT is expected to break down when the Fresnel area (proportional to the wavelength) can no longer be approximated by a thin ray. Thus, the FRT domain of validity is often expressed as $\lambda \ll \Omega$, whereby the wavelength of the wave (λ) must be much smaller than the scale-length of heterogeneity of the earth model (Ω) (see Fig. 2.3). Theoretically, when this condition is not respected, diffraction, scattering and other finite frequency effects are no longer negligible.

One of the goals of this study is to investigate the accuracy of the FRT in modelling fundamental mode ($n = 0$ in Eq. 2.16) long-period surface waves and and to quantify its domain of validity when realistic 3-D earth models are used (see chapter 4).

2.5 NUMERICAL APPROACHES

Numerical methods are used in seismology to solve the wave equation in strongly heterogeneous media, when approximate techniques no longer work. Several methods have been developed for this purpose.

Because of its simplicity, the finite-difference technique has been used in seismology at all scales (from exploration to global scales) (e.g., Virieux, 1984, 1986; Igel & Weber, 1996; Chaljub & Tarantola, 1997). It solves the strong formulation of the seismic wave equation by approximating the displacement derivatives between neighbouring grid points with finite-differences. The drawback of this method is that the discretisation of the domain can produce some numerical dispersion and makes the implementation of the boundary conditions difficult (e.g., at the earth's surface). Pseudo-spectral techniques are also based on the strong formulation of the wave equation but the displacement function is expanded in basis functions (e.g, Kosloff & Baysal (1982); Furumura *et al.* (1998); Cormier (1999); Igel (1999)). This method is affected by less numerical dispersion than the finite-difference approach but the main limitations remain because of the strong formulation. Finite-element methods are based on the weak form of the wave equation (e.g., Toshinawa & Ohmachi, 1992; Bao *et al.*, 1998). These methods subdivide the domain in elements in which the displacement is approximated by a polynomial of low order that generates a large numerical dispersion due to the low-order polynomial used. More details on the finite-element methods are given in section 2.5.1 when the spectral-element method is presented.

In the following subsections we present two numerical methods for the calculation of seismograms at the global scale: the spectral element method, which is a hybrid of finite-element and pseudo-spectral techniques and the Gemini, which uses a numerical approach to calculate the free oscillations of the Earth.

2.5.1 SPECTRAL ELEMENT METHOD

The spectral element method (SEM) allows for calculating the complete seismic wavefield and it incorporates the effects due to velocity/density heterogeneity and related sharp contrasts, anisotropy, anelasticity, Moho depth variations, topography and oceans, ellipticity, rotation and self-gravitation (Komatitsch *et al.*, 2002). It is a purely numerical method and, theoretically, there is no restriction on the maximum frequency which can be simulated with SEM.

The SEM technique was first developed in fluid mechanics in the 1980s (e.g., Patera, 1984) and has started to be used to simulate 2-D and 3-D seismic wave propagation in the 1990s (Priolo *et al.*, 1994; Faccioli *et al.*, 1997; Komatitsch & Vilotte, 1998; Seriani, 1998). Several works demonstrated the feasibility of SEM for studies of global wave propagation (e.g., Komatitsch & Vilotte, 1998; Komatitsch & Tromp, 1999; Paolucci & Faccioli, 1999; Komatitsch *et al.*, 2000a,b). Then, Chaljub *et al.* (2003); Capdeville *et al.* (2003b); Komatitsch & Tromp (2002a,b) applied SEM for such purposes. Today, a SEM code (SPECFEM3D_GLOBE) for global seismology applications is freely available from the Computational Infrastructure for Geodynamics website (www.geodynamics.org, last access: 08.07.2015) and it is in constant update and development by developer seismologists. It is written in fortran (fortran95 and earlier versions) and it runs in parallel computers using the Message-Passing-Interface protocol.

Part of the work in this thesis is based on the versions 5 and 6 of the SPECFEM3D_GLOBE package. We use the acronym SEM to refer to both the method and the code. A few routines of the SEM code have been modified or adapted for the purpose of this research. We run SEM in Grace, the UEA's High Performance Compute Cluster and ARCHER (superceding HECToR), the UK National Supercomputing Service.

The SPECFEM3D_GLOBE package is essentially made of two programs, the mesher and the solver. In the following we report the basic theory behind the two programs giving some technical details useful for the understanding of critical points of this thesis. A detailed presentation of SEM theory and implementation can be found in Komatitsch & Tromp (1999, 2002a,b); Komatitsch *et al.* (2010a).

THE MESHER

SEM subdivides the volume of the globe into a mesh of non-overlapping hexahedral elements, which are isomorphous to the cube, used as reference. The six sides of each element match with the sides of the neighbouring elements. Such a mesh is called conforming in finite-element theory. The shape and position of each element is defined by 27 control points (see Fig. 2.4). The elements are mapped into the reference cube by means of the Jacobian of the mapping. The partial derivatives of the Jacobian are defined in terms of Lagrange Polynomials of degree 2 and their derivatives. The Jacobian should never vanish and its behaviour is a measure of the quality of the mesh.

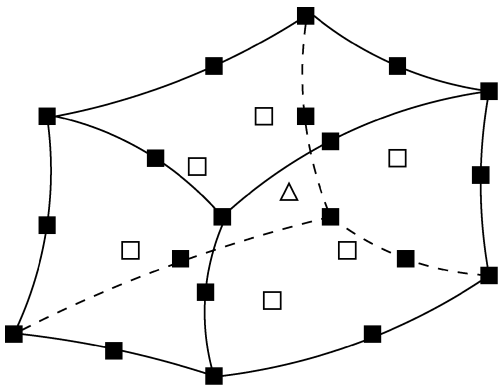

Figure 2.4: Schematic representation of an element with its 27 control points, which is used in the global scale implementation of the spectral element method used in this study. Adapted from Komatitsch & Tromp (2002a).

The SEM mesh is named "cubed sphere" (e.g., Sadourny, 1972) because each face of the reference cube is mapped to the surface of the sphere. The globe is thus subdivided in 6 chunks. Mapping twice, once at the earth's surface and once at the inner-core boundary (ICB) and interpolating in the radial direction, the meshing of the earth in finite-elements is obtained. For seismic wavefield simulations it is important to maintain a relatively constant number of grid points per wavelength. Since in the reference model PREM (Dziewoński & Anderson, 1981) seismic speeds increase with depth, the size of the elements must increase

analogously. In order to do so, the SEM mesh is doubled at the Moho, at the 670 km discontinuities and at the ICB. The SEM mesh honours all the first-order discontinuities of PREM: Moho, 220 km, 400 km, 670 km, core-mantle boundary (CMB) and inner-core boundary (ICB) and the second-order discontinuities at 600 km, 771 km and at the top of the D" layer (see Fig. 2.5). To do so, the faces of the elements match with the position of the discontinuity.

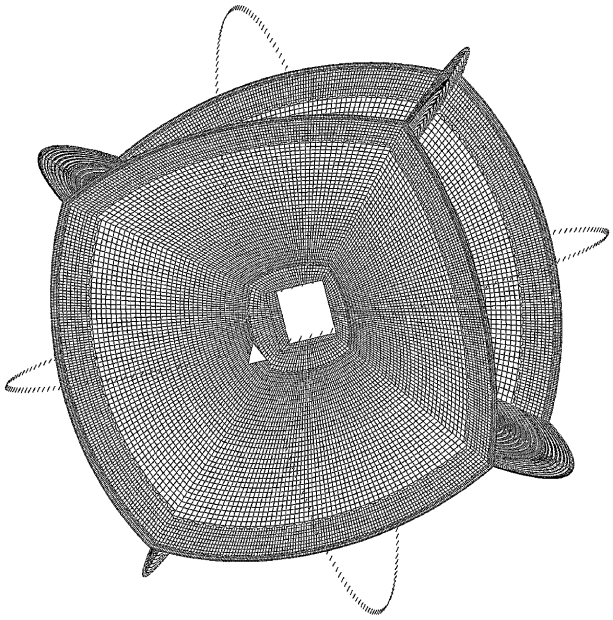

Figure 2.5: The SEM mesh is doubled at the Moho, 670 km and ICB. It honours the discontinuities at the Moho, 220 km, 400 km, 600 km, 670 km, 771 km, CMB and ICB. Modified from Komatitsch & Tromp (2002a).

In each element the seismic displacement has to be represented. Conversely to the traditional finite-element methods where the same degree polynomials are used to describe the shape and the functions within the elements, SEM employs higher-degree polynomials (N=4) based on Gauss-Lobatto-Legendre interpolation points (GLL) to represent the displacement within the element. Then, functions in each elements are defined by $(N+1)^2$ points (125). The GLL quadrature is also used to integrate the displacement over the elements.

Each of the six chunks of the cubed sphere is divided in slices and each slice is managed by a single PC processor (see Fig. 2.6). There are two key input parameters for the mesh calculation. One is NPROC which is the number of slices (and then of processors needed) along one side of a chunk. The other one is NEX that is the number of elements along one side of a chunk at the surface. NEX is actually the value affecting the resolution of the mesher and the accuracy of the seismograms. For example, it is estimated that for NEX=256, the simulations are accurate to a shortest period of ~17 s.

The mesher implements 1-D and 3-D earth models. Since SEM does not include almost any approximation, there is no difference in both accuracy or computational cost between 1-

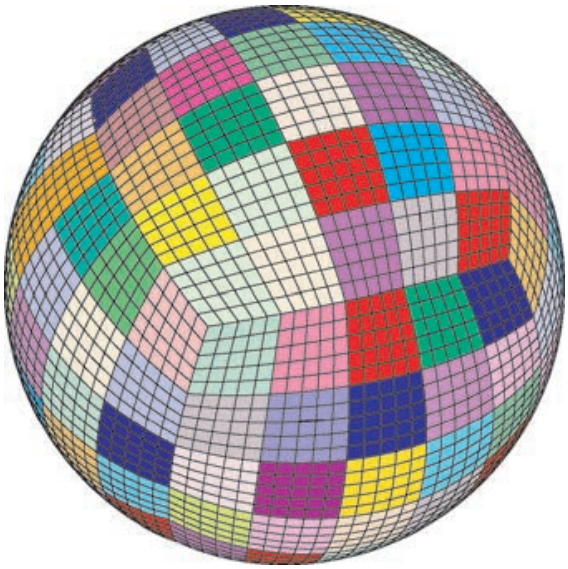

Figure 2.6: Cubed-sphere divided in 6 chunks. Each chunk is divided into slices (highlighted by different colours). In this particular case, each slice contains 25 elements (at the surface). Modified from Komatitsch & Tromp (2002a).

D and 3-D simulations. A difference in the numerical burden can instead be due to different crustal models used (homogeneous, 1-D and 3-D). The complexity of the crust requires a large number of elements

Several crustal and mantle models are implemented in SEM by default and other models have been implemented for the purpose of this research (see section 2.6 for more details).

THE SOLVER

Here we describe the SEM solver with a particular focus on seismic wave propagation in the crust and mantle. More complex equations can be derived for the liquid outer-core and the inner-core (Komatitsch & Tromp, 2002a,b).

In the crust and mantle the seismic wave equation can be written as

$$\rho \partial_t^2 \mathbf{u} = \nabla \cdot \mathbf{T} + \mathbf{f} \tag{2.24}$$

where ρ and $\mathbf{f}$ are the density distribution and a force equivalent to the earthquake, respectively, as seen in the previous sections. $\mathbf{u}$ is the displacement field and $\mathbf{T}$ is the stress tensor. Hooke's law describes the relation between the stress tensor and the gradient of the displacement:

$$\mathbf{T} = \mathbf{c} : \nabla \mathbf{u} \tag{2.25}$$

where $\mathbf{c}$ contains the Love elastic parameters (A, C, L, N, F; Love, 1911). The seismic source is expressed as:

$$\mathbf{f} = -\mathbf{M} \cdot \Delta(\mathbf{r} - \mathbf{r}_s) S(t) \tag{2.26}$$

where $\mathbf{M}$ is the moment tensor, $\mathbf{r}_s$ is the point source location, $\Delta(\mathbf{r}-\mathbf{r}_s)$ is the Dirac delta function for the source at $\mathbf{r}_s$ and $S(t)$ is the source-time function. While finite-difference and spectral-element methods solve the differential (or strong) formulation of the wave equation (Eq. 2.24) for the appropriate boundary conditions, SEM, as well as finite-element methods, solves the weak formulation of the wave equation:

$$\int_M \rho \mathbf{w} \cdot \partial_t^2 \mathbf{u} d^3\mathbf{r} = -\int_M \nabla \mathbf{w} : \mathbf{T} d^3\mathbf{r} + \mathbf{M} : \nabla \mathbf{w}(\mathbf{r}_s) S(t) - \int_{CMB} \mathbf{w} \cdot \hat{\mathbf{n}} d^2\mathbf{r} \tag{2.27}$$

This expression is obtained by taking the dot product of the Eq. 2.24 with a test vector $\mathbf{w}$, integrating by parts over the crust and the mantle (volume M) and imposing the stress-free boundary condition. $\hat{\mathbf{n}}$ is the unit outward normal on the CMB. The term in the left-hand side of Eq. 2.27 is called mass matrix and it is diagonal. The first term of the right-hand side is named stiffness matrix and the second term in the right-hand side is the surface integral over the CMB representing the interaction in traction between the solid mantle and the liquid core. To solve the weak form of the wave equation, the integrals are discretised numerically.

The time dependence of the wave propagation is expressed with the following ordinary differential equation in matrix form::

$$\mathbf{H}\ddot{\mathbf{U}} + \mathbf{K}\mathbf{U} + \mathbf{M}\mathbf{U} = \mathbf{F} \tag{2.28}$$

where $\mathbf{U}$ is the displacement vector, $\mathbf{H}$ is the mass matrix, $\mathbf{K}$ is the stiffness matrix, $\mathbf{I}$ is the boundary interaction at the CMB and $\mathbf{F}$ is the source term. The time discretisation of the Eq. 2.28 is based on the explicit second-order finite-difference scheme to take full advantage of the fact that the mass matrix is diagonal. The iterative scheme used converges after only two iterations.

In the actual implementation of SEM the construction of the mesher and Eqs. 2.27 and 2.28 are more complicated because the method considers the full complexity of the real earth. The globe is made elliptical following the Clairaut's equation (Dahlen & Tromp, 1998). Topography and bathymetry from ETOPO5 (NOAA, 1988) are included. The bathymetry map is also used in the oceans. Self-gravitation is incorporated using the Cowling approximation (Dahlen & Tromp, 1998). The Coriolis effect due to the earth's rotation is also taken into account. Accounting for all these effects is computationally cheap.

On the other hand, when seismic attenuation is fully taken into account, the increase in the numerical cost of the simulations is considerable. SEM only includes the shear quality factor Q_μ because the attenuation in the earth is mainly controlled by it (Komatitsch & Tromp, 2002a) with the quality factor Q_κ being larger than Q_μ by a factor of about 100. The 1-D attenuation model from PREM, which includes 5 layers in the crust and mantle and 1 layer in the core, is used in our simulations. As seen in the section 2.4.2, Q is frequency dependent but within the Earth it is observed to be constant within a band of frequencies. Hence, it can be represented by a series of standard linear solids (e.g., Liu *et al.*, 1976) and in our simulations three linear solids are used. In an attenuating medium the stress tensor becomes

time dependent and Eq. 2.25 can be written as:

$$\mathbf{T}(t) = \int_{-\infty} \partial_t \mathbf{c}(t-t') : \nabla \mathbf{u}(t') dt' \tag{2.29}$$

In this thesis we use SEM for a wide variety of numerical experiments. In chapters 3 and 4, we use SEM as ground truth to assess the accuracy of the Born approximation and full ray theory when modelling long-period surface waveforms. In these cases, the SEM's mesh has NEX=288 (i.e., seismograms are accurate down to T~15 s) for which 60 minutes of simulations need ~3 744 CPU hours (864 processors running for ~6h30 on the ARCHER supercomputer). In chapter 5, we use SEM to validate global tomographic models. For these experiments, SEM waveforms are calculated with NEX=480 (i.e., seismograms are accurate down to T~9 s) for which 60 minutes of simulations need ~5 280 CPU hours (2400 processors running for ~3h18). Finally, in chapter 6, we use SEM to model isotropic, anisotropic and anelastic structure in the lowermost mantle. In this case, NEX=768 is used (seismograms accurate down to T~5.6 s) for which 60 mins of simulations need ~25 574CPU hours (3 456 processors running for ~7h20). From these examples, one can notice that the numerical burden increases both with the wave frequency and the length of the simulation. However, this is irrespective of the number of receivers considered.

2.5.2 GEMINI

Gemini (GEM) is the name of a code based on the algorithm of Friederich & Dalkolmo (1995) for the calculations of seismograms in spherical earth models up to high frequencies (~1 s). It is a numerical method based on the normal mode formalism (see section 2.3).

Starting from the system of Eqs. 2.4-2.7 in the frequency domain, the scalar eigenfunctions U, V, W, and Γ' are directly evaluated by numerical integration using second-order minors. A second-order minor of the matrix (as the one that can be obtained from the system of ordinary differential Eqs. 2.4-2.7) is the determinant of a submatrix whereby two columns and two rows are crossed out. This approach avoids the search of discrete eigenfrequencies and it is particularly suitable for calculating body-wave seismograms at high-frequency (up to 1 s). It honours discontinuities by means of continuous functions of the elastic parameters between layers. The attenuation is accounted by using complex elastic moduli.

The computational cost of GEM depends on the highest frequency, similar to the NMS method. However, while NMS is almost independent of the length of the synthetic seismogram, GEM is more dependent on the length of the time series than the maximum frequency required. This aspect makes GEMINI attractive for body-wave studies where the seismogram required are only 20–40 minutes long. For surface waves studies, at least 60–90 minutes long seismograms are needed and in this case NMS is be preferred.

In chapter 6, we use GEM to model high-frequency body-waves travelling through the lowermost mantle. Our GEM simulations are performed down to wave periods of T~4 s and are 33 minutes long. Less than 10 minutes of computing time are needed using a single processor.

2.6 3-D EARTH MODELS

While the implementation of 1-D earth models in the codes for the calculation of synthetic seismograms is simple and does not pose any particular issue, the use of 3-D global earth models can be more problematic, especially regarding the coupling between the mantle and the crustal models. The forward modelling methods, used in this thesis for calculations in 3-D earth models are BORN, FRT and SEM.

Our reference 3-D crustal model is CRUST2.0 (Bassin *et al.*, 2000). In this model, the crust is divided into blocks that include 7 layers with different compressional and shear wave speed (Vp and Vs, respectively) and density ρ. Fig. 2.7 shows that the crustal thickness in the globe varies from less than 8 km in the oceans to more than 60 km in the Tibetan Plateau. While in the FRT code the implementation of multiple thin layers would just slightly increase the computational cost, it would yield to extremely expensive computations in SEM and BORN where the number of elements in the crust must be increased to match the boundary of the crustal layers. Moreover, since the Moho depth is not constant, the coupling with the mantle model is not straightforward.

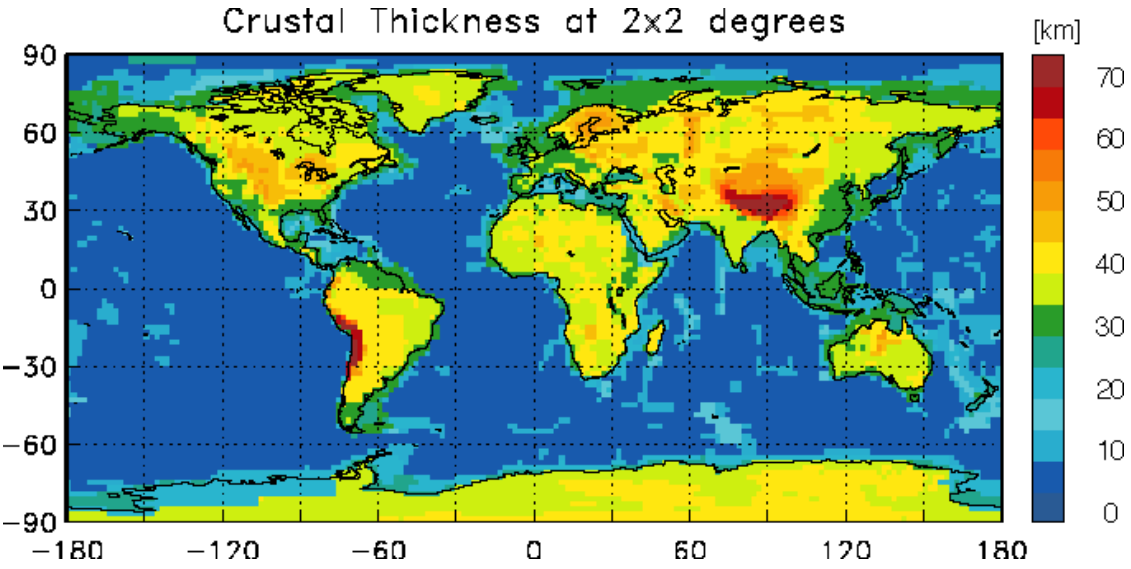

Figure 2.7: Map of crustal thickness from the crustal model CRUST2.0 (Bassin *et al.*, 2000).

To overcome problem of the multiple thin layers we need to smooth or down-sample the crustal model. For the crust-mantle coupling we applied a procedure to ensure that exactly the same crust+mantle models are used by the different codes, when these are used in the same experiment. For example, in chapters 3 and 4 we use SEM to validate FRT and BORN. In this case, the consistent implementation of the earth models is fundamental to avoid biases in the comparisons of the seismograms generated by the different methods.

Hence, we developed a code to build the earth models (named ppm) which are used as input to the BORN, FRT and SEM codes in exactly the same format. We also built a routine to consistently read such earth models in the three codes. The ppm models are defined in a

grid with a horizontal resolution of 2° x 2° and vertical resolution of ~8 km. Our reference crust (CRUST2.0) is defined in blocks of 2° x 2°. Moreover, S40RTS (Ritsema *et al.*, 2011) is the mantle model with highest nominal resolution used in this thesis (~1 000 km). Thus, our 2° x 2° grid seems appropriate for our purpose.

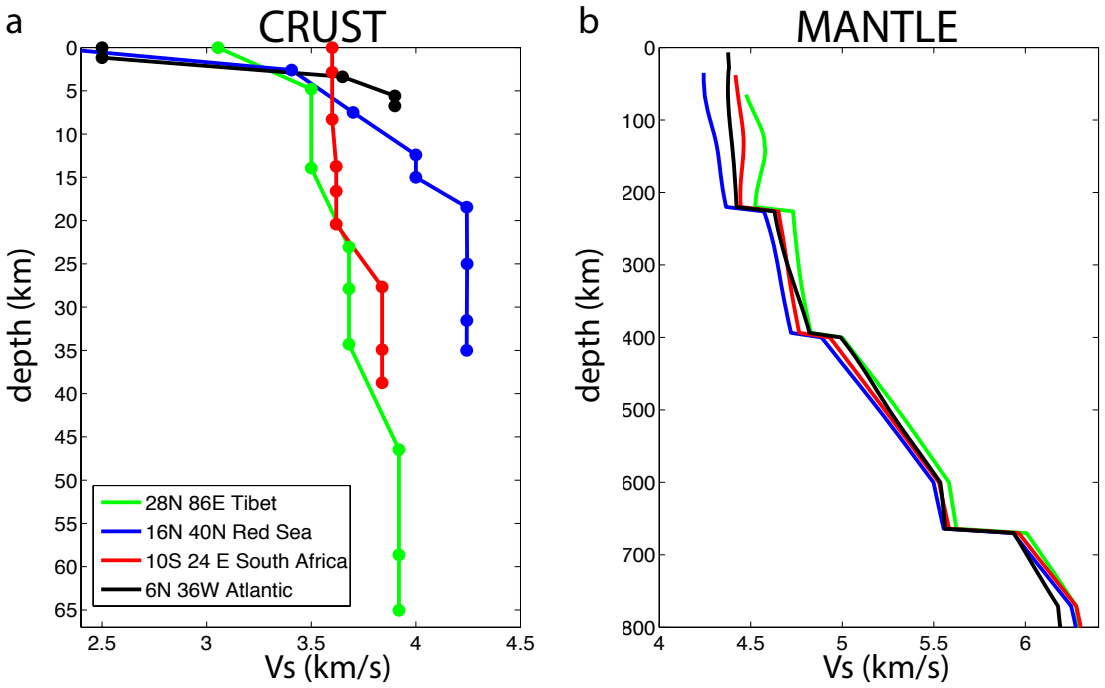

Figure 2.8: Depth profiles of Vs for CRUST2.0 (a) and S40RTS (b) for four different geographical locations for a SEM's mesh with NEX=480. a. Dots correspond to GLL points of the spectral elements. b. The mantle profiles are zoomed within the first 800 km where the differences are larger.

To build the *ppm* models we strictly follow SEM's algorithm (e.g., Komatitsch & Tromp, 2002a,b). The Moho (from either PREM or 3-D crustal models) and the other PREM's discontinuities (220 km, 400 km, 600 km, 670 km, 771 km, core-mantle boundary and inner-core boundary) are included. Multiple crustal thin layers (e.g., in sedimentary basins) are ignored and sharp discontinuities are smoothed. Fig. 2.8 shows the depth-profiles for a few geographical locations for CRUST2.0 and S40RTS as they are sampled by SEM. The dots represent the locations where the model is actually sampled and represent GLL points of the elements. These particular examples are valid for a mesher built with a NEX value of 480. The discontinuities within the crust are substituted by gradients between the layers.

Moreover, when the crust is thinner than 24.4 km (PREM's Moho) the space between the crust and the mantle is filled by extrapolating the mantle from the depth of 24.4 km. When the Moho is deeper than 24.4 km, the crust is overprinted onto the mantle. We have extensively tested that SEM gives the same results when using the models by default and our ppm version of the same models (see Fig. 2.9). This procedure is employed for the numerical experiments presented in chapters 3 and 4.

Finally, we implement the new global tomographic model SGLOBE-rani (Chang *et al.*,

2015) in SEM for the experiments reported in chapters 5 and 6. Both radially anisotropic and voigt average isotropic versions of the models are now available for SEM simulations.

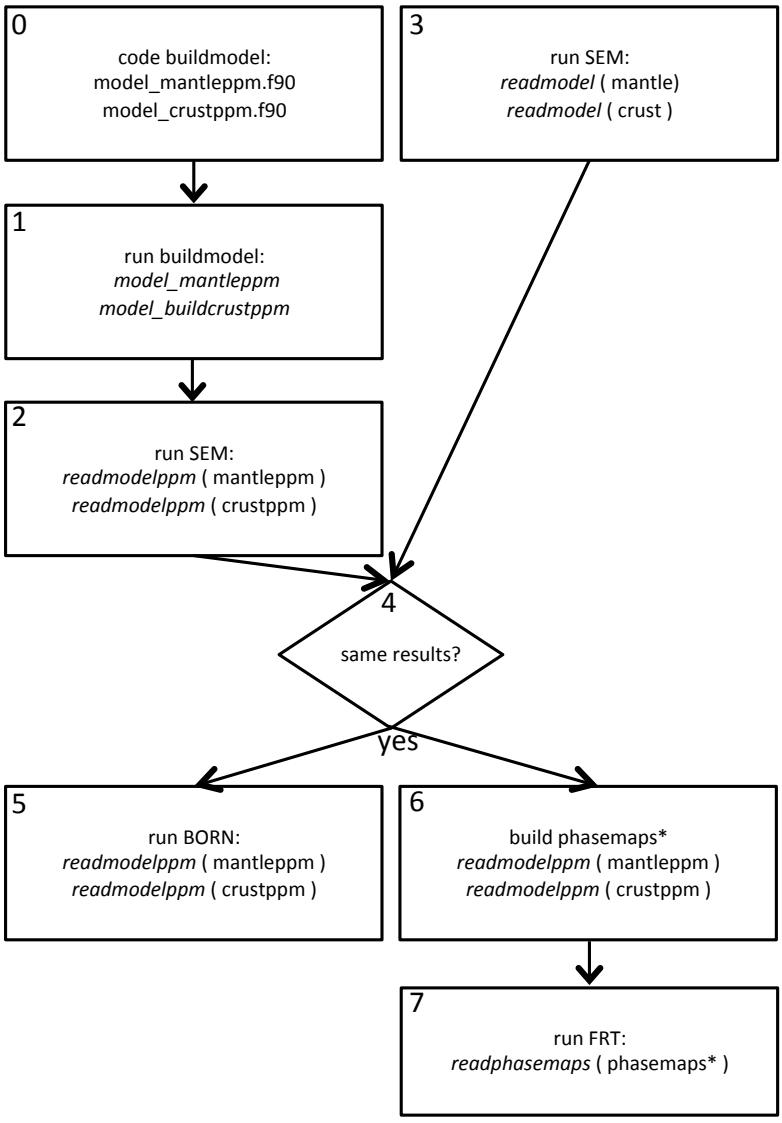

Figure 2.9: Schematic representation of the work flow employed for the consistent implementation of the 3-D earth models in the BORN, FRT and SEM codes. 0. The code *buildmodel*, following the algorithm of the SEM's mesher, is built. It includes subroutines to build and successively read the mantle and crustal ppm models. This step is made only once. 1. *buildmodel* is run to build the ppm models (mantleppm and crustppm). 2. ppm models are read by our subroutine readmodelppm used in SEM to calculate seismograms. 3. SEM is run using the same models of step 2 but using the format of the model and subroutine to read the model implemented by default in SEM itself. 4. Check whether the ppm models give the same result as SEM's default models. 5. ppm models are used in BORN using the same routines of step 2. 6. ppm models are used to calculate Rayleigh and Love phase velocity maps (phasemaps*) using the same routines of step 2. 7 The FRT code is run using the phasemaps*.

3

VALIDITY DOMAIN OF THE BORN APPROXIMATION FOR SEISMIC WAVEFORM MODELLING IN REALISTIC 3-D EARTH STRUCTURE

Most of the material presented in this chapter is included in a peer-review article published in Geophysical Journal International (Parisi *et al.*, 2015) of which I am the first author.

3.1 SUMMARY

While the first-order Born approximation is increasingly being used in many seismic tomography efforts, its domain of validity to forward model seismic waveforms has not been quantified in the context of current 3-D Earth models yet. We here address this issue by comparing teleseismic synthetic surface waveforms calculated using the Born approximation with spectral element method solutions for a variety of realistic global 3-D Earth models. We find that the Born approximation has a very limited domain of validity when applied to seismic waveforms. Specifically, it can only accurately model the phase (amplitude) of surface waveforms for source-receiver paths leading to time shifts smaller than about 15 % (5 %) of the wave period considered. These conditions usually occur in Earth models as S20RTS or S40RTS combined with a homogeneous crust for periods longer than T~80 s–90 s. For models with stronger heterogeneity and/or realistic 3-D crustal structure, only the phase of waveforms with periods longer than ~120 s–130 s can be accurately modelled with the Born approximation.

3.2 INTRODUCTION

With increasing computational power, current efforts to enhance the quality of global seismic tomographic models involve the inversion of waveforms in order to fully exploit the information contained in seismograms. Despite the recent development of highly accurate forward modelling schemes (e.g., Komatitsch *et al.*, 2002; Nissen-Meyer *et al.*, 2014) promising a new generation of high-resolution tomographic images, waveform tomography presents some drawbacks, such as the high computational cost and the strong non-linearity of the inverse problem (e.g., Nolet, 2014).

Because of the intensive computing needs of such accurate seismic wavefield calculations, several approximations such as the great circle approximation (Woodhouse & Dziewoński, 1984) and non-linear asymptotic techniques (Li & Tanimoto, 1993; Li & Romanowicz, 1995) have been developed and used. The Born approximation is a first-order perturbation theory, which is often used in seismology within the normal mode framework (Woodhouse, 1980; Tanimoto, 1984). It takes into account finite-frequency effects and has been successfully used to calculate phase delay kernels in global tomography applications (e.g., Montelli *et al.*, 2004; Zhou *et al.*, 2006). In this paper we test the possibility of using the Born approximation as a forward modelling scheme for waveform tomography instead. Its implementation is relatively simple and efficient. Also, it is particularly appealing in seismic tomography because it naturally gives a linear inverse problem. On the other hand, the disadvantage of the Born approximation is that it is a short-time approximation, i.e., it is only valid for sufficiently small times, and for weak perturbations compared to the reference model (usually 1-D) (Woodhouse, 1980; Tanimoto, 1984; Romanowicz *et al.*, 2008). It is thus of primary importance to understand the domain of validity of the Born approximation in relation to the strength of the heterogeneity obtained from tomographic inversions.

In particular, we are here interested in quantifying the domain of validity of the Born approximation when modelling relatively long-period surface waves in realistic 3-D Earth models. Some previous studies have investigated how good is the Born approximation to compute synthetic seismograms and kernels (Capdeville *et al.*, 2002; Tromp *et al.*, 2005; Romanowicz *et al.*, 2008; Panning *et al.*, 2009; Peter *et al.*, 2009; Dalton *et al.*, 2014). However, its accuracy has been examined only by considering a few simplified situations of mantle heterogeneity or for a few existing 3-D tomographic models. Moreover, a general criterion predicting the situations in which it breaks down has not been established yet. We here aim at filling this gap in the framework of forward modelling techniques.

To achieve this goal we calculate time-domain waveforms with the short-time first-order Born approximation (BORN) by using the approach described by Capdeville (2005). This efficient technique considers the full mode coupling although not explicitly present in the equations. The effect of the perturbations with respect to the 1-D reference model, which is PREM in this study (Dziewoński & Anderson, 1981), is integrated numerically, leading to compute the sum of the scattered fields induced by a finite number of scattering points. The perturbed wavefield is summed to the 1-D reference seismogram calculated by normal mode

summation (NMS, Gilbert (1971)). Refer to section 2.4.1 in chapter 2 for more details regarding the Born approximation and its implementation.

BORN waveforms are then compared with seismograms computed by the spectral element method (SEM, Komatitsch & Vilotte (1998); Komatitsch & Tromp (2002a,b); Komatitsch *et al.* (2010a)), and phase and amplitude accuracy are separately assessed for different dominant wave periods and for a wide range of realistic 3-D Earth models.

3.3 DATA AND METHOD

We generate SEM (SPECFEM3D_GLOBE package) and BORN waveforms and systematically compare the corresponding minor-arc fundamental mode Rayleigh (R1) and Love (G1) waves. We choose SEM as ground truth because it is a highly accurate purely numerical method for the full calculation of the seismic wavefield in realistic 3-D media and represents a powerful tool to assess the accuracy of approximate forward modelling techniques. Refer to section 2.5.1 in chapter 2 for more details regarding SEM and its implementation.

Our FRT and SEM velocity waveforms are sampled at 1 s. A SRO—seismic research observatory' seismometer—instrument response is convolved to the waveforms to highlight the surface waves. Finally, three different cosine bandpass filters with cut-offs at T~60 s–1 000 s, 100 s–1 000 s and 150 s–1000 s are applied.

FRT-SEM waveform comparisons are conducted within time windows capturing 2.5 cycles of the R1 and G1 arrivals, centred around the maximum amplitude, which are manually selected to avoid the interference of surface wave overtones. Errors in phase (E_ϕ) and amplitude (E_A) of time-domain velocity waveforms are estimated for every BORN–SEM pair of waveforms. E_ϕ is computed as the phase shift in seconds by cross-correlation of the two waveforms. In Figs. 3.8, 3.9, 3.10 and 3.12, E_ϕ is expressed as a percentage of the wave period T. E_A is calculated as:

$$E_A = 100 * \frac{\sum_i |A^B_{i+E_\phi} - A^S_i|}{\sum_i |A^S_i|} \tag{3.1}$$

where A^B and A^S are the amplitudes of BORN and SEM waveforms, respectively. The summations are carried out over the waveform time samples i. The subscript $i + E_\phi$ of A^B indicates that the BORN waveform is shifted in time by E_ϕ seconds before computing the difference $A^B - A^S$. Thus, E_A represents the percentual amplitude difference to the SEM amplitude computed for the best waveform phase-matching. We choose a percentage difference rather than a ratio to indifferently consider the cases in which the BORN amplitudes are either larger or smaller than the SEM ones by the same quantity. We also preferred the absolute value for the difference rather than the squared difference to reduce the influence of outliers. For the same reason, we choose to use the medians of the E_ϕ and E_A rather than the average values to summarise the results (presented in section 3.4). To carry out realistic waveform tomography experiments, we calculate theoretical seismograms for three real seismic events ev1, ev2 and ev3 with Mw_{ev1} = 6.4, Mw_{ev2} = 6.2 and Mw_{ev3} = 6.4, and

$depth_{ev1}$ = 16km, $depth_{ev2}$ = 20 km and $depth_{ev3}$ = 15 km. Focal mechanisms are presented in Fig. 3.1. Earthquakes are selected to sample different regions of the Earth and to excite fundamental mode surface waves well. We select 73 stations from the Global Seismic Network whose epicentral distance from the source ranges between 40° and 140°. A sketch of the ray coverage is presented in Fig. 3.1.

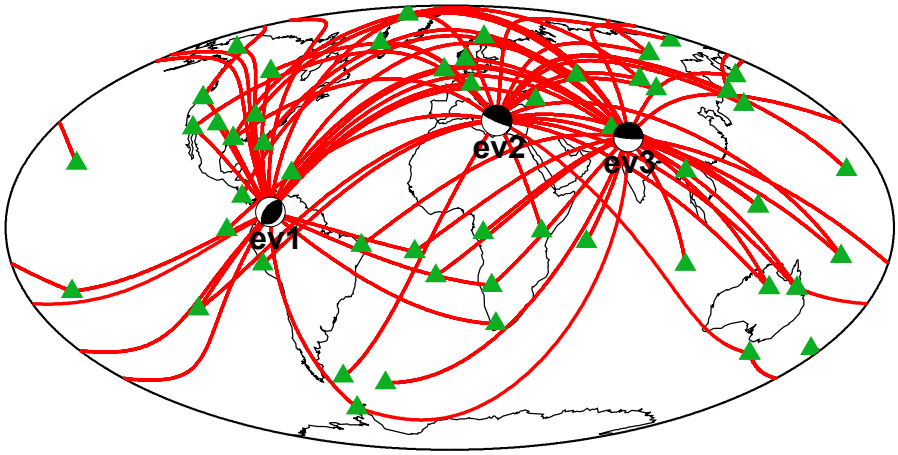

Figure 3.1: Source-receiver geometry used in this work. The sources ev1, ev2 and ev3 are at 16 km, 20 km and 15 km depth and the stations are represented by green triangles.

3.3.1 EARTH MODELS

In this study we adopt six mantle and two crustal models and we combine them to ensure that we use realistic Earth models. The expression *realistic Earth model* is used here to refer to a global tomography model that can be built from a tomographic inversion with the current tomography techniques and amount of available data (e.g., Ritsema *et al.*, 1999, 2011). Such model displays the main tectonic features already known of the Earth and contains heterogeneity with strength comparable to those of the most recent tomography models. A tomography model is smooth by definition but it is the best seismic representation of the Earth available for this study.

We start from S20RTS (Ritsema *et al.*, 1999) and S40RTS (Ritsema *et al.*, 2011) mantle models. S20RTS and S40RTS are represented by 3-D perturbations in shear wave speed (δVs), superimposed upon the spherically symmetric PREM model (Dziewoński & Anderson, 1981). The perturbations in compressional wave speed δVp and density $\delta\rho$ are scaled with respect to the Vs perturbations, $\delta\rho$=0.40δVs (Anderson *et al.*, 1968) and δVp=0.59 δVs (Robertson & Woodhouse, 1995). We build two other models by multiplying the δVs , δVp and $\delta\rho$ of S20RTS by the factors PV=0.5 and PV=1.75. PV=0.5 is adopted to build a model with fairly weak heterogeneity compared to current tomographic models. On the other hand, we choose PV=1.75 as end-member model with heterogeneity as strong as in recent high-resolution upper mantle models (e.g., Schaeffer & Lebedev, 2013). S40RTS is parameterised with spherical harmonic basis functions expanded up to degree 40 (l_{max}=40). We derive two

other models from S40RTS by truncating the maximum degree of the spherical harmonics to 20 and 12, gradually eliminating the smaller scale-lengths of heterogeneity.

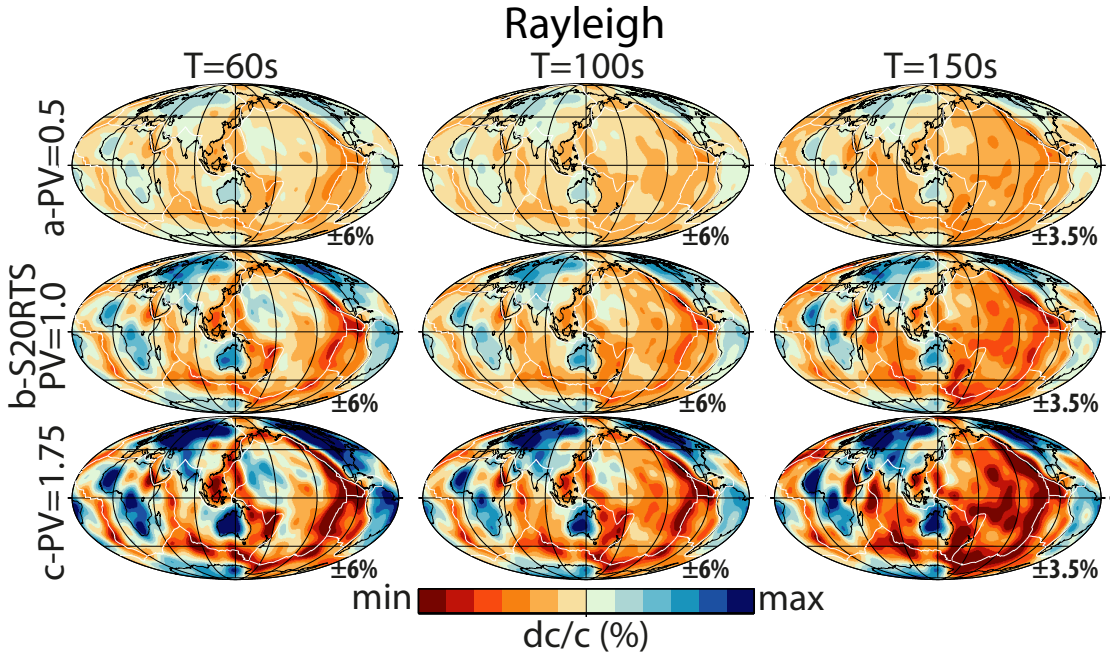

Figure 3.2: Rayleigh wave phase velocity maps at T~60 s, 100 s, 150 s for the models obtained by varying the PV factor. *a*- PV=0.5 + homogeneous crust; *b*- PV=1 (S20RTS) + homogeneous crust; *c*- PV=1.75 + homogeneous crust. The scale of perturbations in the phase velocity maps is shown on the left for each row.

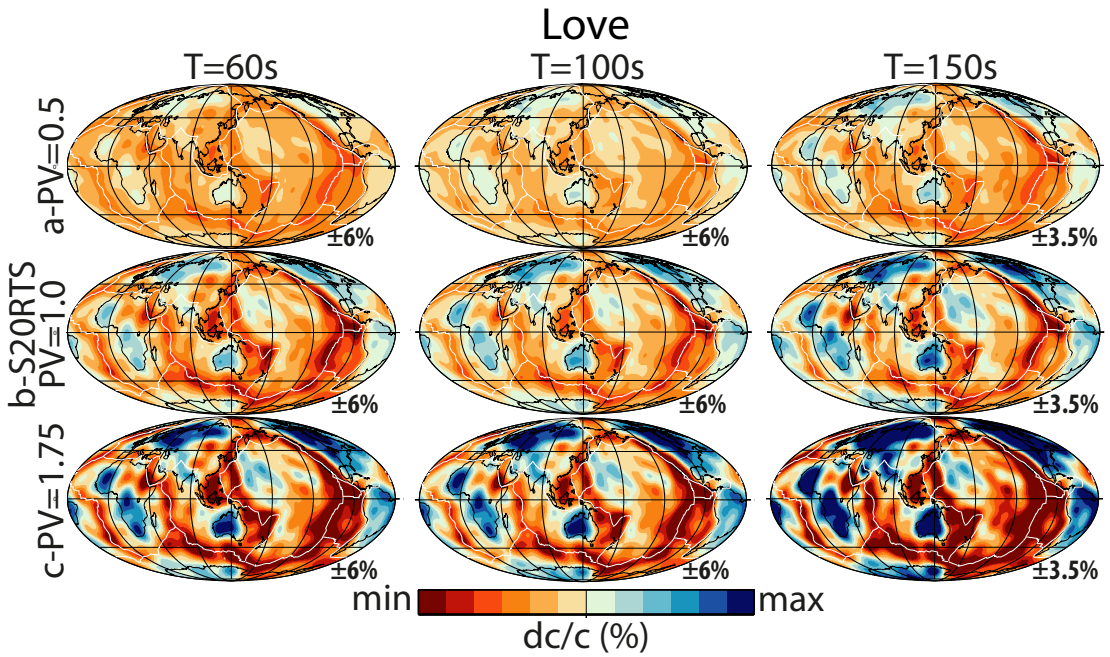

Figure 3.3: As in Fig. 3.2 but for Love waves.

At first we couple the six mantle models with a homogeneous crust layer (Moho depth=24.4 km, Vs=3.2 km/s, Vp=5.8 km/s, ρ=2.6 g/cm^3). The models obtained by varying the PV factor and combined with the homogeneous crust shall be referred as models a (PV=0.5), b (PV=1.0) and c (PV=1.75) and the corresponding Rayleigh and Love phase velocity maps are shown in Figs. 3.2 and 3.3. The models obtained by varying l_{max} and combined with the homogeneous crust shall be referred as models d (l_{max}=40), e (l_{max}=20) and f (l_{max}=12) and the corresponding Rayleigh and Love phase velocity maps are shown in Figs. 3.4 and 3.5.

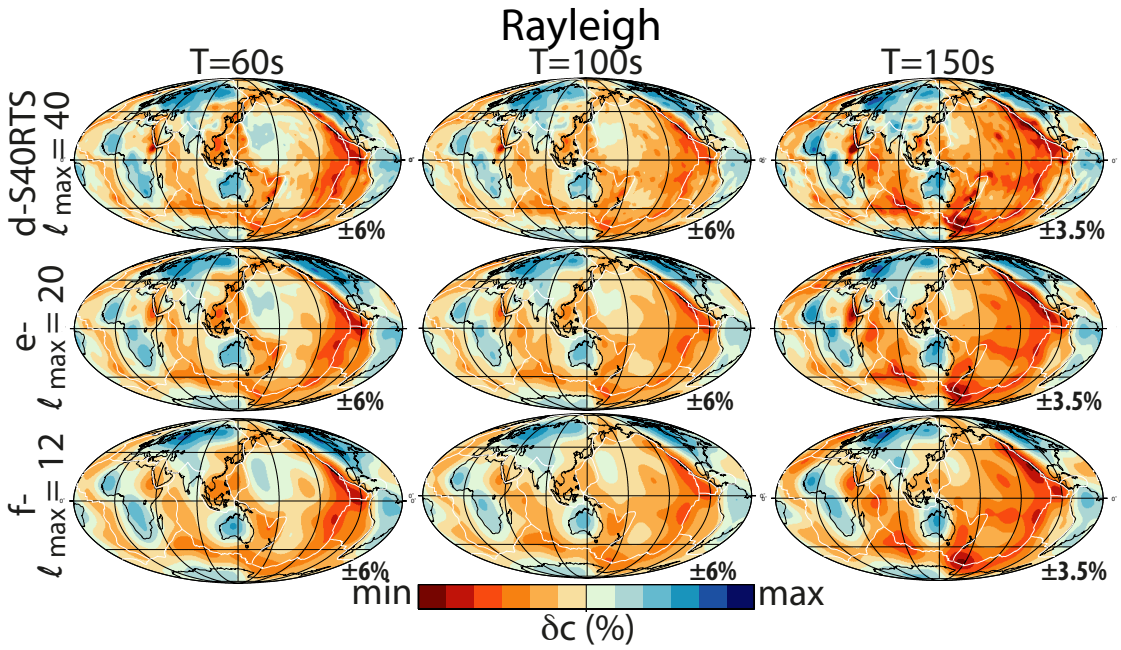

Figure 3.4: As in Fig. 3.2 for the models obtained by varying the l_{max}. d- l_{max}=40 (S40RTS) + homogeneous crust; e- l_{max}=20 + homogeneous crust; f- l_{max}=12 + homogeneous crust.

In addition, we couple S20RTS with a 3-D crustal model derived from CRUST2.0 (Bassin *et al.*, 2000). For the sake of simplicity in the calculations and to avoid the need to mesh complex crustal discontinuities in SEM (which could introduce numerical errors), the corresponding crust has a constant Moho depth (24.4 km). Effects of the increase (or decrease) of the Moho depth with respect to CRUST2.0 are compensated by an increase (or decrease) of the wave speeds above (or below) the Moho, applying the trade-off relationship between the Moho depth and the seismic shear-wave speed reported by Lebedev *et al.* (2013). This model will be referred as g (Figs. 3.6 and 3.7).

We carried out extensive tests to ensure that the Earth models are consistently implemented in the SEM and BORN codes (see section 2.6 in chapter 2 for more details).

3.4 RESULTS

We calculate E_ϕ and E_A for BORN-SEM pairs of R1 and G1 waveforms at T~60 s, 100 s and 150 s for every path shown in Fig. 3.1. For each model, the medians of E_ϕ, expressed as percentage

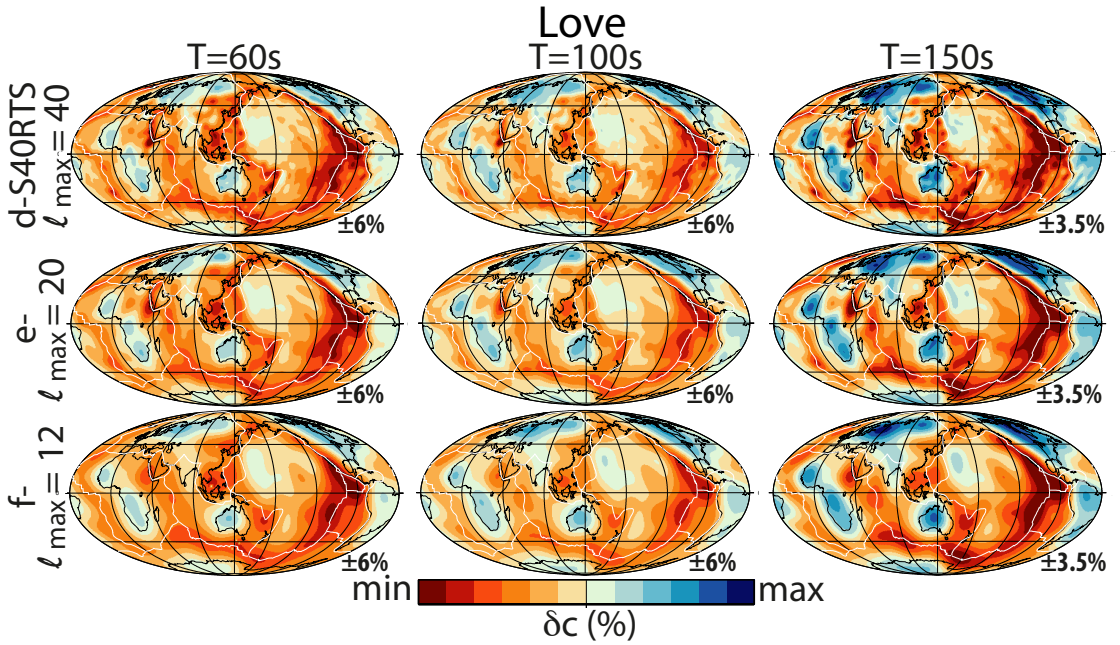

Figure 3.5: As in Fig. 3.4 but for Love waves.

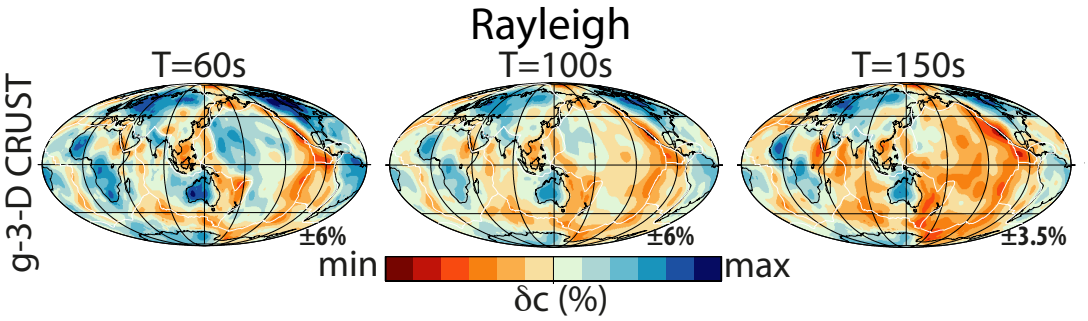

Figure 3.6: Rayleigh wave phase velocity maps at T~60 s, 100 s, 150 s for model *g* obtained combining the S20RTS (PV=1) mantle model with the 3-D crustal model. The scale of perturbations in the phase velocity maps is shown on the left for each row.

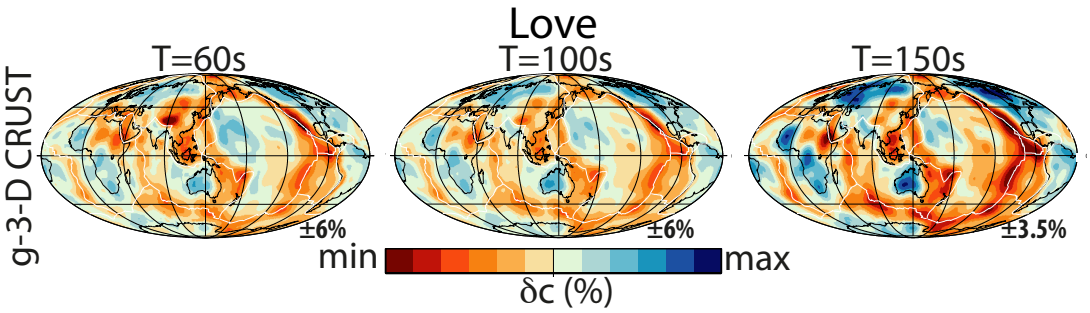

Figure 3.7: As in Fig. 3.6 but for Love waves.

of a wave cycle, and E_A, as defined by Eq. 3.1, are summarised in Figs. 3.8 and 3.9. Figs. 3.8 and 3.9 highlight that: (i) the fit between BORN and SEM calculations deteriorates both in amplitude and phase as the dominant period decreases and is particularly poor at T~60 s; (ii) a worsening of the fit is also associated with the increase of the PV factor; (iii) using a 3-D crustal model rather than the homogeneous layer yields a poorer BORN–SEM match; and, iv) BORN is not affected by the scale length of heterogeneity of the model (expressed by l_{max}). These considerations are valid regardless of the type of waves (Rayleigh or Love).

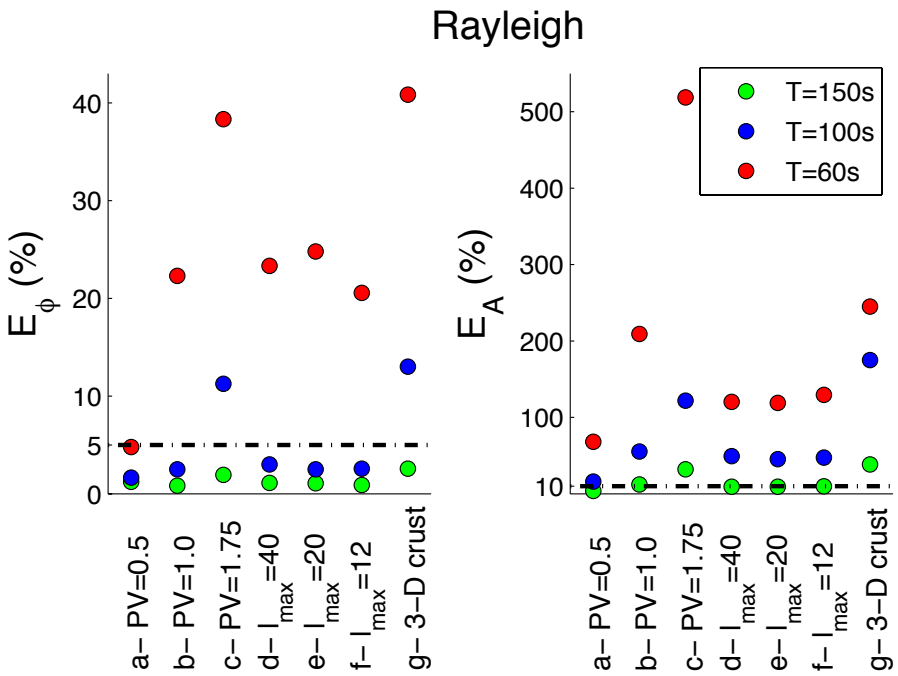

Figure 3.8: Summary of the phase (E_ϕ) and amplitude (E_A) errors for R1 at T~60 s, 100 s and 150 s as a function of the different models used in this work. E_ϕ is the percentual ratio of the BORN–SEM time-shift to the dominant period. E_A is calculated with equation 3.1. E_ϕ and E_A values are the medians for each model computed for all the paths illustrated in Fig. 3.1. The black dash-dot lines are our reference thresholds corresponding to E_ϕ=5 % and E_A=10 %. Model labels: *a*- PV=0.5 + homogeneous crust; *b*- PV=1 (S20RTS) + homogeneous crust; *c*- PV=1.75 + homogeneous crust; *d*- l_{max}=40 (S40RTS) + homogeneous crust; *e*- l_{max}=20 + homogeneous crust; *f*- l_{max}=12 + homogeneous crust; *g*- PV=1.0 (S20RTS) + 3-D crust.

By visual inspection of the waveforms and associated errors, we setup error thresholds to define a good modelling. These thresholds are 5 % of a wave cycle for E_ϕ and 10 % for E_A . For illustration, examples of waveform comparisons for various values of E_ϕ and E_A are shown in Fig. 3.10. By means of these thresholds (black dash-dot lines in Figs. 3.8 and 3.9), it arises that BORN matches well the phase of Rayleigh waves predicted by SEM only in case of mantle models with: (i) PV=0.5 for T>60 s; (ii) PV=1.0, such as S20RTS (but also S40RTS and models derived from it) for T>100 s; (iii) PV=1.75 and PV=1.0 mantle when the latter is combined with a heterogeneous crust model similar to CRUST2.0, for T>150 s. On the other hand, surface wave amplitudes modelled with BORN only match SEM results for waves with T 150 s and for the models: (i) S20RTS with PV=0.5; (ii) S40RTS; and, (iii) models

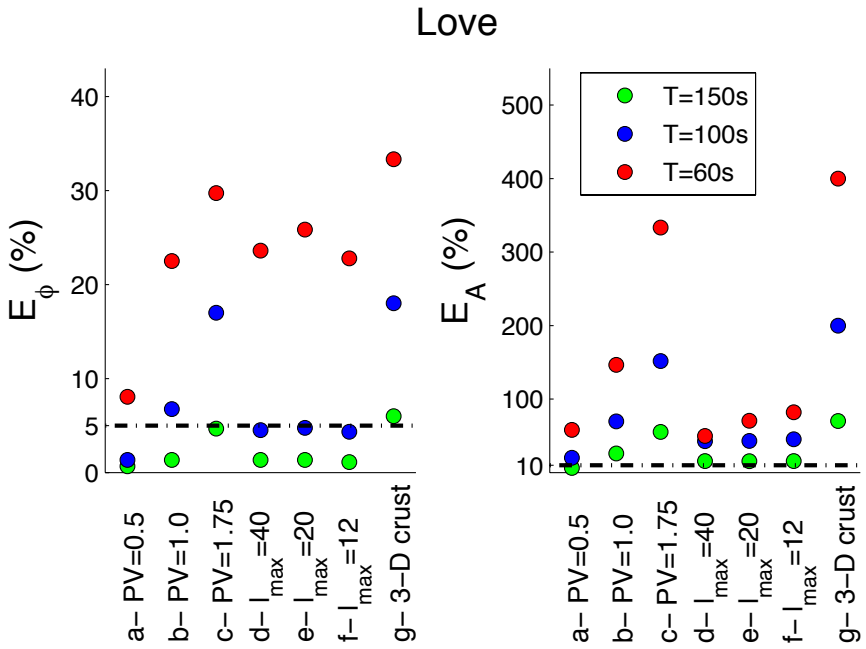

Figure 3.9: As in Fig. 3.8 but for G1.

derived from S40RTS with l_{max}=20 and l_{max}=12. Regarding Love waves, the performance of the Born approximation follows similar trends but with slightly poorer fits to SEM results. On the whole, the performance of the Born approximation is not encouraging in the framework of the forward modelling for waveform tomography based on current 3-D tomographic models.

3.4.1 DOMAIN OF VALIDITY

In order to define the domain of validity of BORN applied to waveforms, we analyse the correlation between the individual BORN errors and the phase delays in seconds accumulated along the paths ($\delta\phi$), with respect to the reference waveforms (Fig. 3.11). Namely, $\delta\phi$ is the phase-shift in seconds between the SEM seismogram for a 3-D Earth model and the NMS reference waveform calculated for PREM. $\delta\phi$ is calculated by cross-correlation and it is expected to be linearly related to the perturbations of the 3-D model along the path (Mercerat & Nolet, 2013). Fig. 3.11 shows that BORN fits well SEM in phase when $\delta\phi$ is less than 15 % of a waveform cycle, quantifying a narrow but well-defined domain of validity. For $\delta\phi$ larger than 15%, E_ϕ linearly grows with $\delta\phi$. This behaviour is valid for all the periods and models considered. A correlation between E_A and $\delta\phi$ is also reported in Fig. 3.11. The validity domain for the amplitude modelling is narrower ($\delta\phi$<5%) and less defined. Note that E_ϕ and E_A against $\delta\phi$ show a similar behaviour for both Rayleigh and Love waves (represented in Fig. 3.11 with different symbols).

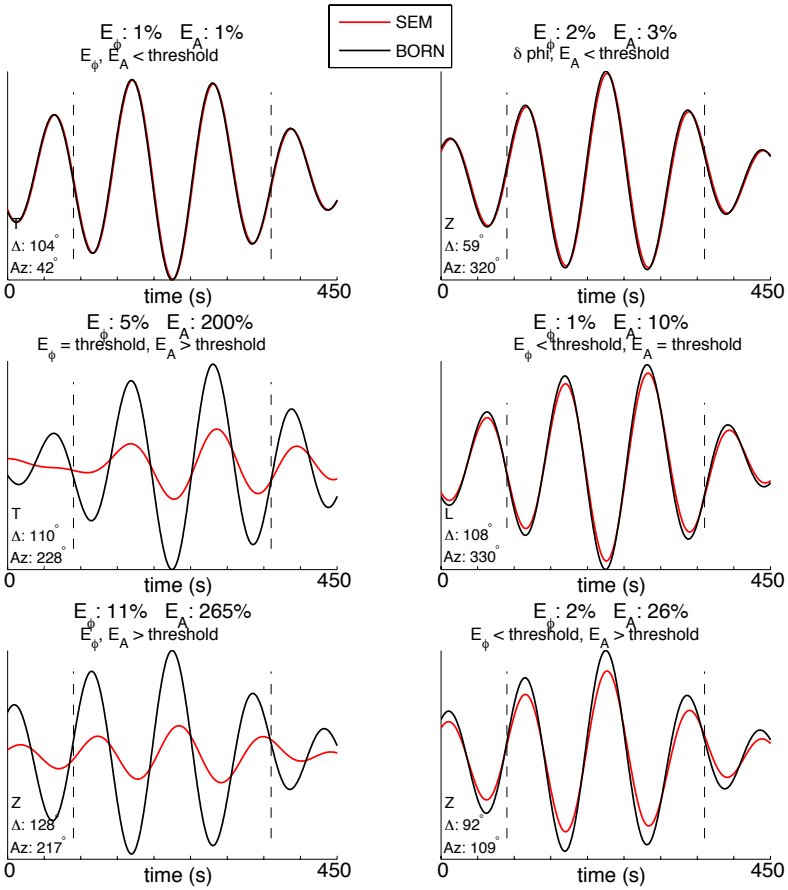

Figure 3.10: BORN–SEM comparison examples of R1—visible in the Z (vertical) and L (radial) seismogram components—and G1—visible in the T (transverse) component—waveforms at T~100 s for the event ev1. E_ϕ and E_A are reported above each pair specifying the relation with the threshold of goodness used in this work (E_ϕ=5 % and E_A=10 %). Seismogram component, epicentral distance and azimuth are indicated in the left-bottom corner. The black dashed lines indicate the selected time windows for the errors calculations.

3.5 DISCUSSION

The Born approximation is a short-time approximation, which depends on: (i) the strength and scale of heterogeneity; (ii) the number of wave cycles in the heterogeneous regions, which in turn depends on the wave frequency and path length. Indeed, increasing the wave frequency will lower the wavelength and thus increase the number of wave cycles in a given fixed heterogeneous region and fixed time window length. Likewise, using longer paths and thus longer time windows to reach seismic surface waves leads to a larger number of wave cycles. To study the effects of the short-time condition, we analyse E_ϕ as a function of the epicentral distance (Fig. 3.12). A low positive correlation between the errors and distance is found for all the periods considered. Thus, we only show the correlation of E_ϕ for T~100 s for conciseness. Despite the average error (green line, Fig. 3.12) showing a slightly positive slope, the large amount of small errors at large distances suggests that the Born approximation can

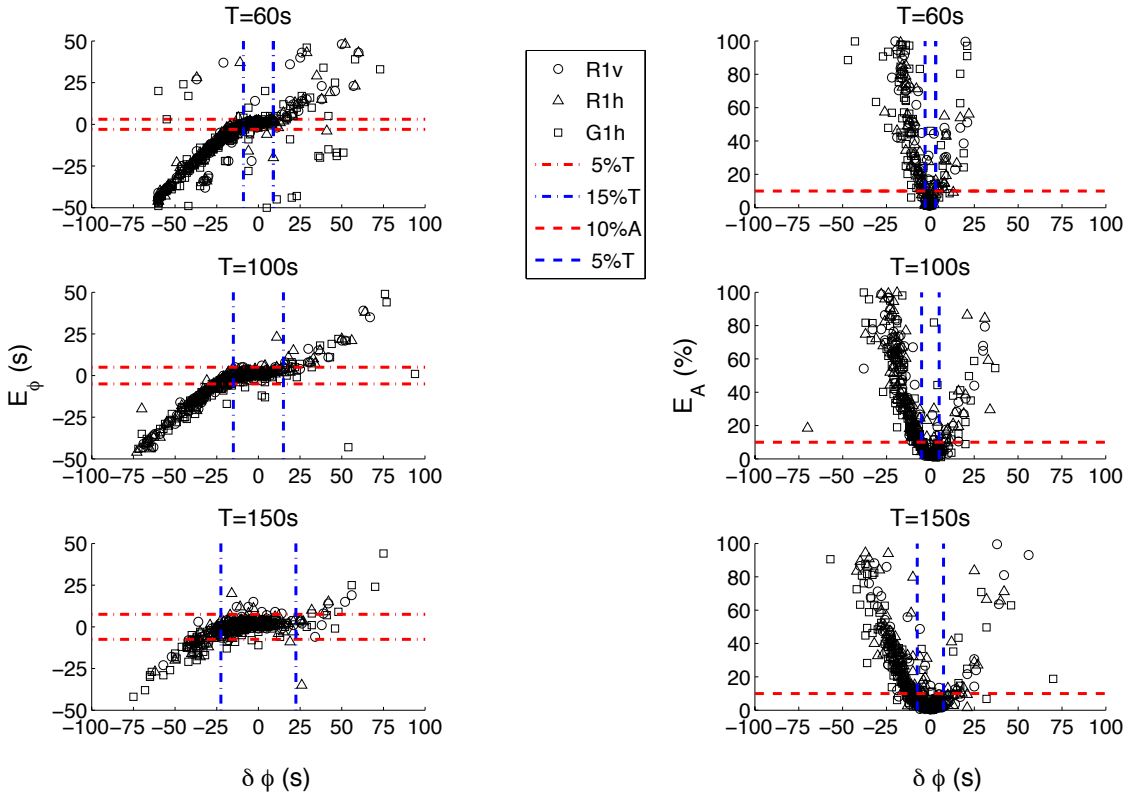

Figure 3.11: Phase (E_ϕ) and amplitude (E_A) errors of BORN with respect to SEM synthetics at T~60 s, 100 s and 150 s, for PV=0.5, 1.0 (S20RTS) and 1.75 mantle models combined with a homogeneous crustal layer versus the accumulated phase-delay on the path ($\delta\phi$). Each point corresponds to a BORN–SEM pair. $\delta\phi$ is the time-shift between SEM^{3D} and SEM^{1D} waveforms. E_ϕ is calculated as time-shift between a BORN-SEM pair and E_A using equation 3.1 for each BORN-SEM pair. Only -50 s< E_ϕ <50 s and E_A <100 % are included to zoom the plot around the window of validity. R1v and R1h refer to Rayleigh waves windowed in the vertical and radial components of the seismogram, respectively. G1h refers to Love waves windowed in the transverse component. Red lines are the reference thresholds (E_ϕ=±5 % and E_A=10 %). Blue lines enclose the BORN validity domain, $\delta\phi$ <15 % for the phase and $\delta\phi$ <5 % for the amplitude. See section 3.4.1 for more details.

virtually model well surface waves propagating even at distances of 140° (maximum distance considered in this work). This is due to the fact that the heterogeneity in 3-D Earth models is not distributed uniformly. Thus, the performance of the Born approximation is more strongly correlated with the total phase delay accumulated along the path ($\delta\phi$) than with the path length.

This fact explains why the medians of the errors rise with strength of heterogeneity of the 3-D Earth models (expressed by the PV factor) and the frequency of the wave. In fact, because of the dispersion of surface waves, the shorter is the period the shallower are the regions of the Earth sampled by the wave. In realistic models, surface waves with dominant period of 60 s, for example, are sensitive to structure down to 250 km–300 km where stronger heterogeneities are present. Conversely, for longer period surface waves the sampled regions include larger depths with weaker heterogeneity. This can be easily noticed from the phase velocity maps at different periods presented in Figs. 3.2-3.5. Thus, we can expect that at periods shorter than

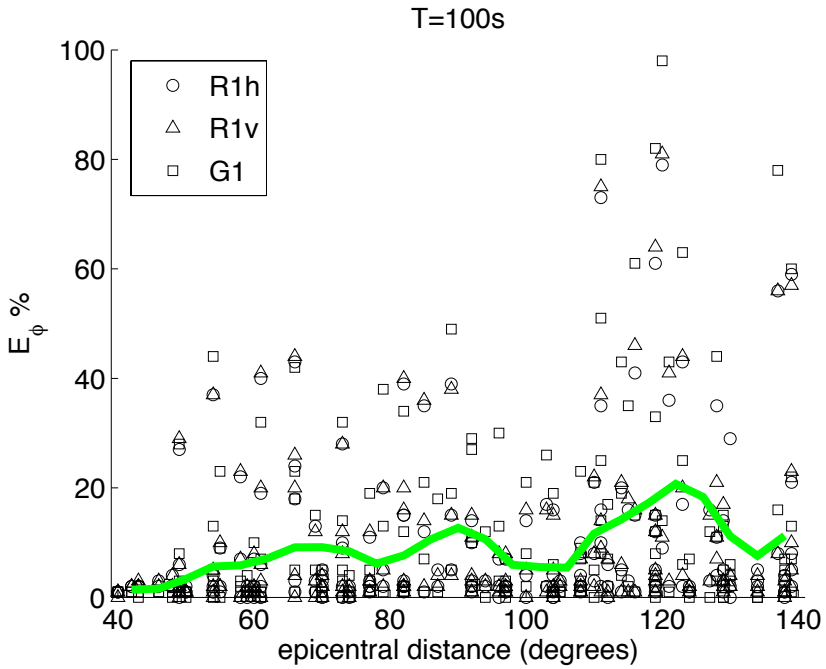

Figure 3.12: Correlation between E_ϕ (in percentage) and the epicentral distance at T~100 s for PV=0.5, 1.0 (S20RTS) and 1.75 mantle models combined with a homogeneous crustal layer. R1v and R1h refer to Rayleigh waves windowed in the vertical and radial components of seismogram, respectively. G1h refers to Love waves windowed in the transverse component. In green, a moving average with a window of 4° is shown.

60 s BORN will perform even worse due to the even stronger heterogeneity in the uppermost mantle and crust. Also, the slightly larger discrepancies obtained for Love waves (Fig. 3.9) are indeed related to the stronger heterogeneities in the Love phase velocity maps. In fact, in our calculations, the Love wave phase velocity maps (Figs. 3.3 and 3.5) have on average anomalies 20 % stronger than the corresponding Rayleigh maps. Finally, the observed worsening in the performance of BORN when using a 3-D crust compared to a homogeneous crustal model is due to the large heterogeneities in CRUST2.0

The high correlation between BORN's performance and $\delta\phi$ is confirmed by the domain of validity shown in Fig. 3.11. Our analysis shows that the Born approximation can accurately model the waveform phase of Rayleigh and Love waves for $\delta\phi$ not exceeding 15 % of the wave period and the waveform amplitude for $\delta\phi$ not exceeding 5 % of the period. This condition is more stringent than the rough estimate of 25 % reported by Panning *et al.* (2009). Our findings are in agreement with those presented by Dalton *et al.* (2014), which used the technique of Zhou *et al.* (2004) to calculate amplitude kernels based on the Born approximation. The authors showed that the misfits decrease with the dominant period and for T>75 s the misfits also decrease with the epicentral distance.

3.6 CONCLUSIONS

Given the increasing interest in forward modelling schemes for seismic tomography taking finite frequency effects into account, the Born approximation is highly appealing due to its simplicity and relative efficiency. However, this method is valid in a limited range of seismic velocity perturbations and time windows, which prompted us to quantify its domain of validity for forward modelling surface waveforms in a range of realistic current 3-D earth models. Previous studies (e.g., Capdeville *et al.*, 2002; Romanowicz *et al.*, 2008; Panning *et al.*, 2009; Peter *et al.*, 2009; Dalton *et al.*, 2014) investigated the accuracy of the Born approximation but a unique criterion defining its domain of validity has not been determined yet, especially regarding the forward modelling of seismic waveforms. We thus generated synthetic seismograms by using the Born approximation for seven different realistic combinations of 3-D mantle and crustal models and we treat SEM synthetics as ground truth. We separately considered phase and amplitude errors between BORN and SEM synthetics at T~60 s, 100 s and 150 s. We found that the Born approximation can only accurately model the phase of surface waveforms for source-receiver paths leading to time shifts smaller than about 15 per cent of the wave period considered. Regarding the amplitude modelling, the time-shifts cannot exceed 5 per cent of the period. In practice, these conditions are met for 3-D earth structure with the same power of heterogeneity as in the S20RTS or S40RTS models, or lower, at wave periods longer than 80 s–90 s for the phase and 150 s for the amplitude. Hence, the short-time first-order Born approximation has a very restricted domain of validity when applied directly to waveforms. More accurate forward modelling schemes should be used in waveform tomography, or, alternatively, inversions based on secondary measurements such as phase delays or amplitude anomalies remain an attractive possibility.

4

EMPIRICAL ASSESSMENT OF THE VALIDITY LIMITS OF THE SURFACE WAVE FULL RAY THEORY USING REALISTIC 3-D EARTH MODELS

Most of the material presented in this chapter is included in a research article submitted for publication to Geophysical Journal International (Parisi & Ferreira, n.d.) of which I am the first author.

4.1 SUMMARY

The surface wave full ray theory (FRT) is an efficient tool to calculate synthetic waveforms of surface waves. It combines the concept of local modes with exact ray tracing as a function of frequency. The purpose of this study is to evaluate the ability of the FRT approach to model teleseismic long-period surface waveforms (T~60 s–150 s) in realistic 3-D Earth models and to empirically assess its validity domain.

To achieve this goal, we compute vertical and horizontal component fundamental mode synthetic Rayleigh waveforms using the FRT, which are compared with calculations using the highly accurate spectral element method. We use thirteen global earth models including 3-D crustal and mantle structure, which are derived by successively varying the strength and length-scale of heterogeneity in current tomographic models.

We find that the FRT accurately predicts the phase and amplitude of long-period Rayleigh waves (T~60 s–150 s) for almost all the models considered, with errors in the modelling of the phase (amplitude) of Rayleigh waves being always smaller than 5 % (10 %), except for two models. The earth models for which FRT breaks exhibit shear-wave anomalies of up to ~20 %,

which is much larger than in current global tomographic models. This suggests that the FRT approach is a useful means to build the next generation of surface wave tomography models.

We also find that while the FRT errors in modelling the phase of waveforms do not depend strongly on frequency or component, the amplitude errors increase with increasing wave period and are larger for horizontal than for vertical component Rayleigh waves. Moreover, we observe a clear correlation between the FRT amplitude and phase errors and the roughness of the models. This allows us to quantify the limits of validity of the FRT in terms of model roughness thresholds, which can serve as useful guides in future seismic tomographic studies.

4.2 INTRODUCTION

Recent global 3-D whole-mantle tomographic models (e.g., Chang *et al.*, 2015; Moulik & Ekström, 2014; Ritsema *et al.*, 2011; Auer *et al.*, 2014) show an overall good consistency in terms of large-scale isotropic shear-velocity structure, at least in the upper mantle (e.g., Chang *et al.*, 2015). However, smaller-scale features (e.g., smaller than ~1 000 km) can exhibit high levels of disagreement, particularly in the deeper mantle.

Several factors can affect the outcome of a tomographic study, such as the type, amount and distribution of data, the model parametrisation and the forward and inverse modelling schemes used. Most of the current whole-mantle models (e.g., Chang *et al.*, 2015; Moulik & Ekström, 2014; Ritsema *et al.*, 2011; Auer *et al.*, 2014) employ the so-called great-circle approximation, which is an infinite frequency ray theory approach that only takes first-order path effects into account (Woodhouse & Dziewoński, 1984) to calculate either body-wave travel times or surface wave phases. The success of this approach lays in the low computational cost involved, allowing the inversion of large datasets, which may at least partly compensate the theory's limitations.

The current rapid development of powerful computing facilities is pushing tomographers towards the use of more sophisticated theories to increase the resolution of global Earth models. For example, the upper-mantle tomographic study of Schaeffer & Lebedev (2013) goes beyond the great-circle approximation by integrating across approximate sensitivity areas that depend on the wave frequency considered. More recently, French & Romanowicz (2014) used a hybrid approach based on the highly accurate spectral element method (SEM, e.g., Komatitsch & Vilotte, 1998) to build a new whole mantle model. In order to reduce the computational cost of the inverse problem, the non-linear asymptotic mode coupling theory (Li & Romanowicz, 1995) was used for the calculation of sensitivity kernels.

Another forward modelling technique that is more accurate than the great-circle approximation is the surface wave full ray theory, also referred as JWKB approximation or exact ray theory in other studies (Woodhouse, 1974; Woodhouse & Wong, 1986; Tromp & Dahlen, 1992a,b; Ferreira & Woodhouse, 2007a). While maintaining the physical simplicity and numerical efficiency of the great-circle approximation, the FRT approach considers off-great circle path and focussing/defocussing effects. Moreover, it also accounts for the influence of local structures at the source and receiver on the waveforms. However, it still

is an infinite frequency approximation, valid for smooth earth models, and it is expected to break down when the Fresnel zone (which is proportional to the wavelength) can no longer be approximated by a thin ray.

Some previous studies have investigated the quality of surface waveform predictions taking into account off-great circle path effects. For example, Wang & Dahlen (1995) compared FRT surface wave synthetics with coupled-mode theoretical seismograms and showed that the accuracy of the FRT decreases for rougher models. Similarly, Peter *et al.* (2009) also found increasing misfits for rougher media when comparing exact ray theory calculations with results using a "membrane" approach to compute surface waveforms numerically. Romanowicz *et al.* (2008) combined the non-linear asymptotic mode coupling theory (Li & Romanowicz, 1995) with the exact ray tracing (Woodhouse & Wong, 1986; Romanowicz, 1987) showing that, in most of the cases, the predictions improve when focussing effects are considered. Finally, Dalton *et al.* (2014) assessed the quality of FRT amplitude predictions and found that, for periods longer than 50 s, neglecting the broad zone of surface wave sensitivity worsens the accuracy of the FRT. However, these studies have some limitations, such as, e.g., the use of relatively few and/or simplified Earth models and the lack of quantitative criteria establishing the validity domain of the theoretical formulations used.

The goal of this study is to quantify the validity domain of the FRT when modelling long-period surface waveforms in realistic 3-D Earth models. The expressions *realistic Earth model* is used with the same meaning explained in chapter 3 (section 3.3.1). Ultimately, we aim at examining whether the FRT might be a useful forward modelling scheme for future waveform tomography efforts. We calculate fundamental-mode surface waveforms using the FRT for 13 realistic 3-D earth models with various strength and scale of heterogeneity. These waveforms are then compared with synthetic seismograms generated with the SEM by calculating phase and amplitude anomalies between them in the period range T~60 s–150 s. By correlating the anomalies to the roughness of the earth models, we define the validity domain of the FRT, which will be a useful reference for future seismic tomography studies.

4.3 SURFACE WAVE FULL RAY THEORY

4.3.1 THEORY

Surface wave FRT involves the concept of local normal modes (Woodhouse, 1974) and exact ray tracing (Woodhouse & Wong, 1986) as a function of frequency. In the framework of FRT, the seismic displacement of surface waves involves a source, a path and a receiver term. The source term includes the source mechanism, local mode eigenfunctions (and their radial derivatives) for the structure beneath the source, and the ray's take-off angle. The path term takes into account off-great circle path deviations as well as focusing and defocusing effects due to Earth's heterogeneity. Finally, the receiver term includes local mode eigenfunctions for the structure beneath the receiver. In order to calculate the path term, we use fundamental-mode phase velocity maps that we computed for the thirteen 3-D earth models used and for

the wave periods considered (see section 5.3). We refer to section 2.4.2 of chapter 2 for more detail on the FRT and its implementation.

Being a high-frequency approximation, the FRT is valid in a smooth medium on the scale of a wavelength. Hence, diffraction, scattering and other finite frequency effects are not considered, and the FRT domain of validity is often expressed as $\lambda \ll \Omega$, whereby the wavelength of the wave (λ) must be much smaller than the scale-length of heterogeneity of the earth model (Ω). Thus, in this study we use 3-D earth models with different scale lengths of heterogeneity (see section 4.5.1). Moreover, since the most recent tomographic models (e.g., Schaeffer & Lebedev, 2013) seem to show much stronger heterogeneity than in previous models (e.g., Ritsema *et al.*, 2011), here we test the FRT also using earth models with various strengths of heterogeneity (see section 4.5.1). For each phase velocity map used in the FRT calculations, we compute its roughness R as the root-mean-square of the gradient of the map:

$$R = \sqrt{\int_{\Omega} |\nabla_1 \delta c|^2 dA} \tag{4.1}$$

where $\nabla_1 = \hat{\boldsymbol{\theta}}\,\partial_\theta + \hat{\boldsymbol{\Phi}}(\sin\theta)^{-1}\partial_\phi$, θ the colatitude and Φ the longitude. $\int_\Omega$ denotes integration over the surface of the unit sphere and $\delta c = \frac{c - c^{PREM}}{c^{PREM}}$ is the phase velocity perturbation as a function of the frequency. The parameter R will be crucial to quantify the validity domain of the FRT in section 4.7.

4.4 WAVEFORM CALCULATIONS

We generate synthetic waveforms with the FRT and we use SEM (SPECFEM3D_ GLOBE package; Komatitsch & Vilotte (1998); Komatitsch & Tromp (2002a,b); Komatitsch *et al.* (2010a)) as ground truth to assess the accuracy of the FRT calculations. As seen in chapter 2 (section 2.5.1), SEM is a highly accurate method for calculating the complete seismic wavefield even in highly heterogeneous media and has already been previously used in a few studies to benchmark forward modelling methods (Romanowicz *et al.*, 2008; Panning *et al.*, 2009; Dalton *et al.*, 2014; Parisi *et al.*, 2015).

We select 3 real earthquakes and 75 seismic stations to achieve a realistic source-receiver distribution (Fig. 3.1 in chapter 3). The earthquakes are selected attempting to evenly sample most of the regions of the globe and with hypocentral depth less than 25 km to best excite fundamental mode surface waves. Paths are selected with an epicentral length ranging between 40° and 140° to avoid near-source effects, caustics and the overlapping of the wave trains.

FRT and SEM velocity waveforms are processed as explained in section 3.3 in chapter 3. The FRT–SEM pairs of vertical and radial component seismograms considered are compared at wave periods of T~60 s, 100 s and 150 s. We use time windows three times wider than the dominant wave period and centred around the maximum Rayleigh wave amplitude. Picking of the fundamental mode Rayleigh wave in the FRT traces is straightforward because our

FRT calculations only include fundamental modes. Nevertheless, visual inspection of the waveforms and selected windows is carried out to reduce the influence of overtones in the windowed SEM traces.

On the other hand, it is not possible to separate the fundamental mode Love waves in the SEM synthetics with our simple windowing strategy. Fig. 4.1 compares theoretical seismograms calculated by normal mode summation for the 1-D reference model PREM (Dziewoński & Anderson, 1981) for: (i) fundamental modes only (black); and, (ii) fundamental and higher modes summed together (red). In the vertical component there is no difference between the two traces in the window considered, allowing a good separation of the fundamental mode Rayleigh wave. In contrast, the contamination of the fundamental mode Love wave by the overtones is particularly noticeable in the transverse component. Since in this study we are only interested in fundamental mode surface waves, in the remainder of this paper we will focus on Rayleigh waves, for which it is easier to separate the fundamental mode from the overtones. Further details regarding Love waves modelling are reported in appendix A.

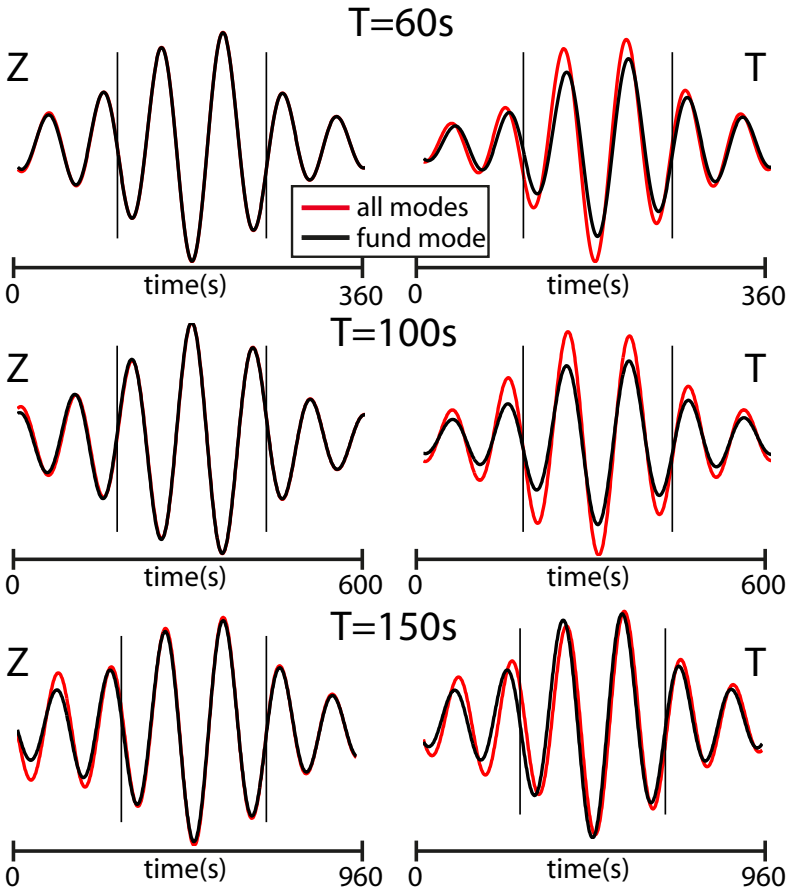

Figure 4.1: Examples of waveforms calculated by normal mode summation in PREM and filtered to have dominant wave periods of T~60 s, 100 s, 150 s at an epicentral distance of 40°. Rayleigh waves are visible in the vertical seismogram component (Z) and Love waves in the transverse component (T). Black waveforms only include fundamental modes, while red waveforms are obtained by summing all the overtones. Vertical black lines show the window within which waveforms are compared, following the method described in section 4.4.

4.4.1 PHASE AND AMPLITUDE ERRORS

For every pair of FRT–SEM waveforms, we calculate the error in phase E_ϕ and amplitude E_A within the selected window for vertical and horizontal component Rayleigh waves. E_ϕ is calculated by cross-correlation and it is expressed in percentage of a wave cycle. The error in amplitude in percentage is calculated in the same way as by Parisi *et al.* (2015):

$$E_A = 100 * \frac{\sum_i |A^F_{i+E_\phi} - A^S_i|}{\sum_i |A^S_i|} \tag{4.2}$$

where A^F and A^S are the waveform amplitudes of the FRT and SEM waveforms, respectively. The sum is calculated over the samples i in the selected window and the subscript $i + E_\phi$ means that the waveforms are aligned before calculating the E_A. To quantify the condition of validity of the FRT, we consider that the modelling is accurate if the errors fall below the following thresholds: E_ϕ<5 % and E_A<10 % (Parisi *et al.*, 2015). Examples of good and poor performances of the FRT are shown in Fig. 4.2 where FRT waveforms are compared to SEM results and the errors are shown.

4.5 EARTH MODELS

We compare FRT and SEM waveforms for 13 different combinations of mantle and crustal models. Specifically, our set of models consists of 11 different mantle and 3 different crustal models, which shall be referred as earth models *a*-*m* (sections 4.5.1 and 4.5.2). The mantle models have been derived from either the S20RTS (Ritsema *et al.*, 1999) or S40RTS (Ritsema *et al.*, 2011) models (section 4.5.1). These models are parameterised with spherical harmonic basis functions and are defined in terms of shear velocity perturbations δVs with respect to the reference model PREM (Dziewoński & Anderson, 1981). In this study, perturbations in compressional wave speed δVp and density $\delta\rho$ are scaled with respect to the Vs perturbations ($\delta\rho = 0.40\delta Vs$, Anderson *et al.* (1968); $\delta Vp = 0.59\delta Vs$, Robertson & Woodhouse (1995)). The two 3-D crustal models have been derived from CRUST2.0 (Bassin *et al.*, 2000) (section 4.5.2).

In order to study separately the effects of 3-D mantle structure from those due to the heterogeneous crust, we started by considering a homogeneous crustal layer with thickness of 24.4 km, Vs=3.2 km/s, Vp=5.8 km/s, ρ = 2.6 g/cm^3, which corresponds to the PREM's upper crustal layer. Subsequently, we carry out SEM-FRT comparisons for 3-D crustal models (section 4.5.2).

We undertook many tests to guarantee that the earth models are implemented in the SEM and FRT codes in a consistent manner (see section 2.6 in chapter 2 for more details).

4.5.1 MANTLE MODELS

We build our set of mantle models varying the strength and the scale length of heterogeneity. All the figures shown in this section correspond to the various 3-D mantle models described

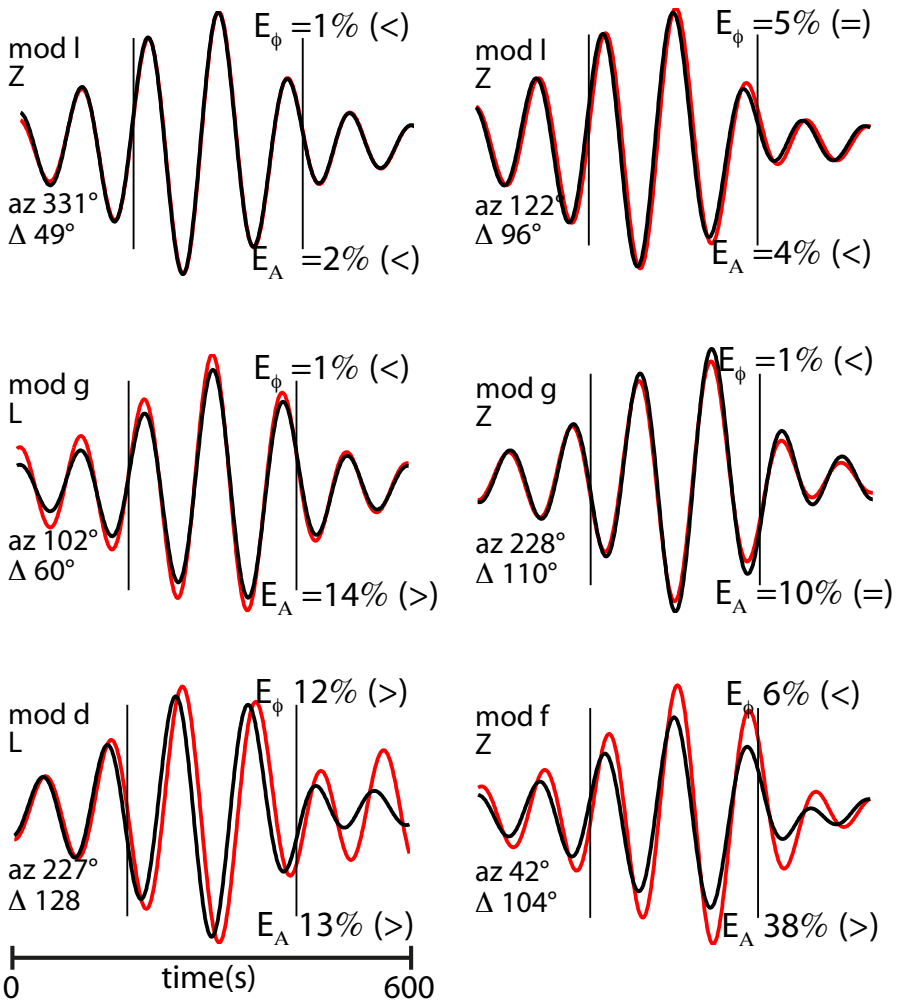

Figure 4.2: Examples of waveform comparisons using the FRT (black) and the SEM (red) with a dominant period of T~ 100 s. Z, L and T refer to the vertical, radial and transverse seismogram components. E_ϕ and E_A are reported on the right of each subplot. The relationship between the errors and the threshold of the fit goodness ($E_\phi \leq 5$ % and $E_A \leq 10$ %) is specified in brackets. The earth model, seismogram component, azimuth and epicentral distance are indicated on the left hand side of each subplot. Vertical black lines indicate the selected time window for the error calculations.

combined with a homogeneous crustal layer.

VARYING THE SCALE-LENGTH OF HETEROGENEITY-l_{max}

S40RTS is parameterised with spherical harmonic basis functions expanded up to degree 40 (l_{max}=40, model *c*). The smallest scale of heterogeneity Ω of a model with l_{max}=40 is ~1 000 km. From S40RTS, we build a subset of models truncating the harmonic basis function to 20 (model *b*) and 12 (model *a*). For l_{max}=20, Ω ~2 000 km and for l_{max}=12, Ω ~3 200 km. Rayleigh wave phase velocity maps for this subset of models are reported in Fig. 4.3. As expected, the maps show more small scale heterogeneity as l_{max} increases. The roughness of these models (Eq. 4.1) increases as the period decreases and it ranges from R=0.7 x 10^{-5} for l_{max}=12 and T~150 s to R=1.8 x 10^{-5} for l_{max}=40 and T~60 s (Table 4.1).

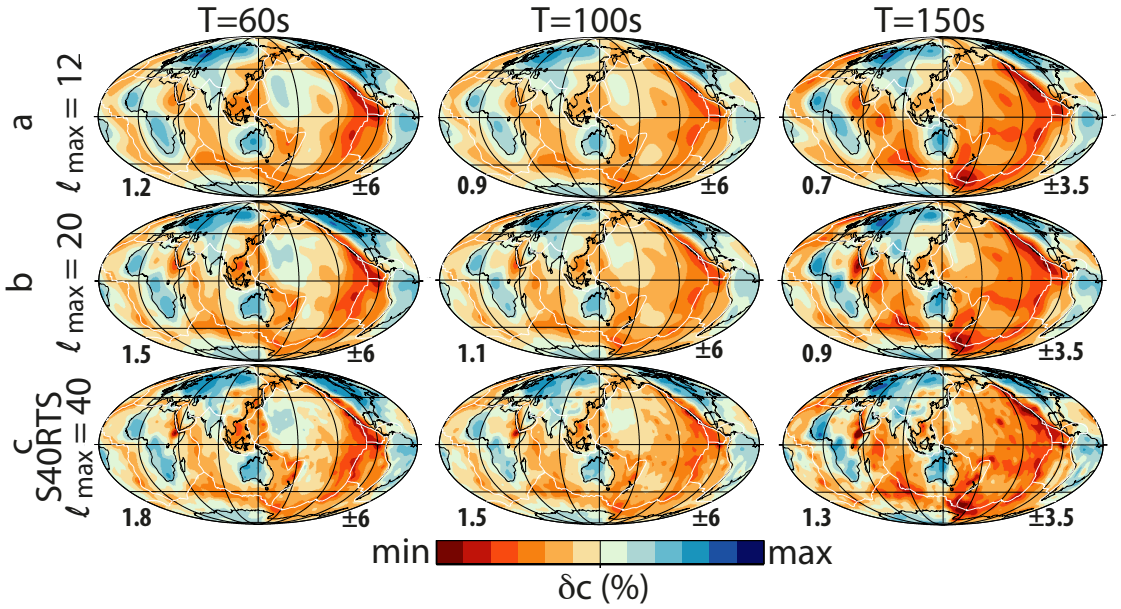

Figure 4.3: Rayleigh wave phase velocity maps calculated for mantle models with l_{max}=40 (S40RTS), 20, 12 for wave periods ~60 s, 100 s, 150 s. These mantle models are combined with a homogeneous crustal layer and shall be referred as models *a*, *b* and *c* throughout this paper. The numbers on the bottom left side of each map are roughness values (R $\cdot 10^{-5}$, Eq. 4.1). The numbers on the bottom right side of the maps represent the colour scale ranges.

		Roughness ($\cdot 10^{-5}$)		
	Models/Periods	60s	100s	150s
a	l_{max}=12	1.2	0.9	0.7
b	l_{max}=20	1.5	1.1	0.9
c	l_{max}=40	1.8	1.5	1.3
d	PV=0.5	0.9	0.7	0.5
e	PV=1.0	1.9	1.3	0.9
f	PV=1.75	3.3	2.3	1.6
g	PO=1.5	2.8	2.0	1.7
h	PO=2.0	3.7	2.6	1.8
i	PO=3.0	5.5	3.9	2.7
j	PO=3.5	6.4	4.6	3.2
k	l_{max}=40 PO=3.0	5.4	4.5	3.9
l	CRUST2.0	2.3	1.5	1.0
m	const_moho	2.2	1.4	1.0

Table 4.1: Roughness (R as in Eq. 4.1) values of all the Rayleigh wave phase velocity maps used in this study for wave periods of T~60 s, 100 s and 150 s.

In this work we consider waveforms with dominant period from T~60 s to T~150 s, which correspond to wavelengths λ ranging from about 240 km to 640 km. From the relation $\lambda \ll \Omega$ we expect an increase of the errors E_ϕ and E_A when either the wave period or l_{max} increase. For l_{max}=40, the relation $\lambda \ll \Omega$ is in principle not strictly respected, at least for the longer

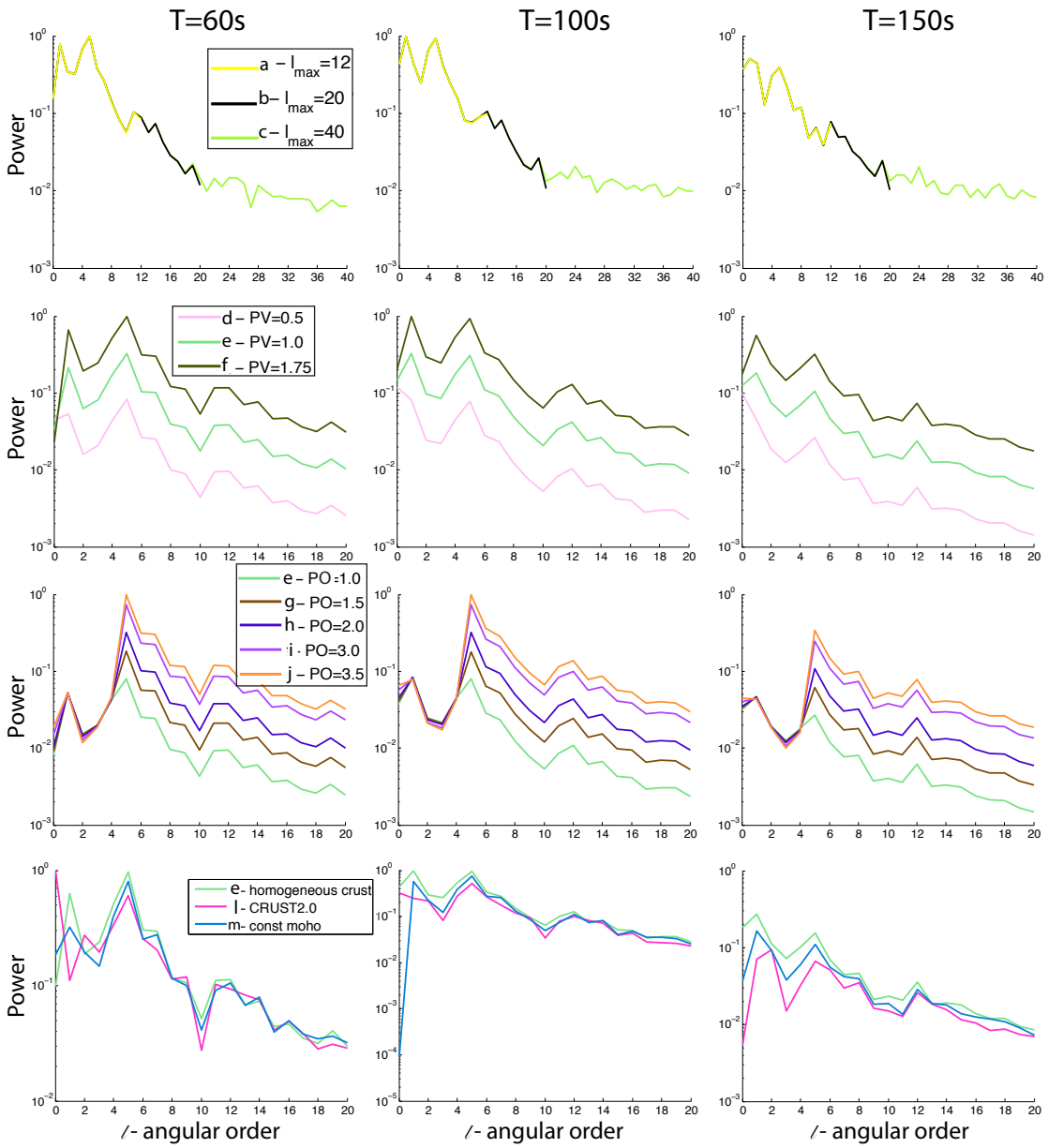

Figure 4.4: Power spectra of Rayleigh wave phase velocity maps at T~60 s (left column), 100 s (middle column), 150 s (right column) for the earth models considered in this study. Top row: models obtained varying l_{max} (subsection 4.5.1); second row: models obtained varying PV factor (subsection 4.5.1); third row: models obtained varying PO factor (subsection 4.5.1). Fourth row: models obtained by varying the crustal model (subsection 4.5.2). Spectra are normalised with respect to the maximum value of each row of subplots.

wave periods, and thus we expect the FRT to break down.

VARYING THE STRENGTH OF HETEROGENEITY—PV FACTOR

We build a second subset of models starting from S20RTS (model *e*) and by applying a multiplicative factor (PV) of 0.5 and 1.75 to δVs of S20RTS. On the one hand, PV=0.5 (model

d) is chosen to be fairly weakly heterogeneous and, on the other hand, PV=1.75 (model *f*) is chosen to obtain a strength of heterogeneity comparable to that in some of the current global upper mantle tomographic models (Debayle & Ricard, 2012; Schaeffer & Lebedev, 2013; French & Romanowicz, 2014). Rayleigh wave power spectra for these models can be seen in Fig. 4.4 (second row). Rayleigh wave phase velocity maps for S20RTS (PV=1.0, PO=1.0) are shown in Fig. 4.5. Maps for PV=0.5 and PV=1.75 are not shown for brevity as they differ from those with PV=1.0 just by a constant factor.

The roughness of these models increases as the period decreases and PV increases. It ranges from R=0.5 x 10^{-5} for PV=0.5 and T~150 s to R=3.3 x 10^{-5} for PV=1.75 and T~60 s (Table 4.1).

As these three models have the same smallest scale of heterogeneity (l_{max}=20, Ω~2 000 km), considering the FRT validity condition $\lambda \ll \Omega$, in theory we do not expect a strong dependency of the FRT's performance on the PV factor.

VARYING THE STRENGTH OF HETEROGENEITY—PO FACTOR

We build another subset of mantle models by varying the strength of the small scale heterogeneity only. We apply a multiplicative factor (PO) to the spherical harmonic coefficients of S20RTS for l larger or equal to 5. In other words, we increase the strength of heterogeneity with size smaller than about 7 300 km, leaving those larger than 7 300 km as in S20RTS. We use PO=1.0 (same than PV=1, S20RTS, model *e*), 1.5 (model *g*), 2.0 (model *h*), 3.0 (model *i*) and 3.5 (model *j*). Rayleigh wave phase velocity maps for these models are displayed in Fig. 4.5 and the power spectra are shown in Fig. 4.4 (third row). Finally, in order to obtain an end-member model with strong and rough heterogeneity, we also applied PO=3.0 to S40RTS (model *k*).

Excluding the model *k*, we do not increase the smallest Ω of this subset of models. For this subset of models R increases as the period decreases and PO increases. It ranges from R=0.9 x 10^{-5} for PO=1.0 and T~150 s to R =6.4 x 10^{-5} for PO=3.5 and T~60 s (Table 4.1).

It is worthy to illustrate the difference between the PV and PO factors. Fig. 4.6 shows examples of depth profiles at two locations when varying PV and PO. These profiles show that whereas the variations of the PV factor have a linear effect on the global strength of the perturbations, the PO factor can even change the sign of the anomalies in some cases (e.g., profile B, top, 600 km of depth).

4.5.2 CRUSTAL MODELS

In addition to considering a homogeneous crust model (Moho depth=24.4 km, Vs=3.2 km/s, Vp=5.8 km/s, ρ=2.6 g/cm^3), we have also combined our set of mantle models with two 3-D crustal models.

We combine the mantle model S20RTS with the 3-D global crust model CRUST2.0 (model *l*). Moreover, in order to investigate the effects of variations in Moho depth, we also use a combination of the S20RTS mantle with a simplified version of CRUST2.0, where the Moho

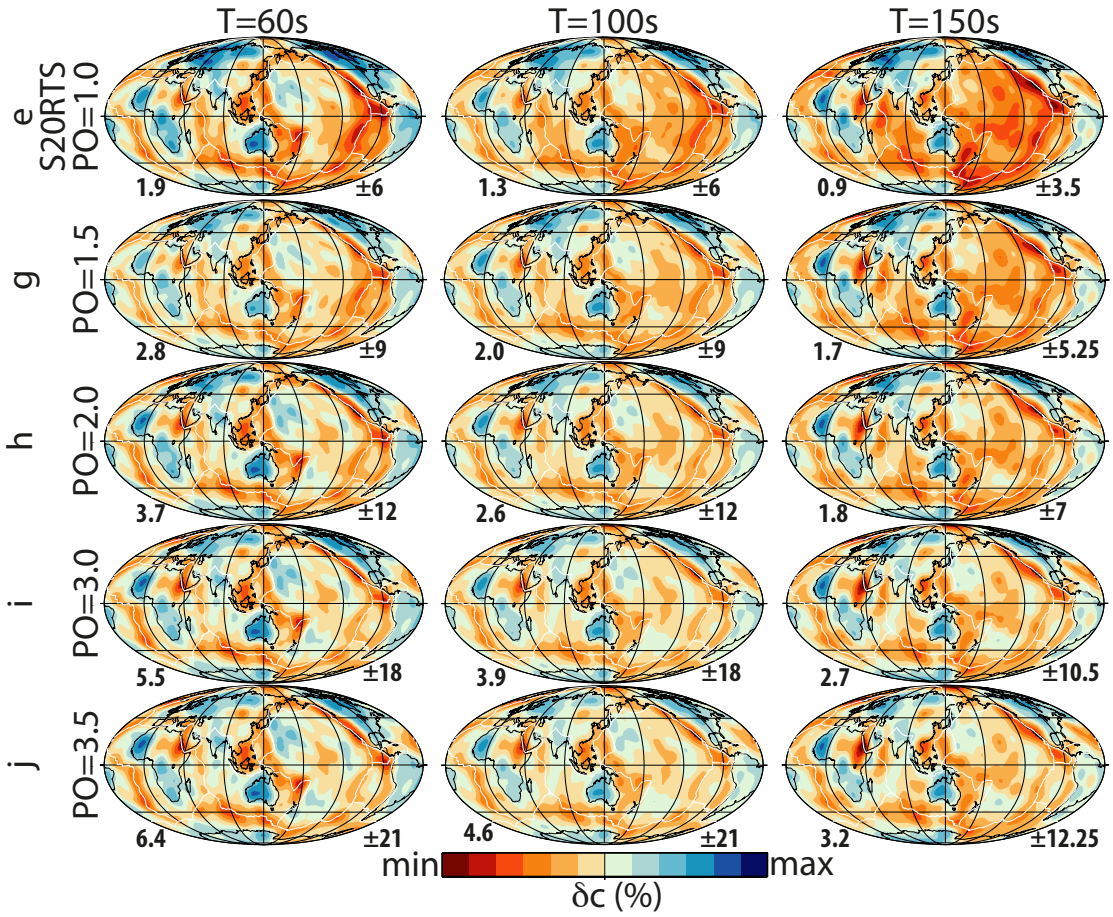

Figure 4.5: Rayleigh wave phase velocity maps calculated for mantle models with PO=1.0 (S20RTS), 1.5, 2.0, 3.0, 3.5 for wave periods T~60 s, 100 s, 150 s. These mantle models are combined with a homogeneous crustal layer and shall be referred as models *e*, *g*, *h*, *i* and *j*, respectively, throughout this paper. The numbers on the bottom left side of each map are roughness values ($R \cdot 10^{-5}$, Eq. 4.1). The numbers on the bottom right side of the maps represent the colour scale ranges.

depth is maintained constant to 24.4 km (model *m*). To build this model from CRUST2.0 we follow the same approach as in Parisi *et al.* (2015) whereby an increase (or decrease) of the Moho depth with respect to CRUST2.0 is compensated by an increase (or decrease) of Vs, applying the trade-off relationship between the Moho depth and Vs reported by Lebedev *et al.* (2013).

Rayleigh wave phase velocity maps for S20RTS combined with these two 3-D crustal models are shown in Fig. 4.7. Interestingly, the effects of the crust are visible even for T~150 s. Power spectra are shown in Fig. 4.4 (fourth row) and the roughness values are summarised in Table 4.1.

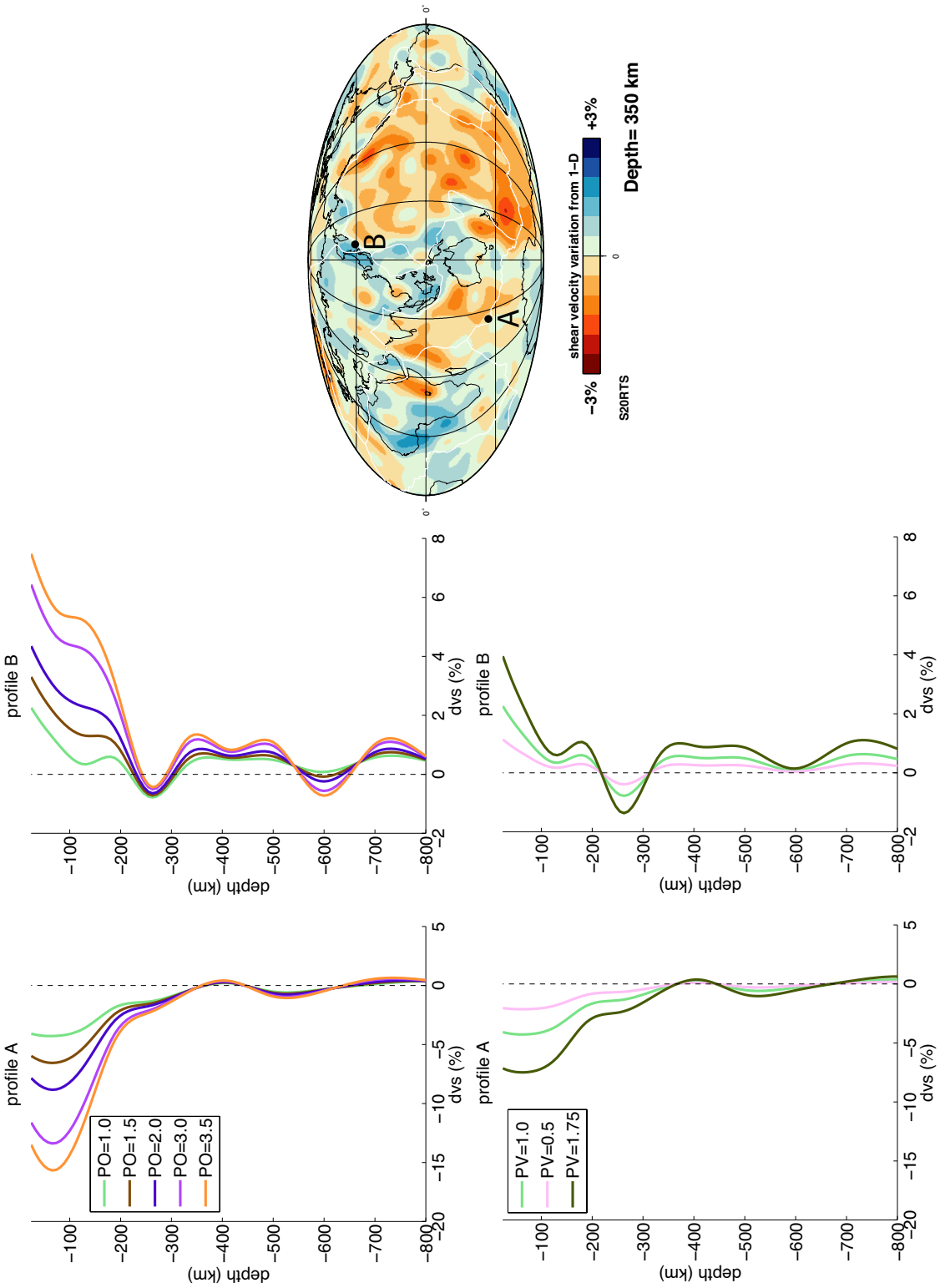

Figure 4.6: Examples of depth-profiles of shear velocity perturbations in the mantle showing the differences of varying PO and PV.

4.6 RESULTS

The results of the FRT–SEM waveform comparisons are summarised in Fig. 4.8 and 4.9 where the medians of all the phase (E_ϕ) and amplitude (E_A) errors are reported for each model and

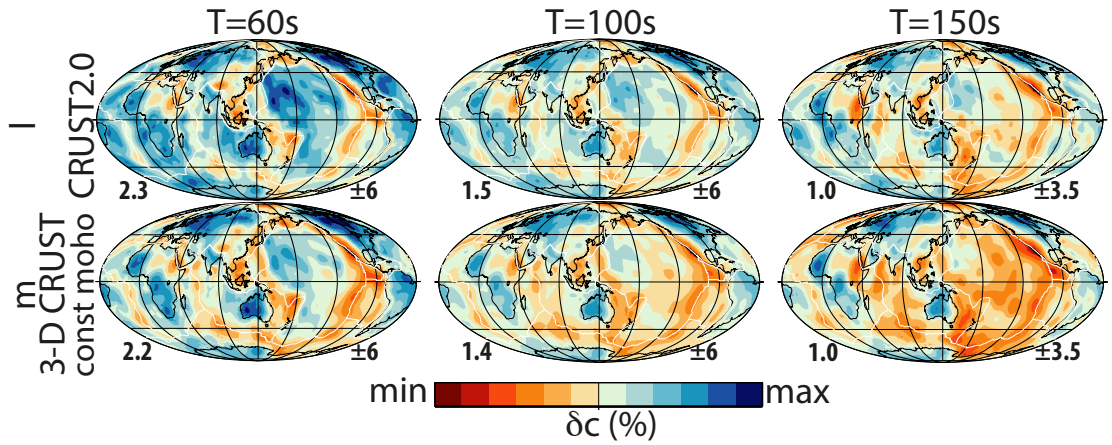

Figure 4.7: Rayleigh wave phase velocity maps for wave periods ~60 s, 100 s, 150 s calculated for mantle model S20RTS combined with CRUST2.0 (top row) and a simplified version of CRUST2.0 with constant Moho depth (bottom row). These crustal models shall be referred as models *l* and *m* throughout this paper. The numbers on the bottom left side of each map are roughness values (R $\cdot 10^{-5}$, Eq. 4.1). The numbers on the bottom right side of the maps represent the colour scale ranges.

each wave period. We prefer to use the median rather than the average to reduce the effects of outliers. In the next subsections we analyse the various factors affecting the performance of the FRT at predicting Rayleigh wave phase and amplitudes.

4.6.1 EFFECTS OF SCALE-LENGTH OF HETEROGENEITY

Fig. 4.8 shows that increasing l_{max} (models *a*, *b* and *c*) does not substantially affect E_ϕ, except for T~60 s. E_ϕ slightly increases with decreasing wave period, but, overall, for models *a*–*c* the FRT accurately models Rayleigh wave phase, with E_ϕ being always below the 5 % error threshold for both vertical and horizontal component Rayleigh waves.

Regarding the amplitude errors, Fig. 4.9 shows a clearer trend of increasing errors with l_{max} and wave period. Nevertheless, E_A are also always under the error threshold of 10 % for models *a*–*c*.

4.6.2 EFFECTS OF STRENGTH OF HETEROGENEITY

PV FACTOR

Fig. 4.8 for models *d*, *e* and *f* shows a strong correlation between E_ϕ and the PV factor for both vertical and horizontal component Rayleigh waves. Also, similar to the previous section, E_ϕ is anti-correlated with wave period and it never exceeds the phase misfit threshold.

E_A for these models (models *d*–*f*; Fig. 4.9) is directly correlated to the wave period. The threshold for E_A is exceeded for the horizontal component of Rayleigh waves for PV=1.75 and T~150 s but the overall FRT performance in modelling Rayleigh wave amplitudes for this subset of models is good.

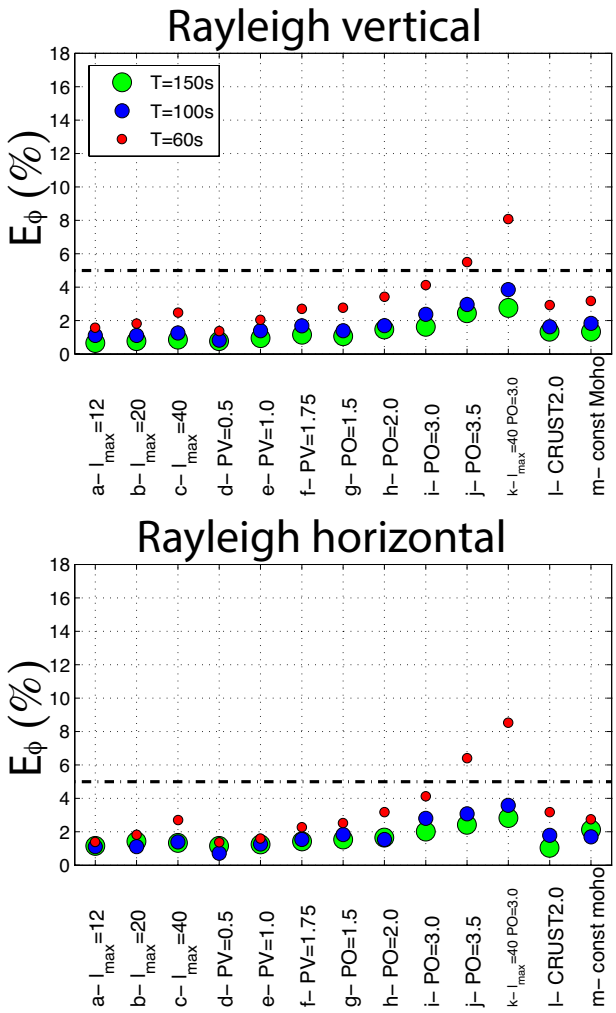

Figure 4.8: Summary of the phase error E_ϕ at T~60 s, 100 s and 150 s for all the models used in this study. E_ϕ values are the medians for each model and period computed for all the paths illustrated in Fig. 3.1 in chapter 3. The horizontal black dash-dot lines correspond to the error thresholds of 5 %.

PO FACTOR

Similar to the PV factor effect studied in the previous section, there is a strong correlation between E_ϕ and the PO factor (models e,g–j; Fig. 4.8). The rate of increasing errors with PO is highest for T~60 s. The overall FRT performance for this subset of models is good, since E_ϕ is only slightly above the misfit threshold for a PO factor of 3.5 and for a wave period of T ~60 s.

The trend of E_A (Fig. 4.9, models e, g–j) against the period for this subset of models is similar to that observed for the PV factor. For this subset of models, we also observe that E_A is larger for horizontal component Rayleigh waves than for vertical components. The FRT performs poorly when modelling Rayleigh wave amplitudes for models with PO=3.0 and 3.5 for all periods considered.

Figs. 4.8 and 4.9 also show the results for the model k, which is built applying PO=3.5 to S40RTS. The phase and amplitude errors for this model are consistent with the results

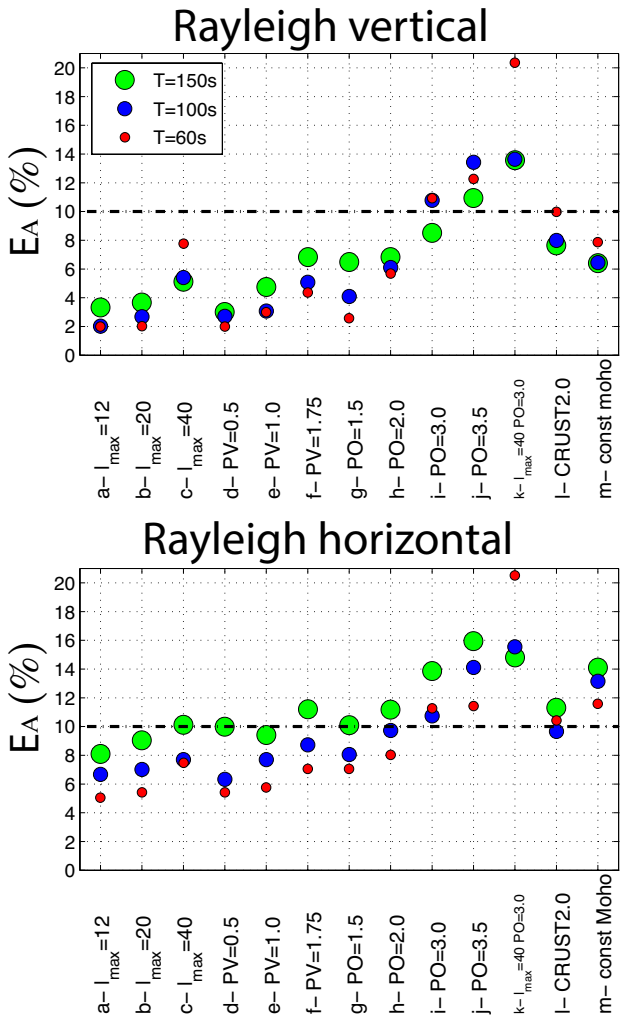

Figure 4.9: Summary of the amplitude error E_A at T~60 s, 100 s and 150 s for all the models used in this study. E_A values are the medians for each model and period computed for all the paths illustrated in Fig. 3.1 (in chapter 3). The horizontal black dash-dot lines correspond to the error thresholds of 10 %.

obtained when varying l_{max} and the PO factor. The amplitude modelling for this model is poor for all the wave periods considered.

4.6.3 CRUSTAL EFFECTS

When comparing the effects of different crustal models, the errors in phase E_ϕ are slightly lower when using a homogeneous crust and slightly higher for the 3-D constant-Moho crustal model (see models *e*, *l*-*m* in Fig. 4.8). Nevertheless, E_ϕ are below the phase misfit threshold in all cases for these three models. On the other hand, E_A increases substantially when considering 3-D crustal effects (compare models *e*, *l*–*m* in Fig. 4.9). However, the FRT amplitude modelling is still accurate for vertical component Rayleigh waves.

4.6.4 EFFECTS OF THE PATH LENGTH

E_ϕ and E_A are also analysed for different ranges of path lengths (Fig. 4.10). E_ϕ and E_A clearly increase with the epicentral distance at all periods considered. E_ϕ is always under the phase misfit threshold (5 %) except for T~150 s horizontal component Rayleigh waves, for distances larger than 110°. On the other hand, the errors in amplitude E_A are under the amplitude misfit threshold (10 %) for paths shorter than 110°.

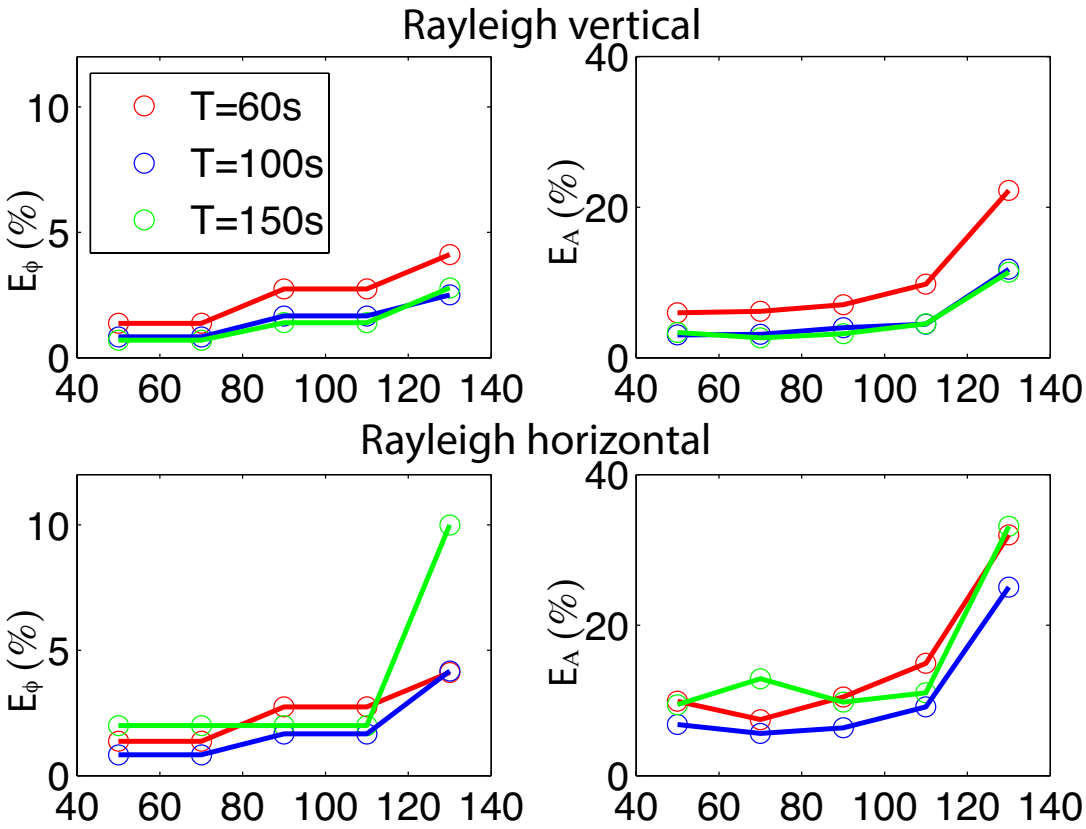

Figure 4.10: Phase (left) and amplitude (right) errors plotted as functions of epicentral distance, for models obtained varying PV, PO and l_{max} (models from a to j shown in Fig. 4.8 and 4.9). Every point (circle) of the curves corresponds to the median of the errors obtained using 20° wide bins.

4.7 DISCUSSION

4.7.1 ROUGHNESS TO DEFINE THE FRT VALIDITY DOMAIN

As explained previously, the goal of this study is to assess the domain of validity of the full ray theory when modelling long period surface waves in earth models that potentially can be either used or built during realistic waveform tomography experiments. In particular, we aim at obtaining quantitative criteria, which may provide guidance for future tomographic inversions.

The results presented in the previous section clearly highlight that the FRT is a highly accurate technique to model the phase of Rayleigh waves in almost all the models considered. E_ϕ is, in fact, slightly above the threshold of 5 % only for models with heterogeneity more than 3 times stronger than the heterogeneity of the S20RTS or S40RTS mantle models and at periods shorter than 80 s–70 s (Fig. 4.8).

The increase in FRT phase error with decreasing wave period is a common feature for all the models considered. We also observe that the shortest wave period here considered, T~60 s, is the most affected by the PO factor, i.e., by the strength of small scale heterogeneity. Due to the dispersion of surface waves, the shorter is the period, the shallower are the parts of the Earth sampled by the waves. In realistic earth models the shallower parts of the mantle are those with the stronger anomalies and this increases wave scattering effects (especially due to small scale anomalies affecting short period waves), which are not taken into account by the FRT. Inaccuracies in phase of Rayleigh waves can be controlled by considering paths shorter than 110°.

Conversely, the accuracy of the amplitude modelling of Rayleigh waves mostly increases for the shorter periods, respecting the general ray theory validity condition $\lambda \ll \Omega$. The amplitude of the surface waves is a function of the second derivative of the phase velocity map, calculated transversely to the ray (e.g., Ferreira & Woodhouse, 2007a) within the Fresnel zone. For longer wave periods, the ray approximation is less accurate because it neglects the finite area of the Fresnel zone, whose width is proportional to the period. However, in more complex cases (e.g., in models with 3-D crust), we observe that E_A for vertical component Rayleigh waves decreases as the wave period increases. The difference in behaviour between the vertical and horizontal components of Rayleigh waves when 3-D crusts are taken into account suggests that heterogeneity of the shallower parts of the models, as well as horizontal discontinuities, are the factors that mostly affect the accuracy of the modelling. Overall, our waveform comparisons indicate that FRT is accurate at calculating even the amplitude of Rayleigh waves as long as models with PO and PV factors larger than 3.0 and periods longer than 150 s are avoided. These inaccuracies in modelling the amplitude of Rayleigh waves can be controlled by considering paths shorter than 110°. Moreover, it should be noted that the models with PO and PV factors ≥ 3 lead to seismic velocity anomalies of ~20 %, which may not be realistic.

To generalise the outcome of our FRT–SEM waveform comparison experiment, in Fig. 4.11 we have plotted E_ϕ and E_A against the model roughness R (Eq. 4.1; see Table 4.1 for a summary of R for all the models considered in this study). E_ϕ is related to R with a correlation coefficient of 0.90. The plot highlights that FRT is a valid approximation to calculate the phase of Rayleigh waves when R of the phase velocity map is less than 6×10^{-5} .

E_A has distinct trends for the three different wave periods. In this case, the correlation coefficients are 0.70 (T~60 s) and 0.85 (T~100 s and 150 s). The scatter plot suggests that FRT is a good approximation to model the amplitude of vertical component Rayleigh waves when $R<3 \times 10^{-5}$ for T~150 s, $R<3.2 \times 10^{-5}$ for T~100 s and $R<5 \times 10^{-5}$ for T~60 s. The same thresholds are valid for horizontal components for T<100 s. At longer periods, the FRT should

be used for models with R<1 x 10^{-5} .

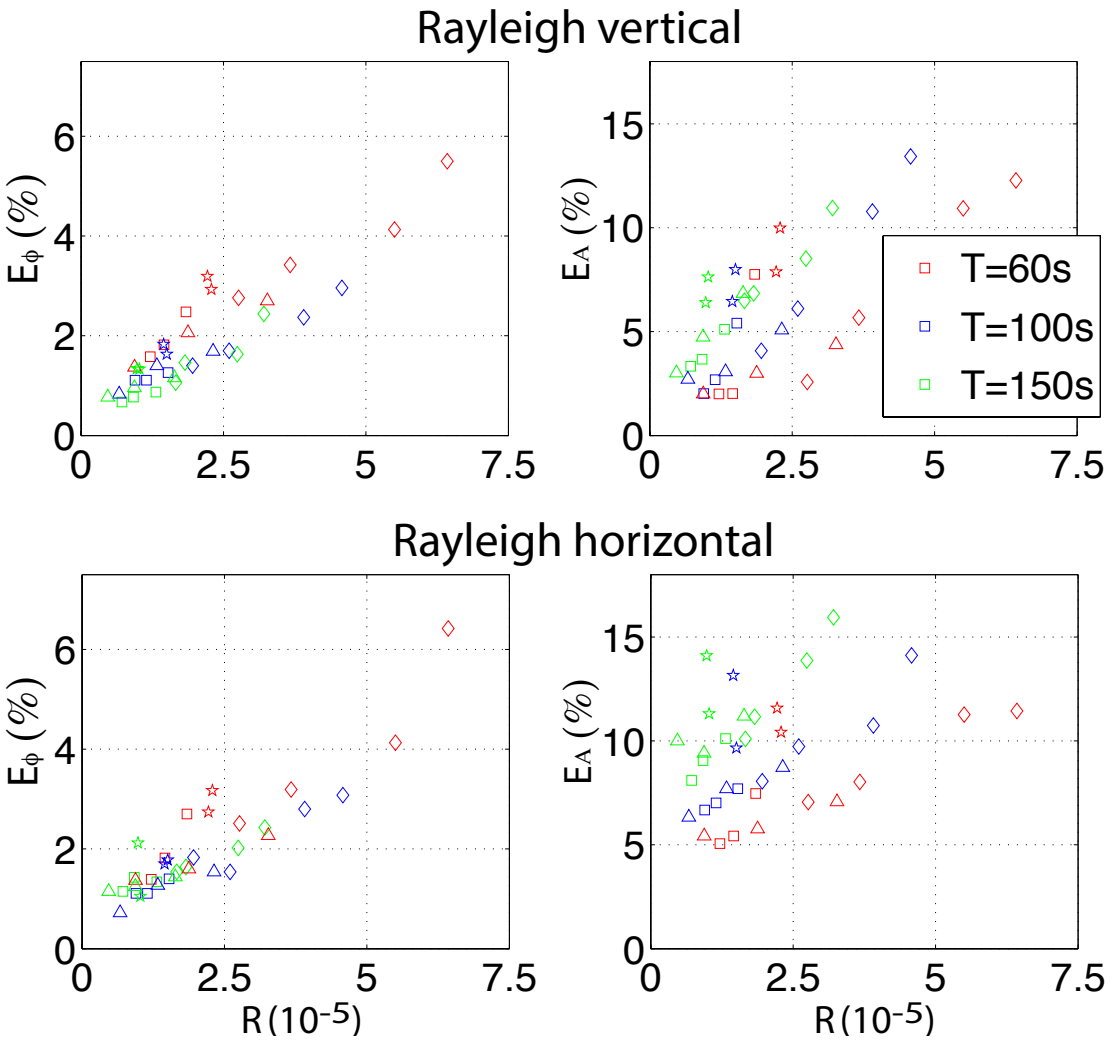

Figure 4.11: Scatter plot of E_ϕ and E_A against the roughness R (Eq. 4.1) of the corresponding phase velocity map. The different symbols correspond to distinct families of models: (i) varying l_{max} (models a–c; squares); (ii) varying the PV factor (models d–f; triangles); (iii) varying the PO factor (models g–j; diamonds); and, (iv) with 3-D crustal structure (models l–m; stars).

4.7.2 COMPARISON WITH PREVIOUS STUDIES

Several studies have already demonstrated the larger accuracy of the FRT with respect to the great-circle approximation (Woodhouse & Dziewoński, 1984), especially when modelling surface wave amplitudes. Early studies (Wang & Dahlen, 1994; Larson *et al.*, 1998) achieved this result by direct comparison of the FRT and great-circle approximation predictions. Wang & Dahlen (1994) compared the amplitude predictions for the FRT—with and without the local source and receiver excitations taken into account (in this work local excitations are taken into account)—and they found that the differences in the wave amplitude were around 30 %. These were even larger between the complete FRT and the great-circle approximation.

Larson *et al.* (1998), comparing FRT and great-circle approximation predictions, concluded that, whilst for the phase modelling the great-circle approximation could be adequate, the amplitude modelling needed the more sophisticated calculations of the FRT.

More recent works used accurate numerical methods as ground truth to compare the FRT and great-circle approximation accuracies. Romanowicz *et al.* (2008) applied the non-linear asymptotic mode coupling theory (Li & Romanowicz, 1995) taking into account off great-circle effects. They found that, in most of the cases, the waveform errors (a combination of the phase and amplitude errors) decrease when the exact ray-tracing was used. Peter *et al.* (2009) used a simplified membrane approach and highlighted that the improvement of the phase anomalies predictions of the FRT over the great-circle approximation increases with the number of the surface wave orbits. Dalton *et al.* (2014) focussed on the amplitude predictions only and found that the errors of the great-circle approximation were systematically larger than the errors of the FRT.

All these studies consistently proved the larger accuracy of the FRT with respect to the great-circle approximation, especially when modelling surface wave amplitudes. Thus, in this study we only focus on the accuracy of the FRT when compared with the more accurate SEM.

The domain of validity of the FRT was investigated in a few previous studies. Wang & Dahlen (1995) tested the FRT for three earth models and found that δc and $\nabla\nabla\delta c$ are good proxies for the errors in phase and amplitude, respectively, but general values of guidance were not given. A remarkable difference with our study is that the earth models used by Wang & Dahlen (1995) did not have crustal structure and consisted of only three mantle models with different l_{max} (from 12 to 36). In addition, ground truth synthetics were calculated using a normal mode coupling technique, which involves some theoretical approximations (Um & Dahlen, 1992).

Other studies (e.g., Kennett & Nolet, 1990; Lebedev *et al.*, 2005; Schaeffer & Lebedev, 2013) attempted to define the validity bounds of their modelling of the phase of Rayleigh waves when considering a sensitivity area around the ray. The corresponding domain of validity was defined by analysing the trade-off between wave frequency and epicentral distance (Schaeffer & Lebedev, 2013). Similar to our study, these authors also found a decrease in the accuracy of the phase modelling with decreasing wave period for the epicentral distances considered in our work. This is probably due to enhanced scattering effects with decreased wave periods.

The trends of amplitude errors of Rayleigh waves are in line with the results of Dalton *et al.* (2014). The authors used two different earth models differing by a factor similar to our PO factor, but for l_{max}>18, to test the FRT against other amplitude modelling techniques. As in this paper, they found an increase of the error in amplitude with increasing PO factor, wave period and epicentral distance.

4.8 CONCLUSIONS

We have assessed the accuracy of the surface wave full ray theory when modelling the phase and amplitudes of relatively long period surface waves (T~60 s–150 s), using the spectral

element method as ground truth.

We have found that the FRT is accurate in modelling the phase and the amplitude of Rayleigh waves in almost all the models considered. In the range of wave period studied, the accuracy when modelling Rayleigh wave phase decreases as the period decreases. This is probably due to strong small scale heterogeneities sampled by the shorter period waves, resulting in strong scattering effects.

We have also found that the roughness, expressed as the gradient of the phase velocity maps, is a good indicator of the accuracy of the FRT. Our results suggest that the FRT is a good approximation for predicting the phase of Rayleigh waveforms when the average roughness of $\delta c(\theta,\Phi)$ is less that 6 x 10^{-5} . The accuracy of the amplitude modelling depends on the wave period considered and is poorer for horizontal component Rayleigh waves than for vertical components. We predict a good amplitude modelling of the vertical component Rayleigh wave for models with R less that 3 x 10^{-5}, 3.2 x 10^{-5} and 5 x 10^{-5} for dominant periods of ~60 s, 100 s and 150 s, respectively. Similar thresholds are valid for the amplitude modelling of horizontal component Rayleigh waves with periods shorter than 100 s. At longer periods, even low roughness values can compromise the accurate modelling of amplitudes, unless paths shorter than 100°–110° are considered.

Our results show that there is scope to build future improved global tomographic models based on the FRT. The domain of validity defined in this study can serve as a useful guide in future seismic tomographic inversions using the FRT as a forward modelling scheme.

5

ASSESSMENT OF GLOBAL MANTLE TOMOGRAPHY MODELS USING SPECTRAL ELEMENT METHOD SEISMOGRAMS

5.1 SUMMARY

Estimating the quality of global tomography models is fundamental for robust geodynamical interpretations. Global tomographic models are often assessed using the same theoretical approach applied in the inverse problem. However, this strategy does not enable the estimation of the errors due to the approximations of the theory used. Other approaches, such as the comparison with existing models or estimation of the misfit reduction present a large margin of subjectivity and do not allows for the quality assessment across different models.

Here we assess the quality of the new global tomographic model SGLOBE-rani using an independent real dataset and synthetic seismograms calculated with the spectral-element method (SEM), an accurate numerical technique for the modelling of the complete seismic wavefield. SGLOBE-rani is a radially anisotropic whole mantle model (SGLOBEfull). Yet, to test the effects of the anisotropy on the waveforms we also modelled the wavefield confining the anisotropy to the upper mantle (SGLOBEup) and using the voigt average isotropic version of SGLOBE-rani (SGLOBEvoigt).

We compare fundamental mode Rayleigh and Love waveforms calculated with SEM in the SGLOBE-rani set of models to the waveforms from the independent dataset. For three dominant wave periods (T~60 s, 100 s and 150 s) we calculate phase and the amplitude misfits between data and synthetics. As reference, we also compared the data to the waveforms calculated for the S40RTS mantle model.

We find the SGLOBE-rani explains the phase and the amplitude better than S40RTS.

However, the small differences in the phase misfits between SGLOBE-rani and S40RTS compared to the data misfits suggests that there is still room for improvement of the tomographic models. Both SGLOBE-rani and S40RTS show large amplitude misfits indicating that the tomographic models have a lack of small scale heterogeneity and/or the 1-D attenuation model for PREM used in this study is not adequate to explain the amplitude of surface waveforms.

The differences in phase misfits among the SGLOBE-rani models are small but in most cases SGLOBEfull performs better than the other two models. For the cases whereby either SGLOBEvoigt or SGLOBEup outperform SGLOBEfull, the hypothesis of the leakage of the isotropic structure within the anisotropic structure of the SGLOBE-rani model is considered. The misfit differences between the SGLOBE-rani set of models decrease as the wave period increases. Our hypothesis is that the unmodelled short scale heterogeneity generates strong scattering effects, which are more evident in the shorter period waves.

5.2 INTRODUCTION

The quantitative assessment of the quality of 3-D tomography mantle models is crucial for robust geodynamical interpretations and for several practical applications, such as for reliable earthquake source inversions. So far the evaluation of the quality of tomography models has mostly relied on subjective choices by their authors. For example, new mantle tomographic models are usually compared with existing models, being verified that well-known large-scale structures are reproduced (e.g., low velocities associated with oceanic ridges and high velocities associated with subducting slabs). A more quantitative parameter used in model assessments is the final data misfit and the misfit reduction compared to the starting model used in the tomographic inversion. However, data misfit values are not always comparable across the studies because they depend on specific choices in the inverse problem's set up. Another common method to verify the robustness of tomography images is to carry out 'checkerboard tests', whereby synthetic data are calculated for a given input model with an alternating pattern using the same source-receiver pairs as in the real data. The synthetic data are then inverted to verify how well the input model is recovered. Whilst this technique assesses the suitability of the source-receiver path distribution used, it does not allow the evaluation of errors due to the approximations used in the tomographic problem, notably due to assumptions in the forward modelling scheme (Leveque *et al.*, 1993).

An alternative method to assess the reliability of a tomographic model is to test how well it explains independent seismological observations (e.g., data not used in the model's construction). Moreover, a useful way to assess the impact of simplifying forward modelling approaches on the tomographic imaging is to use more sophisticated techniques to compute theoretical seismograms for the retrieved model and compare them with real data. The spectral element method (SEM, e.g., Komatitsch & Vilotte, 1998) is a very useful tool to carry out such tests, since, as explained in chapter 2, it is a very accurate technique, without (almost) any approximations. Tape *et al.* (2009), followed by Chen *et al.* (2015), pioneered

these approaches by validating their regional/continental scale models with independent SEM waveforms for events not used in the construction of their models. Moreover, Qin *et al.* (2009) used a coupled SEM-normal mode approach (CSEM, Capdeville *et al.*, 2003a)) to assess the performance of four global mantle models at modelling Love and Rayleigh waveforms. They found that, as expected, the 3-D tomographic models explain the data better than PREM. Moreover, two of the global 3-D models (S20RTS by Ritsema *et al.* (1999) and Smean by Becker & Boschi (2002)) fitted the data slightly better than the other two (SB4L18, Masters *et al.* (2000) and SAW24B16, Megnin & Romanowicz (2000)). The main limitation of that study was the implementation of the crust, which only included as horizontally varying structure, with further simplifications for the Moho depth in the oceans. Finally, Bozdağ & Trampert (2010) used SEM seismograms to study how differently damped mantle models explain the data. They found small differences in the theoretical seismograms calculated for the different models and slightly better performance for the smoother models.

While an objective assessment and comparison of global tomographic models is important for isotropic 3-D structure (for which there is a good agreement of large scale structure between models), it is crucial for anisotropic structure, since there are large discrepancies between existing anisotropy models (e.g., Chang *et al.*, 2015). Images of seismic anisotropy in the Earth's mantle are important because they provide key information to reconstruct the patterns of mantle flow when interpreted together with mineral physics and geodynamics information.

The effects of seismic anisotropy on seismic waveforms can be subtle, leading to difficulties in separating them from isotropic effects. For example, crustal effects (Ferreira *et al.*, 2010), trade-offs between isotropic and anisotropic properties due to data's sensitivity (Chang *et al.*, 2014; Bodin *et al.*, 2015; Chang *et al.*, 2015) and limitations in isolating the individual modes of Love waves (see, e.g., appendix A) can all influence the retrieved anisotropic images.

In this study we assess the reliability of the recent whole mantle radially anisotropic model SGLOBE-rani (Chang et al., 2015) using SEM seismograms (SPECFEM3D_GLOBE package, Komatitsch & Vilotte (1998); Komatitsch & Tromp (2002a,b); Komatitsch *et al.* (2010a)), which are compared with real Rayleigh and Love waveforms with wave periods of T~60 s, 100 s, and 150 s. To the best of our knowledge, this is the first attempt to evaluate global anisotropic models with this approach. For reference, we also carry out comparisons between real waveforms and SEM synthetics for the global isotropic 3-D mantle S40RTS (Ritsema *et al.*, 2011). The choice of this model is due to the facts that it is widely used and that SGLOBE-rani uses a similar parameterisation and has been constructed with a data set including, amongst others, the data used to build S40RTS.

In the following sections we briefly explain how the S40RTS and SGLOBE-rani models have been built (section 5.3) and implemented in the SPECFEM3D_GLOBE package (section 5.4). The independent data used for the assessment of the models are presented in section 5.5. Examples of waveform comparisons and phase and amplitude misfits are summarised in sections 5.6 and 5.7. Our results are discussed in section 5.8 and plans for future developments

are explained in section 5.9.

5.3 TOMOGRAPHIC MODELS

In this section we report the main common features in the construction of the S40RTS (Ritsema *et al.*, 2011) and SGLOBE-rani (Chang *et al.*, 2015) mantle models. The distinctive characteristics of the two models are reported in the subsections 5.3.1 and 5.3.2.

The models are both expressed in terms of perturbations with respect to the PREM model. Spherical harmonic basis functions are used to parameterise the horizontal variations in the parameters and 21 depth spline functions parameterise variations in depth (e.g, Ritsema *et al.* (1999)). The spacing of the splines is smallest in the uppermost mantle, where the data's resolving power is highest.

A linearised damped least-squares approach (e.g., Tarantola, 1987) is employed in both studies whereby the data are linearly related to the model parameters by depth-dependent sensitivity kernels as illustrated in Fig. 5.1 for fundamental mode Rayleigh waves with wave periods of T~60 s, 100 s, and 150 s. The great-circle approximation is used (Woodhouse & Dziewoński, 1984), which is computationally very efficient.

The S wave travel-times dataset is the same for both models. Rayleigh wave phase velocity measurements used in S40RTS are also used in SGLOBE-rani. These include fundamental and higher modes up to the 4th overtones within the period range 40 s–275 s.

The crust has a strong effect on both body-wave travel-times and surface wave phase velocity (see Ritsema *et al.*, 2009). In this thesis, such effects for Rayleigh waves can be noticed comparing Figs. 3.2-b in chapter 3 (homogeneous crust) and Fig. 4.7 in chapter 4 (3-D crustal structure). For Love waves, this can be noticed comparing Fig. 3.3-b in chapter 3 (homogeneous crust) and Fig. A.2 in appendix A.

In the construction of both S40RTS and SGLOBE-rani crustal corrections are used whereby the contribution of the crust to the observed data are theoretically calculated and subtracted from the measurements before inverting them. Crustal corrections in both models are calculated by normal-mode summation (Takeuchi & Saito, 1972) combining CRUST2.0 (Bassin *et al.*, 2000) with PREM.

Both studies assume constant scaling factors of $\delta\rho$ and δVp to δVs.

5.3.1 S40RTS

The S40RTS (Ritsema *et al.*, 2011) mantle model is parameterised in terms of δVs expanded up to degree 40 ($l_{max} = 40$). The horizontal resolution of this model is of ~1 000 km. Tomographic maps at different depths down to 800 km are shown in Fig. 5.2 (left column).

In addition to the dataset described in section 5.3, S40RTS also includes the normal mode splitting functions dataset by Deuss *et al.* (2011). While the ratio $\frac{\delta\rho}{\delta Vs}$ is kept constant to 0.5 during the inversion, $\frac{\delta Vs}{\delta Vp}$ increases from 2 (at the surface) to 3 (at CMB). The regularisation parameter ϵ is chosen so that the model S40RTS has 8 000 effective unknowns.

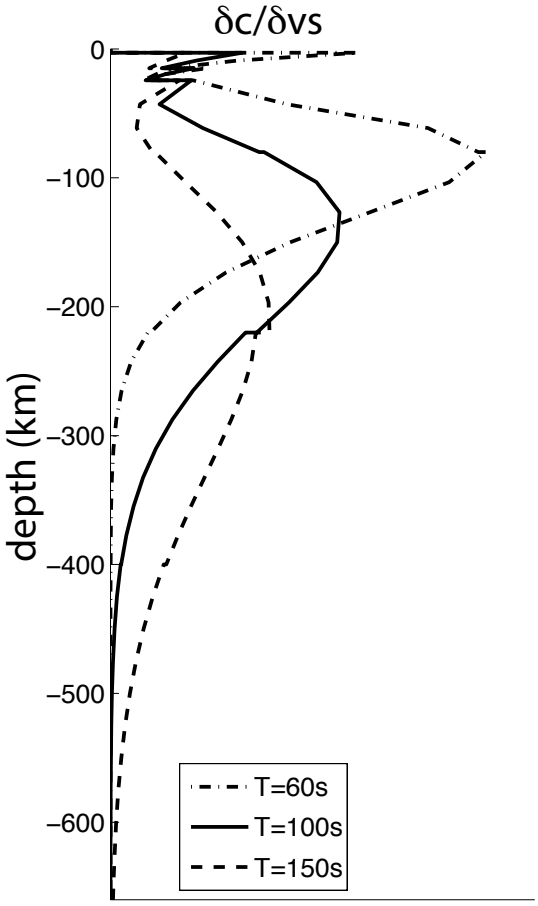

Figure 5.1: Normalised fundamental mode Rayleigh wave phase velocity (δc) kernels with respect to shear velocity (δVs) at periods of 60 s, 100 s, and 150 s calculated for PREM.

5.3.2 SGLOBE-RANI

SGLOBE-rani (Chang *et al.*, 2015) is defined in terms of perturbations of isotropic shear speed δVs and S radial anisotropy $\delta\zeta$ ($\delta\zeta = \frac{Vsh^2 - Vsv^2}{2Vs}$) with respect to PREM. It also includes perturbations of crustal thicknesses δd with respect to CRUST2.0. The three perturbation distributions are expanded up to degree 35 (l_{max} = 35 in Eq. 2.8, nominal horizontal resolution of around 1 300 km).

Re-parametrised tomographic maps of SGLOBE-rani in terms of δVs_{voigt} $\left(\sqrt{\frac{2Vsv^2+Vsh^2}{3}}\right)$ and ξ $\left(\frac{Vsh^2}{Vsv^2}\right)$ are depicted down to 800 km in Fig. 5.2 (middle and right column, respectively).

One strength of the SGLOBE-rani model is the combination of multiple datasets. In addition to the Rayleigh wave phase velocities and body wave travel times used in S40RTS, SGLOBE-rani is built using further Rayleigh and Love wave overtones and fundamental mode phase velocity dispersion measurements from Ekström *et al.* (1997) (35 s–300 s), Ekström (2011) (25 s–250 s) and Visser *et al.* (2008) (35 s–375 s). Group-velocity measurements from Ritzwoller & Levshin (1998) (16 s–150 s) are also included to constrain crustal structure.

Another improvement in the SGLOBE-rani model is the handling of the crustal structure.

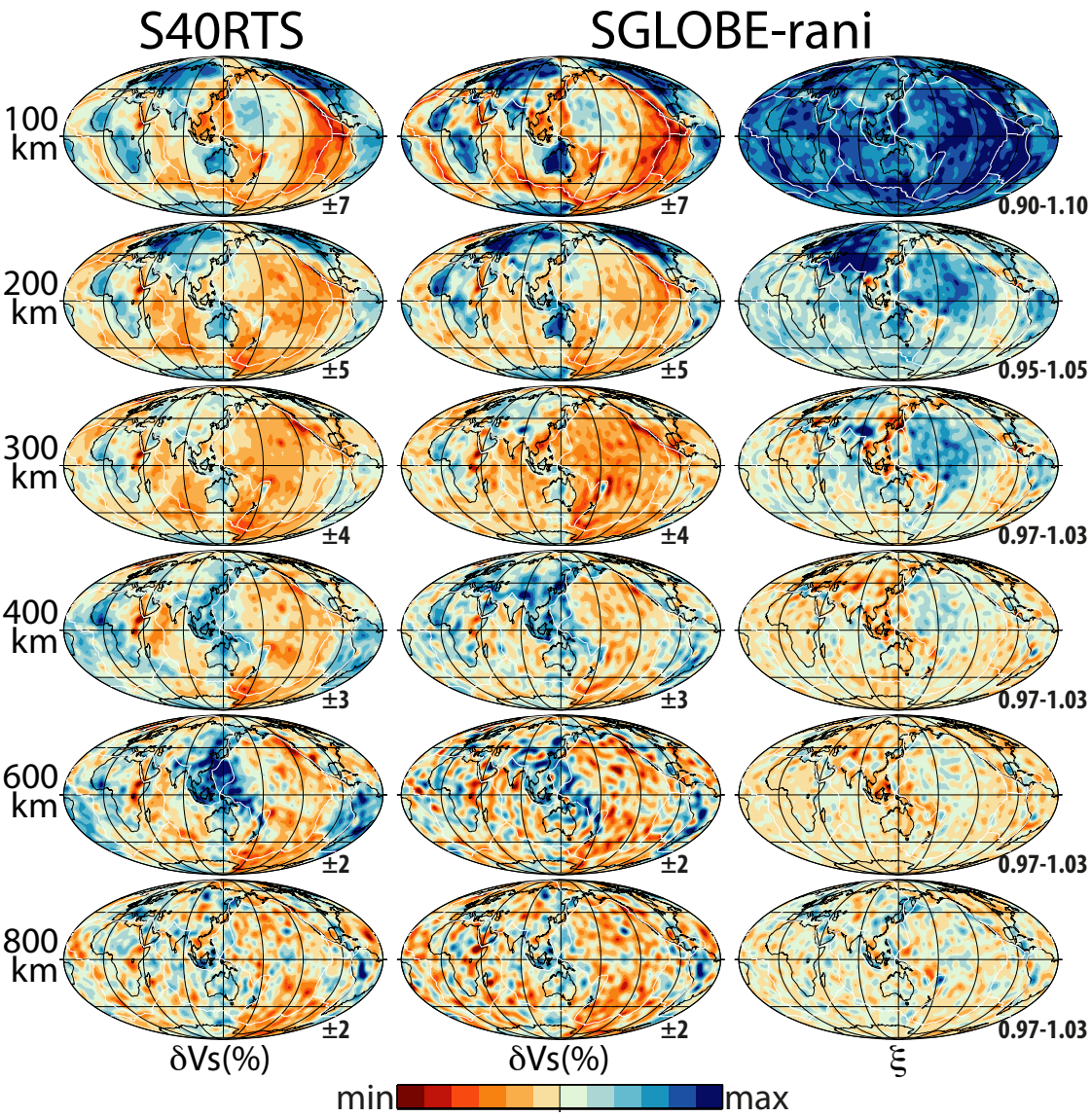

Figure 5.2: Tomographic maps at 100 km, 200 km, 300 km, 400 km, 600 km, 800 k for, from left to right, δVs of S40RTS , δVs_{voigt} and $\delta\xi$ of SGLOBE-rani. Perturbations are calculated with respect to the reference model PREM. Numbers on the bottom right of each map indicate the range of the colour scale.

The authors firstly applied the crustal corrections as explained in section 5.3 and secondly inverted for crustal thickness using 1-D kernels.

During the inversion $\delta\rho$ and δVp are scaled using the scaling factors δVp=0.5δVs and $\delta\rho$=0.4δVs.

5.4 SEM IMPLEMENTATION

We use the spectral element method (package SPECFEM3D_GLOBE, Komatitsch & Vilotte, 1998; Komatitsch & Tromp, 2002a,b; Komatitsch *et al.*, 2010a) to run our global simulations.

We shall refer to both method and package as SEM. All the simulations are run with NEX=480 and thus are accurate down to wave periods of T~10 s. See section 2.5.1 in chapter 2 for more details on the SEM.

5.4.1 EARTH MODELS

MANTLE MODELS

Whereas S40RTS is already implemented in the currently available version of the code, we had to add a subroutine to simulate the wavefield in the SGLOBE-rani mantle model. We implement and test three different versions of SGLOBE-rani: i) SGLOBEvoigt, in which the voigt average perturbations δVs_{voigt} are superimposed to both Vsv and Vsh of PREM. The radial anisotropy from PREM model, confined to the upper mantle (220 km of depth), is taken into account. ii) SGLOBEup, in which the perturbations of radial anisotropy $\delta\xi$ with respect to PREM model are confined to the upper mantle (down to 220 km of depth). Below 220 km, the δVsv perturbations of SGLOBE-rani are applied to both Vsv and Vsh of PREM. iii) SGLOBEfull, which is the whole mantle anisotropic version of SGLOBE-rani.

We assess these three different versions primarily to evaluate the effects of the radial anisotropy on the seismic wavefield. A secondary reason is that the computational cost increases from model i) (SGLOBEvoigt) to model iii) (SGLOBEfull). Thus, it is interesting to check whether, for future simulations, one could limit the anisotropy in the upper mantle to save CPU time in case of limited effects on the waveforms.

For all simulations, a degree-12 δVp model (Ritsema & van Heijst, 2002) is superimposed to Vp of PREM and $\delta\rho$ is scaled as 0.4 of δVs.

CRUSTAL MODELS

The SGLOBE-rani model set and S40RTS are combined with CRUST2.0 (Bassin *et al.*, 2000) because the crustal corrections for both models are calculated from this crustal model. CRUST2.0 is already available in the SEM package and we use its default implementation. At this stage, we do not consider the perturbations of the Moho depth for the calculations with the SGLOBE-rani set of models. Thus, the crustal model is the same for all the mantle models used in this chapter. More details regarding the implementation of the crust in SEM are explained in section 2.5.1 in chapter 2.

5.5 DATA AND SYNTHETICS

We select 10 shallow earthquakes chosen to evenly sample the globe. Deep events excite overtones of surface waves and since in this study we are interested in the fundamental mode only, we exclude earthquakes with hypocentral depth larger that 50 km. Although SEM models the complete wavefield including surface wave overtones we prefer to avoid overtone contamination to have a clearer idea regarding the depths of the models sampled with our selected periods of fundamental Rayleigh and Love waves. The moment magnitude

of the events is chosen larger than 6.4 to sufficiently excite the surface waves above the noise level. For each earthquake, we select 90 minute-long three component broadband waveforms recorded at stations of the II and IU seismic networks from the IRIS seismograph network (www.iris.edu). We manually select between 20 and 30 stations for each earthquake with a reasonable noise level within an epicentral distance $40°<\Delta<140°$ to avoid near-source effects, caustics and multiple orbit overlapping wave trains. The source-receivers distribution used is shown in Fig. 5.3 and a list of the earthquakes is reported in Table 5.1.

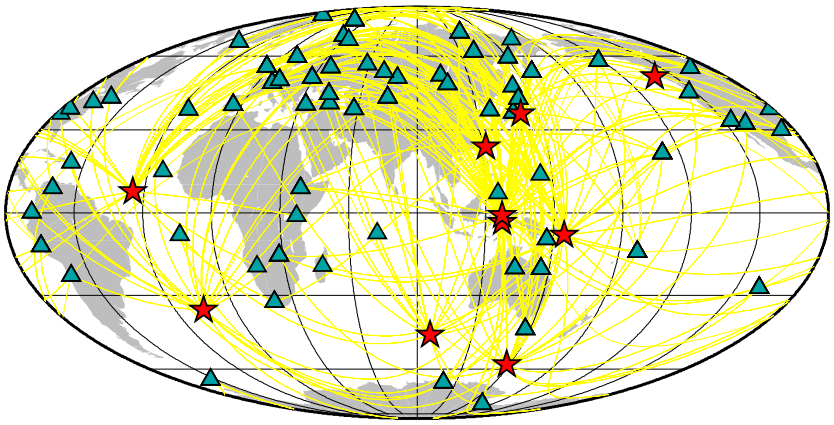

Figure 5.3: Earthquake and station distribution for the data used in this work. Earthquakes are represented by red stars and seismic stations by green triangles.

Event code	Location	Magnitude Mw	Depth (km)
200502162027A	Southern Mid-Atlantic Ridge	6.6	13.0
200510290405A	Southeast Indian Ridge	6.5	12.0
200603140657A	Seram, Indonedia	6.7	13.0
200702200804A	Southern Molucca Sea	6.7	12.0
200704161320A	West of Macquarie Island	6.7	12.0
200706280252A	Solomon Islands	6.7	18.0
200801051101A	Queen Charlotte Islands	6.6	12.0
200805071645A	Near East Coast of Honsh	6.8	26.3
200805231935A	Central Mid-Atlantic Ridge	6.5	12.6
200912191302A	Taiwan	6.4	48.25

Table 5.1: List of seismic events from the Global CMT catalogue (www.globalcmt.org) used in this work.

We use the CMT solutions of the selected events from the CMT catalogue (www.globalcmt.org) as a source input for the SEM code. We run point source simulations for the selected sources and receivers, setting the source half duration to 0 s and subsequently convolving a gaussian source-time function with a half-width equal to the half duration of the CMT solution. We are aware that uncertainty of the source parameters that can affect the accuracy of the simulations when compared with real data. However, CMT solutions are the

best choice we have available.

Displacement data and synthetics are re-sampled at 1 s. The instrument response is deconvolved from the data before convolving data and synthetics with a SRO instrument response to highlight the surface waves. Finally, three different cosine band pass filters with cutoff periods of T~60 s–1 000 s, 100 s–1 000 s and 150 s–1 000 s are applied.

5.6 SURFACE WAVEFORM COMPARISONS

As mentioned in section 5.4, SEM waveforms are calculated for S40RTS and for the three variants of the SGLOBE-rani model: (i) SGLOBEfull (the actual, whole mantle SGLOBE-rani model); (ii) SGLOBEup (only with radially anisotropic structure in the upper mantle); and, (iii) SGLOBEvoigt (only laterally varying isotropic structure). These models are assessed by comparing fundamental mode Rayleigh and Love synthetic and observed waveforms at dominant periods of T~60 s, 100 s and 150 s. Fig. 5.1 shows the sensitivity of the fundamental mode Rayleigh waves at these three different periods. Rayleigh waves at ~60 s have the peak of sensitivity to mantle structure at around 80 km. At ~100 s they are mostly sensitive to mantle structure at around 150 km depth and around 200 km depth for T~150 s waves. However, they also show non-negligible sensitivity to structures deeper and shallower than the peak sensitivity. For brevity we do not show the sensitivity of Love waves whose peaks are, in general, shallower than than those for Rayleigh waves at the same period. Hence, we can assume that with our tests we are assessing the mantle models down to 600 km–800 km.

We separately calculate phase and amplitude misfits, δ_ϕ and δ_A respectively, between real and synthetic waveforms within a time window with a width about 3.5 times the dominant wave period. Firstly, the waveforms are windowed waveforms around the maximum amplitude of the SEM seismograms. Since the seismograms are 90 mins-long, in most cases the maximum amplitude corresponds to the maximum amplitude of the fundamental mode surface wave. Nevertheless, a visual check of all the waveforms is performed before using the corresponding misfits. The phase misfits are calculated by cross-correlation and are expressed either in seconds (in section 5.7.1, where it is referred as δ_t) or as a percentage of the wave cycle (δ_ϕ). δ_A is calculated with the Eq. 3.1 where the reference traces are the real data. An example of Rayleigh (Z and L components) and Love (T component) waveform comparisons for a dominant wave period of T~100 s for one event and three stations, for the S40RTS and SGLOBEfull models is shown with the respective misfit values in Fig. 5.4.

5.7 RESULTS

In this section we present the misfits δ_ϕ and δ_A for the models assessed. Results are summarised as average misfits for S40RTS and the SGLOBE-rani set of models, separately considering the three components and the three dominant periods in the Tables 5.2 and 5.3. The choice to use the average rather than the median as in chapters 3 and 4 is due to the fact the median does not allow one to identify the small differences in the misfits obtained for the

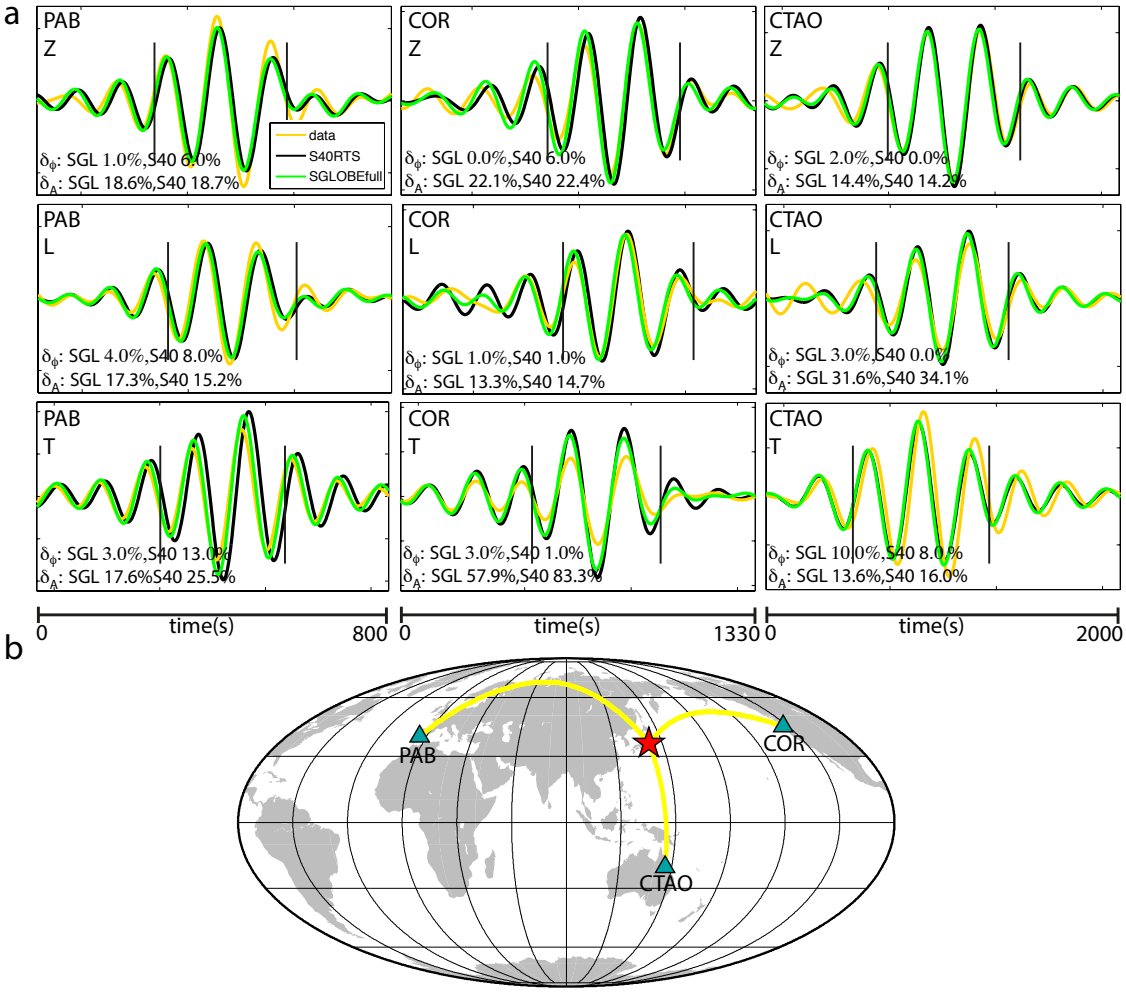

Figure 5.4: a. Three component waveforms for the 200805071645A event in Japan recorded at PAB, COR and CTAO stations at T~100 s calculated in the S40RTS (black traces, S40) and SGLOBEfull models (green traces, SGL) compared to the data (gold traces). Within each subplot, the name of the station and the component (vertical Z, radial L and transverse T) are reported on the top left corner. Values of δ_ϕ and δ_A for the two models are reported on the bottom left corner of each subplot. Vertical lines on top of the waveforms bound the window where the misfits are calculated. b. Great circle paths between the event (red star) and the stations (green triangles). The structure crossed by these paths roughly corresponds to the tomographic maps at 100 km and 200 km shown in Fig. 5.2.

different models. This fact will be discussed further in the following sections.

5.7.1 PHASE MISFITS

Distributions of misfits in seconds (δ_t) between data and synthetics are shown in Fig. 5.5 for S40RTS and the SGLOBE-rani set. A positive δ_t means that the synthetic waveform is in delay with respect to the real waveform. The distributions are all close to a Gaussian distribution and for all the variants of the SGLOBE-rani model the mean of the phase shifts is around zero, for every component and dominant period. Differences among the distributions of the SGLOBE-rani set of models are small and become even less evident for the larger periods. The

		S40RTS	SGLOBE voigt	SGLOBE up	SGLOBE full
Z	150s	8.03	**6.42**	6.66	6.62
	100s	8.17	6.03	5.96	**5.90**
	60s	9.16	7.44	**7.29**	8.19
L	150s	9.38	8.44	8.45	**8.05**
	100s	8.40	6.70	6.91	**6.61**
	60s	8.36	7.17	**7.13**	8.05
T	150s	9.64	7.85	6.97	**6.68**
	100s	8.61	6.84	**6.37**	6.70
	60s	8.56	7.29	7.47	**7.16**

Table 5.2: Summary of δ_ϕ misfits (in %) calculated as the average of the absolute values. The smallest misfits for each period and component are highlighted in bold.

		S40RTS	SGLOBE voigt	SGLOBE up	SGLOBE full
Z	150s	31.75	**31.46**	31.90	32.74
	100s	37.95	**36.34**	36.55	36.95
	60s	68.83	62.40	62.05	**61.87**
L	150s	38.35	**37.83**	38.11	38.14
	100s	38.44	**38.14**	38.24	38.29
	60s	59.10	55.59	55.71	**55.14**
T	150s	36.89	37.16	**36.88**	37.09
	100s	42.49	39.70	39.90	**39.48**
	60s	75.75	73.05	73.94	**72.29**

Table 5.3: Summary of δ_A misfit (%). The lowest misfits for each period and component are in bold.

distributions for S40RTS are wider than for the SGLOBE-rani models and show that in most cases the S40RTS waveforms are delayed compared to the real data.

Average values of δ_ϕ as percentage of a wave cycle are reported in Table 5.2. Phase misfits for SGLOBE-rani are between 6 % and 8 %, while for S40RTS are between 8 % and 9%. Thus, in all cases, SGLOBE-rani performs better than S40RTS in modelling the phase of the surface waveforms. As anticipated when analysing the distributions in Fig. 5.5, the misfit differences between the various variants of the SGLOBE-rani model are small. In most cases, SGLOBEfull explains the data slightly better than SGLOBEup and SGLOBEvoigt. However, Rayleigh waves at ~60 s are modelled slightly better when the radial anisotropy is confined to the upper mantle.

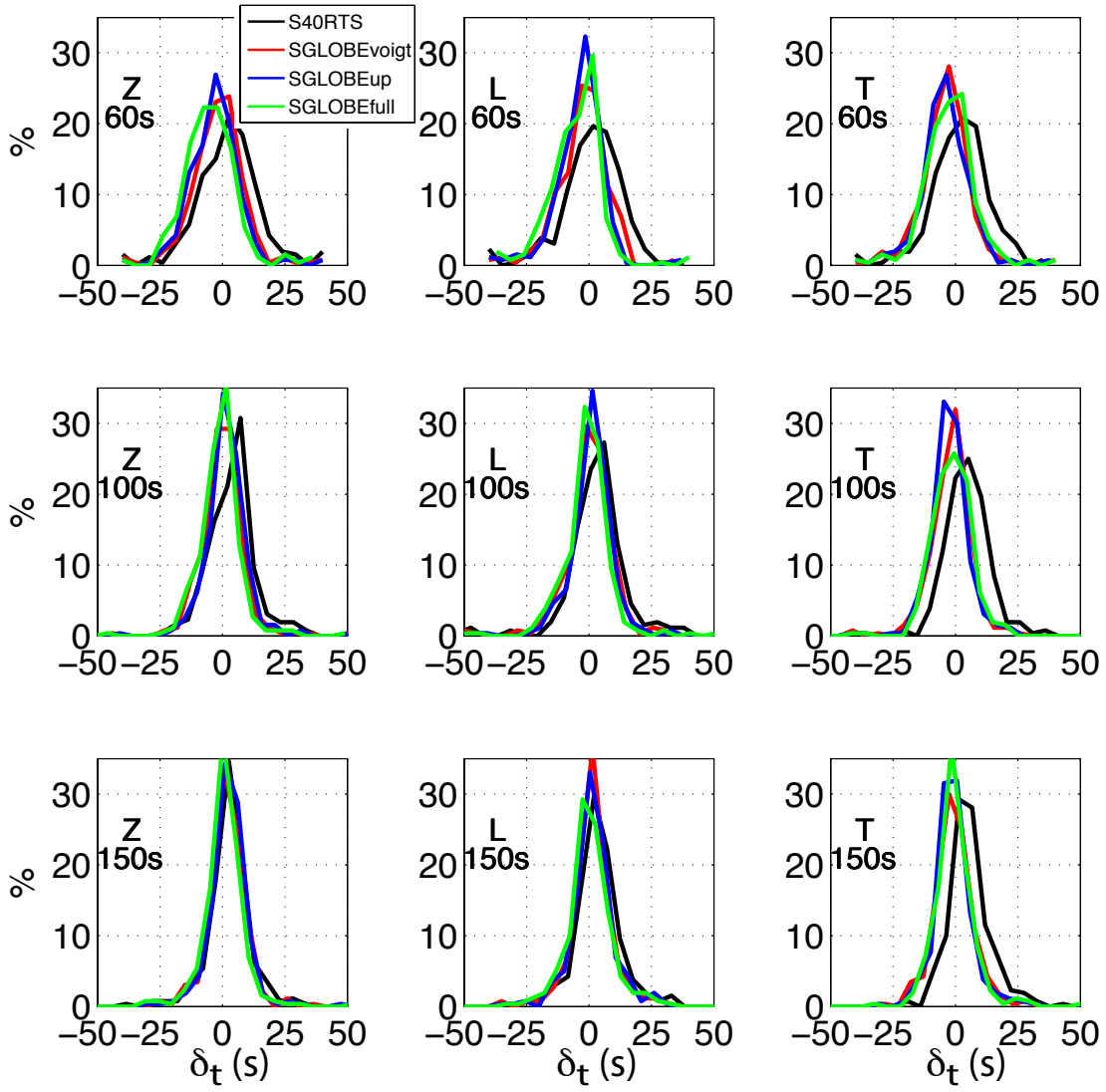

Figure 5.5: Frequency distributions of the time misfits δ_t for the S40RTS model and the SGLOBE-rani set of models for each period and seismogram component. Z, L and T refer to the vertical, radial and transverse seismogram components, respectively.

5.7.2 AMPLITUDE MISFITS

Distributions of the amplitude misfits δ_A are shown in Fig. 5.6 and the averages are summarised in Table 5.3. Amplitudes are overall very poorly modelled in all the models with δ_A ranging from 31 % (Rayleigh waves at ~150 s) to 76 % (Love waves at ~60 s) .

Peaks of distributions (Fig. 5.6) are far from 0 for all the models and become larger and shorter as the period decreases. The difference in the distributions for S40RTS and all the SGLOBE-rani model are quite small. Although these small differences, Table 5.3 reports that SGLOBE-rani set explains the amplitude of data slightly better than S40RTS. Rayleigh wave amplitudes at ~100 s and 150 s are modelled better in SGLOBEvoigt and at ~60 s in SGLOBEfull. Amplitude of Love waves are better explained by the anisotropic models at every

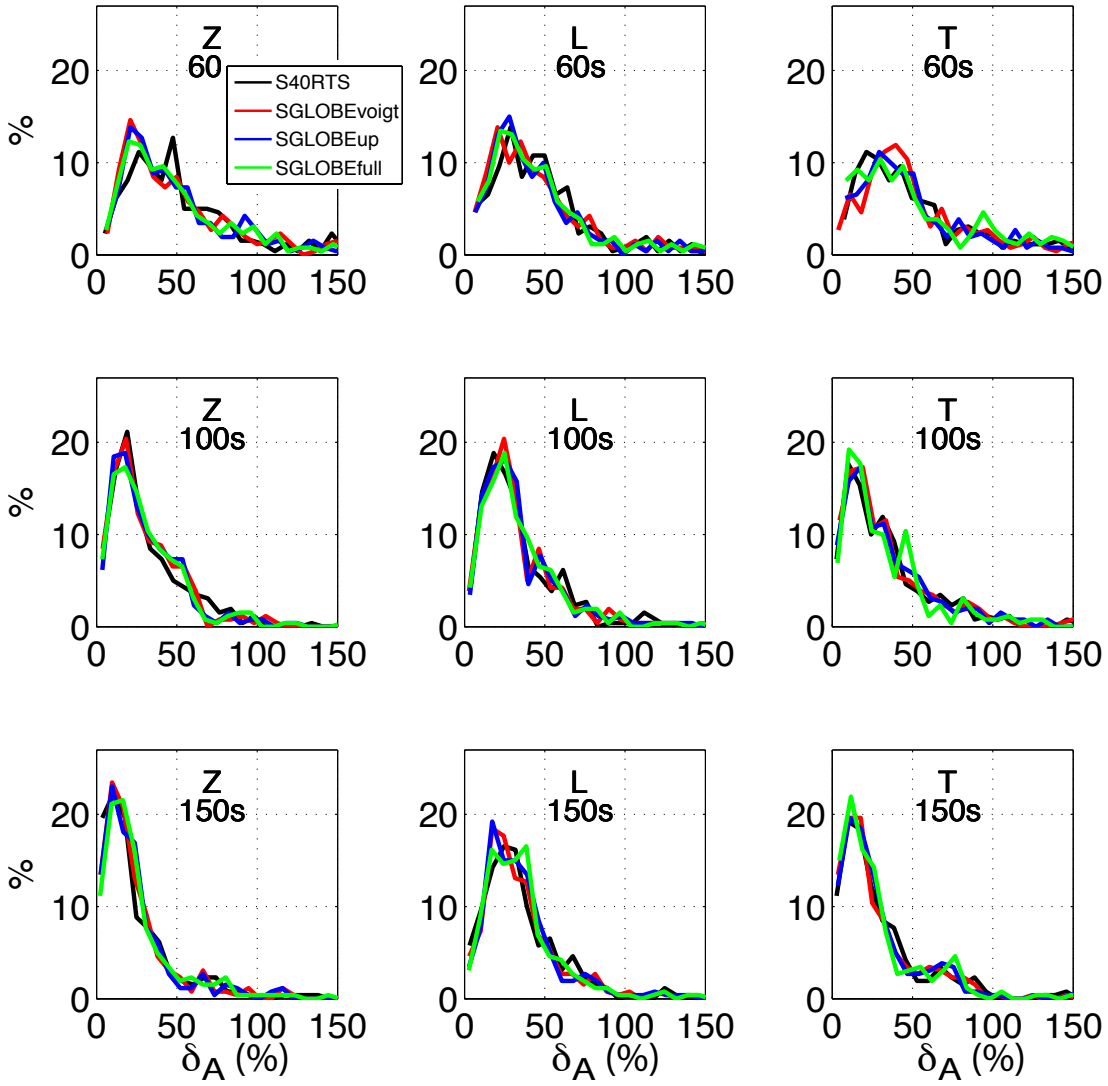

Figure 5.6: Frequency distributions of the amplitude misfits δ_A for the S40RTS model and the SGLOBE-rani set of models for each period and seismogram component. Z, L and T refer to the vertical, radial and transverse seismogram components, respectively. NB: the metric used for the amplitude anomalies is far from ideal to plot distributions, because it will never lead to a Gaussian-like distribution.

period but are always modelled worse than the corresponding Rayleigh waves.

5.8 DISCUSSION

The use of independent datasets in combination with highly accurate synthetics provides an objective way to assess global tomographic earth models. In this chapter we use this approach to assess the quality of the recent global radial anisotropy model SGLOBE-rani. We test three different variants of this model—SGLOBEvoigt, SGLOBEup, SGLOBEfull—which include only: (i) laterally varying isotropic structure; (ii) 3-D radial anisotropy in the upper mantle; and,

(iii) 3-D radial anisotropy in the whole mantle, respectively. For reference, we also test the widely used S40RTS mantle model. The differences in waveform predictions of SGLOBE-rani with respect to S40RTS can essentially be attributed to the use of a larger dataset, to the inversion for Moho depth perturbations and, most importantly, to the inclusion of 3-D radial anisotropic structure in the modelling.

We find that SGLOBE-rani fits the data better than S40RTS, both for phase and amplitude measurements (although for the latter there is only a slight improvement, with the significance of the amplitude misfit differences being unclear). Comparing the results obtained for the various wave periods, the data fits are poorest at T~60 s. The misfits for each earthquake are not shown for brevity since they are consistent with each other. Overall, in most of the cases considered, the actual full version of SGLOBE-rani with anisotropy in the whole mantle (SGLOBEfull) gives the best predictions. However, it is important to note that the differences in misfit between the different variants of SGLOBE-rani are often very small.

Qin *et al.* (2009) used both shallow (depth<50 km) and deeper earthquakes (depth>500 km) to limit the effects of the unmodelled crustal structure in the assessment of various global tomographic models and they found that shallow earthquakes gave rise to poorer data fits. In our dataset, we have an earthquake that is deeper than the others (depth ~48 km, CMTCODE 200912191302A) and the Moho depth beneath this event's location is ~25 km. Despite the source being located in the mantle, the misfits for this event do not show significant differences compared to the other earthquakes. This is encouraging regarding the implementation of the crust in our study.

While the results obtained for the individual earthquakes considered are overall consistent with each other, it is important to note that some source-receiver paths show some peculiarities, as illustrated in Figs. 5.4 and 5.7. Fig. 5.4 shows three examples of waveform comparisons (data vs SGLOBEfull vs S40RTS) for an event in in Japan (GCMT code 200805071645A) at T~100 s. Waveforms at this period mainly sample earth structure at depths of ~100 km–200 km (Fig. 5.2). SGLOBEfull models Love and Rayleigh waves better than S40RTS for a path crossing Europe (PAB station), consistent with the average results found over all the events. For a path crossing the Pacific Ocean (station COR), SGLOBEfull gives better predictions than S40RTS for Rayleigh waves, but slightly worse for Love waves. In the last example, for a path crossing the Western Pacific (station CTAO), SGLOBEfull's accuracy is slightly worse than S40RTS for both Rayleigh and Love waves.

Fig. 5.7 shows other examples of waveform comparisons for the event 200706280252A in the Solomon Islands recorded at the station ERM for wave periods of T~60 s T~100 s and T~150 s. SGLOBEfull explains the data overall better than S40RTS, particularly for T~60 s (consistent with the average results for all the events in Tables 5.2 and 5.3), but the differences in misfit between these two models decrease as the wave period increases. Fig. 5.8 also shows that the differences among theoretical waveforms obtained for the SGLOBEup, SGLOBEfull and SGLOBEvoigt models decrease with increasing period for this wave path, especially for Rayleigh waves. Overall the waveforms are quite similar for the three different models considered, with some slight differences for T~60s, for which SGLOBEup and SGLOBEfull

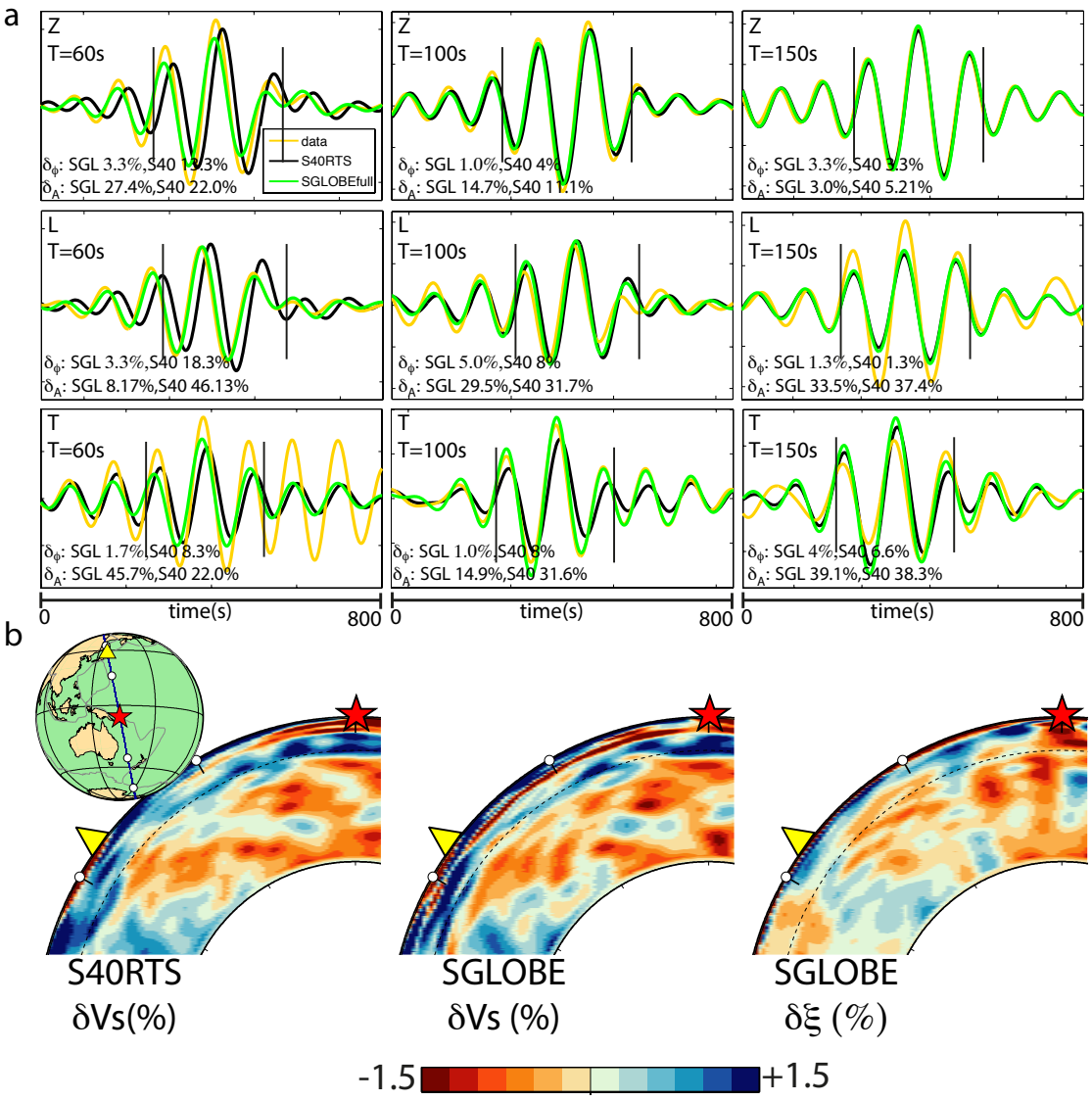

Figure 5.7: a. As top in Fig. 5.4 but for the event 200706280252A in the Salomon Islands recorded at the station ERM (Δ 51° , az: 349°) for T~60 s T~100 s and T~150 s. Black traces and S40 denote the S40RTS model. Green traces and SGL denote the SGLOBEfull model (green traces, SGL). Gold traces are the data. b. Vertical section along the great circle path between the event (red star) and the station ERM (yellow triangle) for δVs of S40RTS, δVs_{voigt} and $\delta\xi$ of SGLOBE-rani.

waveforms have phase shifts of about 4 s ($\delta\phi$~6.7 %). The largest waveform differences observed for the shortest wave periods both when comparing the various synthetics, and synthetics versus real data might be due to the stronger scattering effects associated with small-scale heterogeneity. Also, the fact that SGLOBEup slightly outperforms SGLOBEfull at T~60 s for Rayleigh waves (Tables 5.2 and 5.3) could be due to the leakage of small scale isotropic heterogeneities (generating scattering effects) into the anisotropic structure. This possible issue was also highlighted by (Chang *et al.*, 2014, 2015).

Bozdağ & Trampert (2010) found that using different global mantle tomographic models produces small differences in the corresponding theoretical seismograms. The authors

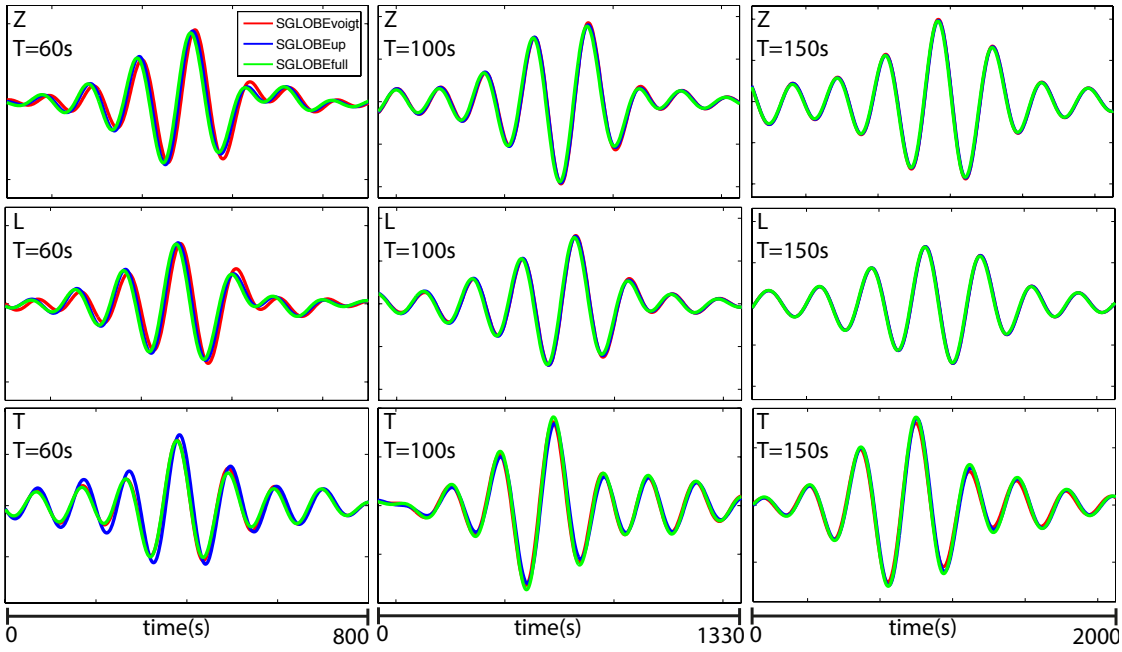

Figure 5.8: As in Fig. 5.7-a but comparing theoretical waveforms generated using the three variants of the SGLOBE-rani model.

associated this waveform convergence to crustal structure effects, which strongly affect seismic surface waves. However, if that would be the case, we would expect a larger convergence of the waveforms for the shorter wave periods for which the crustal effects are larger. Yet, this was not the case. Moreover, the authors also found that the smoother models considered in their study led to slightly better data fits and that, consistently with our results, the data fit increases for the longer wave periods for all the models considered. The data fit improvement as the wave period increases could suggest a different resolution of the models at the different depths. Another hypothesis is that the poorer data fit (noticed in both our study and Bozdağ & Trampert (2010)) for shorter wave periods due to scattering effects affecting more such short period waves. That is, even small differences between tomographic models produce larger larger differences on the seismograms because of the larger scattering effects. This hypothesis would also explain the larger difference among synthetic waveforms (noticed in this study). This would also be supported by the results of Fig. 4.8 (chapter 4) where the FRT (e.g., Ferreira & Woodhouse, 2007a), which does not take into account the scattering effects, systematically displays poorer predictions for the shorter periods, despite of the fact that this behaviour does not respect the theoretical domain of validity $\lambda \ll \Omega$. Nevertheless, the differences in synthetic and real waveforms are very small. Thus, in order to support the idea that the crust is not the main cause of the waveform convergence and that the scattering effects affect differently surface waves at different periods, further tests are necessary. Future development of this study could include a systematic assessments of crustal effects on the surface waveforms at different wave periods. It would also be interesting to evaluate whether the convergence of synthetics at longer periods for different earth models differs in the case of

synthetics calculated with an approximate method that does not consider scattering effects, such as the great-circle path approximation (Woodhouse & Dziewoński, 1984) or FRT.

This study has shown that SGLOBE-rani leads to an improved surface wave data fit than S40RTS, notably for the phase of surface waves. However, the small misfit differences between S40RTS and SGLOBE-rani compared to the actual real data misfit values suggests that there is still room for the improvement of the global tomographic models. Although the amplitude predictions for SGLOBE-rani are slightly better than for S40RTS, overall the surface wave amplitudes are poorly modelled, highlighting our poor knowledge of 3-D small scale elastic heterogeneity and/or 3-D attenuation within the earth. Scattering effects due to unmodelled elastic structure may in particular play an important role even for the unexplained amplitudes (Ferreira & Woodhouse, 2007b).

The approach used in this study is currently one of the most objective ways to quantitatively test tomographic models. However, it also has some limitations. For example, similarly to most global tomographic studies, we use global CMT source parameters Dziewoński *et al.* (1981) to run our simulations and assume that they represent the earthquake source parameters perfectly well. CMT solutions are built inverting long period waveforms in a very long-wavelength (degree 12) 3-D Earth model. Ferreira *et al.* (2011) show that the use of various recent 3-D Earth models can have a strong impact on the source inversions. Inaccuracies in the origin time and location of the source can affect the phase of the waveforms and the seismic moment is linearly related to the seismic amplitudes. Valentine & Woodhouse (2010) show that surface waveforms can be shifted by a few seconds due to the inaccuracy of the source parameters and that tomographic models may have an imprint of errors in CMT solutions. Nevertheless, since we use the exact same source parameters to assess the different Earth models, errors in the CMT parameters in principle should affect all model comparisons in the same way. Likewise, the crustal model used in the SEM simulations (CRUST2.0, which is combined with all the mantle models assessed) likely contains errors that may affect the waveform comparisons with real data. In future work we are planning to also use the Moho depth perturbations associated with the SGLOBE-rani model (Chang *et al.*, 2015). Another factor that probably affects the waveform comparisons is the use of a simple 1-D attenuation model. The amplitude misfits obtained suggest that this model is probably not sufficient to explain the data.

5.9 CONCLUSIONS AND FUTURE WORK

This work aimed at using SEM seismograms to assess the accuracy of global tomographic models. In particular, we tested the accuracy of the predictions of the anisotropic model SGLOBE-rani against the predictions of S40RTS when Rayleigh and Love waves at T~60 s 100 s and 150 s are considered.

We found that SGLOBE-rani explains the phase and amplitude of real surface waveforms better than S40RTS. In order to investigate the effects of the anisotropic structure we tested three versions of SGLOBE-rani: SGLOBEfull (whole anisotropic mantle),

SGLOBEup (anisotropic upper mantle) and the average voigt isotropic structure (δVsv=δVsh). Interestingly, SGLOBEup models Rayleigh waves at T~60 s slightly better than SGLOBEfull suggesting that part of the smaller scale heterogeneity could have been wrongly mapped in the anisotropic structure instead. We also noticed a waveforms convergence (decrease of the differences) among the synthetic waveforms as the period increases, which might be due to decreasing seismic scattering effects for larger wave periods. Nevertheless, the misfit differences between the three variants of SGLOBE-rani are small and their statistical significance is unclear. This issue will be further investigated in future work.

Although SGLOBE-rani showed an improvement in the phase modelling of surface waves, a higher resolution 3-D elastic model is desirable. In fact, especially at short scale, 3-D structure generates strong scattering effects and the shorter period waveforms are those affected more strongly. The poor amplitude modelling for all the models highlights the urgent need for robust 3-D elastic and anelastic models including small-scale heterogeneity. This should be ideally built starting from a high-resolution 3-D elastic model or obtained jointly inverting for elastic, anelastic and anisotropic structure. Advances in computational power should allow such large scale inversions soon.

In order to complete this study, we plan to repeat the simulations for SGLOBE-rani taking into account the Moho depths obtained together with the elastic and anisotropic structure. Combinations of SGLOBE-rani mantle with different crustal models could also be accommodated to check how this affects the modelling. We shall also test the lowermost mantle structure considered in this study by investigating S waveforms with wave periods down to T~10 s.

In order to provide a comprehensive guide for scientists interested in using the available tomographic models, we also aim to implement and test other recent elastic and anisotropic global tomographic models (e.g., Debayle & Ricard, 2012; Schaeffer & Lebedev, 2013; Auer *et al.*, 2014; Moulik & Ekström, 2014; French & Romanowicz, 2014). Comparing the predictions of models obtained by waveform inversion (e.g., French & Romanowicz, 2014) against traditional approximate methods (e.g., Ritsema *et al.*, 2011; Chang *et al.*, 2015) could give interesting insights on the accuracy of the approximate techniques complementary to those obtained in chapters 3 and 4.

6

WAVEFORM MODELLING OF HIGH-FREQUENCY BODY-WAVES

6.1 SUMMARY

Taking advantage of accurate waveform modelling techniques such as Gemini and the spectral element method we investigate the effects of elastic, anelastic and anisotropic structure on S waveforms travelling in the lowermost mantle. Our three component theoretical waveforms are generated in a wide set of 1-D and 3-D, isotropic and radially anisotropic earth models, and are accurate down to a wave period of ~5.6 s. It has been observed that vertical (SV) and horizontally (SH) polarised S waves crossing the lowermost mantle sometimes are split by a few seconds and present different pulse widths. The splitting of such waves is usually interpreted in terms of seismic anisotropy in the D" region, the deepest mantle layer at the boundary with the liquid core. Here we investigate systematically the effects of elastic, anelastic, isotropic and anisotropic structure on shear-wave splitting, including 3-D effects in some of these physical properties. Our numerical simulations in isotropic earth models show that the contamination of S waves by other phases can generate an apparent splitting between SH and SV waves. In particular, in the case of very shallow sources, the sS phase can interfere with the direct S phase, resulting in split SH and SV pulses when the SH and SV (or sSH and sSV) waves have different polarity or a substantial amplitude difference. In the case of deep earthquake sources, a positive shear velocity jump at the top of the D" can cause the triplication of the S waves and the ScSH and ScSV phases can have different polarity. Thus, when the triplicated S wave is combined with the ScS phase, the resulting SH-ScSH and SV-ScSV can seem split. When there is not a sharp vertical variation of the shear wave velocity, the difference in polarity between ScSH and ScSV can make the SH pulse larger than SV and thus also lead to apparent splitting between these phases. This effect depends on the thickness of the D" and the Vs gradient within it. S waveforms simulated in radially anisotropic models reveal that a radial anisotropy of ξ=1.07 in the D" seems to be

necessary to explain the ~2 s–3 s of splitting observed in waveforms recorded in Tanzania from an event in the Banda Sea. However, our analysis also shows that other factors such as sharp vertical variations at the top of D" and gradients of Vs and η within the D" may also affect the observed waveforms. This study suggests that caution should be taken when interpreting SH-SV splitting of deep mantle body waves in terms of anisotropy in the lowermost mantle.

6.2 INTRODUCTION

In the previous chapters we discussed the importance of the forward modelling of seismic waveforms as part of the inverse tomographic problem (see chapters 3-4) and as a strategy to assess the accuracy of tomographic models (chapter 5). We also demonstrated that current global tomographic models produce waveform differences that are quite small, especially when compared to the differences with the real waveforms. A possible cause for such synthetic waveform convergence is the limited resolution of the global tomographic models. While such models are very useful to investigate large-scale, whole-mantle geodynamical processes, they do not image small-scale heterogeneity (e.g., strong gradients and discontinuities of seismic properties).

The forward modelling of high-frequency seismic data in regions of interest is a useful means to constrain strong velocity gradients and discontinuities in the Earth's interior (e.g., Ritsema, 2000; Kawakatsu *et al.*, 2009; Tauzin *et al.*, 2010). Starting from an hypothetical model, waveforms can be calculated and compared to the real data. From the interpretation of the waveform differences, the model can be changed to improve the data fit. Moreover, during this trial-and-error procedure,the effects on the waveforms of various seismic properties (e.g., Vp, density, attenuation, discontinuities, etc, often kept fixed in tomographic inversions) can be systematically analysed.

The main limitations of such trial-and-error forward modelling approaches are that they can be difficult to automate and usually involve small data sets. Moreover, previous studies typically used simple forward modelling tools (e.g., ray theory) in 1-D Earth models. Thus, using more accurate forward modelling schemes such as the spectral element method (SEM, e.g., Komatitsch & Vilotte, 1998) for realistic 1-D and 3-D Earth models is highly desirable.

In this chapter we use a trial-and-error forward modelling approach to study systematically the effects of isotropic, anisotropic and anelastic structure on high-frequency body waveforms. We use two numerical techniques (GEMINI and SEM; see chapter 2) to calculate waveforms accurate down to wave period of ~5.6 s in 1-D and 3-D models and we target the structure of the lowermost mantle, notably of the D" region (in the bottom 150 km–300 km of the lowermost mantle).

The splitting (phase shift) of horizontally and vertical polarised S waves has been extensively used to study the anisotropy in this region of the Earth (e.g., Kendall & Silver, 1996, 1998; Garnero & Lay, 1997; Vinnik *et al.*, 1995, 1998; Ritsema, 2000). In this study we test whether other factors may produce significant shear-wave splitting.

In the remainder of this section we describe our current understanding of the D" region

(subsection 6.2.1). We then describe the most commonly used seismic body-wave data to investigate the D" (subsection 6.2.2) and related previous studies (subsection 6.2.3). Section 6.3 briefly summarises the forward modelling methods used in this chapter, and results from purely synthetic experiments are presented in section 6.4. Finally, section 6.5 shows results from the modelling of real data and a discussion of the results is given in section 6.6.

6.2.1 THE D" REGION

After the classification of Bullen (1940) in seven concentric shells (from A, the crust, to G, the inner core), Bullen (1949) realised that the bottom few hundred km of the lower mantle have a seismic velocity gradient lower than the rest of the layer D, representing a thermal boundary between the mantle and the core. It was named D" to differentiate it from the rest of the lower mantle (D' layer). Although Bullen's classification is not used anymore, the name D" has remained.

Since then, many exciting discoveries about the D" have been made. For example, Wysession *et al.* (1998) demonstrated that the top of the D" shows a sharp velocity increase. A possible explanation for this observation is the presence of subducted slabs at the bottom of the mantle, highlighted by a geographical correspondence between these high velocity zones and the projected locations of ancient slabs (e.g., Wysession, 1996; Loubet *et al.*, 2009). On the other hand, seismic tomography imaged two Large Low Shear Velocity Provinces (LLSVPs) at the bottom of the mantle under Africa and Pacific (Fig. 6.3) that, although with large uncertainties, are believed to have distinctive composition because of reported very low S wave velocity, moderately low P wave velocity and possible high density (e.g, McNamara & Zhong (2005); Garnero & McNamara (2008); Lekić *et al.* (2012)). Waveform studies also recognised Ultra Low Velocity Zones (ULVZs) mostly near the edges of LLSVPs (e.g., McNamara *et al.*, 2010) whose shear speed decreases in the range of 20 %–30 %.

Another interesting and debated feature of the D" is the presence of anisotropy (e.g., Meade *et al.*, 1995; Montagner & Kennett, 1996; Chang *et al.*, 2015). The lower mantle is mainly composed of magnesium silicate perovskite. The discovery of a phase change from perovskite (Pv) to post-perovskite (pPV, Iitaka *et al.*, 2004; Murakami *et al.*, 2004; Oganov & Ono, 2004) provided a possible explanation for the reported D" anisotropy because pPv minerals have a structure that is intrinsically more anisotropic than Pv. Moreover, this phase transition may also explain the observed seismic discontinuities at the top of the D". However, there are still many uncertainties regarding pPv, with some studies even suggesting that it may only occur in core conditions (Iitaka *et al.*, 2004; Murakami *et al.*, 2004; Oganov & Ono, 2004). Hence, the strong complexity of the D" remains largely unexplained.

6.2.2 SHEAR WAVE SPLITTING AND DEEP MANTLE BODY-WAVES

Seismic anisotropy has been observed globally in the uppermost and lowermost mantle (see, e.g., reviews by Savage, 1999; Chang *et al.*, 2014). While the presence of anisotropy in the uppermost mantle is widely recognised and included, e.g., in the 1-D reference model PREM

(Dziewoński & Anderson, 1981), the anisotropy in the D" is still object of debate since only local studies based on few wave paths have reported its presence.

The simplest type of anisotropy is the so-called radial anisotropy (or vertical transverse isotropy, VTI), which is investigated in this study (e.g., Nowacki *et al.*, 2011). In the experiments performed in this chapter we will only consider the radial anisotropy and we shall refer to negative (positive) radial anisotropy when Vsh>Vsv (Vsh<Vsv). Anisotropy in the lowermost mantle is often studied using shear wave splitting data. When an S wave travels through an anisotropic medium, differences between Vsv and Vsh lead to a time shift between the SV and SH phases, which can be observed in the radial and transverse components of seismograms, respectively. In the theory, the observed SH-SV arrival time differences are proportional to the length of the path within the anisotropic medium. As reference, Kendall & Silver (1998) inferred 1.8 % of anisotropy, defined as $\frac{2(Vsh-Vsv)}{Vsh+Vsv}$, from a SH-SV splitting of about 5 s recorded at an epicentral distance of ~100°.

The lower mantle is often investigated using body-waves travelling through the deep mantle. In particular, studies of anisotropy in the D" are mainly based on S, Sdiff, ScS waves (see Figs. 6.1 and 6.2). When the direct S wave grazes the core-mantle boundary (CMB) it is named Sdiff (Fig. 6.2). The S wave starts to be diffracted (Sdiff) along the CMB at epicentral distances of about 100° when the ScS phase is no longer observable. S and Sdiff waves can be studied to investigate the lowermost mantle at epicentral distances of around 90° - 120°. Moreover, at shorter epicentral distances, the S phase can be used in investigations based on differential travel-times between S and ScS phases. Since S and ScS have a very similar path until the turning point of the S phase, the differential arrival-times can be associated to the path of the ScS in the lowermost mantle.

When using shear wave splitting data to infer D" anisotropy, the observations have to be corrected for anisotropy in the upper mantle. This is usually done by using SKS data (see Fig. 6.1). The path of SKS in the lowermost mantle is short; thus, D" anisotropy should not affect this phase. Hence, SKS splitting data is often used to correct the receiver-side splitting in S, Sdiff and ScS phases for upper mantle anisotropy. Finally, source-side splitting can be avoided by using earthquakes deeper than 500 km, where anisotropy is thought to be small or negligible.

6.2.3 PREVIOUS STUDIES

Several studies have investigated radial anisotropy in the lowermost mantle using S and Sdiff waves ((for a recent review, see, e.g., Nowacki *et al.*, 2011, ; Fig. 1.2). While beneath Alaska various studies have found negative (Vsh>Vsv) anisotropy (e.g., Garnero & Lay, 1997; Wysession *et al.*, 1999), mixed-signal anisotropy has been reported beneath the central and southern Pacific (e.g., Vinnik *et al.*, 1995, 1998; Pulliam & Sen, 1998; Ritsema *et al.*, 1998; Kendall & Silver, 1998; Fouch *et al.*, 2001). The coexistence of both positive and negative anisotropy beneath the central Pacific has been previously interpreted as horizontal mantle flow into mantle plumes (Russell *et al.*, 1998). Moreover, negative radial anisotropy has also

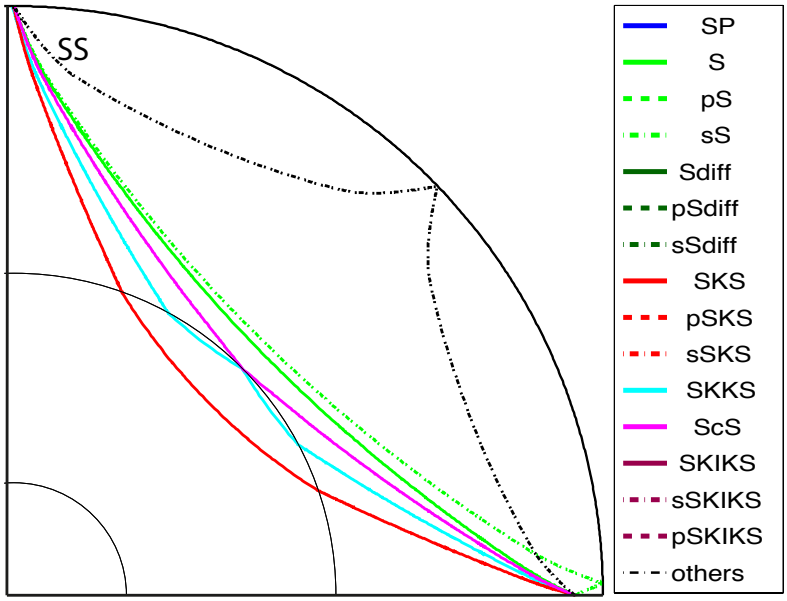

Figure 6.1: Raypaths for different body-wave phases mentioned in this study. They are calculated in the PREM model (Dziewoński & Anderson, 1981) for a seismic source at 300 km depth. The legend is also used for the arrival-time bars in several figures throughout this chapter.

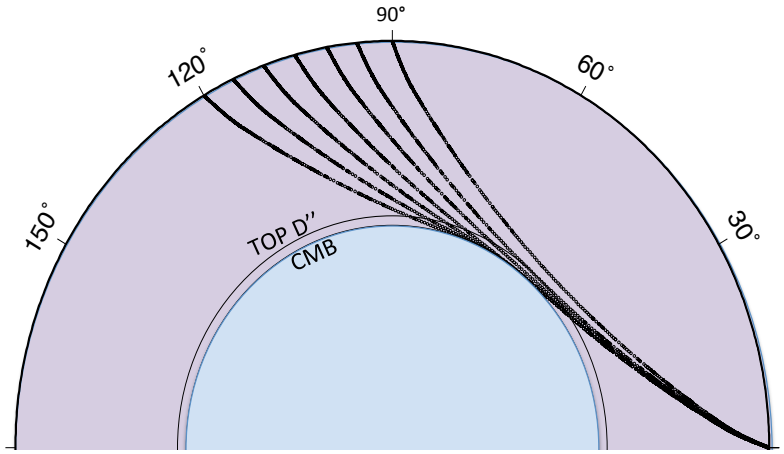

Figure 6.2: Raypaths for S and Sdiff waves travelling at an epicentral distance ranging from 90° to 120° in PREM. In PREM, the D" is 150 km thick and S waves start to be diffracted at about 100°.

been observed in the Indian Ocean (Ritsema, 2000), Caribbean (Kendall & Silver, 1996) and Siberia (Thomas & Kendall, 2002).

Almost all the cited studies estimated the SH-SV splitting by picking the onset times of the polarised waves or were limited to a qualitative analysis of the increase of the splitting with the epicentral distance. Due to the difficulties of such picking because of noise and complexity of the waveforms, Garnero & Lay (1997) preferred to pick the wave peaks, although this can be problematic when the wavelengths of the SH and SV phases differ. Fouch *et al.* (2001) used a more sophisticated technique based on cross-correlation. However, cross-correlations are

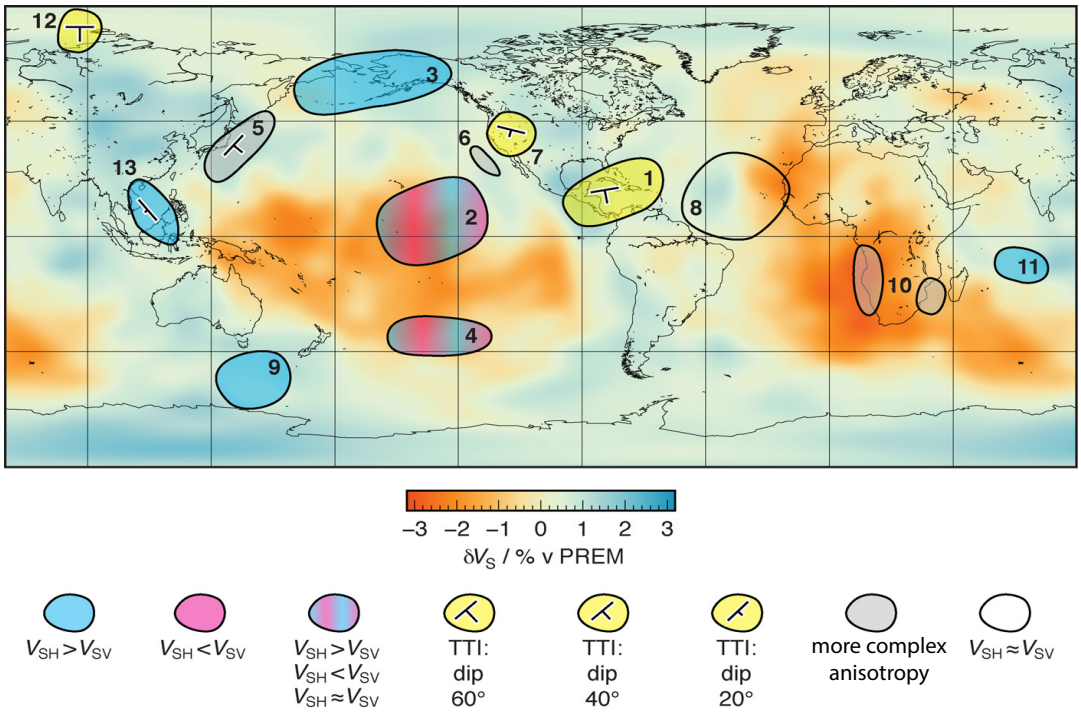

Figure 6.3: Summary of previous studies of D" anisotropy. Region IDs: 1. Caribbean; 2. Central Pacific; 3. Alaska; 4. South East Pacific; 5. North West Pacific; 6. East Pacific; 7. Western USA; 8. Atlantic Ocean; 9. Antarctic Ocean; 10. Southern Africa; 11. Indian Ocean; 12. Siberia; 13. Southeast Asia. In the background: Vs global tomographic model of Becker & Boschi (2002). Regions with Vsh>Vsv are shown in blue; those where Vsh<Vsv are in pink. Pink and blue stripes indicate that both positive and negative anisotropy have been reported. Other reported types of anisotropy more complex than radial anisotropy are shown in grey. TTI: transverse tilted anisotropy. Modified from Nowacki *et al.* (2011).

often avoided in these analyses by other authors due to waveform differences between SH and SV phases. Finally, Kawai & Geller (2010) applied a waveform inversion approach to retrieve D" anisotropy in Central Pacific and found values of anisotropy much larger than other studies focussing on the same region (e.g., Vinnik *et al.*, 1995; Kendall & Silver, 1998).

Other studies found that radially anisotropic models could not explain their observations and modelled the S wave splitting with more complex types of anisotropy, such as for Tilted Transverse Isotropic (TTI) media under the Caribbean (e.g., Garnero *et al.*, 2004; Maupin *et al.*, 2005; Nowacki *et al.*, 2010), northern Pacific (Wookey *et al.*, 2005), western USA (Nowacki *et al.*, 2010), Siberia (Wookey & Kendall, 2008) and southeast Asia (Thomas *et al.*, 2007).

6.2.4 MOTIVATION

Some previous forward modelling studies of phases sensitive to the D" have investigated shear wave splitting in isotropic mantle models. In this thesis we shall refer to such splitting (i.e., not due to anisotropy) as "apparent splitting". Maupin (1994) used a method based on the Langer approximation (Richards, 1976; Aki & Richards, 1980) and on perturbation theory (Garmany, 1988) to model Sdiff waves in isotropic and anisotropic models and found that the

discrimination between isotropic and anisotropic effects is not straightforward.

Komatitsch *et al.* (2010b), which shall be referred as KO10 throughout this chapter, modelled S waves accurately down to wave period of 5 s travelling at an epicentral distance ranging from 90° to 120° in both the isotropic 1-D IASP91 model (Kennett & Engdahl, 1991) and a simple laterally varying model, using the spectral element method. The authors demonstrated that even such models can cause an apparent splitting of SV(diff) and SH(diff) phases. To reduce the computational cost and simplify the shape of the waveforms, the authors did not take into account the attenuation effects and used a simplified version of the IASP91 model by approximating the crust to a homogeneous layer and smoothing the discontinuities at 410 km and 660 km depth (see Fig. 6.4). The laterally varying model was built just by combining the simplified IASP91 with a further 1-D variation of IASP91.

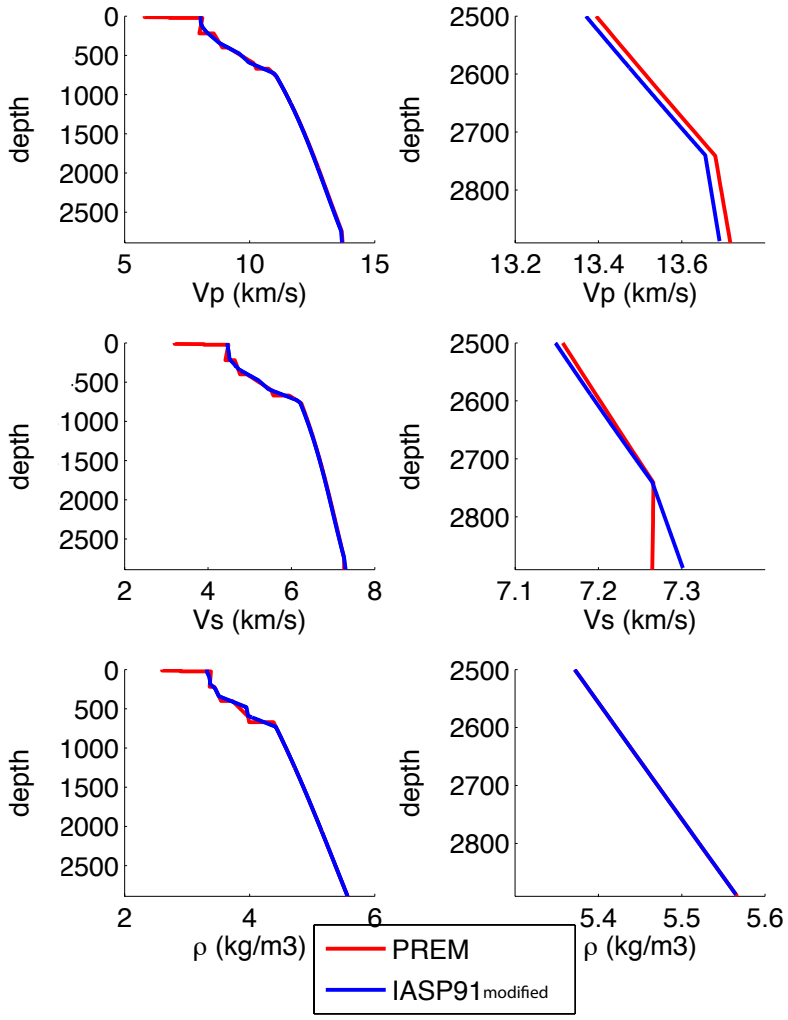

Figure 6.4: Left: velocities and density profiles for the smoothed version of IASP91 used by KO10 and PREM. Right: zoom in the lowermost mantle.

Fig. 3 of KO10 (reported here in Fig. 6.5) shows the waveforms calculated for the simplified IASP91 model, for an event at the Earth's surface with an oblique-reverse focal mechanism

(see Fig. 6.6). The figure reports a SH-SV apparent splitting increasing from Δ=100° to Δ=120° , reaching 2.4 s, which roughly corresponds to the average splitting found in the studies summarised in section 6.2.3 , which is usually explained by the presence of anisotropy in the D" region. Motivated by these findings, in this study we start by reproducing and interpreting the results of KO10. We then carry out a more general, systematic analysis of the effects of elastic (1-D and 3-D), anelastic and anisotropic structure on S waves travelling through the D".

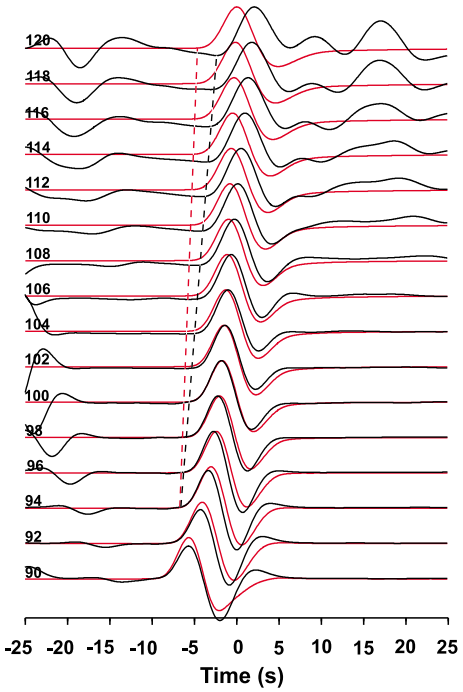

Figure 6.5: Red (black) lines represent the horizontally (vertically) polarised S waves. Every waveform is normalised with respect to its own maximum amplitude. Numbers in the right of each pair of waveforms represent the epicentral distances in degrees. Dashed lines are onset manual pickings of S waves. The largest apparent splitting, measured as the difference of the onset times, is 2.4 s at Δ=120° . The earthquake used is at the Earth's surface and has an oblique-reverse focal mechanism. Modified from Fig. 3 of Komatitsch *et al.* (2010b).

6.3 METHODS

In order to accurately model the seismic wavefield, we use the spectral element method (Komatitsch & Vilotte, 1998, SEM, e.g.,)) and Gemini (Friederich & Dalkolmo, 1995, GEM,). We considered a wide range of isotropic (1-D and 3-D), attenuation and anisotropic models, leading to a total of 35 models tested, as explained below. SEM simulations presented in this chapter are run using a NEX parameter of 768 (element size around 14 km) which allows obtaining waveforms accurate down to wave period of ~5.6 s (see section 2.5.1 in chapter 2 for more technical details). Due to the high computational cost and being interested in the S waves recorded at epicentral distance between 90° and 120°, our simulations are only 33

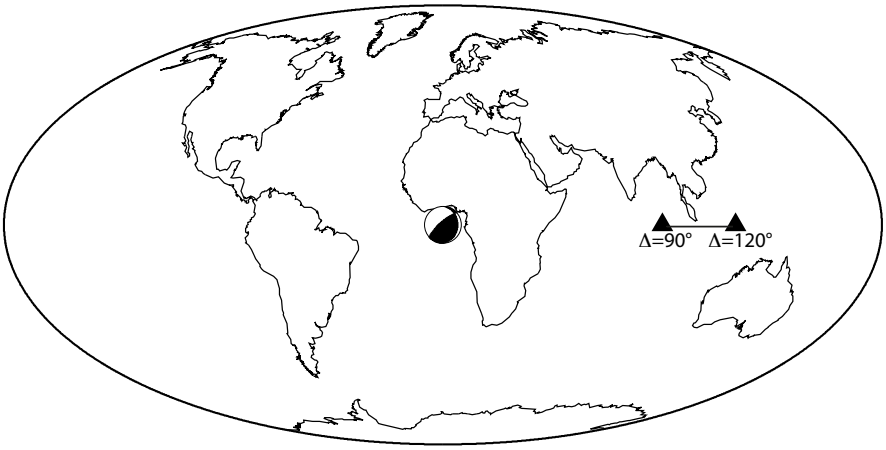

Figure 6.6: Source-receiver geometry used by Komatitsch *et al.* (2010b) and for the simulations presented in sections 6.3 and 6.4. The source is at the Earth's surface (0.1 km in our simulations) and the beach ball shows the focal mechanism. Triangles represent the range of epicentral distances considered in the experiments.

minutes long.

6.3.1 VALIDATION

Since the SPECFEM3D_GLOBE code (SEM; Komatitsch & Tromp (2002a,b); Komatitsch *et al.* (2010a); see section 2.5.1 in chapter 2) has not been extensively used at at such high frequencies, we start by reproducing some of the results of KO10 and we benchmark SEM against GEMINI (GEM; Friederich & Dalkolmo (1995)). The latter algorithm calculates spheroidal and toroidal motions numerically in a 1-D earth model by integrating a system of ordinary differential equations followed by summation over vector spherical harmonics (for more details, see chapter 2). As SEM, the computational cost of GEM depends on the maximum frequency and duration length of the seismograms. It is quite accurate but, conversely to SEM, is computationally more affordable. However, it cannot take into account 3-D heterogeneity in the models. Our GEM simulations are run with a cut-off wave period of 4 s.

To reproduce the results of KO10 (Fig. 6.5), we use the simplified version of IASP91 (Fig. 6.4) and the same source-receiver configuration (Fig.
refequatorialgeometry). Due to numerical reasons, the source cannot be placed at exactly 0 km of depth but it is placed at 0.1 km. The focal mechanism was chosen by KO10 to avoid nodal planes along the equator line where the virtual stations are located. The stations are placed every 2° of longitude between 90° and 120°. Attenuation is not considered. Waveforms are calculated using a point-source with half-duration set to 0 s. In the processing stage, the waveforms are then convolved with a Gaussian source time function with half duration of 6.5 s. We perform this simulation using both SEM and GEM.

Our plot equivalent to Fig. 3 of KO10 (Fig. 6.5) is shown in Fig. 6.7. Our SEM and GEM

simulations fit each other very well. Our results are also very similar to the results of KO10. Thus, we successfully use both SEM and GEM to reproduce the splitting reported in KO10 in a isotropic 1-D earth model. Since SEM and GEM produce identical 1-D Earth seismograms, in the remainer of this chapter all the simulations for 1-D Earth models are carried out using GEM.

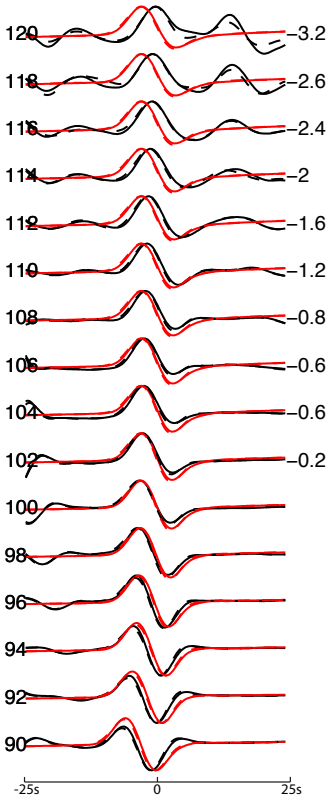

Figure 6.7: Comparison between velocity seismograms calculated with SEM (solid lines) and GEM (dashed lines). Black and red traces are radial (SV) and transverse (SH) seismogram components, respectively. Numbers on the left show the epicentral distance; numbers on the right represent the apparent splitting in seconds calculated by cross-correlation. Our traces are convolved with a Gaussian source time function with a half duration of 6.5 s and and are filtered with a low-pass Butterworth filter with corner period of 5s (order 6). Source and stations as in Fig. 6.6. Every waveform is normalised with respect to its own maximum amplitude.

In this work, we focus on the phase of the waveforms only. For this reason, all the waveforms shown in this chapter are normalised in amplitude, except when stated otherwise. Waveform splitting is measured by cross-correlation in seconds, but we only discuss measurements obtained when the correlation coefficient is larger than 0.85. This approach is chosen to limit the subjectivity of the interpretation of the observations. When the splitting measured is 0 s or the associate correlation coefficient is less than 0.85, it is not shown.

6.4 SYNTHETIC TESTS

In this section we focus on the study of synthetic waveforms, without any regards to real data. We start is subsection 6.4.1 by carrying out additional numerical experiments that help explain the splitting observed in Fig. 6.7. We then repeat the same simulations but for more realistic 1-D and 3-D earth models using the same (or similar) source-receiver configuration (subsection 6.4.2).

6.4.1 1-D EARTH MODELS

Here we attempt to explain the apparent splitting observed in the S waves modelled for the simplified version of IASP91 and then we examine the differences when the PREM is considered.

Isotropic IASP91 model

We repeat the KO10 experiment for same earth model, epicentre, moment tensor, stations location, no attenuation but changing the source's depth. Fig. 6.8 shows the resulting waveforms calculated at Δ=100° and Δ=110° for sources placed at the surface (0.1 km), 10 km, 20 km, 30 km, 40 km, 50 km, 100 km and 500 km. The waveforms at Δ=100° and Δ=110° for the source at the surface are the same as those shown in Fig. 6.7. Vertical bars on top of the waveforms indicate the theoretical arrival-time of the various phases. These are calculated by using the TauP tools (Crotwell *et al.*, 1999) based on the ray theory and the same model used for the waveform calculations. To keep the figure simple, only the phases relevant for the discussion are plotted. The legend for the phase bars is shown in Fig. 6.1 and is the same for all the figures in this chapter.

At Δ=100°, the S wave is already diffracted (dark green bar) along the CMB and of course it continues to be also at Δ=110°. The sS (point-dashed light green bar) and sSdiff phases (point-dashed dark green bar) are also shown. Onsets of pS (dashed light green bar) and pSdiff (dashed dark green bar) waves are also reported. Please note the difference between the point-dashed (e.g., sS, sSdiff, sSKS, etc.) and the dashed bars (e.g., pS, pSdiff, pSKS, etc.). A pS(diff) wave is similar to a sS wave with the difference that the wave leaves the source as P wave and then is converted into S when it bounces at the surface (see Fig. 6.1).

The analysis of Fig. 6.8-a and 6.8-b suggests that when the source is at the surface, the arrival of the S wave coincides with the arrival of the pSdiff and sSdiff phases (they are not actually distinguishable). On the other hand, these phases clearly separate as the source goes deeper. At 30 km depth, the separation of the phases starts to be evident. At 100 km, it is clear that the two superimposed phases are Sdiff and sSdiff while the pSdiff phase does not contain any energy in the radial component. At 500 km depth, the only clear phase in the radial component is the sSdiff wave.

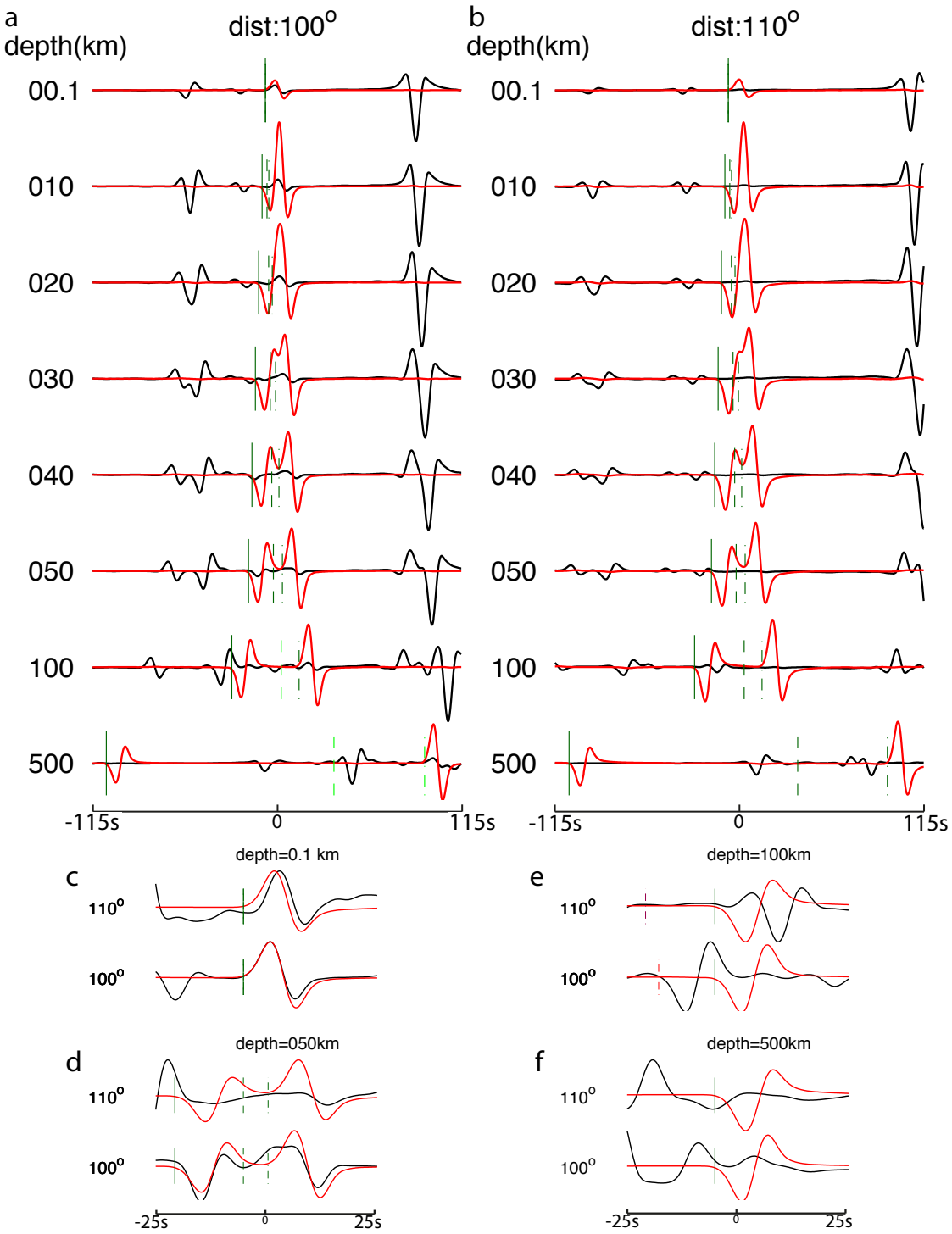

Figure 6.8: Black and red traces are radial (SV) and transverse (SH) seismogram components, respectively. Only arrival times for S(diff), pS(diff), sS(diff) are plotted (phase legend is in Fig. 6.1). The source epicentre and stations are the same as in Fig. 6.6 and the processing of the waveforms is carried out as in Fig. 6.7. a-b: Waveforms are calculated with different hypocentral depths (numbers on the left) and recorded at epicentral distances of 100° and 110°. Amplitudes are normalised with respect to the maximum amplitude of all the waveforms shown in each of the subplots. c-f: Zooms of some of the waveforms in the plots a and b, for different depths (reported on the top) at 100° and 110° (reported on the left of the waveforms). Each waveform is normalised with respect to its own maximum amplitude.

The subplots in Figs. 6.8-c to 6.8-f show a zoom around the Sdiff arrivals. When the source is at the surface (Fig. 6.8-c), the apparent splitting is visible for the Sdiff wave recorded at Δ=110°. When the source is placed at 100 km (Fig. 6.8-c), waveforms at Δ=100° and Δ=110° could be still interpreted as being split. At 500 km depth, the Sdiff phase is well isolated and no apparent splitting is noticed.

In conclusion, it seems that the apparent splitting in the KO10 experiment is due to the superposition of different phases (notably Sdiff and sS(diff)) associated with the use of a source placed just under the Earth's surface. The fact that the superposition of these phases results in different pulse/arrival-time in the radial and transverse components might be due to the difference in the polarity of the superposed phases (e.g., constructive superposition the transverse component, destructive in the radial). This issue disappears when the source is deep enough to avoid the sS(diff) contamination.

Isotropic PREM

In the following experiment, we simulate S waves in a slightly modified PREM model (Fig. 6.4). Specifically, we replace PREM's crust by the same simple homogeneous crust model as before, we consider a purely isotropic earth model (i.e., Vsh=Vsv even between 24.4 km and 220 km depth). We include the discontinuities in the mantle at 220 km, 410v and 660 km depth. Although they create reverberations that complicate the waveforms, they are necessary for realistic simulations. We carry out calculations both taking and not taking into account PREM's attenuation.

We modelled S waveforms in the isotropic PREM model using the same source-geometry configuration as before (stations at azimuth of 90°), but adding other virtual stations at the opposite azimuth (270°). We plot the waveforms recorded at the azimuth of 90° on top of those recorded at the azimuth of 270°to highlight the differences (Fig. 6.9-a). As before, attenuation is not taken into account. An apparent SH-SV splitting can be noticed from Δ=90° to Δ=106°, although it varies in sign and there is not a clear correlation with the epicentral distance. From an epicentral distance larger than Δ=108°, there is not a clear S pulse in the radial component. Also, although the model used is 1-D, different estimates of apparent splitting are obtained from stations at the same epicentral distance but for different azimuths (Fig. 6.9-a, red and green numbers at the right of the waveforms). In particular, SV waves are almost identical for the two azimuths but SH waves differ. As a consequence, stations at azimuth of 90° always present larger splitting than stations at azimuths of 270°. The maximum apparent splitting is 1.8 s with a positive sign for Δ=96° and azimuth of 90°.

To make our simulations more realistic, we simulate the same wavefield taking into account PREM's attenuation. Results are shown in Fig. 6.9-b. The attenuation changes the shape and the onset time of both SH and SV waveforms because it eliminates the higher frequencies. As result, the SH-SV splitting is evident in fewer stations.

The distinct results that we obtained as a function of the azimuth and attenuation suggest that: (i) the radiation pattern, which depends on the moment tensor/azimuth does affect the shape of the waveforms. Two wavefronts propagating in the opposite direction can have

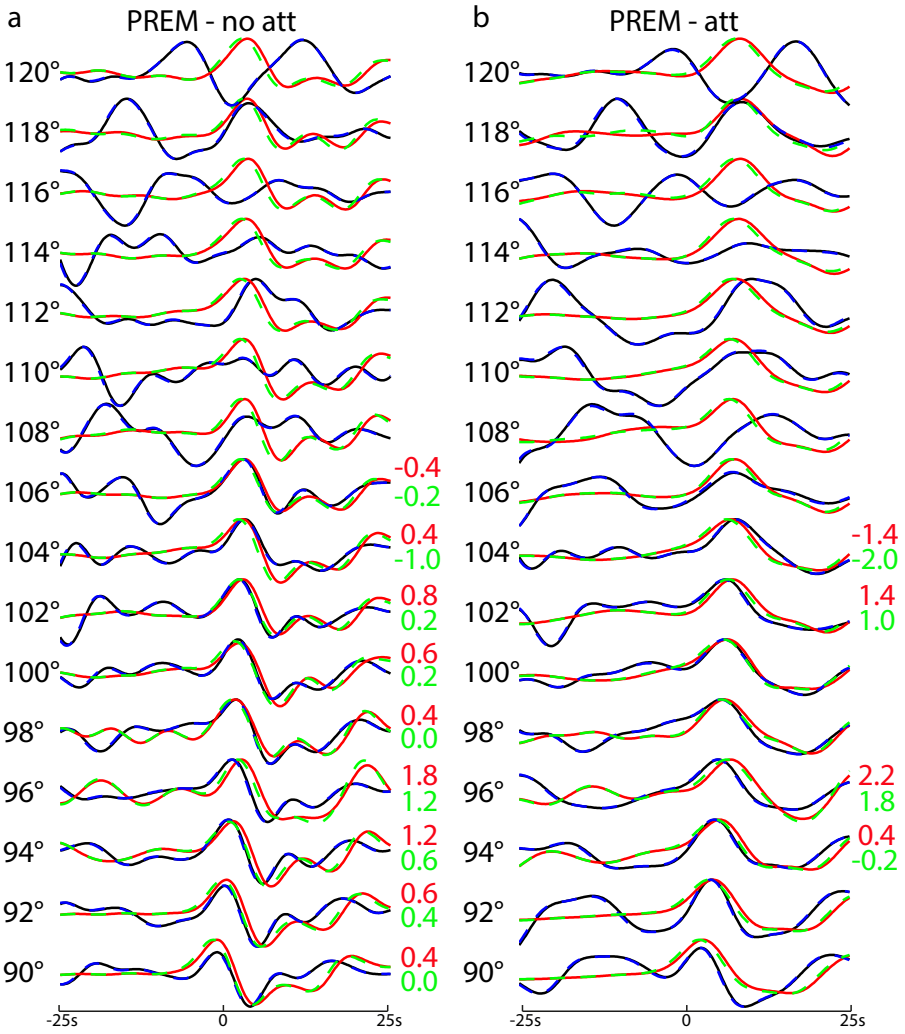

Figure 6.9: S waveforms calculated in the isotropic PREM model. a- attenuation not taken into account. b- attenuation taken into account. Solid waveforms are for stations with azimuth of 90°. Dashed waveforms are for stations with azimuth of 270°. Black and blue waveforms are SV waves, for azimuth of 90° and 270°, respectively. Note that the black are blue waveforms are almost identical. Red and green waveforms are SH waves for azimuth of 90° and 270°, respectively. Red and green numbers on the left of the waveforms are the SH-SV apparent splitting in seconds for azimuth of 90° and 270° , respectively. The source, amplitude normalisation and processing are the same as in Fig. 6.7. The stations with azimuth of 90° are those shown in Fig. 6.6. The stations for azimuth 270° are at 180° with respect to the previous ones.

opposite polarity and differently interact with discontinuities, giving rise to different wave fields. ii) The attenuation is another factor which can change the shape of the waveform, even changing the apparent onset time, and the measured apparent splitting.

6.4.2 3-D ISOTROPIC EARTH MODELS

In this section, we render the simulations even more realistic using two 3-D mantle models, S40RTS (Ritsema *et al.*, 2011) and SGLOBE-rani (Chang *et al.*, 2015) combined with CRUST2.0 (Bassin *et al.*, 2000). By default, S40RTS is defined in terms of perturbations of Vs with respect

to the transversely isotropic PREM. SGLOBE-rani is defined as Vsv and Vsh perturbations with respect to the transversely isotropic PREM. However, in these simulations the radial anisotropy in both PREM and SGLOBE-rani is neglected. Both models are combined with a degree 12 δVp model (Ritsema & van Heijst, 2002) and $\delta\rho$ is scaled from δVs, using the relationship $\delta\rho$=0.4δVs.

Simulations for SGLOBE-rani are run fully taking into account the attenuation effects. On the other hand, to limit the CPU time needed, simulations with S40RTS are run taking into account only the physical dispersion due to the anelasticity, for which waves at different frequency travels at different velocity. Therefore, the arrival times of the individual pulses are corrected for the attenuation in the earth but the decay of waveform amplitude is neglected. This approximation should have limited effects on our analysis as we are not considering the amplitude of the waveforms.

We consider exactly the same source-receiver configuration as in our previous experiments (subsection 6.4.1) and start by placing the source at the Earth's surface. We then place the source at 604 km of depth to limit the superposition between the S(diff) and sS(diff) phases.

Isotropic 3-D earth models - shallow source

Fig. 6.10-a shows the 3-D Vs perturbations of S40RTS with respect to PREM crossed by the S waves recorded at an azimuth of 90°. S waves cross the the so-called African superplume just before travelling near-horizontally across the D" region, where slightly positive and negative Vs anomalies alternate. Waveforms for S40RTS and SGLOBE-rani for a source placed at the surface (0.1 km) and recorded along the equator by stations with an azimuth of 90° are shown in Figs. 6.10-b and 6.10-c. S waves for S40RTS (SGLOBE-rani) recorded from 90° (92°) to 108° (106°) show a clear SH-SV apparent splitting with SV(diff) leading SH(diff).

Fig. 6.11-a shows the structure in S40RTS crossed by the S waves recorded at an azimuth of 270°. All the waves cross the edge of the Pacific mid-ocean ridge before entering into the D" region. Waveforms for the azimuth of 270° and shallow source are shown in Figs. 6.11-b and 6.11-c. The S waves recorded at Δ>108°–110° also cross a high velocity region from the D" to the surface. While only few station for S40RTS show S waveforms with apparent splitting, the SGLOBE-rani model leads to an apparent splitting from -1.6 s to -2.0 s at distances ranging from 90° to 100°.

These tests for a shallow source show that 3-D Vs perturbations from different Earth models and at different azimuths can affect the shape of the S waves substantially, leading to important variations in the apparent SH-SV splitting.

Isotropic 3-D earth models—deep source

The same simulations as in the previous section were repeated, but now placing the source at a depth of 604 km. Figs. 6.10-d and 6.10-e shows waveforms recorded along an azimuth of 90° and Figs. 6.11-d and 6.11-e for an azimuth of 270° .

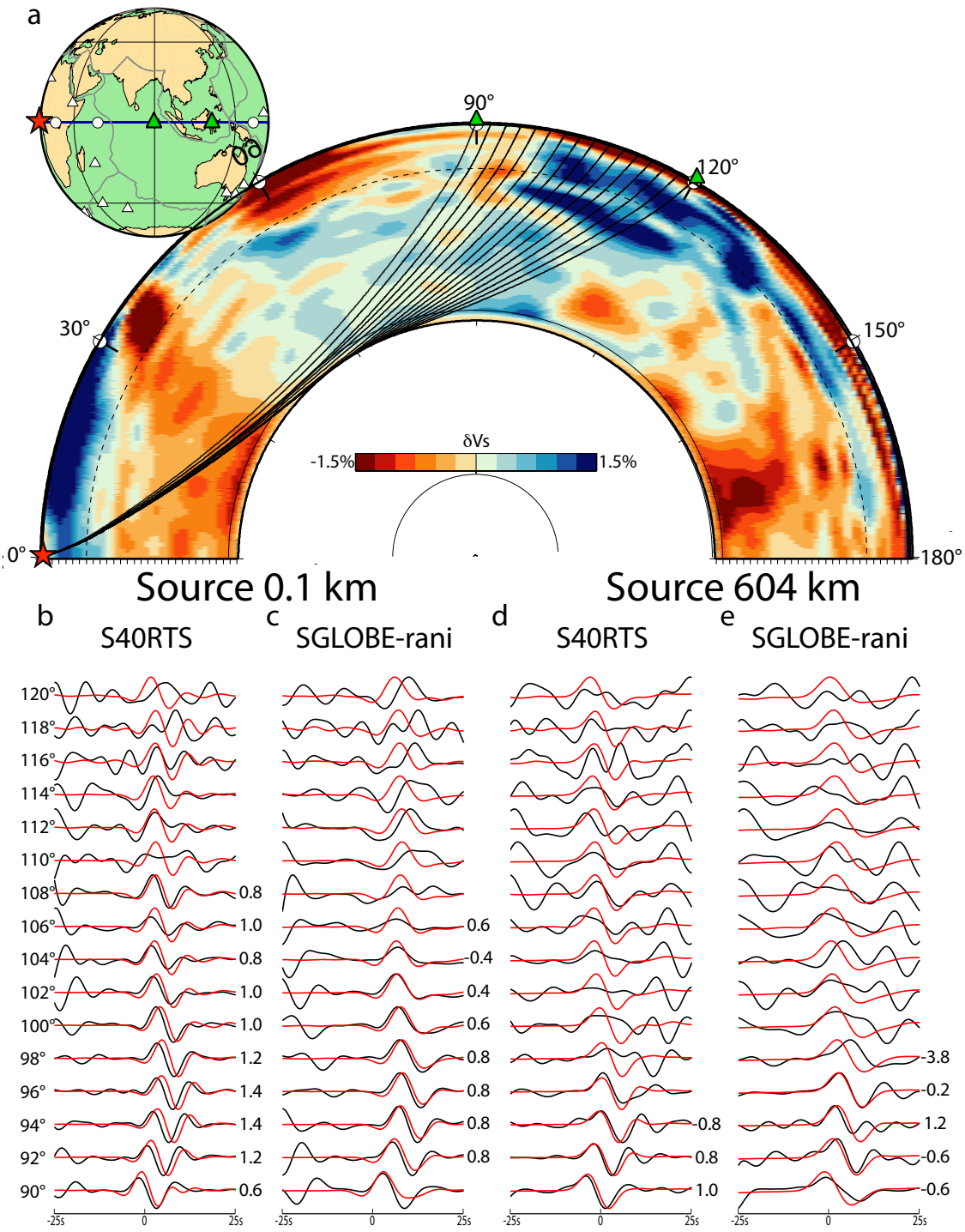

Figure 6.10: a) S(diff) rays traced in PREM for a source at 0.1 km superimposed on S40RTS Vs perturbations from PREM. Stations are at an azimuth of 90° from the source. b) and c) S waveforms calculated with a source at 0.1 km for the S40RTS model (b) and the isotropic version of the SGLOBE-rani model (c). d) and e) show the same as in b) and c), respectively, but for a source placed at 604 km depth. The red traces are SH waveforms and the black traces are SV waveforms. The numbers on the left correspond to the epicentral distance. The numbers on the right of the subplots correspond to the SH-SV apparent splitting in seconds. The source, amplitude normalisation and processing are the same as in Fig. 6.7.

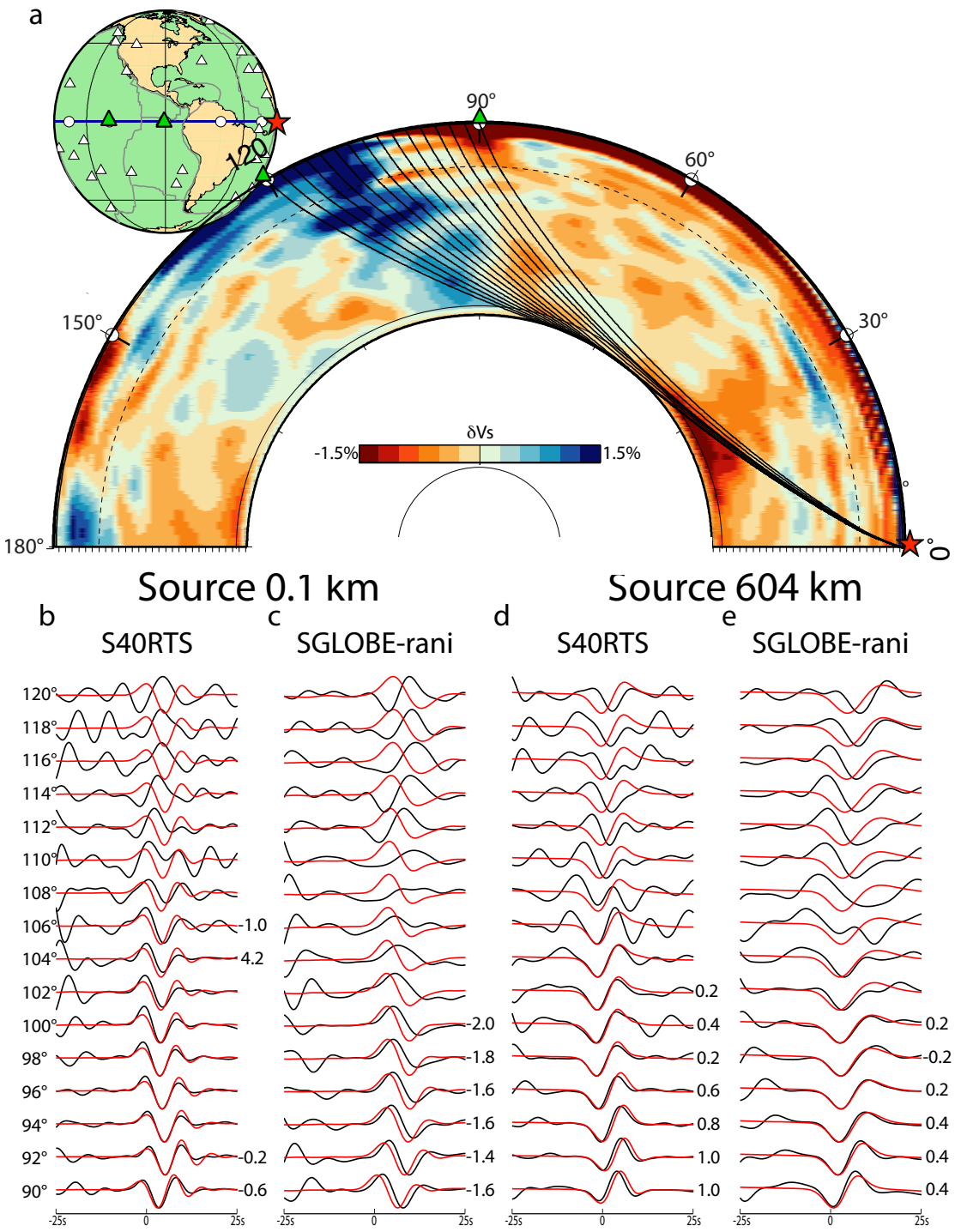

Figure 6.11: As in Fig. 6.10 but for stations with azimuth of 270°.

These figures show that when the source is deeper (e.g., 604 km) the apparent splitting is reduced for both azimuths and both models. However, it can still reach 3.8 s in some cases (e.g., for SGLOBE-rani at an azimuth of 90° and epicentral distance of 98°, Fig. 6.10-e).

6.5 REAL DATA APPLICATIONS

In this section we model S(diff) waves using a real source-receiver distribution for which clear SH-SV splitting observations have been reported (Ritsema, 2000). In order to model real waveforms with 1-D and 3-D, isotropic and anisotropic models, we analyse the effects of several model parameters on the waveforms.

6.5.1 MODELLING THE MW 5.8 AUGUST 30 1994 BANDA SEA EARTHQUAKE

We model waveforms recorded by stations of a temporary network in Tanzania generated by the Mw 5.8 Banda Sea earthquake that occurred on the 30th of August 1994 with a depth of ~600 km. This event was studied by Ritsema (2000) (event C in that study), with observed waveforms as shown in Fig. 6.12. Data used in this section are available from the IRIS website (www.iris.edu).

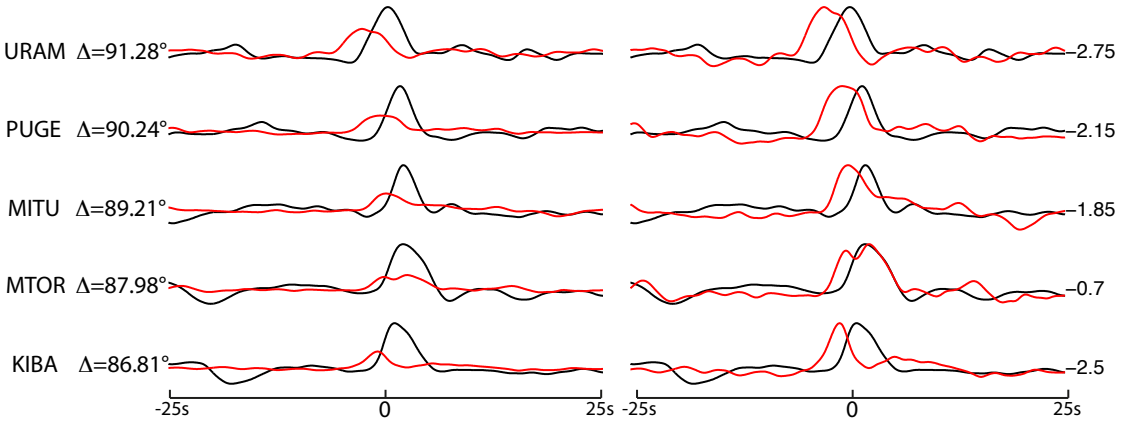

Figure 6.12: Broadband displacement waveforms for the Mw 5.8 August 30 1994 Banda Sea earthquake on the arrival of the S wave. The red traces are SH waveforms and the black traces are SV waveforms. On the left of the waveforms: name and epicentral distance of the station. Numbers on the right: splitting in seconds. Waveforms on the left are normalised with respect to the largest amplitude of SV and SH for every station. Each waveform on the right is normalised with respect to its own maximum amplitude. The instrument's response is deconvolved from the waveforms and a high pass-cosine filter at 80 s is applied.

In the study of Ritsema (2000), the recordings of this earthquake were compared to the recordings of two other events that occurred at a shorter epicentral distance from the network considered. All the recordings have similar azimuth (~265°). While waveforms from event C, recorded at an epicentral distance ranging from Δ=~87° to Δ=~91°, show a SH-SV splitting of ~1s–3 s, the SH and SV waveforms generated by the two other closer events do not show any SH-SV splitting. Ritsema (2000) invoked velocity jump at about 300 km above the CMB to explain the wave shape difference and a radial anisotropy ranging from 1.4 %–2.7 % (calculated as $1 - \frac{Vsv}{Vsh}$) to explain the SH-SV splitting observed for the event C. The source-receiver geometry and the 3-D earth structure of S40RTS along these S paths are shown in Fig. 6.13. In PREM, the D" has a thickness of 150 km (see Fig. 6.13-a). In order for S-waves at Δ=87°

–92° to sample the D" layer, it must be at least 300 km thick (see Fig. 6.13-b). Hence, in our modelling we also consider models with a D" layer with a thickness of 300 km.

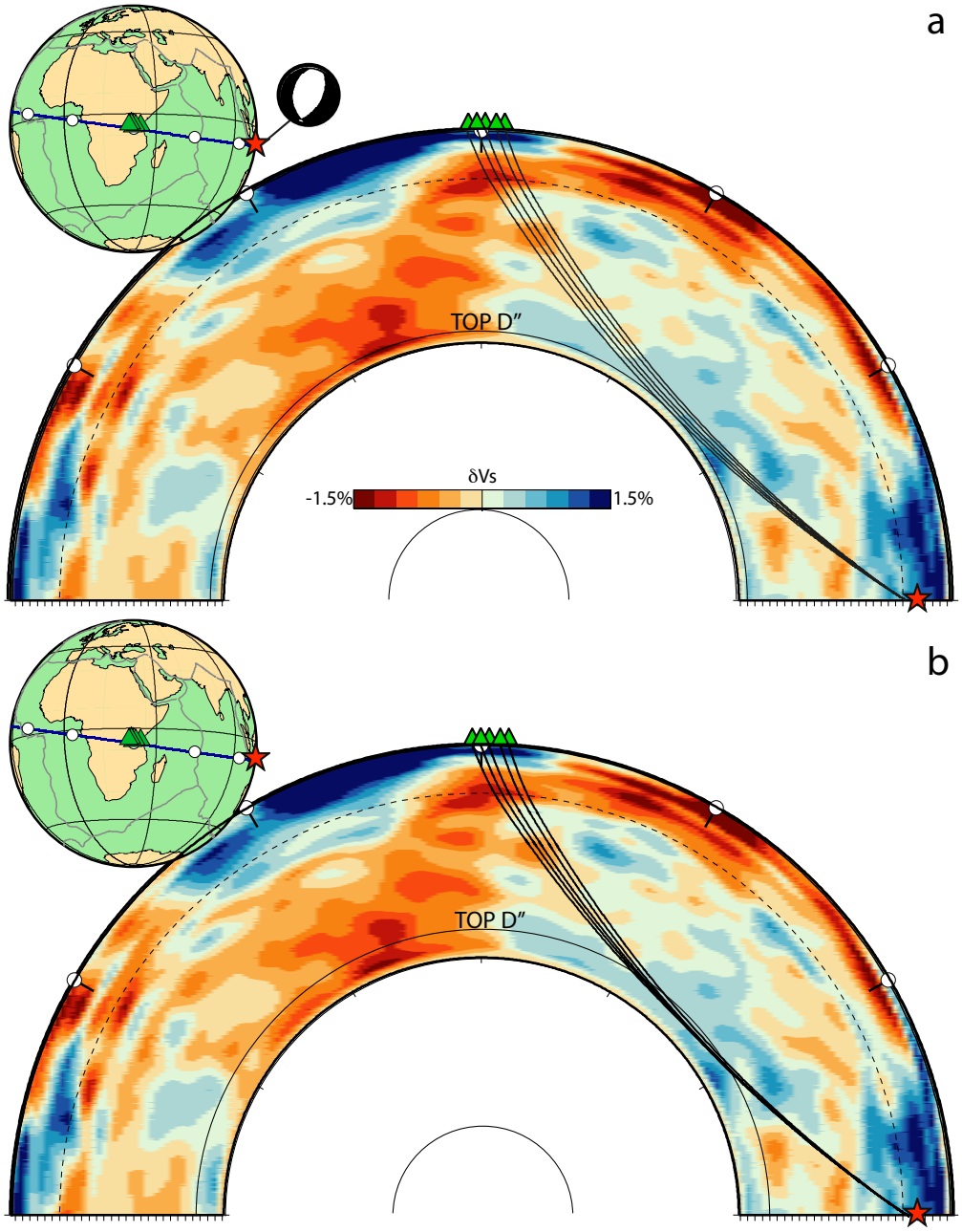

Figure 6.13: Source-receiver geometry for the Mw 5.8 August 30 1994 Banda Sea earthquake. S40RTS mantle model in background of the cross sections. Red star: location of the event; green triangles, from East to West, are the stations URAM, PUGE, MITU, MTOR, KIBA. Top: rays are traced in PREM (mod2 of Fig. 6.15); focal mechanism for the studied event. Bottom: rays are traced in the mod16 of Fig. 6.15 (double thickness for the D").

We use GEM and the SEM to model the waveforms shown in Fig. 6.12 for various 1-D and 3-D Earth models, and for the source parameters as reported in the global CMT catalogue (www.globalcmt.org). All the real and theoretical seismograms are filtered with a low pass

cosine filter—cut off of 7 s—because the SEM synthetics are only accurate for wave periods longer than T~5.6 s.

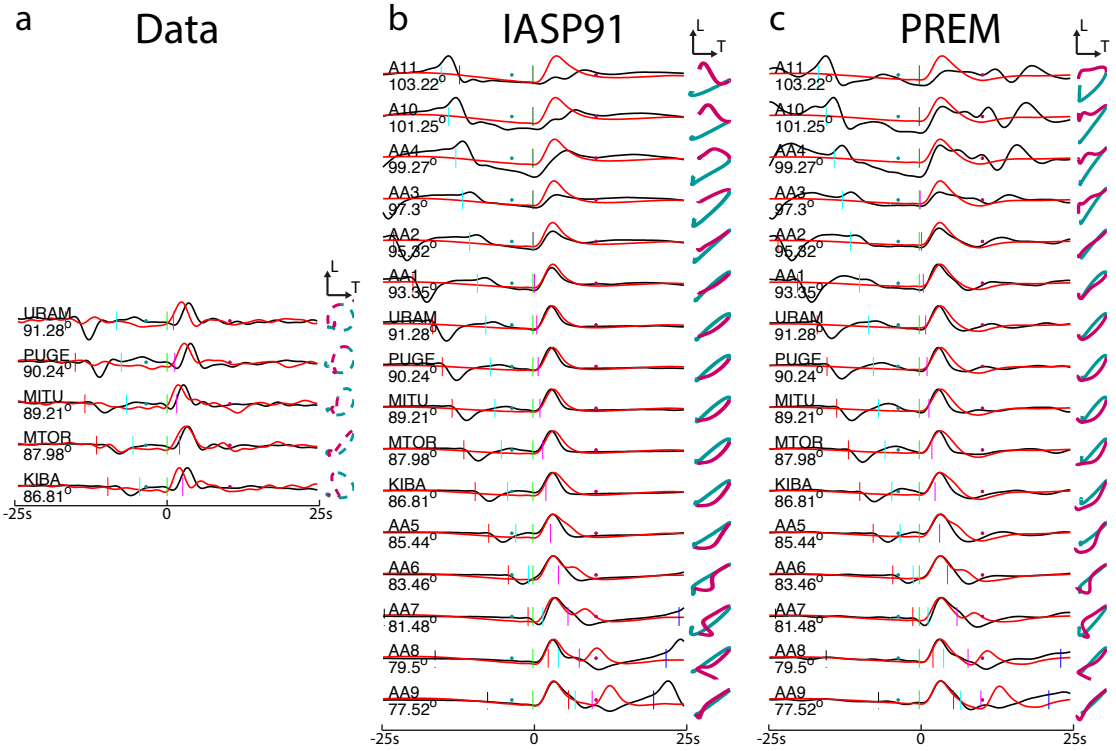

Figure 6.14: Comparison between observed displacement waveforms (subplot a) and synthetics calculated for the simplified version of IASP91 (subplot b) (mod1 in Fig. 6.15) and PREM (subplot c) (mod2 in Fig. 6.15). Black and red traces are radial (SV) and transverse (SH) seismogram components, respectively. Name and epicentral distance of the stations are reported on the left of the waveforms. Vertical bars represent the theoretical arrival-times for different phases (legend in Fig. 6.1). Arrival-times for synthetic waveforms are calculated for the correspondent earth models. Arrival-times for the data are calculated for PREM. Waveforms are aligned with respect to the S(diff) arrivals. Traces are convolved with a Gaussian source time function with a half duration of 2.9 s and filtered using a cosine low-pass filter leading to a dominant period of T~7 s. Particle motions are reported on the right of each pair of waveforms, aquamarine and magenta dots on the waveforms mark the start and the end of the particle motion plots.

For completeness, in our simulations we add several virtual stations with the same azimuth as the real stations but at shorter and larger epicentral distance from the hypocentre (whole real/virtual network is from Δ=~72° to Δ=~103°).

6.5.2 ISOTROPIC EARTH MODELS

Firstly, we attempt to model the Banda sea event data with the simplified version of IASP91 and PREM (now named mod1 and mod2, respectively) used in the previous experiments (subsection 6.4.1). Fig. 6.14 shows the modelled S waveforms. All the main theoretical onsets for the corresponding models are marked with vertical bars on top of the waveforms (same legend as in Fig. 6.1). We also plot the particle motion for every pair of transverse and radial seismograms to facilitate the comparison with the real data. Fig. 6.14 shows that the

real data S waves arrive slightly before PREM (mod2) synthetics because they cross a high velocity structure in the lowermost mantle (see Fig. 6.13). mod1 and mod2 generate synthetics with a large dissimilarity with respect to the data, both in terms of shape of the pulse and splitting. It seems that the effects of the attenuation model used (from PREM) are too strong as the synthetic pulses are too wide compared to the data. However, we will not change the attenuation models in the following experiments to keep the trial-error process simpler and consistent. An interesting point of the synthetics calculated for the stations AA9, AA8 and AA7 is the evidence that the ScS waveform (magenta bars) has opposite polarity in the radial and transverse components. Hence, interference with the ScS phase is a possible cause of the different width pulse between SH and SV in the synthetics at the stations from KIBA to URAM and in the data at the station MTOR.

Waveform modelling is then performed by using several other 1-D isotropic models built varying the seismic properties of the D" (Fig. 6.15). In the following paragraphs we will investigate the effects of these properties on the waveforms with the ultimate goal of attempting to fit the real waveforms.

Vs gradient in the D"

mod2, mod3, mod10, mod13, mod14 and mod15 have the same D" thickness (150 km) but different Vs gradient in the D" (Fig. 6.15). While the differences in waveforms between mod2 (gradient almost null) and mod3 and mod10 (positive gradient) are quite small (not shown for brevity), the differences between mod2 and models with negative gradients (mod13 to mod15) are more evident (Fig. 6.16).

As expected, the SKS phase (red bar) is only evident on the longitudinal component (black traces, SV) and the SP and SSP phases (blue bars) do not show any energy in the seismograms.

The main differences between the waveforms for the models mod2 and mod15 are related to the S (light green bar) and ScS (magenta bar) phases, which have distinct theoretical arrival times in these two models. For mod15, the ScSH pulse is clearly evident before the complete superposition with the SH phase as the epicentral distance increases. Indeed, the superposition between SH and ScSH leads to a pulse with two peaks at stations KIBA and MTOR. For larger epicentral distances, the SH/ScSH superposition gives rise to a pulse larger than the SV/ScSV waveform. Conversely, the ScSV phase does not appear in the seismograms (possibly it has opposite polarity to SV and hence may be obscured by the latter).

The smaller differential arrival time between S and ScS for mod2 is the cause of the wider SH pulse than SV for the stations at smaller epicentral distance (from KIBA to URAM). Hence, the wider SH pulse than SV observed in the real data (e.g., station MTOR in Fig. 6.14) may be at least partly due to the superposition of the SH and ScSH phases. Nevertheless, it is worth noting that while the widening of the SH synthetic waveforms seems to occur mainly towards the tail of the pulses (e.g., from KIBA to URAM), in the real data, it occurs at earlier times.

In conclusion, variations in D" Vs gradient can affect the differential arrival times between S and ScS substantially. Interferences between these phases can lead to wider SH than SV pulses. The broadening of the waveforms is another factor that should be considered when

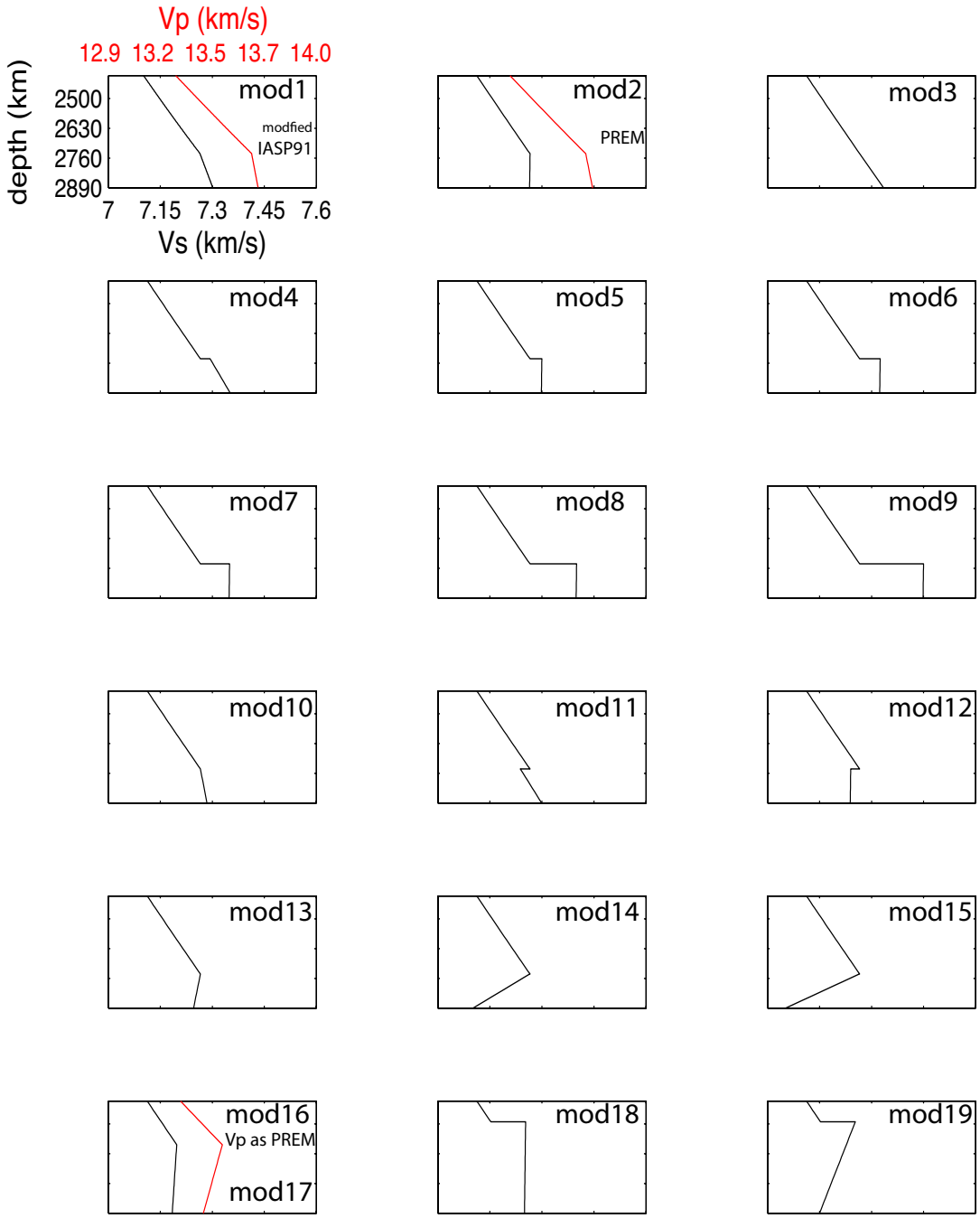

Figure 6.15: Lowermost mantle structure in the 1-D isotropic models used to model waveforms for the Banda Sea earthquake considered in this study. mod1 is the modified version of IASP91 already used in the previous section. mod2 is PREM. When Vp (in red) is not shown, it is the same as in PREM, except for mod16 (mod17 has the same Vs structure as mod 16, but different Vp, shown in red). The shallower parts of the models are as in the modified IASP91 model for mod1 and as in the PREM model for all other cases. The ranges of depth (y-axis), Vp and Vs (x-axis) are the same for all the models.

the wave splitting is interpreted.

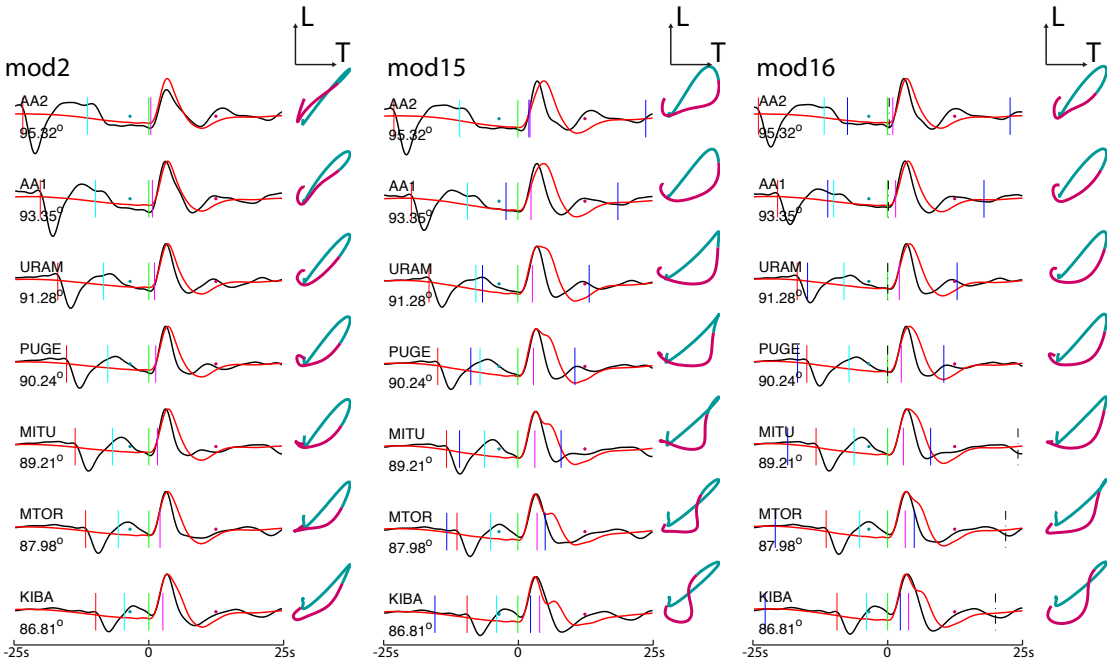

Figure 6.16: S waveforms and particle motions for three different 1-D isotropic models. Black and red traces are radial (SV) and transverse (SH) seismogram components, respectively. The main differences between models mod2 and mod15 are their Vs gradients in the D", whereas mod2 and mod16 differ in their D" thickness. Models are shown in Fig. 6.15. Name and epicentral distance of the stations are reported on the left of the waveforms. Vertical bars represent the theoretical onsets for different phases (legend in Fig. 6.1), which are calculated for the correspondent earth models. Waveforms are aligned with respect the S(diff) arrivals. Traces are convolved with a Gaussian source time function with a half duration of 2.9 s and filtered using a cosine low-pass filter leading to a dominant period of T~7 s. Particle motions are reported on the right of each pair of waveforms, aquamarine and purple dots on the waveforms mark the start and the end of the particle motion plots.

Discontinuities at the top of the D" layer

mod11 and mod12 have a negative shear velocity jump at the top of a 150 km thick D". These models generate S waveforms very similar to those obtained for model mod15 with a negative Vs gradient (Fig. 6.16) and hence we here do not show them for conciseness.

The models from mod5 to mod9 (Fig. 6.15) have positive jumps of Vs at the top of the 150 km thick D". S waves for models mod6 to mod9 show a negative apparent splitting up to ~4s (Vsh>Vsv) which starts at an epicentral distance that depends on the strength of the velocity jumps (Fig. 6.17, for brevity we only show waveforms for models from mod7 to mod9). S waveforms for models with stronger Vs jumps (e.g., mod9) start to show apparent splitting at smaller epicentral distances than waveforms for models with weaker jumps (e.g., mod7). The positive jump at the top of D" in mod5 is too weak and the apparent splitting is not evident. S waves, at distances larger than 96°–97° (not shown for conciseness) do not show any apparent splitting because they start to be diffracted and SV waves dissipate all their energy.

It is important to note that ray theory predicts that for station KIBA (Δ=87°, Fig. 6.13) the direct S wave does not cross a 150 km thick D". Yet, the waveforms for different models in Fig. 6.17, which differ only for earth structure deeper than 150 km, show some slight differences

at this station (Fig. 6.17), highlighting the non-ray character of these waves.

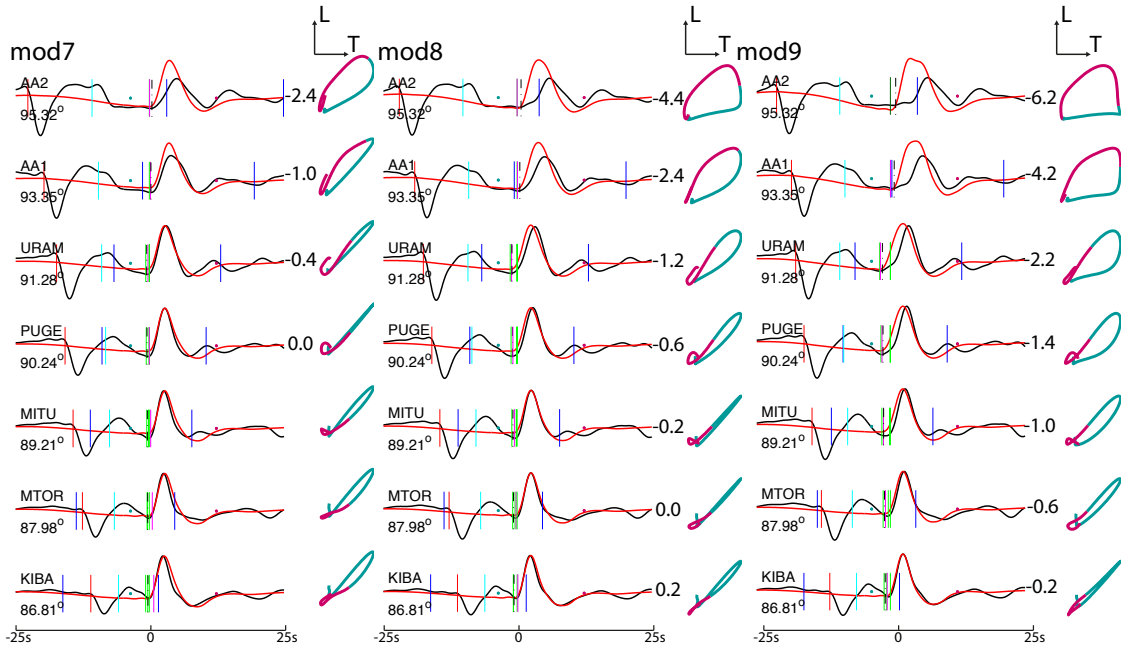

Figure 6.17: Same as in Fig. 6.16 but for models with a positive Vs jump at the top of a 150 km thick D". The Vs jump at the top of the D" causes the triplication of the S wave so three light green bars are reported.

The models mod18 and mod19 (Fig. 6.15) have a positive Vs jump at the top of D" as in the models previously discussed but in these models the thickness of the D" is 390 km. For these models, Fig. 6.18 shows that the waveforms show a widening of the SH pulses, but no clear apparent splitting as in Fig. 6.17. A possible explanation for this is given by Fig. 6.19 where travel-time curves of S and ScS for mod9 (150 km thick D") and mod19 (390 km thick D") are compared. The strong high-velocity discontinuity at the top of the D" in both models causes the triplication of the S wave.

The Vs jump in mod19 causes a triplication of the S waves at an epicentral distance range of 70°–95°, where there is no interaction with the ScS arrival. In mod9, as well as in mod6 to mod8, the triplication due to the Vs jump occurs at distances of 85°–95°. In this case, the ScS phase arrives after the first S of the triplet and before the end of the triplicated arrivals. As seen in Fig. 6.14, ScSH and ScSV have opposite polarity. Thus, the different interference between the S triplet and ScS in the radial and transverse component probably causes the apparent splitting observed in models mod6 to mod9. Conversely, in mod18 and mod19, in the range of epicentral distance considered, the ScS arrives soon after the S arrivals. In this case, the effect of the triplication is that the SH pulse seems broader than the SV pulse.

In summary, in this subsection we found that a positive shear wave velocity jump at the top of the D" causes a triplication of the S wave. In a range of epicentral distance that depends on the Vs jump and the thickness of the D", the ScS wave can arrive within the time window of the S triplet interfering with it and apparently anticipating the S arrival (and thus leading to

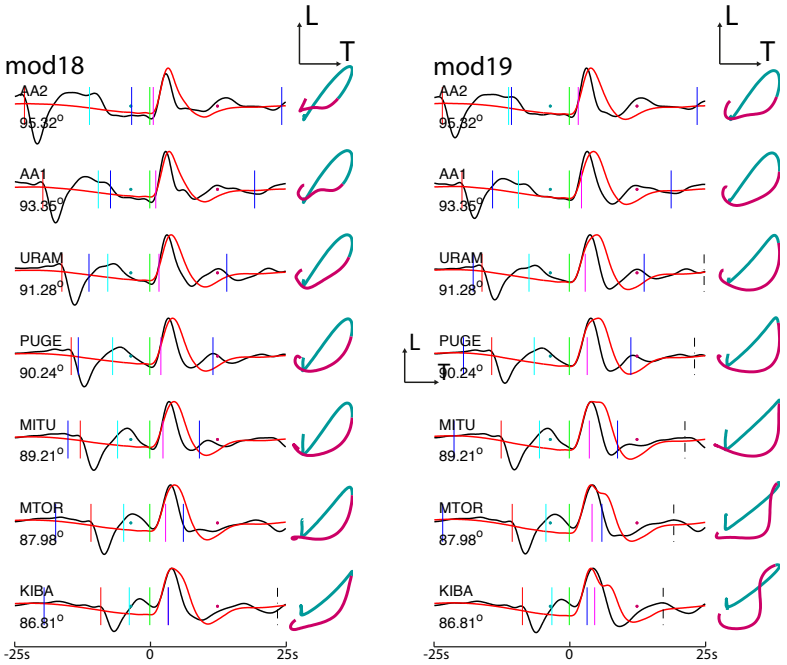

Figure 6.18: Same as in Fig. 6.16 but for models with positive Vs jump at the top of 390 km thick D".

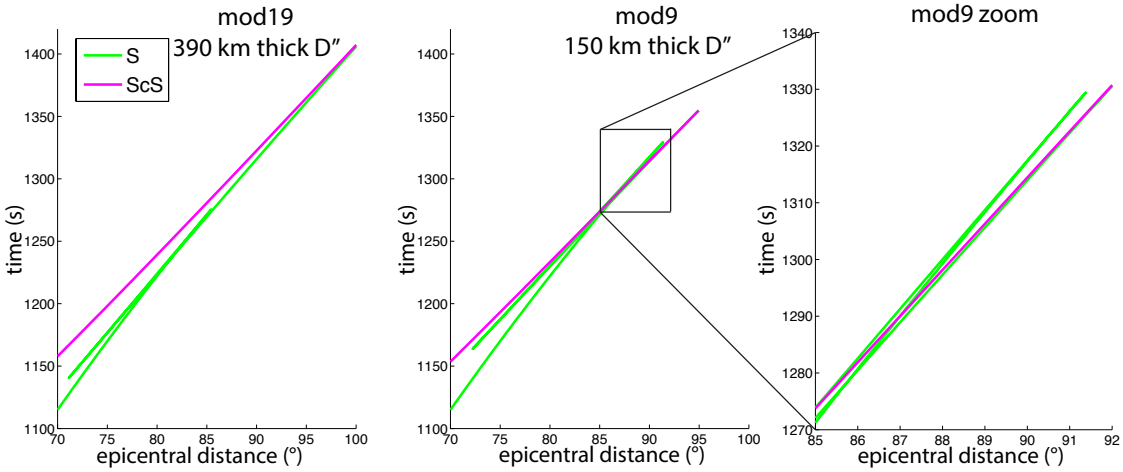

Figure 6.19: Travel-time curves calculated for models mod19 and mod9. In mod9, the ScS phase arrives after the first triplicated S wave and before the end of the triplication.

apparent SH-SV splitting).

D" thickness effects

Models as mod2 and mod16 have the same gradient in the D" region, differing only in its thickness. In mod16 the SH waveforms are broader than in mod2 (Fig. 6.16) because of the S-ScS superposition. As seen in the previous paragraphs discussing the differences between e.g. mod9 and mod19, varying the D" thickness affects the way the S and ScS phases interfere. Hence, for the epicentral distances considered here, variations in D" thickness affect S-ScS interferences, which can broaden the pulses.

Vp/Vs ratio in the D"

Starting from mod16, we change the Vp profile, obtaining mod17 (Fig. 6.15), to verify if apparent SH-SV splitting could be caused by the interference of the S wave with SP and PS waves in the radial and transverse component, respectively. However, changes in the waveforms are visible only in the radial component when the first P wave arrives. No changes in the waveforms are visible around the S arrivals at least in the epicentral distance considered.

Hence, nSP (SP, SSP, . . .) and nPS (PS, PPS, . . .) do not seem to interfere with the direct S waveform in the range of epicentral distance and for the source model considered in this study.

Non uniqueness of the problem

The models mod15 and mod19 have distinct D" thickness, Vs jump at the top of the D" and Vs gradient within the D". Despite these differences, the waveforms generated by these models are quite similar (not shown for brevity). This highlights that there are strong trade-offs between the various properties of the D", which complicate the interpretation of seismic observations of this region.

3-D Earth models

In order to examine the influence of 3-D structure on the waveforms we carried out simulations using three different 3-D Earth models: (i) S40RTS (Ritsema *et al.*, 2011) (ii) S40RTS in which δVs are multiplied by a factor of 1.75; and, (iii) the isotropic version of S362WMANI (Kustowski *et al.*, 2008), which shall be referred to as S362iso model. In our simulations the Vs perturbations in these models are superimposed to the isotropic PREM model. To reduce the computational cost, these 3-D simulations are run taking into account only the physical dispersion due to the anelasticity.

S waveforms for these 3-D earth models are shown in Fig. 6.20. Theoretical arrival times (vertical bars) for PREM are plotted on top of the waveforms. S40RTS and S362iso present positive Vs perturbation along the S paths in the lowermost mantle; thus, the S waves arrive before PREM's theoretical arrival time for all the models. Small apparent SH-SV splitting is observed in some cases (e.g., at KIBA station the splitting is more than 1 s). However, the 3-D models seem to have limited effects on the shape of the waveforms compared to the effects considered in the previous paragraphs.

6.5.3 ANISOTROPIC EARTH MODELS

In this section we investigate the effects of radial anisotropy on the waveforms generated by the Banda sea earthquake. We use twelve 1-D models with an anisotropic D" layer (Fig. 6.21). Essentially, these models in Fig. 6.21 differ from each other in terms of their Vsv and Vsh gradients and the D" thickness. The strength of the anisotropy is defined by the parameters $\xi = \frac{Vsh^2}{Vsv^2}$ and η that relates the velocity at intermediate angle. All the anisotropic simulations

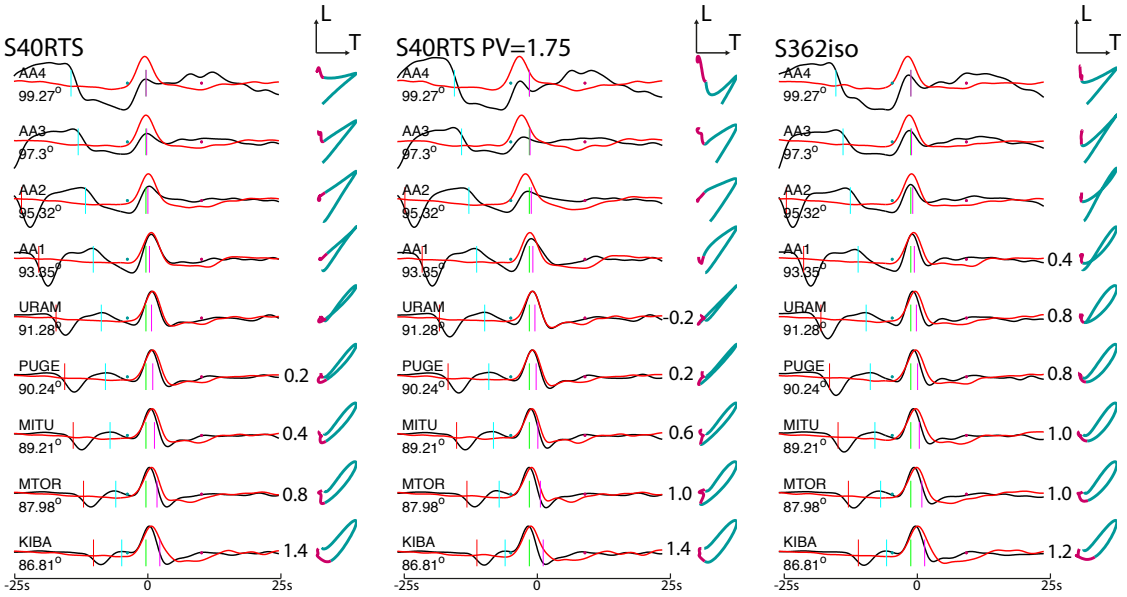

Figure 6.20: Same as in Fig. 6.16 but for the 3-D earth models S40RTS (Ritsema *et al.*, 2011), S40RTS multiplied by a factor of 1.75 and the isotropic version of S362WMANI (S362iso) (Kustowski *et al.*, 2008). Theoretical arrival-times are calculated in PREM.

of this section, except where stated otherwise, are run with a constant η=0.9 in the D"; η=1, ξ=1 everywhere else. As in the previous section, only the waveforms generated by models for which we obtain the most interesting results are displayed for brevity. After modelling the S waves with 1-D anisotropic models, we superimpose 3-D isotropic heterogeneity on the 1-D anisotropic model that better explains the data.

Parameter ξ

modA8 to modA10 (Fig. 6.21) have the same values (and gradient) of Vsh in the D" and the same gradient of Vsv. Thus, the main difference between them is ξ (that is constant through the D" layer). S waveforms for these models are shown in Fig. 6.22. For a given epicentral distance, where evident, as expected, the SH- SV splitting increases as ξ increases.

In principle, for an S wave travelling through an anisotropic D" layer, the SH-SV splitting is expected to increase with the epicentral distance because of the longer horizontal path within the anisotropic layer. However, this behaviour is clear only for model modA9, suggesting that the radial anisotropy is not the only factor affecting the splitting. Indeed, even for model modA9, interferences between the ScS and S phases make the SH pulses complex (especially for the shortest distances), rendering the interpretation of the splitting difficult.

To conclude, as expected, ξ causes real SH-SV splitting, which, however, does not have a linear effects on the S waveforms. Again, waveform interference (notably superposition with ScS) can complicate the interpretation of the splitting.

Parameter η

Fig. 6.23 compares waveforms for modA10 with η = 0.9 (default value for all the models in Fig.

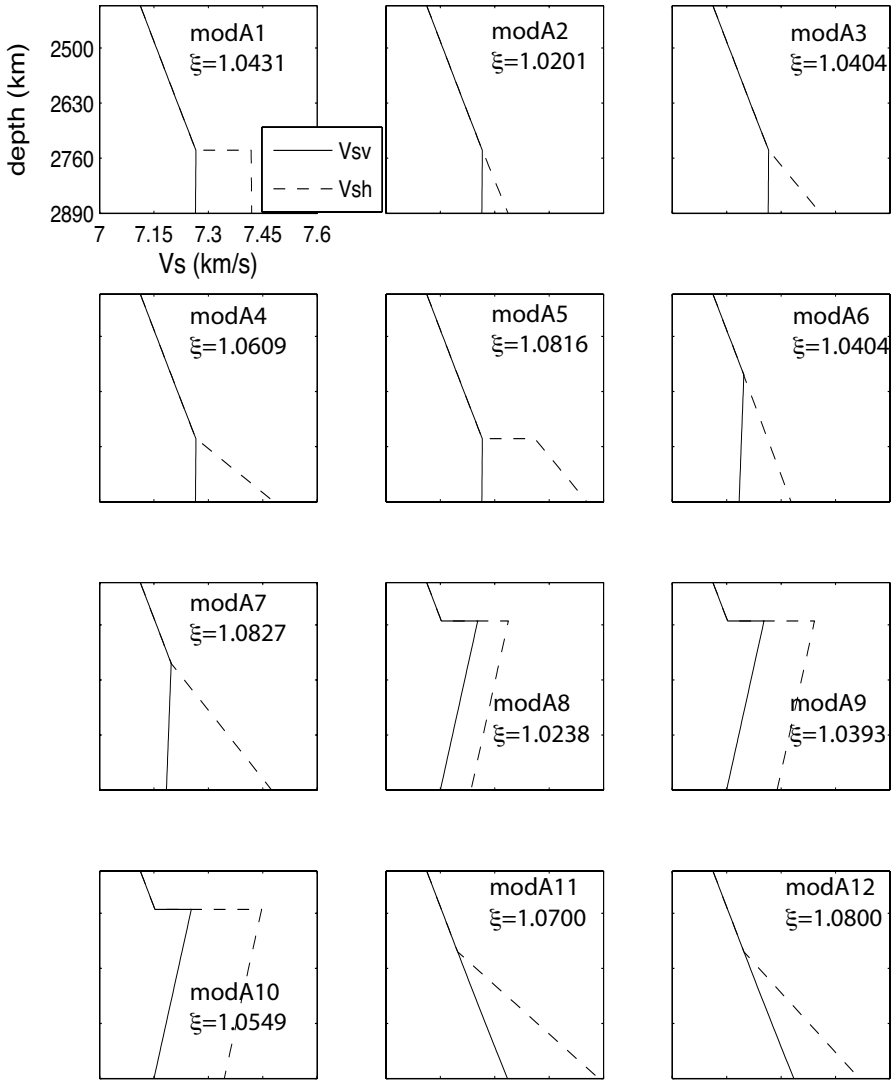

Figure 6.21: Anisotropic models used in this section. $\xi=\frac{Vsh^2}{Vsv^2}$ is calculated just above the CMB. The same x-axis and y-axis scales are used in all the sub-plots.

6.21) and modA10 with $\eta = 1.0$. We notice that while η does not affect SH, it changes the shape of the SV pulse. In particular, for η=1.0, SV arrives around 2 s later compared to SV for η=0.9, affecting the SH-SV splitting. Simulations with intermediate values of η show that η is almost linearly correlated to the SV shift.

Hence, the η parameters is a fundamental parameter in the modelling of radial anisotropy and it should be carefully considered when modelling S waves.

Data fitting

The models modA5, modA7 and modA11 generate S waveforms with features similar to those shown in the data, although these features are not always present at the same epicentral distance (Fig. 6.24). This is probably due to the fact that the arrival of the S wave paths do not depend only on the seismic parameters in the D" but also along the whole path of these

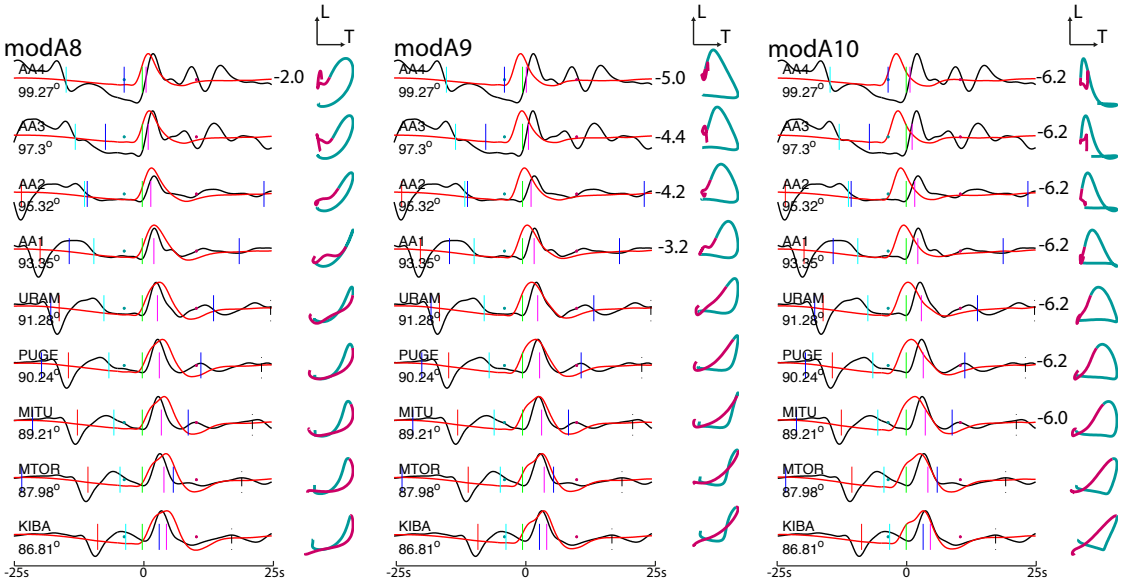

Figure 6.22: Same as in Fig. 6.16 but for radially anisotropic models differing from each other for ξ (see Fig. 6.21). Vertical bars correspond to the theoretical SV arrival times calculated for the corresponding earth models.

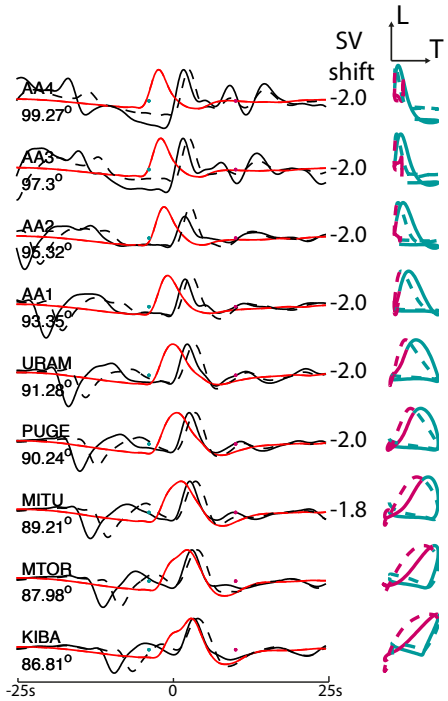

Figure 6.23: Setting of the plot and waveform processing as in Fig. 6.16 except for: Solid lines are for modA10 with η=0.9. Dashed lines are for the same model but with η=1.0. Vertical bars correspond to the theoretical SV arrival times. Numbers on the right of the waveform represent the shift between SV calculated for the two different models. Vertical bars correspond to the theoretical SV arrival times.

waves. However, to maintain the trial and error problem simple and to isolate the effects of D" properties, in this study we mainly varied primarily seismic parameters within the D".

The model modA5 has a D" layer that is 150 km thick (Fig. 6.21). The Vsv profile is as in the isotropic PREM and Vsh has a positive jump at the top of the D". ξ at the CMB is 1.0816. S waves for this model (Fig. 6.24) do not show a well defined SH-SV splitting as in the real data, probably because the S waves at the epicentral distances considered do not go deep enough to sample the anisotropy in the D". However, the SH waveforms from Δ=93° to Δ=97° (from station AA1 to AA4) have a double-peak pulse similar to the real waveform observed at station MTOR (even if with a different wavelength, as noted previously).

modA7 and modA11 are the models that better explain the SH-SV splitting observed in the real data. These models have a 300 km thick D" and Vsv and Vsh profiles without any jump. The S waveforms for modA7 present a SH-SV splitting consistent with the splitting observed in the real for all the stations. However, the SH pulses do not show any broadening. On the other hand, modA11 generates SH-SV splitting larger than that observed in the real data, but it also leads to a widening of the SH pulse. Hence, overall, model modA11 is our preferred model, leading to the best data fit.

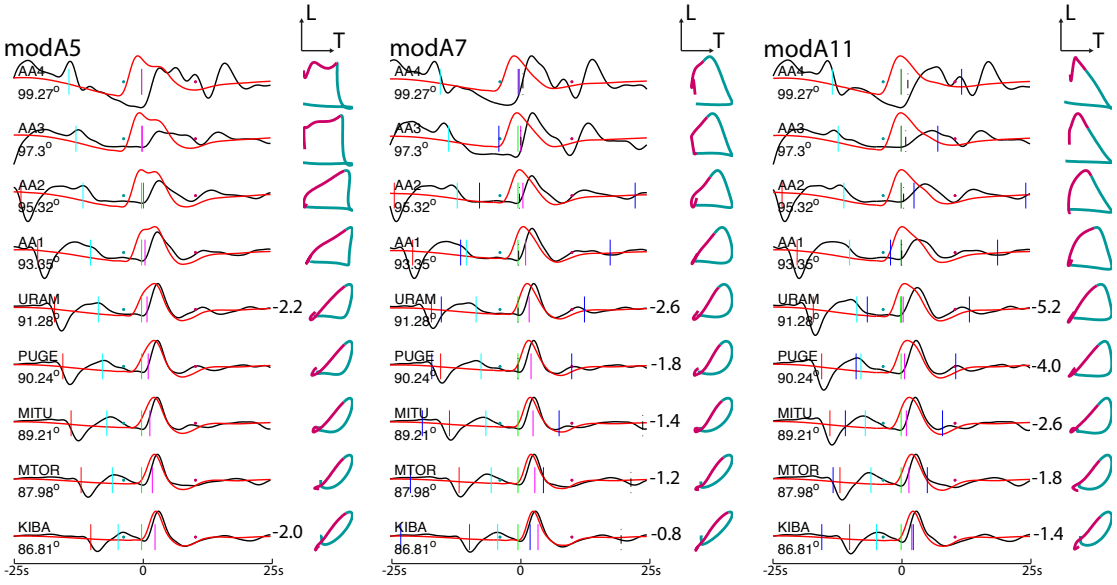

Figure 6.24: As in Fig. 6.16 but for the anisotropic models modA5, modA7 and modA11. Vertical bars correspond to the theoretical SV arrival times for the corresponding earth models.

3-D Earth models.

Fig. 6.25 compares real data observations for the Banda sea earthquake with theoretical calculations for our preferred 1-D anisotropic model (modA11) and for the 3-D model S40RTS superimposed on modA11. The 3-D structue has an effect not only on the onset of the S waves but also on the shape of the waveforms. It increases the SH-SV splitting by around 1 s.

To first order, synthetics calculated in the 3-D radially anisotropic structure match the data relatively well in terms of S onset, wave shape and SH-SV splitting, but some differences

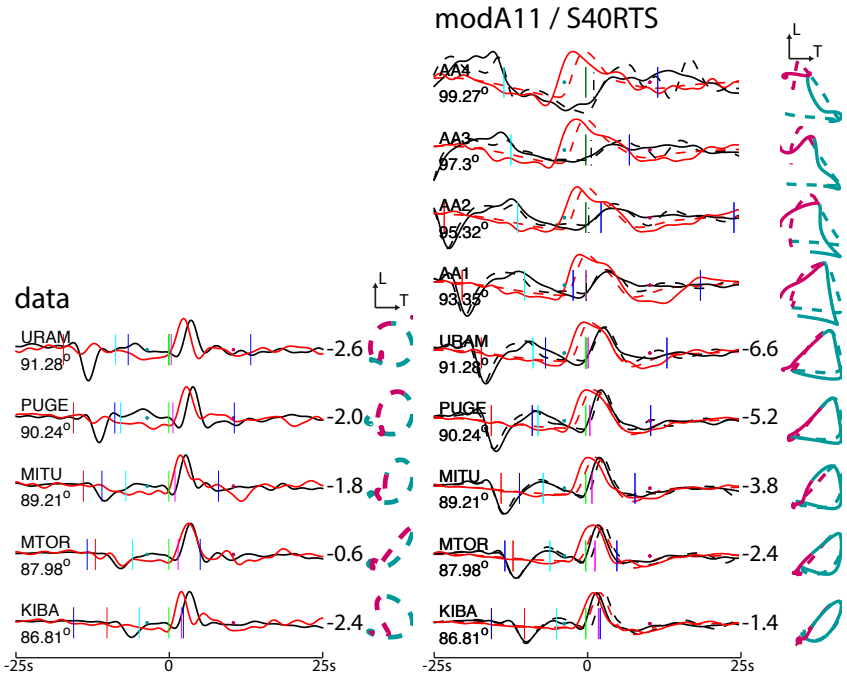

Figure 6.25: a) Observed displacement S(diff) waveforms for the Banda Sea earthquake. (b) Comparison between theoretical waveforms calculated for our preferred 1-D anisotropic model modA11 (dashed lines) and for S40RTS superimposed on modA11 (solid lines). The vertical bars correspond to the theoretical SV arrival times for model modA11. Black and red traces are radial (SV) and transverse (SH) seismogram components, respectively. Waveforms are aligned with respect the S(diff) arrivals. All the traces are convolved with a Gaussian source time function with a half duration of 2.9 s and filtered using a cosine low-pass filter leading to a dominant period of T~7 s. Particle motions are reported on the right of each pair of waveforms, aquamarine and purple dots on the waveforms mark the start and the end of the particle motion plots.

remain. This may be due to the fact that uppermost mantle anisotropy has not been included in the modelling, which will be the subject of future work.

6.6 DISCUSSION AND CONCLUSIONS

Several seismological and multidisciplinary studies have been carried out on the enigmatic D" layer (see, e.g., the review by Nowacki *et al.*, 2011, and references therein). Some previous seismic studies focussed on the possibility of anisotropy based on the splitting observed between horizontally and vertically polarised S waves travelling in the lowermost mantle (e.g., Kendall & Silver, 1996).

One of the limitations in previous SH-SV splitting studies is the subjectivity of peak/onset picking. SH-SV splitting measurements are complicated by noise, waveform complexity and uneven data coverage in the globe. For example Garnero & Lay (1997) and Kawai & Geller (2010) based their studies on waveform cross-correlation and waveform inversion, respectively, to overcome this problem but these techniques require strong waveform similarity, which is not always the case. Moreover, the accuracy of such studies is limited by

the approximate forward modelling techniques usually employed in the analysis (e.g., ray-based approaches). This is problematic because the finite frequency of the S waves is an important factor that influences the region of sensitivity of such waves. Moreover, sharp transitions of the seismic parameters also produce strong scattering effects that cannot be neglected.

Taking advantage of accurate modelling techniques as the SEM method (e.g., Komatitsch & Vilotte, 1998) and Gemini (Friederich & Dalkolmo, 1995), we extensively modelled the complete seismic wavefield for over 30 different Earth models. We focussed on waveforms recorded at epicentral distances ranging from 90° to 120° in the radial and transverse components and on a time window centred on the theoretical S arrival. We measured the splitting between the theoretical SH and SV polarised waves by cross-correlation and discussed only the splitting values associated with a cross-correlation coefficient larger than 0.85.

Our study was motivated by the findings of Maupin (1994) and Komatitsch *et al.* (2010b), which showed that apparent SH-SV splitting of S waves travelling in the lowermost mantle could be generated without invoking an anisotropic D" layer. Using a simple 1-D isotropic model, KO10 modelled a negative SHdiff-SVdiff apparent splitting (SH in advance) increasing with epicentral distance and reaching 2.4 s at Δ=120°. After reproducing the same experiment, we showed that the the SHdiff phase is apparently in advance because of interference between Sdiff and sS waves. Different polarities of the S and sS phases in the radial and transverse components lead to different interference effects for SV and SH waves. In order to avoid such phase superimposition effects, earthquake sources deeper than a few hundreds of km should be used. Moreover, even the combination moment tensor/azimuth of the stations can enhance or weaken the apparent splitting measured. Maupin (1994) suggested, in fact, that the study of more than one source mechanism for the same ray path can help to distinguish the effects of isotropic and anisotropic structure. However, this option is not always available when dealing with real data.

We then tried to model the observed SH-SV splitting of ~2 s generated by a deep earthquake in the Banda Sea, recorded by several stations azimuthally aligned with the source (Ritsema, 2000), using 1-D and 3-D isotropic models. We found that a 1-D model with a 150 km-thick D" layer and a positive Vs jump of ~2% at its top can generate SH-SV splitting comparable to that observed in the real data. Ray-theory helped us understand that such apparent splitting is caused by the interference of the ScS wave with a S wave triplicated at the top of the D". However, ray-theory could not predict that structure at a depth of ~3 040 km can affect S waves with dominant period of about 7 s and travelling at Δ<90°. In fact, from a ray viewpoint, the ray paths should not reach that depth, but accurate wavefield calculations highlighted the non-ray, finite frequency character of the S waves considered in this study.

For some epicentral distances, the ScS and S phases can also interfere as a function of the Vs gradient in the D". Hence, the widths of the SV and SH pulses are different. Since the ScS pulse can have different polarity in the radial and transverse components, S-ScS interference may be different in the two components. For example, Kendall & Silver (1998) recognise that

the S and ScS phases are very close in the seismograms, so that they preferred to study them as a single phase. Thus, studies of S waves travelling in the lower mantle should only consider relatively short epicentral distances (less then 95°) to avoid ScS contamination. Another factor that strongly affects the width of the S pulse is the attenuation model. In particular, we found that the attenuation in the PREM model seems too strong to fit waveform data travelling down to the lowermost mantle.

Testing the effects of radially anisotropic structure on the waveforms, we found that they are more complex than expected. In particular, the SH-SV splitting due to anisotropy can be complicated by Vs jumps at the top of the D" and by velocity gradients within the D". A radial anisotropy of ξ=1.07–1.08 in a 300 km thick D" layer is necessary to explain the splitting observed in the data here analysed. However, 3-D heterogeneity, values of η and gradient of ξ can also strongly affect the modelling. Moreover, more complex types of anisotropy not tested in this study (e.g., azimuthal anisotropy) may also affect our results.

To conclude, S waves crossing the lowermost mantle offer a great opportunity to study the elusive D" layer. However, these waves are affected by several factors along their path as well as by uncertainties in the source model. Hence, the forward modelling of such waves and its interpretation can be quite challenging when used to fit the data. Interpretations on the shape, polarisation and splitting of such waves should be cautiously performed.

7

CONCLUSIONS AND FUTURE WORK

7.1 CONCLUSIONS

In this thesis we extensively simulated the seismic wavefield at global scale. We employed two approximate methods, the first-order Born approximation (BORN, e.g., Capdeville, 2005) and surface wave full ray theory (FRT, e.g., Ferreira & Woodhouse, 2007a), to model long-period (~60 s–150 s) surface waveforms and assess whether their accuracy is satisfactory in the framework of waveform tomography. We compared the predictions of BORN and FRT against complete seismic wavefield calculations based on a purely numerical approach, the spectral element method (SEM, e.g., Komatitsch & Vilotte, 1998).

Although BORN is increasingly being used in many seismic tomography efforts, notably to model travel-times, because it takes into account finite-frequency and scattering effects, we found that it has a very limited validity domain when applied to seismic waveforms and realistic earth models. Rayleigh and Love waveform phase predictions are accurate for earth models with small scale-length/weak heterogeneity, notably for source-receiver paths leading to time shifts smaller than about 15 per cent of the dominant period of the surface waves. On average, this condition occurs for global mantle models such as S20RTS (Ritsema *et al.*, 1999) or S40RTS (Ritsema *et al.*, 2011) only for wave periods longer than T~80 s–90 s and when crustal heterogeneity is neglected. For stronger mantle heterogeneity and/or heterogeneous crustal structure, only the phase of surface waves with periods longer than T~120 s–130 s can be accurately modelled. Amplitude predictions are accurate only for waves with period longer than ~150 s and when mantle models with unrealistically weak heterogeneity are considered.

Conversely, despite the computational simplicity of the FRT, we found that it is able to model phase and amplitude of Rayleigh waves accurately for almost all the realistic earth models considered. We found that the general ray-theory validity condition $\lambda \ll \Omega$ is too stringent. Also, a worsening of the FRT predictions with the increase of the wave-length (and the wave period) is found only for the amplitude modelling and not for the phase.

The cases whereby the FRT failed (errors in phase larger than 5% and in amplitude larger than 10%) involved earth models with unrealistically rough heterogeneity. This suggests that the FRT is useful to build the next generation of models based on surface waves, which is encouraging, since intensive numerical wavefield simulations useful for global tomography are still computationally unaffordable when using standard academic HPC facilities. We could not obtain final results on the performance of FRT for Love waves because of the strong contamination of fundamental mode waveforms by overtones. However, our initial results suggest that FRT's performance may be as good as for Rayleigh (see appendix A).

We chose to assess BORN and FRT because in principle the domains of applicability of the ray-theory and scattering theory are different. BORN is expected to work for weak media and the FRT should be valid for smooth earth models. We expected that when the domains of validity intersect the results are the same. However, we conclude that the finite-frequency, scattering and diffraction effects neglected by the FRT are minimal, at least in the range of frequencies here considered, making BORN's validity domain to be actually included in the FRT's domain. Our findings reflect experimental observations of seismic waveforms in realistic earth models. That is, our results are not suggesting that the FRT is a better mathematical approximation than the Born approximation. Our findings rather suggest that heterogeneity in the real Earth is too strong to be modelled using BORN calculations of seismic waveforms, but perhaps smooth enough to be modelled by the FRT (at least given our current knowledge of 3-D Earth structure and for the wave periods considered).

On the other hand, purely numerical approaches, such as the spectral element method, represent a powerful and affordable tool in seismology when only tens of simulations are needed. In addition to the tests of BORN and FRT, in this thesis we used SEM in two further applications. We assessed the quality of the new global radially anisotropic mantle model, SGLOBE-rani (Chang *et al.*, 2015). The two reasons why performing these tests on global models is important are: i) despite new developments of anisotropic tomography in the past few years, there are still large discrepancies between existing models, suggesting large uncertainties; (ii) SGLOBE-rani is based on ray theory, and thus it is important to estimate the errors introduced in the model due to theoretical shortcomings using independent datasets and accurate waveform simulations.

We found that SGLOBE-rani explains the data better than the widely used S40RTS mantle model. However, the small differences in phase predictions between SGLOBE-rani and S40RTS compared to real data misfits suggest that more efforts must be done to improve current tomographic models (e.g., including higher frequency datasets, improving crustal corrections, using more accurate theories such as the FRT). The large amplitude misfits (> 30% between predictions and real data) obtained for both SGLOBE-rani and S40RTS might be in part attributed to errors in focussing and defocussing effects due to laterally varying elastic structure. However, an accurate global 3-D attenuation tomography model is probably also necessary to better explain observed amplitudes of surface waves. Finally, tests performed using different versions of SGLOBE-rani show that there are small misfit differences between them, highlighting the difficulties in constraining global anisotropy in the Earth's mantle.

Finally, we carried out forward modelling experiments of short-period (T>5 s) body waves travelling through the Earth's lowermost mantle and investigated the effects of isotropic (1-D and 3-D), anisotropic and attenuation structure on wave propagation. We found that, even if a radially anisotropic D" layer can partially explain the splitting observed in SH and SV polarised waves, the effects of radial anisotropy on the waveforms are not simple and linear as might be expected. In fact, the ratio Vsh/Vsv is not the only factor affecting the SH-SV wave splitting but other seismic parameters, as η, strongly influence the splitting amplitude. Moreover, even isotropic earth models can generate an apparent SH-SV wave splitting. In fact, we found that the interference between phases arriving close to each other can change the shape and the apparent arrival-time of the wave pulses. For example, a strong positive seismic discontinuity at the top of an isotropic D" layer can generate an apparent splitting between SV and SH polarised waves of more than 1 seconds. The constructive or destructive interference of phases with small differential arrival-times strongly depends on the polarity and amplitude of the wave pulses. The latter are strongly affected by factors not taken into account by ray-theory, such as scattering and diffraction occurring at the discontinuities of spherically symmetric earth models and at the edges of seismic anomalies in laterally varying models. We have been able to model these effects because of the complete wavefield calculations allowed by the purely numerical approaches used in this study.

We believe that there is not a best or worst forward modelling theory. There must be a responsible choice by seismologists to use the appropriate method depending on the purpose of the designed study (e.g., type of seismic wave, frequency band, study region, etc) and errors due to the forward modelling used should be quantified.

7.2 FUTURE WORK

In the following we present some directions of how we might develop further the research work carried out in this thesis:

- Calculate surface wave overtones with the FRT. This would enable to check whether the boundary of the validity domain found for the fundamental mode Rayleigh waves is also valid for the overtones. If a similar error–roughness relationship is found, the FRT would be sufficiently accurate to also model the deeper regions of the upper mantle and transition zone, since overtones sample regions deeper than the correspondent fundamental mode and the mantle's heterogeneity is expected to be smoother from depths greater than 250 km–350 km. Moreover, we would be able to rigorously assess the accuracy of the FRT when modelling Love waves and systematically estimate the correlation between overtone contamination effects, for both Rayleigh and Love waves, and the accuracy of the modelling. These results could allow the inclusion of both fundamental and overtones, Rayleigh and Love waves, in a waveform inversion scheme. The so obtained seismograms could be inverted using a "full" waveform approach, without the need to measure the arrival-times of the individual modes.

- Implement the crustal thickness variations from SGLOBE-rani in our experiments assessing tomography models. This would allow checking whether the surface wave predictions of SGLOBE-rani improve when using its own crustal model. The numerical experiments could be extended to other crustal models (varying Moho depth and seismic wave speed distributions) to systematically assess the effects of crustal structure on surface waves with different dominant periods.

- Assess the quality of SGLOBE-rani in the lower mantle using short-period body-waves (T~10 s).

- Assess the accuracy of a wide set of existing global isotropic and anisotropic mantle models. This could give interesting insights on the accuracy of the approximate techniques in the construction of the models and, more generally, on the tomographic procedures employed.

- Simulate SEM wave fields both propagating into the lowermost mantle (e.g., generated by other earthquakes) and targeting other interesting regions of the Earth, such as the mantle transition zone and the lithosphere-astenosphere boundary.

A

CONTAMINATION OF FUNDAMENTAL MODE LOVE WAVES BY OVERTONES

A.1 INTRODUCTION

In chapter 4 we investigate the accuracy of the full ray theory (FRT) when modelling fundamental mode surface waves. Whereas the windowing of the fundamental mode Rayleigh waves is straightforward because the mode is well isolated, we notice that Love wave overtones are often superimposed in time onto the fundamental mode (see Fig. 4.1 in chapter 4). This fact does not allow us to isolate the fundamental mode of Love waves with our simple strategy (see section 4.4 in chapter 4).

Our FRT calculations only contain the fundamental mode. Conversely, the SEM seismograms represent the complete seismic wavefield. Hence, the FRT–SEM comparisons for Love waves are affected by a source of errors difficult to estimate. Despite these errors, our results suggest that the FRT performs well when modelling the phase of Love waves in almost all the models used. However, we cannot be sure whether this positive result is due to the chosen thresholds of goodness employed (E_ϕ<5 % and E_A<10 %, see section 4.4.1 in chapter 4) or because the contamination of the fundamental mode by the overtones has limited effects in such models. Whilst this aspect will be investigated further in the future, the analogous analysis performed for Rayleigh waves in chapter 4 is here reported for Love waves.

A.2 LOVE WAVE PHASE VELOCITY MAPS

Love wave phase velocity maps for some of the models used in chapter 4 have already been shown in chapter 3, though the nomenclature of the models is slightly different. Fig. 3.5 (chapter 3) shows the phase velocity maps for the models obtained by varying l_{max} (in the FRT studys these models correspond to: third row–models *a*; second row–model *b*; first row–model *c*). Fig. 3.3 (chapter 3) depicts the phase velocity maps for the models obtained by

varying the PV factor (first row–model *d*; second row–model *e*; third row–models *f*). Love

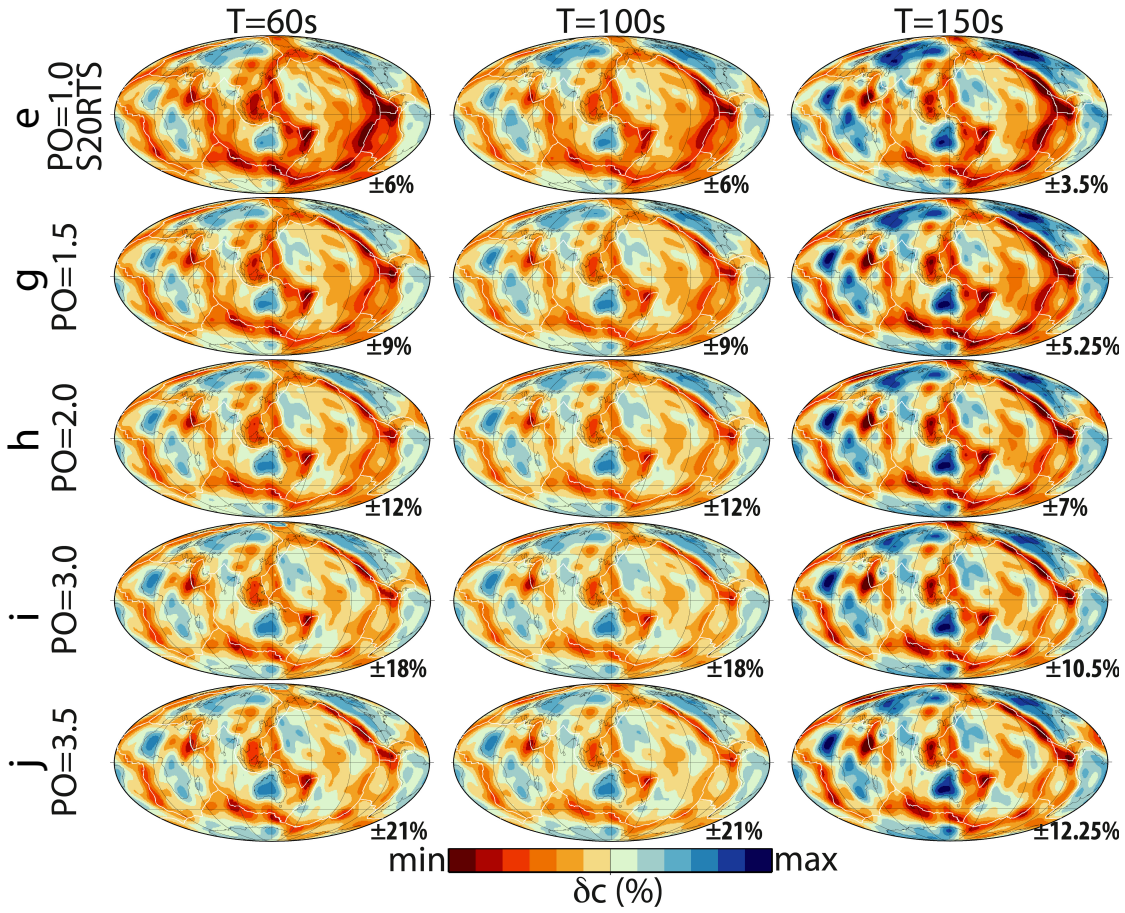

Figure A.1: Fundamental mode Love wave phase velocity maps calculated for mantle models with PO=1.0 (S20RTS), 1.5, 2.0, 3.0, 3.5 for wave periods T~ 60 s, 100 s, 150 s. These mantle models are combined with a homogeneous crustal layer and are referred as models *e*, *g*, *h*, *i* and *j*, respectively, throughout chapter 4 and this appendix. The numbers on the bottom right side of the maps represent the colour scale ranges.

wave phase velocity maps of models obtained by varying the PO factor are shown in Fig. A.1 (models *e*, *g*, *h*, *i* and *j*). Finally, maps for the S20RTS mantle model combined with the two 3-D crustal models are depicted in Fig. A.2 (models *l* and *m*). The *R* values (roughness, Eq. 4.1 of chapter 4) and power spectra for all these Love wave phase velocity maps are reported in Table A.1 and Fig. A.3, respectively. Fig. A.3 also reports the power spectra for Rayleigh waves for comparison.

By comparing the roughness values (see Tables A.1 and 4.1 in chapter 4) and power spectra (Fig. A.3), we notice that heterogeneity of the Love wave phase velocity maps are always stronger (and then rougher) than the heterogeneity for the Rayleigh wave phase velocity maps at the same wave period. This is due to the fact Love waves have different depth sensitivities. In fact, in the range of wave period considered in this thesis, Love waves have the peak of sensitivity at shallower depth (where the earth heterogeneity is stronger) compared to the depth of the sensitivity peak of Rayleigh waves at the same period.

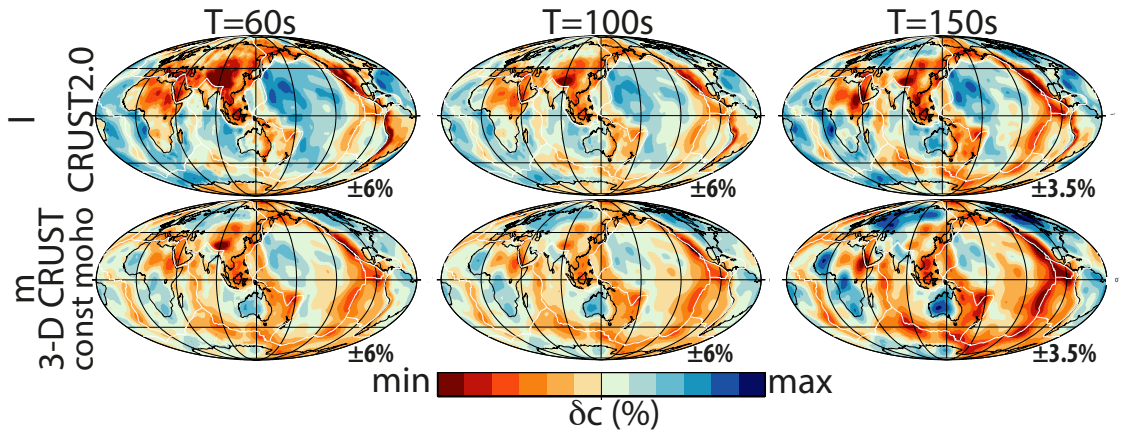

Figure A.2: Fundamental mode Love wave phase velocity maps for wave periods T~ 60 s, 100 s, 150 s calculated for the mantle model S20RTS combined with CRUST2.0 (top row) and a simplified version of CRUST2.0 with constant Moho depth (bottom row). These crustal models are referred as models l and m throughout chapter 4 and this appendix. The numbers on the bottom right side of the maps represent the colour scale ranges.

		G1		
	Models/Periods	60s	100s	150s
a	l_{max}=12	1.3	1.2	1.0
b	l_{max}=20	1.5	1.4	1.3
c	l_{max}=40	2.0	1.8	1.6
d	PV=0.5	1.0	0.9	0.7
e	PV=1.0	2.0	1.7	1.5
f	PV=1.75	3.4	0.3	2.5
g	PO=1.5	2.9	2.6	2.3
h	PO=2.0	3.8	3.4	2.8
i	PO=3.0	6.0	5.1	4.3
j	PO=3.5	8.3	5.9	5.0
k	l_{max}=40 PO=3.0	6.1	5.4	4.8
l	CRUST2.0	2.7	2.0	1.6
m	const_moho	2.0	1.7	1.4

Table A.1: Roughness (R as in Eq. 4.1) values of all the Love wave phase velocity maps used in this study for wave periods of T~60 s, 100 s and 150 s.

A.3 ERROR ANALYSIS

Analogously to the waveform comparisons carried out for Rayleigh waves in chapter 4, here we calculate phase E_ϕ and amplitude E_A errors at T~60 s, 100 s and 150 s by comparing SEM and FRT Love waveforms. The summary of these comparisons is shown in Fig. A.4.

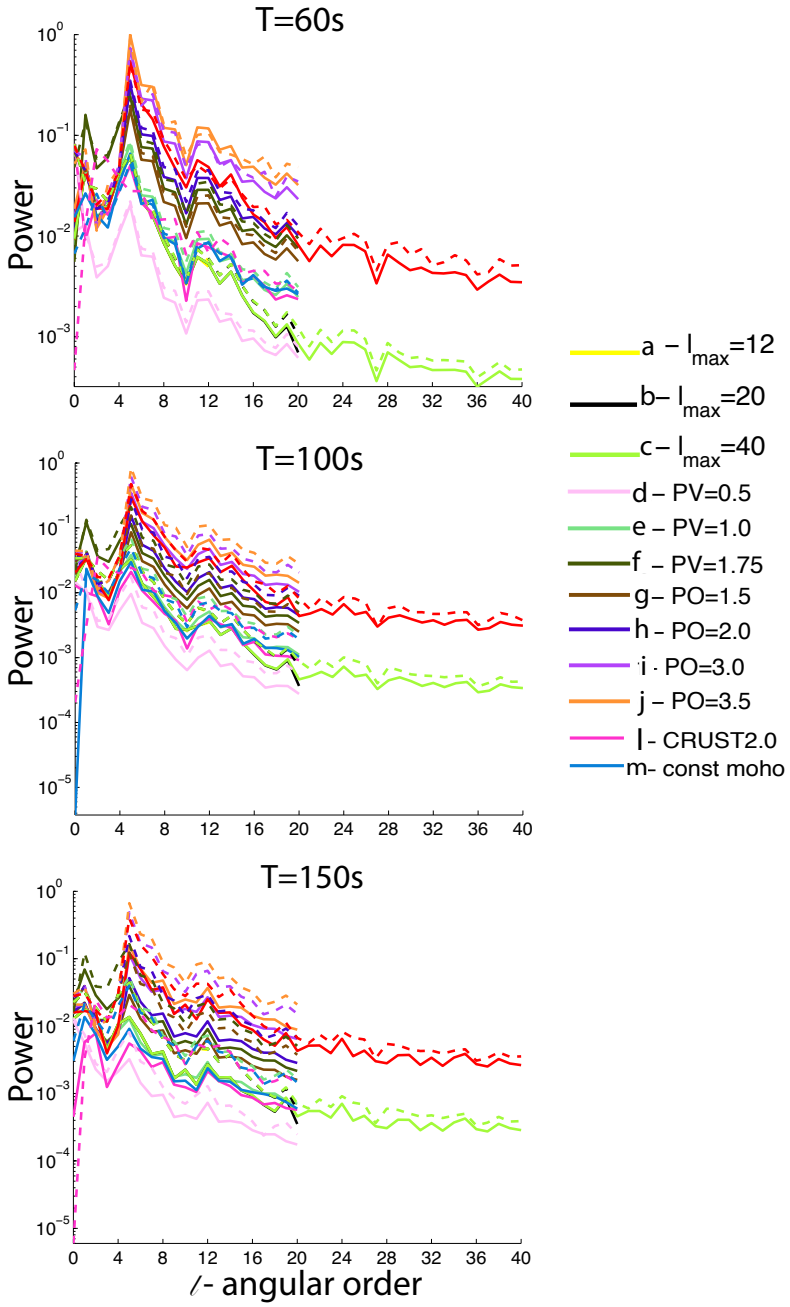

Figure A.3: Power spectra of Rayleigh (solid lines) and Love (dashed lines) wave phase velocity maps at T~ 60 s, 100s and 150 s for all the earth models considered in this study.

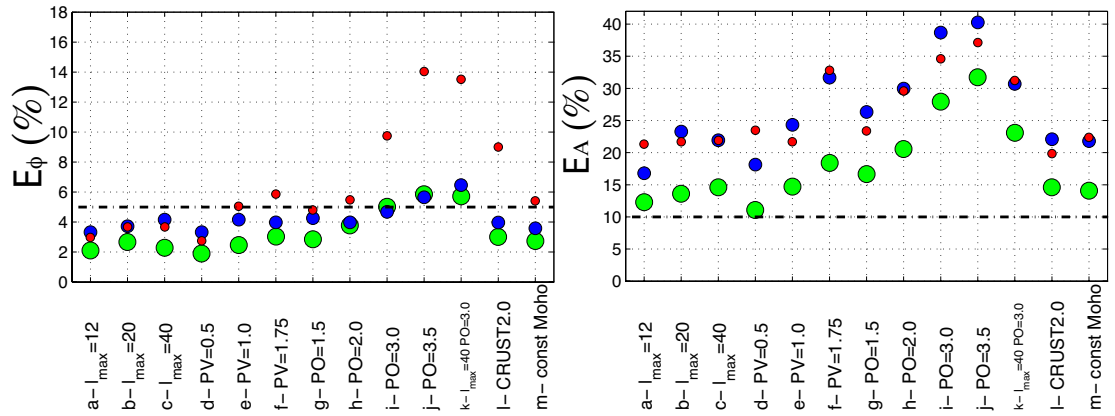

Figure A.4: Summary of the phase E_ϕ and amplitude E_A errors at T~60 s, 100 s and 150 s for all the models used. E_ϕ and E_A values are the medians for each model and period computed for all the paths illustrated in Fig. 3.1 (chapter 3). The horizontal black dash-dot lines correspond to the error thresholds of 5 % for E_ϕ and 10 % for E_A.

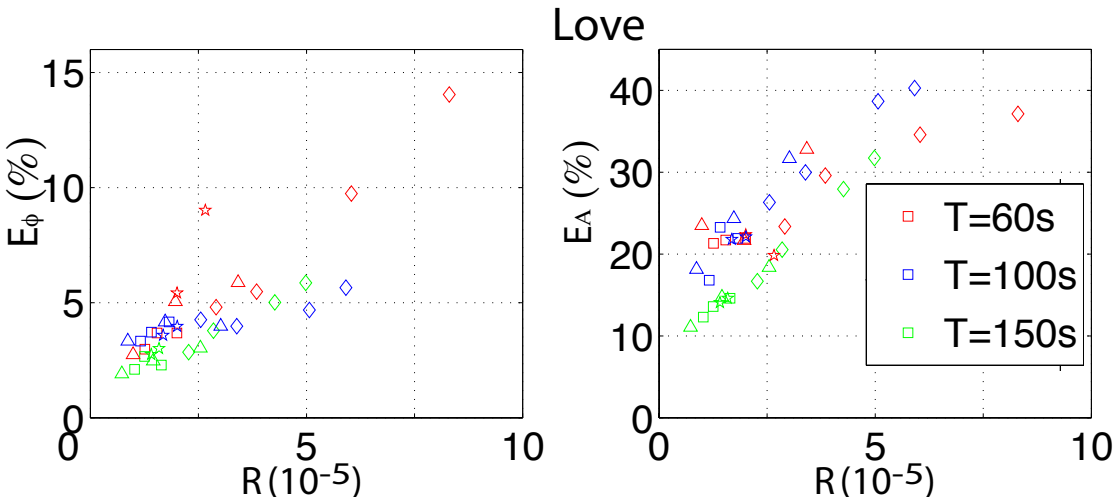

Figure A.5: Scatter plot of E_ϕ and E_A against the roughness R (Eq. 4.1) of the corresponding Love wave phase velocity maps. The different symbols correspond to distinct families of models: (i) varying l_{max} (models *a*–*c*; squares); (ii) varying the PV factor (models *d*–*f*; triangles); (iii) varying the PO factor (models *g*–*j*; diamonds); and, (iv) with 3-D crustal structure (models *l*–*m*; stars).

We notice E_ϕ and E_A for Love waves are both negatively correlated to the wave period. While the relation E_ϕ–period is the same as that observed for Rayleigh waves, the relation E_A–period is the opposite of what observed for Rayleigh waves. The anticorrelation between E_A and the wave period is probably due to the contamination by the overtones which has a larger effect at shorter periods(see Fig. 4.1 in chapter 4).

Moreover, the contamination effects seem to impact more the amplitude than the phase modelling. In fact, E_A is above the goodness threshold (10 %) for all the models and periods considered. On the other hand, despite the overtone contaminations, E_ϕ is (almost) under the threshold of goodness (5 %) for all the models with PO≤2.0 for all the wave periods considered, except for T~60 s when the complex 3-D crustal structure as that in CRUST2.0 is considered.

Despite the overtone contamination, E_ϕ for Love waves is related to R with a correlation coefficient of 0.82 (Fig. A.5). For R less than 2.5 x 10^{-5}, the FRT models the phase of Love waves with an error smaller than 5 %. The R limit would be probably larger if the fundamental mode was isolated. The correlation between E_A and R present different trends for the three different periods (correlation coefficients equal to 0.88 for T~60 s, 0.97 for T~100 s and 0.99 for T~150 s) but, as already discussed, in no case a satisfying amplitude modelling of Love wave is obtained.

A.4 CONCLUSIONS

The contamination of the fundamental mode by the overtones did not allow us to accurately assess the accuracy of the FRT in modelling Love waveforms. In future studies, the Love overtones will also be modelled with the FRT enabling a more complete analysis of these surface waves, similarly to what obtained in the Born approximation study (BORN, see chapter 3). In light of these considerations, we point out that the results obtained for the modelling the fundamental mode of surface waves with BORN, can possibly be extended to the overtones.

REFERENCES

Aki, K., & Richards, P.G. 1980. *Quantitative Seismology: Theory and Methods,*. Vol. 1. Freeman.

Anderson, D.L., Schreiber, E., Liebermann, R.C., & Soga, N. 1968. Some elastic constant data on minerals relevant to geophysics. *Rev. Geophys.*, 491–524.

Auer, L., Boschi, L., Becker, T.W., Nissen-Meyer, T., & Giardini, D. 2014. Savani: A variable resolution whole-mantle model of anisotropic shear velocity variations based on multiple data sets. *Journal of Geophysical Research: Solid Earth*, **119**(4), 3006–3034.

Backus, G. E., & Gilbert, F. 1967. Numerical applications of a formalism for geophysical inverse problems. *Geophys. J. R. Astron. Soc.*, **13**.

Bagley, B., & Revenaugh, J. 2008. Upper mantle seismic shear discontinuities of the Pacific. *Journal of Geophysical Research: Solid Earth*, **113**(12).

Bao, H., Bielak, J., Ghattas, O., Kallivokas, L.F., O'Hallaron, D.R., Shewchuk, J.R., & Xu, J. 1998. Large-scale simulation of elastic wave propagation in heterogeneous media on parallel computers. *Computer Methods in Applied Mechanics and Engineering*, **152**(1-2), 85–102.

Bassin, C, Laske, G., & Masters, G. 2000. The current limits of resolution for surface wave tomography in North America. *EOS Trans. AGU*, **F897**, 81.

Becker, T., & Boschi, L. 2002. A comparison of tomographic and geodynamic mantle models. *Geochemistry Geophysics Geosystems*, **3**, 1003+.

Bercovici, D., & Karato, S.-I. 2003. Whole-mantle convection and the transition-zone water filter. *Nature*, **425**(6953), 39–44.

Bhattacharyya, J., Masters, G., & Shearer, P. 1996. Global lateral variations of shear wave attenuation in the upper mantle. *Journal of Geophysical Research B: Solid Earth*, **101**(B10), 22273–22289.

Bodin, T., Capdeville, Y., & Romanowicz, B. 2015. *The Earth's heterogeneous mantle*. Springer. Chap. Interpreting Radial Anisotropy in Global and Regional Tomographic Models.

Boschi, L., & Ekström, G. 2002. New images of the Earth's upper mantle from measurements of surface wave phase velocity anomalies. *Journal of Geophysical Research B: Solid Earth*, **107**(4), 1–1.

Bozdağ, E., & Trampert, J. 2008. On crustal corrections in surface wave tomography. *Geophysical Journal International*, **172**(3), 1066–1082.

Bozdağ, E., & Trampert, J. 2010. Assessment of tomographic mantle models using spectral element seismograms. *Geophysical Journal International*, **180**(3), 1187–1199.

Bullen, K. 1940. The problem of the Earth's density variation. *B. Seismol. Soc. Am.*, **30**.

Bullen, K. 1949. An Earth Model Based on a Compressibility-Pressure Hypothesis. *Mon. Not. R. Astron. Soc.*, **109**.

Capdeville, Y. 2005. An efficient Born normal mode method to compute sensitivity kernels and synthetic seismograms in the Earth. *Geophys. J. Int.*

Capdeville, Y., Stutzmann, E., & Montagner, J.P. 2000. Effect of a plume on long period surface waves computed with normal modes coupling. *Physics of the Earth and Planetary Interiors*, **119**(1-2), 57–74.

Capdeville, Y., Larmat, C., Vilotte, J.-P., & Montagner, J.-P. 2002. A new coupled spectral element and modal solution method for global seismology: A first application to the scattering induced by a plume-like anomaly. *Geophysical Research Letters*, **29**(9), 32–1.

Capdeville, Y., To, A., & Romanowicz, B. 2003a. Coupling spectral elements and modes in a spherical Earth: An extension to the 'sandwich' case. *Geophysical Journal International*, **154**(1), 44–57.

Capdeville, Y., Chaljub, E., Vilotte, J.P., & Montagner, J.P. 2003b. Coupling the spectral element method with a modal solution for elastic wave propagation in global earth models. *Geophysical Journal International*, **152**(1), 34–67.

Chaljub, E., & Tarantola, A. 1997. Sensitivity of SS precursors to topography on the upper-mantle 660-km discontinuity. *Geophysical Research Letters*, **24**(21), 2613–2616.

Chaljub, E., Capdeville, Y., & Vilotte, J. . 2003. Solving elastodynamics in a fluid-solid heterogeneous sphere: A parallel spectral element approximation on non-conforming grids. *Journal of Computational Physics*, **187**(2), 457–491.

Chang, S.-J., Ferreira, A.M.G., Ritsema, J., Van Heijst, H.J., & Woodhouse, J.H. 2014. Global radially anisotropic mantle structure from multiple datasets: A review, current challenges, and outlook. *Tectonophysics*, **617**, 1–19.

Chang, S.-J., Ferreira, A. M. G., Ritsema, J., van Heijst, H. J., & Woodhouse, J. H. 2015. Joint inversion for global isotropic and radially anisotropic mantle structure including crustal thickness perturbations. *Journal of Geophysical Research: Solid Earth*, **120**(6), 4278–4300.

Chen, M., Niu, F., Liu, Q., Tromp, J., & Zheng, X. 2015. Multiparameter adjoint tomography of the crust and upper mantle beneath East Asia: 1. Model construction and comparisons. *Journal of Geophysical Research B: Solid Earth*, **120**(3), 1762–1786.

Chen, P., Zhao, L., & Jordan, T.H. 2007. Full 3D tomography for the crustal structure of the Los Angeles region. *Bulletin of the Seismological Society of America*, **97**(4), 1094–1120.

Cormier, V.F. 1999. Anisotropy of heterogeneity scale lengths in the lower mantle from PKIKP precursors. *Geophysical Journal International*, **136**(2), 373–384.

Crotwell, H. P., Owens, T. J., & Ritsema, J. 1999. The TauP Toolkit: Flexible seismic travel-time and ray-path utilities. *Seismological Research Letters*, **72**, 154–160.

Dahlen, F.A., & Tromp, J. 1998. *Theoretical global seismology*.

Dalton, C. A., Hjörleifsdóttir, V., & Ekström, G. 2014. A comparison of approaches to the prediction of surface wave amplitude. *Geophys. J. Int*, **196**, 386–404.

Dalton, C.A., Ekström, G., & Dziewoński, A.M. 2008. The global attenuation structure of the upper mantle. *Journal of Geophysical Research: Solid Earth*, **113**(9).

Dalton, C.A., Ekström, G., & Dziewoński, A.M. 2009. Global seismological shear velocity and attenuation: A comparison with experimental observations. *Earth and Planetary Science Letters*, **284**(1-2), 65–75.

Debayle, E., & Ricard, Y. 2012. A global shear velocity model of the upper mantle from fundamental and higher Rayleigh mode measurements. *Journal of Geophysical Research: Solid Earth*, **117**(10).

Deuss, A., & Woodhouse, J.H. 2001. Theoretical free-oscillation spectra: The importance of wide band coupling. *Geophysical Journal International*, **146**(3), 833–842.

Deuss, A., Redfern, S.A.T., Chambers, K., & Woodhouse, J.H. 2006. The nature of the 660-kilometer discontinuity in Earth's mantle from global seismic observations of PP precursors. *Science*, **311**(5758), 198–201.

Deuss, A., Ritsema, J., & Van Heijst, H. 2011. Splitting function measurements for Earth's longest period normal modes using recent large earthquakes. *Geophysical Research Letters*, **38**(4).

Durek, J.J., & Ekström, G. 1996. A radial model of anelasticity consistent with long-period surface-wave attenuation. *Bulletin of the Seismological Society of America*, **86**(1 SUPPL. A), 144–158.

Dziewoński, A. M., & Anderson, D. L. 1981. Preliminary reference Earth model. *Physics of the Earth and Planetary Interiors*, **25**(4), 297–356.

Dziewoński, A.M., Hager, B.H., & O'Connell, R.J. 1977. Large scale heterogeneities in the lower mantle. *J. Geophys. Res.*, **82**, 239–255.

Dziewoński, A.M., Chou, T.-A., & Woodhouse, J.H. 1981. Determination of earthquake source parameters from waveform data for studies of global and regional seismicity. *Journal of Geophysical Research*, **86**(B4), 2825–2852.

Ekström, G. 2011. A global model of Love and Rayleigh surface wave dispersion and anisotropy, 25-250s. *Geophysical Journal International*, **187**(3), 1668–1686.

Ekström, G., & Dziewonski, A.M. 1998. The unique anisotropy of the Pacific upper mantle. *Nature*, **394**(6689), 168–172.

Ekström, G., Tromp, J., & Larson, E.W.F. 1997. Measurements and global models of surface wave propagation. *Journal of Geophysical Research B: Solid Earth*, **102**(B4), 8137–8157.

Faccioli, E., Maggio, F., Paolucci, R., & Quarteroni, A. 1997. 2D and 3D elastic wave propagation by a pseudo-spectral domain decomposition method. *Journal of Seismology*, **1**(3), 237–251.

Ferreira, A. M. G., & Woodhouse, J. H. 2007a. Source, path and receiver effects on seismic surface waves. *Geophys. J. Int*, **168**(1), 109–132.

Ferreira, A.M.G. 2005. *Seismic surface waves in the laterally heterogeneous earth*. University of Oxford: PhD Thesis.

Ferreira, A.M.G., & Woodhouse, J.H. 2007b. Observations of long period Rayleigh wave ellipticity. *Geophysical Journal International*, **169**(1), 161–169.

Ferreira, A.M.G., Woodhouse, J.H., Visser, K., & Trampert, J. 2010. On the robustness of global radially anisotropic surface wave tomography. *Journal of Geophysical Research: Solid Earth*, **115**(4).

Ferreira, A.M.G., Weston, J., & Funning, G.J. 2011. Global compilation of interferometric synthetic aperture radar earthquake source models: 2. Effects of 3-D Earth structure. *Journal of Geophysical Research: Solid Earth*, **116**(8).

Fichtner, A., Kennett, B.L.N., Igel, H., & Bunge, H.-P. 2009. Full seismic waveform tomography for upper-mantle structure in the Australasian region using adjoint methods. *Geophysical Journal International*, **179**(3), 1703–1725.

Fischer, K.M., Ford, H.A., Abt, D.L., & Rychert, C.A. 2010. The lithosphere-asthenosphere boundary. *Annual Review of Earth and Planetary Sciences*, **38**, 551–575.

Fouch, M.J., Fischer, K.M., & Wysession, M.E. 2001. Lowermost mantle anisotropy beneath the Pacific: Imaging the source of the Hawaiian plume. *Earth and Planetary Science Letters*, **190**(3-4), 167–180.

French, S., Lekić, V., & Romanowicz, B. 2013. Waveform tomography reveals channeled flow at the base of the oceanic asthenosphere. *Science*, **342**(6155), 227–230.

French, S.W., & Romanowicz, B.A. 2014. Whole-mantle radially anisotropic shear velocity structure from spectral-element waveform tomography. *Geophysical Journal International*, **199**(3), 1303–1327.

Friederich, W., & Dalkolmo, J. 1995. Complete synthetic seismograms for a spherically symmetric Earth by a numerical computation of the Green's function in the frequency domain. *Geophys. J. Int*, **122**(2), 537–550.

Fukao, Y., & Obayashi, M. 2013. Subducted slabs stagnant above, penetrating through, and trapped below the 660 km discontinuity. *Journal of Geophysical Research: Solid Earth*, **118**(11), 5920–5938.

Furumura, M., Kennett, B.L.N., & Furumura, T. 1998. Anomalous surface waves associated with deep earthquakes, generated at an ocean ridge. *Geophysical Journal International*, **134**(3), 663–676.

Garmany, J. 1988. Seismograms in stratified anisotropic media - II. Uniformly asymptotic approximations. *Geophys. J.*, 379–389.

Garnero, E. J., & Lay, T. 1997. Lateral variations in lowermost mantle shear wave anisotropy beneath the north Pacific and Alaska. *Journal of Geophysical Research: Solid Earth*, **102**(B4), 8121–8135.

Garnero, Edward J., & McNamara, Allen K. 2008. Structure and Dynamics of Earth's Lower Mantle. *Science*, **320**(5876), 626–628.

Garnero, E.J., Maupin, V., Lay, T., & Fouch, M.J. 2004. Variable azimuthal anisotropy in earth's lowermost mantle. *Science*, **306**(5694), 259–261.

Gilbert, F. 1971. Excitation of normal modes of the Earth by earthquake sources. *Geophys. J. R. astr. Soc.*, **22**.

Gilbert, F. 1980. *Proc. 'Enrico Fermi' Int. Sch. Phys.* Vol. vol. LXXVII. Chap. An introduction to low-frequency seismology, pages 41–81.

Gu, Y.J., & Dziewoński, A.M. 2002. Global variability of transition zone thickness. *Journal of Geophysical Research B: Solid Earth*, **107**(7).

Gung, Y., & Romanowicz, B. 2004. Q tomography of the upper mantle using three-component long-period waveforms. *Geophysical Journal International*, **157**(2), 813–830.

Hess, R. 1964. Seismic anisotropy of the uppermost mantle under the oceans. *Nature*, **203**.

Hofmann, A.W. 1997. Mantle geochemistry: The message from oceanic volcanism. *Nature*, **385**(6613), 218–229.

http://www.orfeus eu.org. *Observatories and Research Facilities for European Seismology*.

Hwang, Y.K., Ritsema, J., & Goes, S. 2011. Global variation of body-wave attenuation in the upper mantle from teleseismic P wave and S wave spectra. *Geophysical Research Letters*, **38**(8).

Igel, H. 1999. Wave propagation in three-dimensional spherical sections by the Chebyshev spectral method. *Geophysical Journal International*, **136**(3), 559–566.

Igel, H., & Weber, M. 1996. P-SV wave propagation in the Earth's mantle using finite differences: Application to heterogeneous lowermost mantle structure. *Geophysical Research Letters*, **23**(5), 415–418.

Iitaka, T., Hirose, K., Kawamura, K., & Murakami, M. 2004. The elasticity of the MgSiO3 post-perovskite phase in the Earth's lowermost mantle. *Nature*, **430**(6998), 442–445.

Kawai, K., & Geller, R.J. 2010. The vertical flow in the lowermost mantle beneath the Pacific from inversion of seismic waveforms for anisotropic structure. *Earth and Planetary Science Letters*, **297**(1-2), 190–198.

Kawakatsu, H., Kumar, P., Takei, Y., Shinohara, M., Kanazawa, T., Araki, E., & Suyehiro, K. 2009. Seismic evidence for sharp lithosphere-asthenosphere boundaries of oceanic plates. *Science*, **324**(5926), 499–502.

Kendall, J.-M., & Silver, P.G. 1996. Constraints from seismic anisotropy on the nature of the lowermost mantle. *Nature*, **381**(6581), 409–412.

Kendall, J.M., & Silver, P.G. 1998. *The Core-Mantle Boundary Region. Geodynamics Series.* Vol. 28. American Geophysical Union. Chap. Investigating causes of D" anisotropy.

Kennett, B.L.N., & Engdahl, E.R. 1991. Traveltimes for global earthquake location and phase identification. *Geophys. J. Int*, **105**(2), 429–465.

Kennett, B.L.N., & Nolet, G. 1990. The interaction of the S-wavefield with upper mantle heterogeneity. *Geophys. J. Int*, **101**(3), 751–762.

Komatitsch, D., & Tromp, J. 1999. Introduction to the spectral element method for three-dimensional seismic wave propagation. *Geophysical Journal International*, **139**(3), 806–822.

Komatitsch, D., & Tromp, J. 2002a. Spectral-element simulations of global seismic wave propagation - I. Validation. *Geophys. J. Int*, **149**(2), 390–412.

Komatitsch, D., & Tromp, J. 2002b. Spectral-element simulations of global seismic wave propagation - II. Three-dimensional models, oceans, rotation and self-gravitation. *Geophys. J. Int*, **150**(1), 303–318.

Komatitsch, D., & Vilotte, J.-P. 1998. The spectral element method: An efficient tool to simulate the seismic response of 2D and 3D geological structures. *Bulletin of the Seismological Society of America*, **88**(2), 368–392.

Komatitsch, D., Barnes, C., & Tromp, J. 2000a. Simulation of anisotropic wave propagation based upon a spectral element method. *Geophysics*, **65**(4), 1251–1260.

Komatitsch, D., Barnes, C., & Tromp, J. 2000b. Wave propagation near a fluid-solid interface: A spectral-element approach. *Geophysics*, **65**(2), 623–631.

Komatitsch, D., Ritsema, J., & Tromp, J. 2002. Geophysics: The spectral-element method, beowulf computing, and global seismology. *Science*, **298**(5599), 1737–1742.

Komatitsch, D., Erlebacher, G., Göddeke, D., & Michéa, D. 2010a. High-order finite-element seismic wave propagation modeling with MPI on a large GPU cluster. *Journal of Computational Physics*, **229**(20), 7692–7714.

Komatitsch, D., Vinnik, L.P., & Chevrot, S. 2010b. SHdiff-SVdiff splitting in an isotropic Earth. *Journal of Geophysical Research: Solid Earth*, **115**(7).

Kosloff, D.D., & Baysal, E. 1982. Forward modeling by a Fourier method. *Geophysics*, **47**(10), 1402–1412.

Kustowski, B., Ekström, G., & Dziewoński, A.M. 2008. Anisotropic shear-wave velocity structure of the earth's mantle: A global model. *Journal of Geophysical Research: Solid Earth*, **113**(6).

Larson, E.W.F., Tromp, J., & Ekström, G. 1998. Effects of slight anisotropy on surface waves. *Geophys. J. Int*, **132**(3), 654–666.

Lawrence, J. F., & Wysession, M. E. 2006. Chap. Seismic evidence for subduction-transported water in the lower mantle.

Lebedev, S., Chevrot, S., & Van der Hilst, R.D. 2002. Seismic evidence for olivine phase changes at the 410- and 660-kilometer discontinuities. *Science*, **296**(5571), 1300–1302.

Lebedev, S., Nolet, G., Meier, T., & van der Hilst, R.D. 2005. Automated multimode inversion of surface and S waveforms. *Geophys. J. Int*, **162**(3), 951–964.

Lebedev, S., Adam, J.M.-C., & Meier, T. 2013. Mapping the Moho with seismic surface waves: A review, resolution analysis, and recommended inversion strategies. *Tectonophysics*, **609**, 377–394.

Lekić, V., & Romanowicz, B. 2011. Inferring upper-mantle structure by full waveform tomography with the spectral element method. *Geophysical Journal International*, **185**(2), 799–831.

Lekić, V., Panning, M., & Romanowicz, B. 2010. A simple method for improving crustal corrections in waveform tomography. *Geophysical Journal International*, **182**(1), 265–278.

Lekić, V., Cottaar, S., Dziewoński, A., & Romanowicz, B. 2012. Cluster analysis of global lower mantle tomography: A new class of structure and implications for chemical heterogeneity. *Earth and Planetary Science Letters*, **357-358**, 68–77.

Leveque, J.-J., Rivera, L., & Wittlinger, G. 1993. On the use of the checker-board test to assess the resolution of tomographic inversions. *Geophysical Journal International*, **115**(1), 313–318.

Li, Xiang-Dong, & Romanowicz, B. 1995. Comparison of global waveform inversions with and without considering cross-branch modal coupling. *Geophys. J. Int*, **121**(3), 695–709.

Li, Xiang-Dong, & Tanimoto, T. 1993. Waveforms of long-period body waves in a slightly aspherical Earth model. *Geophysical Journal International*, **112**(1), 92–102.

Liu, H. P., Anderson, D. L., & Kanamori, H. 1976. Velocity dispersion due to anelasticity; implications for seismology and mantle composition. *Geophysical Journal International*, **47**(1), 41–58.

Lognonné, P. 1991. Normal modes and seismograms in an anelastic rotating Earth. *J. geophys. Res.*, **96**(20), 309–319.

Loubet, N., Ribe, N. M., & Gamblin, Y. 2009. Deformation modes of subducted lithosphere at the core-mantle boundary: An experimental investigation. *Geochemistry, Geophysics, Geosystems*, **10**(10).

Love, A. E. H. 1911. *Some problems of geodynamics*. Cambridge: Cambridge University Press.

Masters, G., Laske, G., Bolton, H., & Dziewoński, A. 2000. The relative behavior of shear velocity, bulk sound speed, and compressional velocity in the mantle: implications for chemical and thermal structure. *Earth's Deep Interior,eds. Karato S., Forte A.M., Liebermann R.C., Masters G. and Stixrude L., AGU Monograph 117, AGU, Washington, DC.*

Maupin, V. 1994. On the possibility of anisotropy in the D" layer as inferred from the polarization of diffracted S waves. *Physics of the Earth and Planetary Interiors*, **87**(1-2), 1–32.

Maupin, V., Garnero, E.J., Lay, T., & Fouch, M.J. 2005. Azimuthal anisotropy in the D" layer beneath the Caribbean. *Journal of Geophysical Research B: Solid Earth*, **110**(8), 1–20.

McNamara, A.K., & Zhong, S. 2005. Thermochemical structures beneath Africa and the Pacific Ocean. *Nature*, **437**(7062), 1136–1139.

McNamara, A.K., Garnero, E.J., & Rost, S. 2010. Tracking deep mantle reservoirs with ultra-low velocity zones. *Earth and Planetary Science Letters*, **299**(1-2), 1–9.

Meade, C., Silver, P.G., & Kaneshima, S. 1995. Laboratory and seismological observations of lower mantle isotropy. *Geophysical Research Letters*, **22**(10), 1293–1296.

Megnin, C., & Romanowicz, B. 2000. The three-dimensional shear velocity structure of the mantle from the inversion of body, surface and higher-mode waveforms. *Geophysical Journal International*, **143**(3), 709–728.

Mercerat, D., & Nolet, G. 2013. On the linearity of cross-correlation delay times in finite-frequency tomography. *Geophysical Journal International*, **192**(2), 681–687.

Montagner, J.-P., & Jobert, N. 1988. Vectorial tomography - II. Application to the Indian Ocean. *Geophysical Journal*, **94**(2), 309–344.

Montagner, J.-P., & Kennett, B.L.N. 1996. How to reconcile body-wave and normal-mode reference earth models. *Geophysical Journal International*, **125**(1), 229–248.

Montelli, R., Nolet, G., Dahlen, F.A., Masters, G., Engdahl, E.R., & Hung, S.-H. 2004. Finite-Frequency Tomography Reveals a Variety of Plumes in the Mantle. *Science*, **303**(5656), 338–343.

Morse, P. M., & Feshbach, H. 1953. *Methods of Theoretical Physics*. McGraw Hill.

Moulik, P., & Ekström, G. 2014. An anisotropic shear velocity model of the Earth's mantle using normal modes, body waves, surface waves and long-period waveforms. *Geophys. J. Int*, **199**(3), 1713–1738.

Murakami, M., Hirose, K., Kawamura, K., Sata, N., & Ohishi, Y. 2004. Post-Perovskite Phase Transition in MgSiO3. *Science*, **304**(5672), 855–858. cited By 702.

Nissen-Meyer, T., van Driel, M., Stähler, S. C., Hosseini, K., Hempel, S., Auer, L., Colombi, A., & Fournier, A. 2014. AxiSEM: broadband 3-D seismic wavefields in axisymmetric media. *Solid Earth*, **5**(1), 425–445.

NOAA. 1988. *National Oceanic and Atmospheric Administration (NOAA) Product Information Catalog - ETOPO5 Earth Topography 5-minute digital model*. Tech. rept. U.S. Department of Commerce, Washington D.C., USA. 171 pages.

Nolet, G. 2014. *Handbook of geomathematics*. Chap. Transmission Tomography in Seismology.

Nolet, G., & Dahlen, F.A. 2000. Wave front healing and the evolution of seismic delay times. *Journal of Geophysical Research: Solid Earth*, **105**(B8), 19043–19054.

Nowacki, A., Wookey, J., & Kendall, J.-M. 2010. Deformation of the lowermost mantle from seismic anisotropy. *Nature*, **467**(7319), 1091–1094.

Nowacki, A., Wookey, J., & Kendall, J.-M. 2011. New advances in using seismic anisotropy, mineral physics and geodynamics to understand deformation in the lowermost mantle. *Journal of Geodynamics*, **52**(3-4), 205–228.

Oganov, A.R., & Ono, S. 2004. Theoretical and experimental evidence for a post-perovskite phase of MgSiO3 in Earth's D" layer. *Nature*, **430**(6998), 445–448.

Panning, M.P., Capdeville, Y., & Romanowicz, B.A. 2009. Seismic waveform modelling in a 3-D Earth using the Born approximation: Potential shortcomings and a remedy. *Geophys. J. Int*, **177**(1), 161–178.

Paolucci, R., & Faccioli, E.and Maggio, F. 1999. 3D Response analysis of an instrumented hill at Matsuzaki, Japan, by a spectral method. *Journal of Seismology*, **3**(2), 191–209.

Parisi, L., & Ferreira, A.M.G. Empirical assessment of surface waves full ray theory validity in realistic 3-D earth models. *Submitted to Geophys. J. Int.*

Parisi, L., Ferreira, A.M.G., & Capdeville, Y. 2015. Validity domain of the Born approximation for seismic waveform modelling in realistic 3-D Earth structure. *Geophys. J. Int*, **200**, 908–914.

Patera, A.T. 1984. A spectral element method for fluid dynamics: Laminar flow in a channel expansion. *Journal of Computational Physics*, **54**(3), 468–488.

Pekeris, C. L., & Jarosch, H. 1958. *Contributions in Geophysics in Honor of Beno Gutenberg*. New York: Pergamon. Chap. The free oscillations of the Earth.

Peter, D., Boschi, L., & Woodhouse, J.H. 2009. Tomographic resolution of ray and finite-frequency methods: A membrane-wave investigation. *Geophys. J. Int*, **177**(2), 624–638.

Phinney, R. A., & Burridge, R. 1973. Representation of the elastic-gravitational excitation of a spherical earth model by generalized spherical harmonics. *Geophys. J. R. Astron. Soc.*, **34**.

Priolo, E., Carcione, J.M., & Seriani, G. 1994. Numerical simulation of interface waves by high-order spectral modeling techniques. *Journal of the Acoustical Society of America*, **95**(2), 681–693.

Pulliam, J., & Sen, M.K. 1998. Seismic anisotropy in the core-mantle transition zone. *Geophysical Journal International*, **135**(1), 113–128.

Qin, Y., Capdeville, Y., Montagner, J.-P., Boschi, L., & Becker, T.W. 2009. Reliability of mantle tomography models assessed by spectral element simulation. *Geophysical Journal International*, **177**(1), 125–144.

Richards, P. G. 1976. On the adequacy of plane-wave reflection/transmission coefficients in the analysis of seismic body waves. *Bull Seismol. Soc. Am.*, **66**(3), 701–717.

Ritsema, J. 2000. Evidence for shear velocity anisotropy in the lowermost mantle beneath the Indian Ocean. *Geophysical Research Letters*, **27**(7), 1041–1044.

Ritsema, J., & van Heijst, H. 2002. Constraints on the correlation of P- and S-wave velocity heterogeneity in the mantle from P, PP, PPP and PKPab traveltimes. *Geophysical Journal International*, **149**(2), 482–489.

Ritsema, J., Lay, T., Garnero, E.J., & Benz, H. 1998. Seismic anisotropy in the lowermost mantle beneath the Pacific. *Geophysical Research Letters*, **25**(8), 1229–1232.

Ritsema, J., Van Heijst, H.J., & Woodhouse, J.H. 1999. Complex shear wave velocity structure imaged beneath Africa and Iceland. *Science*, **286**(5446), 1925–1931.

Ritsema, J., van Heijst, H.J., Woodhouse, J.H., & Deuss, A. 2009. Long-period body wave traveltimes through the crust: Implication for crustal corrections and seismic tomography. *Geophysical Journal International*, **179**(2), 1255–1261.

Ritsema, J., Deuss, A., Van Heijst, H.J., & Woodhouse, J.H. 2011. S40RTS: A degree-40 shear-velocity model for the mantle from new Rayleigh wave dispersion, teleseismic traveltime and normal-mode splitting function measurements. *Geophys. J. Int*, **184**(3), 1223–1236.

Ritzwoller, Michael H., & Levshin, Anatoli L. 1998. Eurasian surface wave tomography: Group velocities. *Journal of Geophysical Research: Solid Earth*, **103**(B3), 4839–4878.

Robertson, G.S., & Woodhouse, J.H. 1995. Evidence for proportionality of P and S heterogeneity in the lower mantle. *Geophys. J. Int*, **123**(1), 85–116.

Romanowicz, B. 1987. Multiplet-multiplet coupling due to lateral heterogeneity: asymptotic effects on the amplitude and frequency of the Earth's normal modes. *Geophysical Journal - Royal Astronomical Society*, **90**(1), 75–100.

Romanowicz, B. 1995. A global tomographic model of shear attenuation in the upper mantle. *Journal of Geophysical Research*, **100**(B7), 12,375–12,394.

Romanowicz, B.A., Panning, M.P., Gung, Y., & Capdeville, Y. 2008. On the computation of long period seismograms in a 3-D earth using normal mode based approximations. *Geophys. J. Int*, **175**(2), 520–536.

Russell, S. A., Lay, T., & Garnero, E. J. 1998. Seismic evidence for small-scale dynamics in the lowermost mantle at the root of the Hawaiian hotspot. *Nature*, **396**(6708), 255–258.

Rychert, C.A., & Shearer, P.M. 2009. A global view of the lithosphere-asthenosphere boundary. *Science*, **324**(5926), 495–498.

Sadourny, R. 1972. Conservative finite-difference approximations of the primitive equations on quasi-uniform spherical grids. *Monthly Weather Review*, **100**, 136–144.

Savage, M.S. 1999. Seismic anisotropy and mantle deformation: What have we learned from shear wave splitting? *Reviews of Geophysics*, **37**(1), 65–106.

Schaeffer, A.J., & Lebedev, S. 2013. Global shear speed structure of the upper mantle and transition zone. *Geophys. J. Int*, **194**(1), 417–449.

Schmerr, N., & Garnero, E.J. 2007. Upper mantle discontinuity topography from thermal and chemical heterogeneity. *Science*, **318**(5850), 623–626.

Selby, N.D., & Woodhouse, J.H. 2002. The Q structure of the upper mantle: Constraints from Rayleigh wave amplitudes. *Journal of Geophysical Research B: Solid Earth*, **107**(5).

Seriani, G. 1998. 3-D large-scale wave propagation modeling by spectral element method on Cray T3E multiprocessor. *Computer Methods in Applied Mechanics and Engineering*, **164**(1-2), 235–247.

Shapiro, N.M., & Ritzwoller, M.H. 2002. Monte-Carlo inversion for a global shear-velocity model of the crust and upper mantle. *Geophysical Journal International*, **151**(1), 88–105.

Shearer, P.M., & Masters, T.G. 1992. Global mapping of topography on the 660-km discontinuity. *Nature*, **355**(6363), 791–796.

Snieder, R., & Romanowicz, B. 1988. A new formalism for the effect of lateral heterogeneity on normal modes and surface waves - I: isotropic perturbations, perturbations of interfaces and gravitational perturbations. *Geophysical Journal International*, **92**(2), 207–221.

Takeuchi, H., & Saito, M. 1972. *Methods of Computational Physics*. Vol. 11. Academic Press. Chap. Seismic surface waves.

Tanimoto, T. 1984. A simple derivation of the formula to calculate synthetic long-period seismograms in a heterogeneous Earth by normal mode summation. *Geophys. J. R. astr. Soc.*, **77**, 275–278.

Tape, C., Liu, Q., Maggi, A., & Tromp, J. 2009. Adjoint tomography of the southern california crust. *Science*, **325**(5943), 988–992.

Tape, C.H. 2003. *Waves on a spherical membrane*. University of Oxford: M.Sc. Thesis.

Tarantola, A. 1987. *Inverse Problem Theory*. Amsterdam: Elsevier.

Tauzin, B., Debayle, E., & Wittlinger, G. 2008. The mantle transition zone as seen by global Pds phases: No clear evidence for a thin transition zone beneath hotspots. *Journal of Geophysical Research: Solid Earth*, **113**(8).

Tauzin, B., Debayle, E., & Wittlinger, G. 2010. Seismic evidence for a global low-velocity layer within the Earth's upper mantle. *Nature Geoscience*, **3**(10), 718–721.

Thomas, C., Wookey, J., & Simpson, M. 2007. D" anisotropy beneath Southeast Asia. *Geophysical Research Letters*, **34**(4).

Thomas, Ch., & Kendall, J.-M. 2002. The lowermost mantle beneath northern Asia - II. Evidence for lower-mantle anisotropy. *Geophys. J. Int*, **151**(1), 296–308.

Toshinawa, T., & Ohmachi, T. 1992. Love-wave propagation in a three-dimensional sedimentary basin. *Bulletin - Seismological Society of America*, **82**(4), 1661–1677.

Tromp, J., & Dahlen, F.A. 1992a. Variational principles for surface wave propagation on a laterally heterogeneous earth - I. Time-domain JWKB theory. *Geophys. J. Int*, **109**, 581–598.

Tromp, J., & Dahlen, F.A. 1992b. Variational principles for surface wave propagation on a laterally heterogeneous Earth - II. Frequency-domain JWKB theory. *Geophys. J. Int*, **109**(3), 599–619.

Tromp, J., Tape, C., & Liu, Q. 2005. Seismic tomography, adjoint methods, time reversal and banana-doughnut kernels. *Geophysical Journal International*, **160**(1), 195–216.

Um, J., & Dahlen, F.A. 1992. Normal mode multiplet coupling on an aspherical, anelastic earth. *Geophys. J. Int*, **111**(1), 11–31.

Valentine, A. P., & Woodhouse, J. H. 2010. Reducing errors in seismic tomography: combined inversion for sources and structure. *Geophysical Journal International*, **180**(2), 847–857.

Vinnik, L., Romanowicz, B., Le Stunff, Y., & Makeyeva, L. 1995. Seismic anisotropy in the D" layer. *Geophysical Research Letters*, **22**(13), 1657–1660.

Vinnik, L., Breger, L., & Romanowicz, B. 1998. Anisotropic structures at the base of the Earth's mantle. *Nature*, **393**(6685), 564–567.

Virieux, J. 1984. SH- wave propagation in heterogeneous media: velocity- stress finite-difference method. *Geophysics*, **49**(11), 1933–1942.

Virieux, J. 1986. P- SV wave propagation in heterogeneous media: velocity- stress finite-difference method. *Geophysics*, **51**(4), 889–901.

Visser, K., Trampert, J., Lebedev, S., & Kennett, B.L.N. 2008. Probability of radial anisotropy in the deep mantle. *Earth and Planetary Science Letters*, **270**(3-4), 241–250.

Wang, Z., & Dahlen, F.A. 1994. JWKB surface-wave seismograms on a laterally heterogeneous earth. *Geophys. J. Int*, **119**, 381–401.

Wang, Z., & Dahlen, F.A. 1995. Validity of surface-wave ray theory on a laterally heterogeneous earth. *Geophys. J. Int*, **123**, 757–773.

Woodhouse, J. 1980. The coupling and attenuation of nearly resonant multiplets in the Earths free oscillation spectrum. *Geophys. J. R. astr. Soc.*, **61**, 261–283.

Woodhouse, J. H. 1974. Surface waves in a laterally varying layered structure. *Geophys. J. R. Astron. Soc.*, **37**(2), 461–490.

Woodhouse, J. H. 1976. On Rayleigh's principle. *Geophys. J. R. Astron. Soc.*, **46**.

Woodhouse, J. H. 1983. *Proc. 'Enrico Fermi' Int. Sch. Phys. LXXXV*. Vol. vol. LXXVII. Chap. The joint inversion of seismic waveforms for lateral variations in Earth structure and earthquake source parameters, pages 366–397.

Woodhouse, J.H., & Dziewoński, A.M. 1984. Mapping the upper mantle: three-dimensional modeling of Earth structure by inversion of seismic waveforms. *Journal of Geophysical Research*, **89**(B7), 5953–5986.

Woodhouse, J.H., & Girnius, T.P. 1982. Surface waves and free oscillations in a regionalized earth model. *Geophysical Journal, Royal Astronomical Society*, **68**(3), 653–673. cited By 56.

Woodhouse, J.H., & Wong, Y.K. 1986. Amplitude, phase and path anomalies of mantle waves. *Geophys. J. R. Astron. Soc.*, **87**, 753–773.

Wookey, J., & Kendall, J.-M. 2008. Constraints on lowermost mantle mineralogy and fabric beneath Siberia from seismic anisotropy. *Earth and Planetary Science Letters*, **275**(1-2), 32–42.

Wookey, J., Kendall, J.-M., & Rümpker, G. 2005. Lowermost mantle anisotropy beneath the north Pacific from differential S-ScS splitting. *Geophysical Journal International*, **161**(3), 829–838.

www.geodynamics.org. last access: 08.07.2015. *Computational Infrastructure for Geodynamics*.

www.globalcmt.org. *Global Centroid-Moment-Tensor catalogue*.

www.iris.edu. *Incorporated Research Institutions for Seismology*.

Wysession, M. E., Langenhorst, A., Fouch, M. J., Fischer, K. M., Al-Eqabi, G. I., Shore, P. J., & Clarke, T. J. 1999. Lateral Variations in Compressional/Shear Velocities at the Base of the Mantle. **284**(5411).

Wysession, M.E. 1996. Large-scale structure at the core-mantle boundary from diffracted waves. *Nature*, **382**(6588), 244–248.

Wysession, M.E., Lay, T., Revenaugh, J., Williams, Q., Garnero, E.J., Jeanloz, R., & Kellogg, L. 1998. *The Core-Mantle Boundary Region. Geodynamics Series, 28*. Washington, D.C., USA: American Geophysical Union. Chap. The D" discontinuity and its implications, pages 273–298.

Zaroli, C., Debayle, E., & Sambridge, M. 2010. Frequency-dependent effects on global S-wave traveltimes: Wavefront-healing, scattering and attenuation. *Geophysical Journal International*, **182**(2), 1025–1042.

Zhou, Y., Dahlen, F.A., & Nolet, G. 2004. Three-dimensional sensitivity kernels for surface wave observables. *Geophysical Journal International*, **158**(1), 142–168.

Zhou, Y., Nolet, G., Dahlen, F.A., & Laske, G. 2006. Global upper-mantle structure from finite-frequency surface-wave tomography. *Journal of Geophysical Research: Solid Earth*, **111**(4).